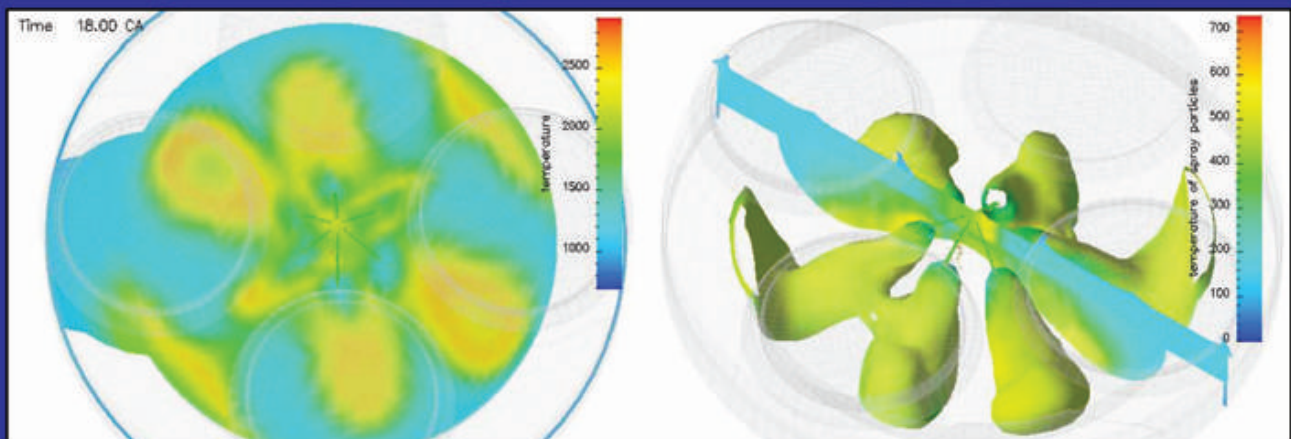


Jost Weber

Optimization Methods for the Mixture Formation and Combustion Process in Diesel Engines



Optimization Methods for the Mixture Formation and Combustion Process in Diesel Engines

Von der Fakultät für Maschinenwesen der
Rheinisch-Westfälischen Technischen Hochschule Aachen
zur Erlangung des akademischen Grades eines Doktors der
Ingenieurwissenschaften genehmigte Dissertation

vorgelegt von

Diplom-Ingenieur

Jost Weber

aus Siegen

Berichter: Univ.-Prof. Dr.-Ing. Dr. h.c. Dr.-Ing. E.h. N. Peters
Univ.-Prof. Dr.-Ing. (USA) S. Pischinger

Tag der mündlichen Prüfung: 21. Januar 2008

Bibliografische Information der Deutschen Nationalbibliothek

Die Deutsche Nationalbibliothek verzeichnet diese Publikation in der Deutschen Nationalbibliografie; detaillierte bibliografische Daten sind im Internet über <http://dnb.ddb.de> abrufbar.

1. Aufl. - Göttingen : Cuvillier, 2008

Zugl.: (TH) Aachen, Univ., Diss., 2008

978-3-86727-724-2

Zugl.: D 82 (Diss. RWTH Aachen University, 2008)

© CUVILLIER VERLAG, Göttingen 2008

Nonnenstieg 8, 37075 Göttingen

Telefon: 0551-54724-0

Telefax: 0551-54724-21

www.cuvillier.de

Alle Rechte vorbehalten. Ohne ausdrückliche Genehmigung des Verlages ist es nicht gestattet, das Buch oder Teile daraus auf fotomechanischem Weg (Fotokopie, Mikrokopie) zu vervielfältigen.

1. Auflage, 2008

Gedruckt auf säurefreiem Papier

978-3-86727-724-2

Für Mo & Max

Vorwort

Diese Arbeit entstand während meiner Tätigkeit als wissenschaftlicher Mitarbeiter am Institut für Technische Verbrennung an der RWTH Aachen.

Herrn Professor Dr.-Ing. Dr. h.c. Dr.-Ing. E.h. N. Peters danke ich für die Betreuung und Unterstützung dieser Arbeit. Herrn Professor Dr.-Ing. S. Pischinger danke ich für seine Tätigkeit als weiterer Berichtler und Herrn Professor Dr.-Ing. H. Murrenhof für die Übernahme des Vorsitzes der Prüfungskommission.

Allen Mitarbeitern des Instituts, die mich bei der Durchführung dieser Arbeit unterstützt haben, möchte ich ebenfalls danken, insbesondere Peter Spiekermann, Sylvie Honnet, Jens Ewald und Frank Freikamp, sowie meinen studentischen Mitarbeitern Michael Gauding, Franziska Schaub, Sven Funk und Bernhard Glodde. Es hat sehr viel Spaß gemacht !

Ein besonderer Dank gilt Donald Stanton von Cummins Inc. für die Bereitstellung von Motordaten. Desweiteren danke ich General Motors R&D Labs, Warren (MI), USA, für die finanzielle Unterstützung dieser Arbeit aus Mitteln des Collaborative Research Labs. Hier gilt mein Dank Sherif El Tahry und Andreas Lippert sowie allen anderen Mitgliedern des CRLs.

Der weitaus größte Dank gebührt meiner lieben Familie Mo und Max; auf Eure Unterstützung konnte ich mich stets verlassen.

Aachen, im Februar 2008

Jost Weber

Optimization Methods for the Mixture Formation and Combustion Process in Diesel Engines

Zusammenfassung

Die vorliegende Arbeit beschäftigt sich mit der Fragestellung, inwieweit heutige Simulationswerkzeuge in der Lage sind, die komplexen Vorgänge der Gemischbildung und Verbrennung im Dieselmotor zu berechnen. Als Simulationswerkzeug wird die numerische, dreidimensionale Strömungssimulation verwendet. Die Simulation des Verbrennungsprozesses stellt jedoch besondere Herausforderungen an die Numerik und die Ressourcen, so daß hier das Representativ Interactive Flamelet (RIF) Modell Anwendung findet. In diesem wird ein detaillierten Reaktionsmechanismus für einen Modellbrennstoff für Dieselkraftstoff verwendet. Die Simulation der Kraftstoffeinspritzung verwendet den weitverbreitete Lagrang'sche Ansatz des Discrete Droplet Models (DDM). Es zeigt sich jedoch, daß insbesondere die Berechnung des Kraftstoffsprays eine Anpassung von bis zu sechs Parametern erfordert. Diese Anpassung erfolgt in dem hier vorgestellten Ansatz mittels eines Optimierungswerkzeuges, einem Genetischen Algorithmus. Das Gütekriterium ist der Vergleich der berechneten und der gemessenen Eindringtiefen des Sprays unter motorähnlichen Bedingungen in einer Hochdruckkammer. Es wird ein Diesel- und ein Ethanol-spray untersucht. Nach Anpassung der Modellkonstanten zeigt sich, daß nicht nur die globalen Eindringtiefen, sondern auch lokale Größen übereinstimmen. Neben den Konstanten des Spraymodells sind bei der Simulation eines Dieselmotors weitere Anpassungen erforderlich. Beginnend von der Kompressionsphase unterliegen die Anfangs- und Randbedingungen bereits einem Optimierungsalgorithmus, um eine möglichst gute Übereinstimmung hinsichtlich der gemessenen und berechneten Zylinderdruckverläufe zu erhalten. Desweiteren muß gerade im Hinblick auf neuere Verbrennungsmoden die Reaktionskinetik für den Bereich der Niedertemperaturzündkinetik verifiziert und angepaßt werden. Nach Anpassung dieser Parameter steht ein Modell zur Verfügung, das an zwei Motorfällen Anwendung findet. Es zeigt sich, daß der Brennverlauf und die Schadstoffemissionen der Simulation gut mit den experimentellen Untersuchungen übereinstimmen.

Contents

1	Introduction	1
2	Fluid Dynamics	3
2.1	Conservation Equations in Fluid Dynamics	3
2.2	Mathematical Description of Turbulent Flows	10
2.2.1	Statistical Description	11
2.2.2	Reynolds Averaging	13
2.2.3	Favre Averaging	14
2.2.4	Length- and Time Scales in a Turbulent Flow	14
2.3	Reynolds Averaged Equations of a Turbulent Flow	16
2.3.1	Boussinesq Approximation	18
2.3.2	Closure of Momentum Conservation Equation	18
2.3.2.1	Algebraic Models	18
2.3.2.2	Turbulent Energy Equation	19
2.3.3	Closure of Enthalpy Conservation Equation	22
2.3.4	Closure of Species Conservation Equation	22
2.4	Favre-Averaged Equations of a Turbulent Flow	23
3	Combustion Model	25
3.1	Physics of Non-Premixed Combustion	25
3.2	Flamelet Model	26
3.2.1	Mixture Fraction Variable	27
3.2.2	Burke-Schumann's Equilibrium Solution	30
3.2.3	Flamelet Equations	31
3.2.3.1	Crocco Transformation	32

3.2.3.2	The Scalar Dissipation Rate	33
3.3	Modeling of Turbulent Transport	34
3.3.1	Turbulent Transport of Reactive Scalars	34
3.3.2	Modeling of Non-Premixed Turbulent Combustion	35
3.3.2.1	Turbulent Mixture Fraction Field	35
3.3.2.2	PDF-Approach for Non-Premixed Turbulent Combustion	36
3.4	The RIF-Model	39
3.5	Chemical Reaction Mechanism	40
3.5.1	Validation of Ignition Delay	42
3.5.2	Pollutant Formation	45
3.5.2.1	NO _x Formation	45
3.5.2.2	Soot-Model	48
3.5.2.3	Formation of Benzene	51
3.5.2.4	Growth of PAH	52
3.5.2.5	Soot Modeling	54
4	Spray Modeling	59
4.1	The Spray Equation	60
4.2	Discrete Droplet Model	60
4.2.1	Drag Force	61
4.2.2	Primary Atomization	62
4.2.3	Secondary Atomization	64
4.2.3.1	Droplet Breakup Regimes	64
4.2.3.2	Modeling of Droplet Breakup	66
4.2.4	Droplet-Droplet Interaction	69
4.2.4.1	Probability of Collision	70
4.2.4.2	Outcome of Collision	72
4.2.5	Droplet Evaporation	76
4.2.5.1	Evaporation Model	76
4.2.5.2	Evaporation Time	79
4.2.5.3	Influence of Temperature and Pressure on Evaporation	79

4.3	Turbulent Dispersion	81
5	Simulation of a Fuel Spray	85
5.1	Introduction	85
5.2	Spray Data	85
5.2.1	Injection Rate Measurement Technique	85
5.2.2	Spray Chamber	86
5.2.3	Optical Measurement Techniques	86
5.2.3.1	Mie/Shadow Imaging Technique	86
5.2.3.2	Raman Scattering Measurements	89
5.2.3.3	Droplet Size and Velocity by PDA Measurements	91
5.3	Calibration of Spray Parameters	91
5.3.1	Spray Model Parameters	91
5.3.2	Genetic Algorithm for Spray Calibration	93
5.3.3	Definition of a Merit Function	93
5.4	Calibration of Fuel Sprays	94
5.4.1	Diesel Spray	94
5.4.1.1	Investigated Nozzles	95
5.4.1.2	Diesel Spray Simulation	96
5.4.1.3	Calibration of Spray Parameters	97
5.4.1.4	Results from PDA-Measurements	99
5.4.1.5	Test Engine Case	104
5.4.2	Ethanol Spray	106
5.4.2.1	Introduction	106
5.4.2.2	Injection System	107
5.4.2.3	Ethanol Spray Simulation	108
5.4.2.4	Calibration of Spray Parameters	111
5.5	Evaporation Controlled Mixing	121
5.5.1	Re-Definition of Parameter Space	121
5.5.2	Comparison of Spray Penetration W/O Breakup and Collision Model	122

6 Diesel Engine Simulation	125
6.1 Optimization Methods for Diesel Engine Simulations	125
6.1.1 Compression Cycle	125
6.1.1.1 Compression Ratio	127
6.1.1.2 Intake Temperature	127
6.1.2 Injection Cycle	128
6.1.3 Expansion Cycle	128
6.2 Cummins Engine	129
6.2.1 Engine Data	129
6.2.2 Computational Mesh	129
6.2.3 Investigated Parameters	130
6.2.4 Optimization of Spray Parameters	131
6.2.5 Simulation Results	133
6.2.5.1 Pressure and Heat Release Data	133
6.2.5.2 Comparison of Emission Data	135
6.2.5.3 Cycle Resolved Emission Data	135
6.2.5.4 3D Temperature Field	136
6.3 Duramax Engine	142
6.3.1 Introduction	142
6.3.2 Engine Set-Up	142
6.3.2.1 Specifications of the Duramax Engine	142
6.3.2.2 Mesh Generation for CFD-Simulation	143
6.3.3 Conventional Combustion Mode	144
6.3.3.1 Operating Point	145
6.3.3.2 Combustion Analysis	145
6.3.3.3 Engine-Out Emissions	146
6.3.4 Premixed Charge Compression Ignition Combustion Mode	154
6.3.4.1 Operating Point	156
6.3.4.2 Combustion Analysis	156
6.3.4.3 Engine-Out Emissions	166
6.3.4.4 Flow-Field Analysis	173

7 Summary	183
A Genetic Algorithms	207
A.1 Evolutionary Algorithms	207
A.1.1 Basic Evolutionary Operators	207
A.1.1.1 Encoding/Decoding	208
A.1.1.2 Selection and Reproduction	209
A.1.1.3 Crossover	210
A.1.1.4 Mutation	211
A.1.2 Operational Rate Settings	212
A.1.2.1 Population Size	212
A.1.2.2 Rate of Mutation	213
A.1.2.3 Rate of Crossover	214
A.1.2.4 Adaptive Methods	214
A.1.3 Evaluation	214
A.1.4 Building Block Hypothesis	215
A.2 GA-Specific Operators	217
A.2.1 Elitism	217
A.2.2 Niching	217
A.2.3 μ GA	218
A.3 Multi-Objective Optimization	219
B Spray Parameter Sensitivity Study	221
B.1 Mesh Size	222
B.2 Time-Step Size	224
B.3 Number of Parcels	224
B.4 Cone-Angle	224
B.5 Nozzle Discharge Coefficient C_d	227
B.6 Fuel Temperature	228
B.7 Droplet Distribution Function	229
B.7.1 SMR of Droplet Distribution Function	229
B.7.2 Initial Droplet Distribution	229
B.7.3 Distribution Function Type	230

Contents

B.8 Droplet Breakup	232
B.8.1 Breakup Model Constant B_1	232
B.8.2 Liquid Breakup Length	233
B.9 Droplet Collision Model	233

Nomenclature

Latin Symbols

A	mol, cm^3 , s	frequency factor
a_{ij}	–	number of atoms j in species i
B	–	frequency factor, statistical property, impact parameter
B_0, B_1	–	spray model constants
b_{cr}	–	coalescence criteria
C	–	spray model constant
C_D	–	closure coefficient, drag coefficient, flow discharge coefficient
c_χ	–	proportionality constant
c_p	J/kgK	heat capacity at constant pressure
c_v	J/kgK	heat capacity at constant volume
d	m	droplet diameter
d_{ij}	–	multi-dimensional distance between two individuals i and j
D	–	relative number of alleles
D	m^2/s	thermal diffusivity
D_i	m^2/s	species diffusion coefficient
Da	–	Damköhler number
e	J/kg	specific energy
E	J	energy
E	J/mol	activation energy
E_{coal}	–	coalescence efficiency
\dot{f}^s	–	momentum exchange in two-phase flows
f	N/ m^3	body forces per unit volume

F	–	merit function, Euclidean norm
f_i	–	fitness of individual i
\bar{f}	–	mean fitness
$f_{\mathbf{u}}(\mathbf{U})$	–	probability density function(pdf)
$F_{\mathbf{u}}(\mathbf{U})$	–	statistical distribution of the velocity \mathbf{u}
f_V	–	soot volume fraction
\mathbf{g}	m/s^2	gravity constant
H	–	schemata
h	J/kg	specific enthalpy
\mathbf{I}	$\text{kg}^{\text{m}}/\text{s}$	momentum vector
\mathbf{I}	–	unit tensor
I_i	–	discretization size of parameter space
\mathbf{j}_i	$\text{mol}/\text{m}^2\text{s}$	molecular flux due to species diffusion
\mathbf{j}_q	$\text{J}/\text{m}^2\text{s}$	heat flux due to thermal diffusion
k	$1/\text{s}, \text{m}^3/\text{mol s}, \text{m}^6/\text{mol}^2 \text{s}$	reaction rate coefficient
k	J/kg	turbulent kinetic energy
KN_{crit}	–	non-dimensional cavitation number
K_r	J	effective reflective kinetic energy
Le_i	–	Lewis number
l	m	integral length scale
l_c	m	path-length of the next collision event
l_i	–	length of gene
l_{mfp}	m	mean free path length
l_{mix}	m	mixing length
L	m	characteristic length
L	–	length of the string
L_b	–	breakup length
L_i	–	lower limit
Le	–	Lewis number
m	kg	mass
\dot{m}	kg/s	mass flow rate
\dot{m}_1	kg/s	fuel stream

\dot{m}_2	kg/s	oxidizer stream
m_i	–	binary number which is denoted as <i>gene</i>
m	kg	mass
M_r	–	statistical moment
n	mol	number of moles
n	–	temperature exponent
\mathbf{n}	–	normal unit vector
n_{diff}	–	number of differing alleles
n_e	–	number of elements
N	–	number of species, population size
N_{dk}	–	number of droplets that are assigned by the parcel k
N_i	–	number of grid points of each parameter
N_j	$1/m^3$	number density
N_P	–	number of parcels
Nu	–	Nusselt number
Oh	–	Ohnesorg number
\tilde{P}	–	probability density function
p	Pa	pressure
p	–	probability
p_i	–	relative fitness
p_{ij}	–	collision probability
P_n	–	number of collision events
Pr	–	Prandtl number
\dot{Q}	J/s	heat source
\dot{q}	J/s kg	specific heat source
\mathcal{R}	J/kgK	specific gas constant
R_m	J/molK	molecular gas constant
r	m	radius
r_c	m	radius of a stable child-droplet
Re	–	Reynolds number
S	m^2	surface of the control volume
\mathbf{S}	m/s^2	strain rate tensor

Contents

Sc	–	Schmidt number
sh(d_{ij})	–	sharing function
Sh	–	Sherwood number
St	–	Stokes number
t	s	time
t_η	s	Kolmogorov time-scale
T	K	temperature
\mathbf{T}	N/m ²	viscous stress tensor
Ta	–	Taylor number
u	J/kg	specific inner energy
u	m/s	mean velocity
u'	m/s	turning velocity of large eddies
\mathbf{u}	m/s	mass center velocity
\mathbf{u}_b	m/s	velocity of moving control surface
\mathbf{u}_d	m/s	droplet velocity
\mathbf{u}_i	m/s	velocity of each species i
U_i	–	upper limit
V	m ²	volume
$\mathbf{v}_{i\alpha}$	m/s	diffusive velocity of species i
v_η	m/s	Kolmogorov velocity
v_{ij}	m/s	relative velocity between a pair of parcels
v_{mix}	m/s	mixing velocity
v_{mol}	m/s	average molecular velocity
W	g/mol	molar weight
We	–	Weber number
\mathbf{x}	m	point in space
x_i	m	spray penetration
X_i	–	species mole fraction
Y_i	–	species mass fraction
Z	–	mixture fraction
Z_j	–	element mass fraction

Greek Symbols

α_P	–	mean effective absorption coefficient
β	mol/g	coupling function
$\beta_{i,j}$	–	frequency factor
δ_{ij}	–	Kronecker symbol
δm	kg	infinitesimal mass
δV	m^3	infinitesimal volume
$\delta V'$	m^3	limit volume of a continuous fluid
Δ	–	droplet diameter ratio
$\Delta_{f,i}^0$	J/kg	heat of formation of species i
ΔH	J/kg	latent heat of vaporization
λ	W/mK	thermal heat conductivity
η	m	Kolmogorov scale
η	–	non-dimensional co-ordinate
ε	mol	reaction extent
$\varepsilon_{i,j}$	–	enhancement factor
ε	m^2/s^3	dissipation
ε_{ij}	–	dissipation term
Λ	m	wavelength
μ	kg/ms	viscosity
$\bar{\mu}$	–	mean expected number of collision events
μ	kg/ms	molecular viscosity
$\mu_{i,j}$	kg	reduced mass
ν	m^2/s	kinematic viscosity
ν_{ij}	1/s	collision frequency for a parcel pair (i, j)
ν_j	–	number of atoms of element j
ν'_{jk}, ν''_{jk}	–	stoichiometric reaction coefficient
Π_{ij}	–	pressure-rate-of-strain correlation term
ρ	kg/m ³	density
σ_{ij}	m^2	collision cross section of two drops
σ_k	–	closure coefficient

σ_i	–	variance
\mathbf{F}	N	force
\dot{Q}	J/kg	energy source
τ	s	integral time scale
τ_a	s	relaxation time
τ_{ij}	N/m ²	viscous part of the stress tensor
$\tau_{ij,t}$	N/m ²	Reynolds stress tensor
τ_{KH}	s	breakup time
τ_{xy}	N/m ²	molecular shear stress
ϕ	–	intensive property
$\overline{\phi}(\mathbf{x})$	–	Reynolds average of ϕ
$\phi'(\mathbf{x}, t)$	–	fluctuation of ϕ
$\tilde{\phi}(\mathbf{x}, t)$	–	Favre average of ϕ
ϕ	–	equivalence ratio
Φ	—	dissipation function
χ	m ² /s	scalar dissipation rate
ψ	–	characteristic function
ψ	–	reactive scalar
$\tilde{\psi}$	–	Favre-averaged reactive scalar
$\tilde{\psi}_i''$	–	fluctuations of $\tilde{\psi}_i$
Φ	–	extensive property
$\dot{\omega}_i$	mol/m ³ s	chemical source term
$\dot{\omega}_k$	mol/m ³ s	net reaction rate
Ω	m ³	control volume
Ω	–	maximum growth rate

Constants

c	300,000 m/s	velocity of light
k	1.381×10^{-23} [J][K]	Boltzmann constant
h	6.626×10^{-34} Js	Planck's constant
R	8.314 J/mol K	universal gas constant

σ_S	$5.670 \times 10^{-8} \text{ W/m}^2\text{K}^4$	Stefan-Boltzmann constant
------------	--	---------------------------

Indici

0	reference condition
1	fuel
2	oxidizer
$\overline{\phi}$	time-averaged mean
ϕ'	fluctuation part
$\tilde{\phi}$	Favre-averaged mean
ϕ''	fluctuation part
$\hat{\phi}$	volume-averaged mean
ad	adiabatic
<i>b</i>	backward, burnt
CV	control volume
CM	control mass
<i>c</i>	chemical, cross-over
<i>cm</i>	creep mutation
<i>d</i>	droplet
eff	effective
exp	experiment
evap	evaporation
<i>f</i>	forward
<i>g</i>	gaseous
<i>i</i>	species
inj	injected
<i>j</i>	atom, class
<i>l</i>	liquid
<i>m</i>	mutation
obj	objective
<i>p</i>	particle

<i>r</i>	radiation
ref	reference
<i>s</i>	surface
sim	simulation
st	stoichiometric
<i>t</i>	turbulent
<i>u</i>	unburnt
vap	vapor

Abbreviations

aTDC	after top dead center
AFR	air fuel ratio
AHRR	apparent heat release rate
BMEP	break mean effective pressure
CAE	computer aided engineering
CFD	computational fluid dynamics
CIDI	compression ignition direct injection
DDM	Discrete Droplet Model
DI	direct injection
EGR	exhaust gas recirculation
EOI	end of injection
EVO	exhaust valve opening
FSN	filtered smoke number
FTP	Federal Test Procedure
HACA	hydrogen-abstraction, carbon-addition
IMEP	indicated mean effective pressure
IVC	intake valve closure
KH	Kelvin-Helmholtz
MIRA	Motor Industry Research Association
MMEP	motoring mean effective pressure

OEM	Original Equipment Manufacturer
RIF	Representative Interactive Flamelet
PAH	polycyclic aromatic hydrocarbons
PCCI	Premixed Charge Compression Ignition
PM	particulates matter
PDA	Phase Doppler Anememotry
PDF	probability density function
RANS	Reynolds averaged Navier-Stokes
RT	Rayleigh-Taylor
SIDI	spark ignition direct injection
SMR	Sauter mean radius
SOI	start of injection
TDC	top dead center
UHC	unburnt hydrocarbons
VCO	valve covered orifice

1 Introduction

All over the world, Diesel engines are in use for power generation and transport with great success. One of the major benefits of the Diesel engine is its efficient energy conversion and high volumetric energy density. High torque at low speed was always a benefit of the Diesel engine for heavy duty applications. For passenger car applications the introduction of the turbo-charger and the direct injection system has released an increase of market shares more than 50% in Europe.

A major disadvantage are nevertheless the emissions formation. Particularly the particulates matter (PM) which consists mostly of soot, and NO_x emissions are subject of the emissions legislations. The emission regulations in the United States of America, Tier 2 / Bin 5 in 2007 and 2010, and in Europe, EURO 5 in 2010 and EURO 6 in 2014, request high challenges for all automotive companies and suppliers. The Diesel engine combustion has to become cleaner everbefore. Solutions for a clean combustion in the Diesel engine foresee a combination of lowered compression ratios, higher boost pressures, cooled EGR on the low- and high pressure side and new combustion concepts, e.g. the use of an early fuel injection strategy for a concept denoted as Premixed Charge Compression Ignition (PCCI).

Conventional combustion and advanced combustion modes are to be evaluated at different loads and speeds to find an optimal point with low engine-out emissions. This calibration work is usually a quite time consuming and cost intensive process. Computational Aided Engineering (CAE) offers here a solution to reduce these costs and shorten the development time. A virtual engine design can evaluate different bowl designs for a wide range of operating points and find optimal parameters much faster. However, this approach assumes that the underlying models for mixture formation, combustion and pollutant formation are physically well based and predictive.

It is therefore the objective of this thesis to study the spray and mixture formation

in Diesel sprays and the ongoing combustion process in Diesel engines by means of computational fluid dynamics (CFD). An optimization procedure is carried out to adjust unknown spray model parameters, denoted as spray model calibration. The same adjustment of spray model parameters can be achieved by applying a Genetic Algorithm if spray data is available. However for most engines, spray data is not available and only pressure trace and engine-out emissions are provided. In that case, a methodology has been developed by which the model is calibrated. Furthermore, validation is required to quote if the model can predict combustion and emissions in Diesel engines.

The thesis will first present the models that are applied in the engine simulation. The flow simulation is based on the numerical solution of the Favre-averaged Navier-Stokes equations for an incompressible fluid. The used spray model with sub-models accounting for droplet-breakup, droplet collision and coalescence, and droplet evaporation is reviewed in detail in chapter 3. The flamelet model approach is used as combustion model in this work. This approach includes models for pollutant formation as well. Both models are presented in chapter 4. Two different studies of the mixture formation in diesel fuel and ethanol spray are presented in chapter 5. The simulation results are compared with measured spray penetration data and results from PDA and Raman measurements. The spray model parameters are optimized by a Genetic Algorithm. This algorithm is suitable to find an agreement between simulation and experiment. Furthermore a simulation of two different engines is presented in chapter 6. In these engine cases, no spray data is available and an a-priori spray calibration cannot be conducted. Instead, a methodology to adjust the spray parameters is introduced. Conventional and PCCI combustion modes are investigated and the prediction of the model is validated. Finally, the results of the thesis are summarized in chapter 7.

2 Fluid Dynamics

It was Claude Louis Marie Henri Navier in 1821 and 1822 in France and George Gabriel Stokes in 1842 and 1843 in England who independently derived equations to describe the motion of fluids for an inviscous fluid similar to an elastic solid. Later this model was extended to a viscous fluid.

Today, the Navier-Stokes equations are widely applied in engineering. An analytical solution is obtained only in a limited number of problems. For practical applications, the Navier-Stokes equations are usually solved numerically. This approach has become very attractive with the on-going development of computer resources although even today, the mathematical fundamentals of the Navier-Stokes equations are unclear as Feffermann claims [52] and included in a collection of unsolved mathematical problems [89].

2.1 Conservation Equations in Fluid Dynamics

In classical mechanics, conservation laws are familiar and derived for a control mass Ω_{CM} . In fluids, no fixed control mass exist since the fluid is streaming. Instead of a control mass, a control volume Ω_{CV} is introduced as a fixed spatial region in which the fluid flows. Within a discrete time between t_1 and t_2 , the fluid is entering and leaving that control volume over its control surface S_{CV} . As in classical mechanics, mass m , momentum $\mathbf{I} = m \cdot \mathbf{u}$ and energy E have to be conserved. Similar as in thermodynamics, intensive properties are introduced, namely the density ρ , momentum per unit mass, namely the velocity \mathbf{u} , and energy per unit mass e . The fluid is assumed to be a continuous medium. Macroscopic intensive properties are obtained from the statistical average state of the molecules' microscopic properties. It is required that

the smallest dimension of the problem and the appropriate control volume are larger than the molecules' mean free path. Thus, the mean density of a fluid is defined as

$$\rho = \lim_{\delta V \rightarrow \delta V'} \frac{\delta m}{\delta V} \quad (2.1)$$

where δm is an infinitesimal mass of an infinitesimal volume δV which cannot be smaller than the smallest volume $\delta V'$ which is the lowest limit of a continuous fluid.

Then, any extensive property Φ is related to its intensive property ϕ by the following integral over the volume Ω_{CM} that includes the control mass

$$\Phi = \int_{\Omega_{\text{CM}}} \rho \phi d\Omega, \Phi = \begin{pmatrix} m \\ \mathbf{I} \\ E \end{pmatrix}, \phi = \begin{pmatrix} 1 \\ \mathbf{u} \\ e \end{pmatrix}. \quad (2.2)$$

The specific energy e is here the sum of inner energy u , potential and kinetic energy. The density ρ as well as the extensive and intensive properties Φ and ϕ , respectively, are field functions and depend on the point \mathbf{x} in space and time t :

$$\phi = \phi(\mathbf{x}, t) \quad (2.3)$$

By applying a time-derivative operator on Eq. (2.2), one yields the control volume equation also denoted as Reynolds' transport theorem [149]

$$\frac{d}{dt} \int_{\Omega_{\text{CM}}} \rho \phi d\Omega = \frac{d}{dt} \int_{\Omega_{\text{CV}}} \rho \phi d\Omega + \int_{S_{\text{CV}}} \rho \phi (\mathbf{u} - \mathbf{u}_b) \cdot \mathbf{n} dS, \quad (2.4)$$

where \mathbf{n} the normal unit vector that points outwards, \mathbf{u} is the velocity vector and \mathbf{u}_b is the velocity of a moving control surface. For short, $\Omega = \Omega_{\text{CV}}$ and $S = S_{\text{CV}}$ will be used further on. Most applications have a fixed control volume so that \mathbf{u}_b becomes zero but in engine cases, the motion of the piston and valves has to be addressed.

The Reynolds' transport theorem Eq. (2.4) is a balance equation. The rate of change of a property Φ of the control mass is equal to the rate of change of the property in the control volume plus the net rate flux over the surface. That flux is caused by the motion of the fluid relative to the boundary and is denoted as convective flux. From Eq. (2.4), the integral form of mass conservation which is the continuity equation,

momentum conservation equation and energy conservation equation are derived:

$$\text{continuity} : \frac{\partial}{\partial t} \int_{\Omega} \rho d\Omega + \int_S \rho \mathbf{u} \cdot \mathbf{n} dS = \rho \dot{S} \quad (2.5)$$

$$\text{momentum} : \frac{\partial}{\partial t} \int_{\Omega} \rho \mathbf{u} d\Omega + \int_S \rho \mathbf{u} \mathbf{u} \cdot \mathbf{n} dS = \sum \mathbf{F} \quad (2.6)$$

$$\text{energy} : \frac{\partial}{\partial t} \int_{\Omega} \rho e d\Omega + \int_S \rho e \mathbf{u} \cdot \mathbf{n} dS = \sum \dot{Q} \quad (2.7)$$

In Eq. (2.6) and Eq. (2.7), the source term on the right hand side $\sum \mathbf{F}$ and $\sum \dot{Q}$ are the forces and energy sources whereas source terms \dot{S} in the continuity equation Eq. (2.5) are only due to the phase-transition from liquid to gas phase.

The main forces that act on a fluid are surface and body forces. Surface forces are due to pressure gradients, normal and shear stresses. Body forces include gravity, centrifugal and Coriolis forces. Here, only gravity force is considered as body force. The gravity forces addresses buoyancy effects but is neglected. Surface forces are induced by pressure forces and by stresses on a micro-molecular level. These have to be correlated to macro-molecular properties such as pressure and velocity by making assumptions. A very popular approach is to assume a Newtonian fluid in which the stress is proportional to the velocity gradient. The molecular rate of momentum transport is expressed by the viscous stress tensor \mathbf{T}

$$\mathbf{T} = - \left(p + \frac{2}{3} \mu \nabla \cdot \mathbf{u} \right) \mathbf{I} + 2\mu \mathbf{S} \quad (2.8)$$

where \mathbf{I} is the unit tensor and \mathbf{S} the strain-rate tensor

$$\mathbf{S} = \frac{1}{2} \left[\nabla \mathbf{u} + (\nabla \mathbf{u})^T \right] . \quad (2.9)$$

In Einstein notation, these equations are rewritten as

$$T_{ij} = - \left(p + \frac{2}{3} \mu \frac{\partial u_j}{\partial x_j} \right) \delta_{ij} + 2\mu S_{ij} \quad (2.10)$$

and

$$S_{ij} = \frac{1}{2} \left(\frac{\partial u_i}{\partial x_j} + \frac{\partial u_j}{\partial x_i} \right) . \quad (2.11)$$

The stress tensor T_{ij} is splitted into a viscous part τ_{ij}

$$\tau_{ij} = 2\mu \left[S_{ij} - \frac{1}{3} \left(\frac{\partial u_k}{\partial x_k} \right) \delta_{ij} \right] \quad (2.12)$$

and a remaining normal part $p \delta_{ij}$ that acts normal on the control surface, using the Kronecker symbol δ_{ij}

$$\delta_{ij} = \begin{cases} 1 & : & i = j \\ 0 & : & i \neq j \end{cases} . \quad (2.13)$$

Finally, the integral form of the momentum conservation equation reads as

$$\frac{\partial}{\partial t} \int_{\Omega} \rho \mathbf{u} d\Omega + \int_S \rho \mathbf{u} \mathbf{u} \cdot \mathbf{n} dS = \int_S \mathbf{T} \cdot \mathbf{n} dS + \int_{\Omega} \rho \mathbf{g} d\Omega + \dot{\mathbf{f}}^s . \quad (2.14)$$

Forces that are exchanged between the liquid and the gaseous phase of the spray are denoted as $\dot{\mathbf{f}}^s$. In the energy conservation equation, sink and source terms are due to work from viscous forces, body forces \mathbf{f} per unit volume, energy transfer over the boundaries of the control volume, sources from chemical reactions \dot{Q}_c , heat radiation \dot{Q}_r and exchange of energy between the liquid and gaseous phase of the spray \dot{Q}_s :

$$\sum \dot{Q} = - \int_S \mathbf{u} \cdot \mathbf{T} \cdot \mathbf{n} dS + \int_V \mathbf{u} \cdot \rho \mathbf{f} dV - \int_S q \mathbf{n} dS + \dot{Q}_c + \dot{Q}_r + \dot{Q}_s \quad (2.15)$$

Instead of the energy e the specific enthalpy

$$h = e + \frac{p}{\rho} \quad (2.16)$$

is used as conserved variable in Eq. (2.7) instead. That is sometimes of advantage, especially when chemical reactions are included because the enthalpy already comprises implicitly the heat of formation of each species in a multi-component flows:

$$h = \sum_{i=1}^N Y_i h_i \quad (2.17)$$

The specific enthalpy h_i of each species i is given as

$$h_i = \Delta_{f,i}^0 + \int_{T^0}^T c_{p,i} dT . \quad (2.18)$$

The heat of formation $\Delta_{f,i}^0$ is defined at the reference temperature T^0 chosen as 298 K. The presented integral form of the conservation equations does not depend on a local or global coordinate. Automatically, global momentum and energy conservation is insured. From the integral form, Gauss' theorem is applied to transform the surface integrals into volume integrals. At the limit, the control volume becomes infinitesimally small and the differential form is obtained for the mass, momentum and energy conservation equation:

$$\frac{\partial \rho}{\partial t} + \frac{\partial \rho u_i}{\partial x_i} = \rho \dot{S} \quad (2.19)$$

$$\frac{\partial \rho u_i}{\partial t} + \frac{\partial \rho u_j u_i}{\partial x_j} = - \frac{\partial p}{\partial x_i} \frac{\partial \tau_{ij}}{\partial x_j} + \rho g_i + \dot{f}_i^s \quad (2.20)$$

$$\frac{\partial \rho h}{\partial t} + \frac{\partial \rho u_j h}{\partial x_j} = \frac{\partial p}{\partial t} + u_j \frac{\partial p}{\partial x_j} - \frac{\partial j_{j,q}}{\partial x_j} + \dot{q}_r + \dot{q}_s + \Phi \quad (2.21)$$

In these equations the dissipation function Φ is defined as

$$\begin{aligned} \Phi &= \frac{\partial(u_i \tau_{ij})}{\partial x_j} - u_i \frac{\partial \tau_{ij}}{\partial x_j} = \tau_{ij} \frac{\partial u_i}{\partial x_j} \\ &= \mu \frac{\partial u_i}{\partial x_j} \left(\frac{\partial u_i}{\partial x_j} + \frac{\partial u_j}{\partial x_i} \right) - \frac{2}{3} \mu \frac{\partial u_i}{\partial x_i} \frac{\partial u_i}{\partial x_i} . \end{aligned} \quad (2.22)$$

This function accounts for the irreversible energy transfer rate due to viscous forces. The dissipation function is usually neglected and is not considered furthermore.

The heat flux $\dot{\mathbf{j}}_q$ due to thermal diffusion is expressed by the temperature gradient, denoted as Fourier's law, and the enthalpy transport by the species diffusion, the diffusion flux $\dot{\mathbf{j}}_i$:

$$\dot{\mathbf{j}}_q = -\lambda \nabla T + \sum_{i=1}^N h_i \dot{\mathbf{j}}_i \quad (2.23)$$

The last term on the r.h.s is the enthalpy of the molecular flux. In the case of a chemical reacting flow the species conservation equation

$$\frac{\partial \rho Y_i}{\partial t} + \frac{\partial \rho u_j Y_i}{\partial x_j} = - \frac{\partial j_{j,i}}{\partial x_j} + \dot{\omega}_i \quad (2.24)$$

for the species mass concentration Y_i

$$Y_i = \frac{m_i}{m} \quad (2.25)$$

has to be added. The molecular transport in a mixture by diffusion is denoted as the molecular or diffusive flux \mathbf{j}_i

$$\mathbf{j}_i = \rho Y_i \mathbf{v}_{i\alpha} . \quad (2.26)$$

$\mathbf{v}_{i\alpha}$ defines the diffusive velocity of species i

$$\mathbf{v}_{i\alpha} = (\mathbf{u}_i - \mathbf{u}) \quad (2.27)$$

as the relative velocity between each species and the mass center velocity \mathbf{u}

$$\mathbf{u} = \sum_{i=1}^N Y_i \mathbf{u}_i . \quad (2.28)$$

Simplifications are made to calculate the diffusive flux where the Duffour and Sorret effect are neglected and a binary flux is assumed

$$v_{i\alpha} = -\frac{1}{Y_i} D_i \frac{\partial Y_i}{\partial x_\alpha} . \quad (2.29)$$

D_i is the binary diffusion coefficient between each species with respect to an abundant species, e.q. N_2 . Similar to the heat flux, the molecular flux is related to the species concentration gradient that is also denoted as Fick's law

$$\mathbf{j}_i = -\rho D_i \nabla Y_i . \quad (2.30)$$

Introducing these definitions into Eq. (2.24), the conservation equation for the species mass fraction is re-written

$$\frac{\partial \rho Y_i}{\partial t} + \frac{\partial \rho u_j Y_i}{\partial x_j} = \frac{\partial}{\partial x_j} \left(\rho D_i \frac{\partial Y_i}{\partial x_j} \right) + \dot{\omega}_i . \quad (2.31)$$

With the definition of the enthalpy from Eq. (2.17) the total differential dh is obtained

$$dh = \frac{\partial h}{\partial T} dT + \sum_{i=1}^N \frac{\partial h}{\partial Y_i} dY_i = c_p dT + \sum_{i=1}^N \frac{\partial h}{\partial Y_i} dY_i . \quad (2.32)$$

The heat flux is rewritten from Eq. (2.23) as

$$\mathbf{j}_q = -\frac{\lambda}{c_p} \nabla h + \sum_{i=1}^N h_i \left(\mathbf{j}_i + \frac{\lambda}{c_p} \nabla Y_i \right) . \quad (2.33)$$

These definitions are used to obtain an equation for the temperature

$$\begin{aligned} \rho \frac{\partial T}{\partial t} + \rho u_j \frac{\partial T}{\partial x_j} &= \frac{\partial}{\partial x_j} \left(\frac{\lambda}{c_p} \frac{\partial T}{\partial x_j} \right) + \rho \frac{\lambda}{c_p^2} \left(\sum_{i=1}^N \frac{c_{p_i}}{\text{Le}_i} \frac{\partial Y_i}{\partial x_j} + \frac{\partial c_p}{\partial x_j} \right) \frac{\partial T}{\partial x_j} \\ &\quad - \frac{1}{c_p} \left(\sum_{i=1}^N \omega_i h_i - \frac{\partial p}{\partial t} - u_j \frac{\partial p}{\partial x_j} - \dot{q}_r - \dot{q}_s \right). \end{aligned} \quad (2.34)$$

Here, the Lewis number Le_i is introduced as the ratio of the thermal diffusivity D

$$D = \frac{\lambda}{\rho c_p} \quad (2.35)$$

and the species diffusion coefficient D_i

$$\text{Le}_i = \frac{D}{D_i} = \frac{\lambda}{\rho c_p D_i}. \quad (2.36)$$

The source term due to chemical reactions in Eq. (2.21) and Eq. (2.24) is denoted as $\dot{\omega}_i$. Typically for combustion phenomena, chemical reactions are expressions of Arrhenius type

$$k = AT^n e^{(-\frac{E}{\mathcal{R}T})}. \quad (2.37)$$

The frequency factor A , the temperature exponent n and the activation energy E are denoted as Arrhenius parameters. The net reaction rate for every reaction is obtained from the forward and backward reaction rate

$$\dot{\omega}_k = k_{f_k} \prod_{j=1}^N \left(\frac{\rho Y_j}{W_j} \right)^{\nu'_{jk}} - k_{b_k} \prod_{j=1}^N \left(\frac{\rho Y_j}{W_j} \right)^{\nu''_{jk}} \quad (2.38)$$

where k_{f_i} and k_{b_i} are the forward and backward reaction rate coefficients. ν'_{jk} and ν''_{jk} denote the stoichiometric reaction coefficients of every reaction k . The source term $\dot{\omega}_i$ is obtained by summing over all reactions r of a chemical reaction mechanism

$$\dot{\omega}_i = W_i \sum_{k=1}^r \nu_{i_k} \dot{\omega}_k. \quad (2.39)$$

The last source term in Eq. (2.21) and Eq. (2.34) is the heat loss \dot{q}_r due to radiation. The radiative heat flux is given from the law of Stefan-Boltzmann [72] as

$$\dot{q}_r = 4\alpha_P \sigma_S T^4 \quad (2.40)$$

where α_P denotes the absorption coefficient and σ_S the Stefan-Boltzmann constant

$$\sigma_S = \frac{2\pi^5 k^4}{15c^2 h^3} = 5.670 \times 10^{-8} \text{ W/m}^2\text{K}^4 . \quad (2.41)$$

α_P is given in [137, 86] as

$$\alpha_P = \rho R_m T \left(\alpha_{P,\text{soot}} f_v + \sum_{i=1}^N \alpha_{P,i} \frac{Y_i}{W_i} \right) . \quad (2.42)$$

Typically only the absorption bands of H₂O and CO₂ are contributing [182] whereas the absorption coefficient for soot $\alpha_{P,\text{soot}}$ is given by Howard [86].

Additionally to the above equations, the equation of state for an ideal gas is included to derive the density:

$$p = \rho R T = \rho \mathcal{R} \sum_{i=1}^N \frac{Y_i}{W_i} T \quad (2.43)$$

R and \mathcal{R} is the specific and the universal gas constant, respectively.

2.2 Mathematical Description of Turbulent Flows

The presented equations are derived for a laminar flow but in most applications, the flow is turbulent. Turbulent flows are characterized by an irregular, chaotic fluid motion whereas laminar flows have no stochastic irregularities, are highly ordered and resistant against extrinsic perturbations. Turbulent flows are always three dimensional, instationary and rotational. The rotational motion in a fluid is often denoted as an eddy. In turbulent flows, the size of these eddies and the velocity they turn is ranging from very small to very large scales. At the smallest scale, the energy of the fluid motion is dissipating into heat because viscous forces are dominating. Thus, turbulent flows are always dissipative. The mixing process by diffusive transport of mass, momentum, and energy is enhanced in comparison to laminar flows.

In order to describe quantitatively a turbulent flow, one has to account for the nature of turbulence that is characterized by a stochastic process on all scales. The stochastic fluctuations in a turbulent flow are induced by instabilities. If viscous forces are large, these instabilities are damped. Therefore, the ratio of inertia and viscous forces,

expressed by the Reynolds number is the criteria for the transition from a laminar to a turbulent flow:

$$\text{Re} = \frac{\rho u L}{\mu} \quad (2.44)$$

u and L are a characteristic velocity and length scale of the flow, e.g. for a pipe-flow, the transition occurs at $\text{Re}_{\text{crit}} \approx 2,300$. At higher Reynolds numbers $\text{Re} > \text{Re}_{\text{crit}}$, the flow is fully turbulent.

2.2.1 Statistical Description

A common approach to describe turbulence is the use of stochastic methods. The velocity \mathbf{u} is characterized by its statistical distribution $F_{\mathbf{u}}(\mathbf{U})$ which express the probability p to find a value $\mathbf{u} < \mathbf{U}$

$$F_{\mathbf{u}}(\mathbf{U}) = p(\mathbf{u} < \mathbf{U}) . \quad (2.45)$$

The probability density function (pdf) is given as

$$f_{\mathbf{u}}(\mathbf{U}) = \frac{dF_{\mathbf{u}}(\mathbf{U})}{d\mathbf{U}} . \quad (2.46)$$

$f_{\mathbf{u}}$ is positive ($f_{\mathbf{u}} \geq 0$) and monotonous. All possible realizations $\mathbf{U} \leq \mathbf{u} \leq \mathbf{U} + d\mathbf{U}$ from $-\infty$ to $+\infty$ lead to a probability of unity that serves as a normalization condition for $f_{\mathbf{u}}$:

$$p = \int_{-\infty}^{+\infty} \int_{-\infty}^{+\infty} \int_{-\infty}^{+\infty} f_{\mathbf{u}}(\mathbf{U}) d\mathbf{U} = 1 \quad (2.47)$$

From this probability function statistical moments are derived. The marginal pdf is given by

$$f_1(u_1; \mathbf{x}, t) = \int_{-\infty}^{+\infty} \int_{-\infty}^{+\infty} f(\mathbf{u}; \mathbf{x}, t) du_1 du_2 . \quad (2.48)$$

Using this marginal pdf, the moments for every component u_i of \mathbf{u} are given as

$$\overline{u_i^n(\mathbf{x}, t)} = \int_{-\infty}^{+\infty} u_i^n(\mathbf{x}, t) f_i(u_i; \mathbf{x}, t) du_i . \quad (2.49)$$

Beside the moments, central moments for the fluctuation $u'_i = u_i - \bar{u}_i$ are introduced

$$\overline{u_i'^n(\mathbf{x}, t)} = \int_{-\infty}^{+\infty} u_i'^n(\mathbf{x}, t) f_i(u_i; \mathbf{x}, t) du_i . \quad (2.50)$$

The first moment for $n = 1$ is equal to the mean value, also denoted as expectation value

$$\overline{u_i(\mathbf{x}, t)} = \int_{-\infty}^{+\infty} u_i(\mathbf{x}, t) f_i(u_i; \mathbf{x}, t) du_i . \quad (2.51)$$

The second central moment for $n = 2$ is the variance. Moments are quite usefull since they can be measured much better than the distribution function itself. Even moments show the width of the pdf whereas symmetry properties of the pdf are obtained from odd moments. If all moments are known, $f_i(u_i; \mathbf{x}, t)$ can be reconstructed.

The Fourier transformation of $f_i(u_i; \mathbf{x}, t)$ yields a characteristic function

$$\psi(k, \mathbf{x}, t) = \int_{-\infty}^{+\infty} e^{iku_i} f_i(u_i; \mathbf{x}, t) du_i . \quad (2.52)$$

The characteristic function is re-written by using a series-expansion of the exponential function

$$\psi(k, \mathbf{x}, t) = \sum_{n=0}^{\infty} \frac{(ik)^n}{n!} \int_{-\infty}^{+\infty} u_i^n f_i(u_i; \mathbf{x}, t) du_i = \sum_{n=0}^{\infty} \frac{(ik)^n}{n!} \overline{u_i^n(\mathbf{x}, t)} . \quad (2.53)$$

Since the characteristic function is expressed by the sum over all moments the pdf is derived from the Fourier transformation

$$f_i(u_i; \mathbf{x}, t) = \frac{1}{2\pi} \int_{-\infty}^{+\infty} e^{-iku_i} \psi(k, \mathbf{x}, t) dk . \quad (2.54)$$

The natural logarithm of $\psi(k, \mathbf{x}, t)$ is developed in a series introducing the cumulants K_n

$$\ln \psi(k, \mathbf{x}, t) = \sum_{n=0}^{\infty} K_n(\mathbf{x}, t) (ik)^n . \quad (2.55)$$

Cumulants, also denoted as semi-invariants, of first order are equal to moments of first order while second and third order cumulants are equal to the central moments of the

same order:

$$K_1 = \overline{u_i} \quad (2.56)$$

$$K_2 = \overline{u_i'^2} \quad (2.57)$$

$$K_3 = \overline{u_i'^3} \quad (2.58)$$

$$K_4 = \overline{u_i'^4} - 3 \left(\overline{u_i'^2} \right)^2 \quad (2.59)$$

$$K_5 = \overline{u_i'^5} - 10 \overline{u_i'^3} \overline{u_i'^2} \quad (2.60)$$

One property of cumulants is that they describe the shape of the pdf. If all cumulants of order greater than two are zero, the pdf is a Gaussian normal distribution function

$$f_i(u_i; \mathbf{x}, t) = \frac{1}{\sqrt{2\pi}\sigma_i} e^{-\frac{(u_i - \overline{u_i})^2}{2\sigma_i^2}} \quad (2.61)$$

where $\sigma_i = \sqrt{\overline{u_i'^2}}$ is the variance.

2.2.2 Reynolds Averaging

The presented Navier-Stokes equations are used to calculate a turbulent flow. It is desirable to resolve the entire scale range from large scales of order L to small scales of order η . Thus the Reynolds number is related to the spread of $\frac{L}{\eta} \sim \text{Re}^{9/4}$ in three dimensions [214]. This type of simulation, denoted as Direct Numerical Simulation (DNS) is a valuable method to understand the fundamentals of turbulence but limited to flows of small Reynolds numbers. An alternative approach is the introduction of averages, the so-called Reynolds-averaging. The instantaneous property $\phi(\mathbf{x}, t)$ from Eq. (2.2) is expressed by a mean $\overline{\phi}(\mathbf{x}, t)$ and a fluctuation $\phi'(\mathbf{x}, t)$

$$\phi(\mathbf{x}, t) = \overline{\phi}(\mathbf{x}, t) + \phi'(\mathbf{x}, t) . \quad (2.62)$$

The mean flow is slowly varying in time, not due to turbulence but due to slowly varying pressure gradients. The averaged mean $\overline{\phi}(\mathbf{x}, t)$ is given as

$$\overline{\phi}(\mathbf{x}, t) = \frac{1}{\Delta T} \int_t^{t+\Delta T} \phi(\mathbf{x}, t) dt . \quad (2.63)$$

From these definitions, the averaged fluctuation part $\overline{\phi'(\mathbf{x}, t)}$ becomes zero

$$\overline{\phi'(\mathbf{x}, t)} = 0 . \quad (2.64)$$

2.2.3 Favre Averaging

In flows that include combustion, density changes are large and Favre-averaging is a better choice than Reynolds-Averaging. The Navier-Stokes equations will be simplified in high Reynolds number flows since convective terms are dominant. A density-weighted average $\tilde{\phi}(\mathbf{x}, t)$, denoted as Favre-average, is introduced as

$$\phi(\mathbf{x}, t) = \tilde{\phi}(\mathbf{x}, t) + \phi''(\mathbf{x}, t) . \quad (2.65)$$

The average of the product of density and fluctuation becomes zero

$$\overline{\rho\phi''(\mathbf{x}, t)} = 0 . \quad (2.66)$$

The average itself and its fluctuation are related to the Reynolds-averages as

$$\tilde{\phi}(\mathbf{x}, t) = \frac{\overline{\rho\phi(\mathbf{x}, t)}}{\bar{\rho}} \quad (2.67)$$

and

$$\widetilde{\phi''(\mathbf{x}, t)} = \frac{\overline{(\rho\phi(\mathbf{x}, t))''}}{\bar{\rho}} . \quad (2.68)$$

2.2.4 Length- and Time Scales in a Turbulent Flow

The structure in a turbulent flow includes various scales. On the one hand, the flow is bounded by the dimensions of the entire geometry of the flow domain. On the other hand, momentum transport on a molecular level has much smaller scales. One concept to illustrate that momentum transport is the energy cascade that is based on a similarity analysis by Kolmogorov in 1941 [107]. Turbulence can be viewed as the sum of fluctuations of a very few large eddies and a large number of very small eddies. Large eddies of the flow dimensions l turn with a velocity fluctuation u' where its kinetic energy is given as

$$k = \frac{1}{2}u_i'^2 . \quad (2.69)$$

The turn-over time l/u' is proportional to the integral time which is expressed due to dimension analysis to k and the eddy dissipation rate ε

$$\tau = \frac{k}{\varepsilon} . \quad (2.70)$$

The eddy dissipation rate can also be viewed as an energy transfer rate since energy is transferred from large to small scales. From dimension analysis ε is related to the turn-over velocity and the integral length scale

$$\varepsilon \sim \frac{u'^3}{l} . \quad (2.71)$$

By hydrodynamical instabilities, large eddies are becoming smaller eddies in a cascading process. In this process energy is transferred from large to small scales. On the smaller scales, viscous forces are dominating and energy dissipates on the smallest scale

$$\eta = \left(\frac{\nu^3}{\varepsilon} \right)^{1/4} , \quad (2.72)$$

denoted as Kolmogorov scale, at which the energy cascade ends. On that Kolmogorov scale, the corresponding time and velocity scale are obtained

$$t_\eta = \left(\frac{\nu}{\varepsilon} \right)^{1/2} \quad (2.73)$$

$$v_\eta = (\nu\varepsilon)^{1/4} . \quad (2.74)$$

In order to estimate the ratio of smallest eddies to the very large ones,

$$\frac{\eta}{l} \sim \text{Re}_t^{-3/4} \quad (2.75)$$

a turbulence Reynolds number Re_t is introduced:

$$\text{Re}_t = \frac{lk^{1/2}}{\nu} \quad (2.76)$$

The idea of energy transfer from large to small scales leads to an identification of four different regimes in the kinetic energy spectrum as sketched in Fig. 2.1. Here, the kinetic energy spectrum

$$E(k) \sim \varepsilon^{2/3} k^{-5/3} \quad (2.77)$$

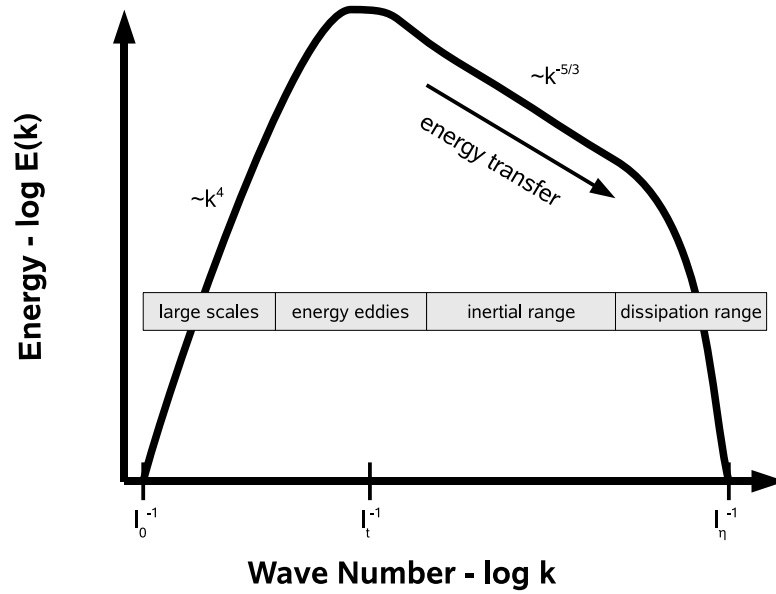


Figure 2.1: Energy spectrum

is plotted as function of the wavenumber k that is the inverse of the eddy length size l . For small wavenumbers, a very few eddies exist because the length scales of the flow-dimensions limits the maximum size of the eddies. On the integral length scale l_t , only a few but large eddies exists containing the most energy. From here, energy is transferred to smaller eddies at a constant rate that is proportional to $k^{-5/3}$ in a cascading process. This energy transfer is dominated by inertial forces and denoted as inertial subrange. At very small scales, the energy is dissipating due to viscous forces. Eddies become smaller upto the smallest scale which is the Kolmogorov-length l_η .

2.3 Reynolds Averaged Equations of a Turbulent Flow

Inserting the definitions of the Favre-average definitions Eq. (2.62), Eq. (2.63) and Eq. (2.64) into the Navier-Stokes equation Eq. (2.19) - Eq. (2.24), the so-called Reynolds averaged Navier-Stokes (RANS) equations are derived:

$$\frac{\partial \bar{\rho}}{\partial t} + \frac{\partial \bar{\rho} \bar{u}_j}{\partial x_j} = \bar{\rho} \bar{S} \quad (2.78)$$

$$\frac{\partial \bar{\rho} \bar{u}_i}{\partial t} + \frac{\partial \bar{\rho} \bar{u}_j \bar{u}_i}{\partial x_j} = -\frac{\partial \bar{p}}{\partial x_i} + \frac{\partial \bar{\tau}_{ij}}{\partial x_j} + \frac{\partial}{\partial x_i} (\overline{\rho u'_j u'_i}) + \bar{\rho} g_i + \bar{f}_i^s \quad (2.79)$$

$$\frac{\partial \bar{\rho} \bar{h}}{\partial t} + \frac{\partial \bar{\rho} \bar{u}_j \bar{h}}{\partial x_j} = \frac{D \bar{p}}{Dt} - \frac{\partial \bar{j}_{j,q}}{\partial x_j} - \frac{\partial}{\partial x_i} (\overline{\rho u'_i h'}) + \bar{q}_r + \bar{q}_s \quad (2.80)$$

$$\frac{\partial \bar{\rho} \bar{Y}_i}{\partial t} + \frac{\partial \bar{\rho} \bar{u}_j \bar{Y}_i}{\partial x_j} = -\frac{\partial \bar{j}_{j,i}}{\partial x_j} - \frac{\partial}{\partial x_i} (\overline{\rho u'_i Y'_i}) + \bar{\omega}_i \quad (2.81)$$

The continuity equation remains unchanged but for the momentum and enthalpy equation, the averaging of the non-linear convective terms $\frac{\partial}{\partial x_j} (\rho u_j u_i)$ yields new correlations of higher order

$$\frac{\partial}{\partial x_j} (\overline{\rho u_j u_i}) = \frac{\partial}{\partial x_j} (\bar{\rho} \bar{u}_j \bar{u}_i) + \frac{\partial}{\partial x_j} (\overline{\rho u'_j u'_i}) . \quad (2.82)$$

The last term of Eq. (2.82) is usually denoted as the Reynolds stress tensor τ_{ij}

$$\tau_{ij} = -\overline{\rho u'_j u'_i} . \quad (2.83)$$

The Reynolds stresses are leading to an unclosed system of equations which is denoted as the closure problem in turbulence. One possible way to close the system would be to introduce an additional transport equation for τ_{ij} :

$$\begin{aligned} \frac{\partial \tau_{ij}}{\partial t} + \bar{u}_k \frac{\partial \tau_{ij}}{\partial x_k} &= -\tau_{ikt} \frac{\partial \bar{u}_k}{\partial x_k} \\ &- \tau_{jkt} \frac{\partial \bar{u}_i}{\partial x_k} + \varepsilon_{ij} - \Pi_{ij} + \frac{\partial}{\partial x_k} \left[\nu \frac{\partial \tau_{ij}}{\partial x_k} + C_{ijk} \right] \end{aligned} \quad (2.84)$$

Π_{ij} is the pressure-rate-of-strain correlation term

$$\Pi_{ij} = p' \left(\frac{\partial u'_i}{\partial x_j} \frac{\partial u'_j}{\partial x_i} \right) , \quad (2.85)$$

ε_{ij} denotes the dissipation term

$$\varepsilon_{ij} = 2\mu \overline{\frac{\partial u'_i}{\partial x_k} \frac{\partial u'_j}{\partial x_k}} \quad (2.86)$$

and C_{ijk} comprises all remaining terms that are written as a gradient

$$C_{ijk} = \overline{\rho u'_i u'_j u'_k} + \overline{p' u'_i \delta_{jk}} + \overline{p' u'_j \delta_{ik}} . \quad (2.87)$$

The last equation contains triple correlations that are again not closed. Due to the non-linearities of the Navier-Stokes equation, every new transport equation leads to the next level of unclosed velocity fluctuation correlations. As a solution, the correlations are expressed by known mean variables and making assumptions to close the system.

2.3.1 Boussinesq Approximation

One solution to find a closure for the velocity fluctuation correlation was proposed by Boussinesq [25] in 1877. The Reynolds stress tensor τ_{ij_t} is approximated by the mean stress tensor τ_{ij}

$$\tau_{ij_t} = -\overline{\rho u'_i u'_j} = \rho \nu_t \frac{\partial \bar{u}_i}{\partial x_j} . \quad (2.88)$$

This approximation depends only on the mean velocity gradient and a momentum exchange constant ν_t , also denoted as turbulent viscosity. Therefore this approximation is denoted as a first order moment closure method. Further approximations are to be made to find an appropriate expression for ν_t .

2.3.2 Closure of Momentum Conservation Equation

2.3.2.1 Algebraic Models

It was Prandtl in 1925 [169] who firstly found an approximation for the turbulent kinematic viscosity for turbulent, two-dimensional shear flows based on an analogy between turbulent and molecular transport.

From the kinetic gas theory, the molecular shear stress is expressed by

$$\tau_{xy} = \mu \frac{d\bar{u}}{dy} \approx \frac{1}{2} \rho v_{\text{mol}} l_{\text{mfp}} \frac{d\bar{u}}{dy} . \quad (2.89)$$

v_{mol} is the average molecular velocity along the mean free path length l_{mfp} of the molecules. The molecular viscosity follows as

$$\mu = \frac{1}{2} \rho v_{\text{mol}} l_{\text{mfp}} . \quad (2.90)$$

Prandtl introduced the concept of a mixing length l_{mix} which is the distance that an eddy travels due to the velocity fluctuations normal in a turbulent boundary layer without losing its momentum in flow direction. The turbulent eddies are assigned a mixing velocity

$$v_{\text{mix}} \propto l_{\text{mix}} \left| \frac{d\bar{u}}{dy} \right| . \quad (2.91)$$

After that movement, the momentum excess is exchanged with the surrounding. That additional momentum flux results in an additional turbulent shear

$$\tau_t = \mu_t \frac{d\bar{u}}{dy}. \quad (2.92)$$

Similar to the molecular viscosity, the turbulent viscosity reads as

$$\mu_t = \frac{1}{2} \rho v_{\text{mix}} l_{\text{mix}} \frac{d\bar{u}}{dy}. \quad (2.93)$$

Assuming that

$$v_{\text{mix}} \propto l_{\text{mix}} \left| \frac{d\bar{u}}{dy} \right| \quad (2.94)$$

it follows that the turbulent viscosity is expressed by the mixing length and the gradient of the mean velocity

$$\mu_t = \rho l_{\text{mix}}^2 \left| \frac{\partial \bar{u}_i}{\partial x_j} \right|. \quad (2.95)$$

The mixing length is modeled by the local velocity gradient. Therefore, algebraic models assume that the flow is in a local equilibrium, meaning that the production and dissipation of fluctuations are of the same order and therefore balancing each other. For this reason algebraic models are classified as zero-dimensional models.

2.3.2.2 Turbulent Energy Equation

Beyond the algebraic models, one- and two equation models have been developed to account for the energy transport of turbulence and its transfer between the various length scales to address for non-local and flow history effects. An estimate for the mixing velocity in Eq. (2.91) is obtained by introducing the kinetic energy k of the velocity fluctuations. From the trace of the Reynolds stress tensor Eq. (2.83), k is obtained as

$$k = \frac{1}{2} \overline{u'_i u'_i}. \quad (2.96)$$

Giving a turbulent length scale l , the turbulent viscosity follows due to dimensionality

$$\mu_t \propto \rho k^{1/2} l. \quad (2.97)$$

In order to determine k , a transport equation is derived by contraction of the transport equation of the Reynolds stress Eq. (2.84). Since the Reynolds stress is given as

$$\tau_{ii} = -2\rho k , \quad (2.98)$$

Eq. (2.84) is re-written as

$$\frac{\partial \rho k}{\partial t} + \rho \bar{u}_j \frac{\partial k}{\partial x_j} = \tau_{ij} \frac{\partial \bar{u}_i}{\partial x_j} - \rho \varepsilon + \frac{\partial}{\partial x_j} \left[\mu \frac{\partial k}{\partial x_j} - \frac{1}{2} \overline{\rho u'_i u'_i u'_j} - \overline{p' u'_j} \right] . \quad (2.99)$$

The dissipation term $\rho \varepsilon$ is here given by

$$\varepsilon = \nu \frac{\partial u'_i}{\partial x_j} \left(\frac{\partial u'_i}{\partial x_j} + \frac{\partial u'_j}{\partial x_i} \right) . \quad (2.100)$$

The pressure-rate-of-strain tensor Π_{ij} vanishes for an incompressible flow. Every term on the r.h.s of the turbulent kinetic energy equation has to be modeled.

First, it is assumed that the assumptions of the Boussinesq approximation are valid. Thus, the Reynolds stress tensor is given as

$$\tau_{ij} = \rho \nu_t \left(2S_{ij} - \frac{2}{3} \frac{\partial u_k}{\partial x_k} \delta_{ij} \right) - \frac{2}{3} \rho k \delta_{ij} . \quad (2.101)$$

Second, the unclosed term for the turbulent transport $-\frac{1}{2} \overline{\rho u'_i u'_i u'_j} = -\overline{\rho u'_j k}$ is related to the gradient of k . It is very difficult to find an appropriate correlation for the pressure velocity correlation $-\overline{p' u'_j}$. That term is assumed to be small and therefore included in the following expression

$$-\frac{1}{2} \overline{\rho u'_i u'_i u'_j} - \overline{p' u'_j} = -\frac{\mu_t}{\sigma_k} \frac{\partial k}{\partial x_j} \quad (2.102)$$

where σ_k is a closure coefficient. For the dissipation ε , a correlation with the kinetic energy and a turbulent length scale is derived by dimension analysis:

$$\varepsilon \propto \frac{k^{3/2}}{l} \quad (2.103)$$

With these correlations, Eq. (2.99) is re-written:

$$\frac{\partial \rho k}{\partial t} + \rho \bar{u}_j \frac{\partial k}{\partial x_j} = \tau_{ij} \frac{\partial \bar{u}_i}{\partial x_j} - \rho \varepsilon + \frac{\partial}{\partial x_j} \left[\left(\mu + \frac{\mu_t}{\sigma_k} \right) \frac{\partial k}{\partial x_j} \right] \quad (2.104)$$

The only remaining unknown is the turbulent length scale l to close the system finally. Further modeling approaches are either one- or two-equation models that introduce assumptions and closure coefficients.

One-Equation Models In order to solve the transport equation for the turbulent kinetic energy, a closure coefficient c has been introduced in Eq. (2.103)

$$\varepsilon = c k^{3/2} l, c = 0.1643 . \quad (2.105)$$

Furthermore, μ_t and σ_k have to be specified. In equilibrium flows, when dissipation and production of turbulence are balancing, μ_t can be assumed as

$$\mu_t = c_1 \rho k^{1/2} l, c_1 = 0.548 . \quad (2.106)$$

Two-Equation Models Two-equation models are an extension of the one-equation models but they inherit both, the turbulence time- and length scale. Beside the conservation equation for the turbulent kinetic energy k , an additional equation for the dissipation rate ε is introduced by Chou [31]. Other authors considered the specific dissipation rate ω Kolmogorov [108] or the turbulence length scale l itself Rotta [179] or a turbulence dissipation time τ Zeiermann et al.[220], Speziale et al.[195], as an additional property. The choice of the dissipation rate as second turbulence property results in the very popular $k - \varepsilon$ model of Jones and Launder [95] with some modifications in the model's closure coefficients done by Launder and Sharman [114]. Additionally to the turbulent kinetic energy equation Eq. (2.104), a transport equation for the dissipation rate is derived from the momentum conservation equation and reads as

$$\frac{\partial \rho \varepsilon}{\partial t} + \rho \bar{u}_j \frac{\partial \varepsilon}{\partial x_j} = C_{\varepsilon 1} \frac{\varepsilon}{k} \tau_{ij} \frac{\partial \bar{u}_i}{\partial x_j} - C_{\varepsilon 2} \rho \frac{\varepsilon^2}{k} + \frac{\partial}{\partial x_j} \left[\left(\mu + \frac{\mu_t}{\sigma_\varepsilon} \right) \frac{\partial \varepsilon}{\partial x_j} \right] . \quad (2.107)$$

The turbulent eddy viscosity μ_t is due to dimensionality analysis given by

$$\mu_t = C_\mu \rho \frac{k^2}{\varepsilon} . \quad (2.108)$$

Finally, five closure coefficients remain which are determined either experimentally or from analytical or numerical solutions:

$$C_{\varepsilon 1} = 1.44, C_{\varepsilon 2} = 1.92, C_\mu = 0.09, \sigma_k = 1.0, \sigma_\varepsilon = 1.3 \quad (2.109)$$

2.3.3 Closure of Enthalpy Conservation Equation

The correlation $\overline{\rho u'_j h'}$ in the enthalpy conservation equation Eq. (2.80) is closed if the turbulent heat transfer is approximated by the mean temperature gradient

$$\overline{j_{j,q}} = \overline{\rho u'_j h'} = -\frac{\mu_t}{\text{Pr}_t} \frac{\partial \bar{h}}{\partial x_j}. \quad (2.110)$$

In analogy to the Prandtl number

$$\text{Pr} = \frac{\mu c_p}{\lambda} \quad (2.111)$$

in laminar flows, the turbulent Prandtl number Pr_t is defined as

$$\text{Pr}_t = \frac{\nu_{\tau_t}}{\nu_{j_i}}. \quad (2.112)$$

In most shock-free flows up to low supersonic speeds, a constant value of $\text{Pr}_t \approx 0.9$ is chosen whereas in free shear layers a value of order $\text{Pr}_t = \mathcal{O}(0.5)$ is more appropriate [214]. Here, a value of $\text{Pr}_t = 0.5 \dots 1.0$ is applied.

2.3.4 Closure of Species Conservation Equation

For the remaining species conservation equation Eq. (2.81), the gradient transport assumption is made for the correlation $\overline{\rho u'_j Y'_i}$:

$$\overline{j_{j,i}} = \overline{\rho u'_j Y'_i} = -\frac{\mu_t}{\text{Sc}_t} \frac{\partial \bar{Y}_i}{\partial x_j} \quad (2.113)$$

where Sc_t is the turbulent Schmidt number. For a laminar flow, the Schmidt number

$$\text{Sc} = \frac{\mu}{\rho D} \quad (2.114)$$

describes the ratio of viscous to diffusive transport. Then the turbulent Schmidt number is given as

$$\text{Sc}_{i_t} = \frac{\nu_{\tau_t}}{\nu_{i_t}}. \quad (2.115)$$

The ratio $\frac{\mu_t}{\text{Sc}_{i_t}}$ has the units of a diffusivity thus denoted as turbulent diffusivity D_{i_t}

$$D_{i_t} = \frac{\mu_t}{\text{Sc}_{i_t}}. \quad (2.116)$$

Assuming analogy between heat and species transport, the mean heat and species gradients are equally, thus the values for turbulent Schmidt number and the turbulent Prandtl number are identical, $Sc_{it} = Pr_t = 0.7$, yielding a Lewis number of unity

$$Le_{it} = \frac{Sc_{it}}{Pr_t} = 1. \quad (2.117)$$

2.4 Favre-Averaged Equations of a Turbulent Flow

Similar as for the Reynolds-averaged Navier-Stokes equations, Favre-averaged properties are introduced in Eq. (2.19)-Eq. (2.21) and Eq. (2.24):

$$\frac{\partial \bar{\rho}}{\partial t} + \frac{\partial \bar{\rho} \tilde{u}_j}{\partial x_j} = \bar{\rho} \tilde{S} \quad (2.118)$$

$$\frac{\partial \bar{\rho} \tilde{u}_i}{\partial t} + \frac{\partial \bar{\rho} \tilde{u}_j \tilde{u}_i}{\partial x_j} = -\frac{\partial \tilde{p}}{\partial x_i} + \frac{\partial \tilde{\tau}_{ij}}{\partial x_j} + \frac{\partial}{\partial x_i} \left(\overline{\bar{\rho} u_j'' u_i''} \right) + \tilde{f}_i^s \quad (2.119)$$

$$\frac{\partial \bar{\rho} \tilde{h}}{\partial t} + \frac{\partial \bar{\rho} \tilde{u}_j \tilde{h}}{\partial x_j} = \frac{D\tilde{p}}{Dt} - \frac{\partial \tilde{j}_{j,q}}{\partial x_j} - \frac{\partial}{\partial x_i} \left(\overline{\bar{\rho} u_j'' h''} \right) + \tilde{q}_r + \tilde{q}_s \quad (2.120)$$

$$\frac{\partial \bar{\rho} \tilde{Y}_i}{\partial t} + \frac{\partial \bar{\rho} \tilde{u}_j \tilde{Y}_i}{\partial x_j} = -\frac{\partial \tilde{j}_{j,i}}{\partial x_j} - \frac{\partial}{\partial x_i} \left(\overline{\bar{\rho} u_j'' Y_i''} \right) + \tilde{\omega}_i \quad (2.121)$$

Favre-averaging is similar introduced to the $k - \varepsilon$ model. The equations for the kinetic energy k from Eq. (2.104) and for the energy dissipation ε from Eq. (2.107) are finally obtained:

$$\frac{\partial \bar{\rho} \tilde{k}}{\partial t} + \frac{\partial \bar{\rho} \tilde{u}_j \tilde{k}}{\partial x_j} = \tilde{\tau}_{ij} \frac{\partial \tilde{u}_i}{\partial x_j} - \bar{\rho} \tilde{\varepsilon} + \frac{\partial}{\partial x_j} \left[\left(\mu + \frac{\mu_t}{\sigma_k} \right) \frac{\partial \tilde{k}}{\partial x_j} \right] + \tilde{W}_k^s \quad (2.122)$$

$$\frac{\partial \bar{\rho} \tilde{\varepsilon}}{\partial t} + \bar{\rho} \tilde{u}_j \frac{\partial \tilde{\varepsilon}}{\partial x_j} = C_{\varepsilon 1} \frac{\tilde{\varepsilon}}{\tilde{k}} \tilde{\tau}_{ij} \frac{\partial \tilde{u}_i}{\partial x_j} - C_{\varepsilon 2} \bar{\rho} \frac{\tilde{\varepsilon}^2}{\tilde{k}} + \frac{\partial}{\partial x_j} \left[\left(\mu + \frac{\mu_t}{\sigma_\varepsilon} \right) \frac{\partial \tilde{\varepsilon}}{\partial x_j} \right] + C_s \tilde{W}_k^s \quad (2.123)$$

Turbulent energy exchange between the liquid fuel droplets and the gas phase is accounted by the additionally term \tilde{W}_k^s in both equations with a model constant $C_s = 1.5$ [4].

It is not feasible to solve these equations analytically. A numerical integration by the volume of fluid method as described in [54, 92] is followed here which is implemented in the AC-FluX code. This code originates from the GMTec code [104] which is very

well suitable for engine simulations as demonstrated in [76]. In the low Mach number regime ($Ma < 0.3$), pressure waves are propagating by the velocity of sound and are much faster than the flow field velocities. Therefore the pressure is constant and does only change due to the bulk compression in the compression or expansion stroke.

3 Combustion Model

3.1 Physics of Non-Premixed Combustion

During the combustion in technical applications, as combustors in gas-turbines, conventional power-plants or reciprocal engines, chemically bounded energy is converted in an exothermal reaction into heat. For safety reasons, fuel and oxidizer are mostly not premixed to prevent an uncontrolled auto-ignition and combustion. By diffusive transport, fuel and oxidizer enters the reaction zone of the diffusion flame where the chemical reaction takes place which is denoted as non-premixed combustion. The design of the combustion process needs therefore an understanding about the molecular and turbulent transport in the reaction zone. For the simulation of a flow that includes chemical reactions, Eq. (2.24) was introduced as species conservation equation and the chemical source terms were given in Eq. (2.39) and Eq. (2.38) where typically Arrhenius type reaction rates are used for the oxidation of hydro-carbon fuels as presented by Eq. (2.37). It is desirable to include a detailed reaction mechanism to address the effects of auto-ignition and pollutant formation. Using elementary reaction mechanism within the species conservation equations increases the stiffness of the system of partial differential equations. Different models have been proposed to address that problem. One proposed way is to reduce the number of species by introducing quasi steady state assumption for intermediate species as shown by Peters in [154, 157]. The result is a skeletal mechanism which incorporates less stiffness but which can still reproduce the desired features for low- and high-temperature auto-ignition as demonstrated in [165]. The extension of these studies from one-dimensional flame configurations to a three-dimensional turbulent flow is complicated due to the computation of the chemical source term $\tilde{\omega}_i$. Small fluctuations T'' around the mean temperature \tilde{T} are due

to the Arrhenius type reaction rate Eq. (2.37) enhanced. A large number of higher moments would be required to achieve a convergent solution.

Alternatively, a new variable is introduced which is a conserved, non-reactive scalar called the mixture fraction variable as the only dependent variable. The flamelet model that is used in this work is based on the mixture fraction variable approach and will be presented here next.

3.2 Flamelet Model

A first understanding of combustion in diffusion flames was given by the work of Burke et al. [27] in 1928 under the assumption of an infinitely fast chemistry. However, if the time-scale of the turbulent diffusion is locally of the same order as the time-scales of the chemical reactions the species cannot relax to the equilibrium state.

Williams [216] proposed that a turbulent flame can be viewed as an ensemble of stretched laminar flamelets. A flamelet is a thin reaction layer that is embedded in a non-reacting flow field. Excluding the process of auto-ignition, the heat release in a steady flame leads to temperatures close to the chemical equilibrium. The chemical reactions are very fast and the corresponding chemical time-scale is much shorter than all the turbulent time-scales. Therefore, the reaction zone appears as a thin layer which is much smaller than the Kolmogorov length scale. The combustion in this thin reaction zone cannot impose any feed-back on the flow except for density changes. The inertial range scaling is not influenced by the combustion and vice versa, the reaction zone is invariant on the Reynolds number because shear forces and viscosity are not of leading order in these thin layers. That phenomena is denoted as scale separation between the time and length scale of combustion and turbulence in the inertial sub-range. The turbulent flow field only imposes strain and stretch on the reaction zone while the reaction zone maintains its laminar characteristic.

The structure of this thin reaction zone was analyzed by Liñán in 1974 [118] who derived an asymptotic solution in the limit of a one-step irreversible reaction. Phenomena like ignition and extinction are related to the Damköhler number Da which is the ratio of the residence time of chemical species in the reaction zone and a time

scale of the chemical reaction:

$$\text{Da} = \frac{t_{\text{res}}}{t_{\text{chem}}} \quad (3.1)$$

In order to study the thin reaction zone further on in detail, the analysis will be carried out with respect to the mixture fraction as the new independent variable. First, the mixture fraction variable is introduced as a conserved scalar. Second, the transition from physical space to phase space is presented and the flamelet equations that describe the transport in the thin reaction layer will be derived.

3.2.1 Mixture Fraction Variable

The mixing process between fuel and oxidizer is similar to that of a two-feed system in a shear layer behind a splitter plate as shown in Fig. 3.1. The oxidizer stream in

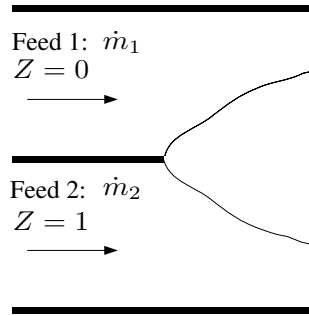
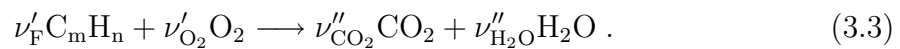


Figure 3.1: Mixing process in a two-feed shear layer behind a splitter plate

feed 1 with a mass flow rate \dot{m}_1 and fuel stream in feed 2 with a mass flow rate \dot{m}_2 are related by the mixture fraction variable

$$Z = \frac{\dot{m}_1}{\dot{m}_1 + \dot{m}_2} . \quad (3.2)$$

$Z = 0$ denotes the oxidizer whereas $Z = 1$ indicates the fuel. A general one-step global reaction for the complete oxidation of a hydrocarbon fuel is given as



The stoichiometric coefficients of oxidizer, carbondioxid and water can be determined as

$$\nu'_{\text{O}_2} = (m + \frac{n}{4})\nu'_F \quad (3.4)$$

$$\nu''_{\text{CO}_2} = m\nu'_F \quad (3.5)$$

$$\nu''_{\text{H}_2\text{O}} = \frac{n}{2}\nu'_F . \quad (3.6)$$

Beside the global reaction, chemical elements have to be conserved and Eq. (3.3) is rewritten yielding the element balance equation



The number of atoms ν_j of element j are obtained by comparison with Eq. (3.3):

$$\nu_C = m \quad (3.8)$$

$$\nu_H = n \quad (3.9)$$

$$\nu_O = m + \frac{n}{4} \quad (3.10)$$

A main interest are the conditions when the oxidizer is fully consumed. These conditions are denoted as stoichiometric mixture and are obtained from the given global reaction Eq. (3.3) in terms of mole fractions

$$\left. \frac{X_{\text{O}_2}}{X_F} \right|_{\text{st}} = \frac{\nu'_{\text{O}_2}}{\nu'_F} \quad (3.11)$$

as well as in terms of mass fractions

$$\nu = \left. \frac{Y_{\text{O}_2}}{Y_F} \right|_{\text{st}} = \frac{\nu'_{\text{O}_2} W_{\text{O}_2}}{\nu'_F W_F} . \quad (3.12)$$

The stoichiometric mixture fraction is given by

$$Z_{\text{st}} = \left[1 + \nu \frac{Y_{F,1}}{Y_{\text{O}_2,2}} \right]^{-1} . \quad (3.13)$$

Another definition is the equivalence ratio ϕ that relates the fuel/air ratio of unburnt and stoichiometric conditions

$$\phi = \frac{Y_{F,u}/Y_{\text{O}_2,u}}{(Y_{F,u}/Y_{\text{O}_2,u})_{\text{st}}} = \nu \frac{Y_{F,u}}{Y_{\text{O}_2,u}} . \quad (3.14)$$

The equivalence ratio is a normalized mixture fraction

$$\phi = \frac{Z}{1-Z} \frac{1-Z_{\text{st}}}{Z_{\text{st}}} . \quad (3.15)$$

As already mentioned, the combustion process is controlled by the ratio of timescales of turbulence and diffusion for that local mixing effects have to be taken into account. In a more general way, the mixture fraction is expressed by the element mass fraction Z_j which relates the mass m_j of atom j to the overall mass

$$Z_j = \frac{m_j}{m} = \sum_{i=1}^N \frac{a_{ij}W_j}{W_i} Y_i \quad , j = 1 \cdots n_e , \quad (3.16)$$

where a_{ij} are the number of atoms j in species i , W_i and W_j is the molar weight of atom j and species i , respectively, N denotes the number of species and n_e the number of elements. That definition is used to re-write Eq. (2.24) as a conservation equation for Z_j

$$\frac{\partial \rho Z_j}{\partial t} + \frac{\partial \rho u_i Z_j}{\partial x_i} = \frac{\partial}{\partial x_i} \left(\rho D \frac{\partial Z_j}{\partial x_i} \right) . \quad (3.17)$$

The chemical source term $\dot{\omega}_i$ in Eq. (2.24) vanishes because in chemical reactions, elements are always conserved. It is assumed here that the diffusion coefficients D_i are all equal. The made assumptions of equal diffusion coefficients is limiting but realistic for most species. Differential diffusion effects can be seen as a small perturbation that is neglectable [21]. Non-unity Lewis numbers effects are only relevant in low Reynolds numbers and appears only close to the exit-nozzle as discussed by Pitsch in [163]. Hence, the influence of differential diffusion will not considered here. Under the assumption of equal diffusion coefficients, the Lewis number Le_i in Eq. (2.36) becomes unity for all species.

Williams [217] introduced a coupling function of Schvab-Zel'dovich type given as

$$\beta = \frac{Z_C}{\nu_C W_C} + \frac{Z_H}{\nu_H W_H} - \frac{Z_O}{\frac{1}{2} \nu_O W_{O_2}} . \quad (3.18)$$

The coupling function β is normalized in the limits between 0 and 1, yielding a definition for the mixture fraction variable based on element mass fractions

$$Z = \frac{\beta - \beta_2}{\beta_1 - \beta_2} . \quad (3.19)$$

Again, index 1 and 2 denotes here the fuel and oxidizer stream, respectively. From the definition of the coupling function an alternative definition of the mixture fraction on the basis of element mass fractions is derived by Bilger [20]

$$Z = \frac{Z_C/(\nu_C W_C) + Z_H/(\nu_H W_H) + 2(Z_{O,2} - Z_O)/(\nu_O W_O)}{Z_{C,1}/(\nu_C W_C) + Z_{H,1}/(\nu_H W_H) + 2Z_{O,2}/(\nu_O W_O)}. \quad (3.20)$$

From the definition of the normalized coupling function Eq. (3.19), the balance equation for the element mass fraction Z_j in Eq. (3.17) is rewritten as

$$\frac{\partial \rho Z}{\partial t} + \frac{\partial \rho u_i Z}{\partial x_i} = \frac{\partial}{\partial x_i} \left(\rho D_Z \frac{\partial Z}{\partial x_i} \right). \quad (3.21)$$

D_Z is set here equally to the thermal diffusivity D assuming that the mixture fraction has a Lewis number of unity.

3.2.2 Burke-Schumann's Equilibrium Solution

Burke et al. [27] assumed a one-step global reaction of an irreversible reaction to be infinite fast for which $Da \rightarrow \infty$. Diffusive mixing is the rate-controlling process and the mass fractions for oxidizer and fuel can hence be expressed by piecewise linear functions of the previously introduced mixture fraction variable Z :

$$Y_{O_2} = \begin{cases} Y_{O_2,1} \left(1 - \frac{Z}{Z_{st}} \right) & : Z \leq Z_{st} \\ 0 & : Z > Z_{st} \end{cases}. \quad (3.22)$$

$$Y_F = \begin{cases} 0 & : Z \leq Z_{st} \\ Y_{F,2} \frac{Z - Z_{st}}{1 - Z_{st}} & : Z > Z_{st} \end{cases}. \quad (3.23)$$

In the unburnt mixture, the temperature is derived from a linear mixing between fuel and oxidizer:

$$T_u = T_1 + Z(T_2 - T_1) \quad (3.24)$$

For the burning diffusion flame, the temperature is related to the massfraction of oxidizer and fuel as well and the mixture fraction variable as a piecewise-linear function. Additionally, the temperature of the unburnt mixture has to be supposed:

$$T(Z) = T_u(Z) + \begin{cases} \frac{Q Y_{F,2}}{c_p \nu'_F W_F} Z & : Z \leq Z_{st} \\ \frac{Q Y_{O_1,2}}{c_p \nu'_{O_2} W_{O_2}} & : Z > Z_{st} \end{cases}. \quad (3.25)$$

The resulting profiles of oxidizer and fuel mass fraction and resulting temperature are shown in Fig. 3.2. The reaction zone is located at stoichiometric mixture Z_{st} . However, the assumption of an irreversible reaction is not justified. If the reaction

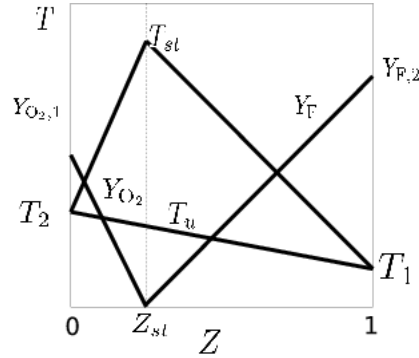


Figure 3.2: Burke-Schumann solution in phase space

rate is to be assumed infinitely fast but reversible reactions are considered, species can reach the chemical equilibrium at the limit. The temperature and species composition of the equilibrium state are calculated by iterative methods, e.g. Newton's method. The calculated temperature at equilibrium state is denoted as adiabatic flame temperature. As mentioned, the equilibrium state represents a limit, e.g. combustion in hydrogen flames are in equilibrium state. In hydrocarbon flames, species are only close to an equilibrium and the reaction rates are finite. Finite-rate chemistry and near-equilibrium chemistry are therefore to be considered for alkane fuel types.

3.2.3 Flamelet Equations

A first attempt to analyse the structure of the thin reaction zone was made by Peters [152] and Kuznetsov [113] for steady state conditions and later extended to instationary conditions [153] and reviewed in [155]. The previously introduced mixture fraction variable is used as a coupling function between the physical space and mixture fraction space. The mixing process between a fuel-jet into its surrounding is shown in Fig. 3.3. The surface of the flame and its reaction zone is attached to the iso-surface of stoichiometric mixture. In the following, two different approaches are presented,

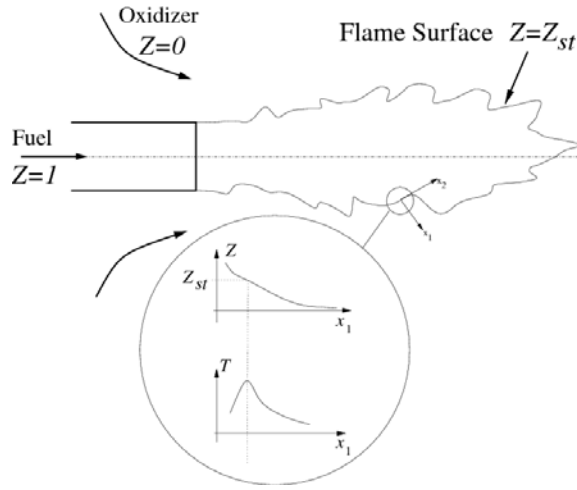


Figure 3.3: Structure of a diffusion flame

leading to the same form of the flamelet equations.

3.2.3.1 Crocco Transformation

The original approach applies the Crocco type transformation [38]

$$(t, x_1, x_2, x_3)^T \rightarrow (\tau, Z_1, Z_2, Z_3)^T \quad (3.26)$$

to the laminar species- and temperature conservation equations. The time- and space derivatives are obtained as:

$$\frac{\partial}{\partial t} = \frac{\partial}{\partial \tau} + \frac{\partial Z_1}{\partial t} \frac{\partial}{\partial Z_1} \quad (3.27)$$

$$\frac{\partial}{\partial x_1} = \frac{\partial Z_1}{\partial x_1} \frac{\partial}{\partial Z_1} \quad (3.28)$$

$$\frac{\partial}{\partial x_j} = \frac{\partial}{\partial Z_j} + \frac{\partial Z_1}{\partial x_j} \frac{\partial}{\partial Z_1}, \quad j = 1, 2 \quad (3.29)$$

By this transformation, a local coordinate system is defined with its origin located in the reaction layer. Z_1 represents a normal coordinate on the iso-surface of the flame whereas the other two components, Z_2 and Z_3 , are ortho- and bi-normal. Applying the new operators from Eq. (3.29) to the species- and temperature conservation equation

Eq. (2.24) and Eq. (2.34), one can argue that only gradients in Z_1 normal on the flame surface are of leading order whereas gradients in Z_2 and Z_3 which are tangential on the flame surface are of first order in analogy to the boundary layer theory. The final form of the flamelet equations for the species and temperature are obtained as

$$\rho \frac{\partial Y_i}{\partial t} - \rho \frac{\chi}{2Le_i} \frac{\partial^2 Y_i}{\partial Z^2} = \dot{\omega}_i \quad (3.30)$$

and

$$\rho \frac{\partial T}{\partial t} - \rho \frac{\chi}{2} \frac{\partial^2 T}{\partial Z^2} - \rho \frac{\chi}{2c_p} \left[\sum_{i=1}^N \frac{c_{p_i}}{Le_i} \frac{\partial Y_i}{\partial Z} + \frac{\partial c_p}{\partial Z} \right] \frac{\partial T}{\partial Z} = \frac{1}{c_p} \left(\frac{\partial p}{\partial t} - \dot{q}_R - \sum_{i=1}^N \dot{\omega}_i h_i \right). \quad (3.31)$$

In [152] and recently in [156], the same flamelet equations are derived by a two scale asymptotic analysis which is a more general approach.

3.2.3.2 The Scalar Dissipation Rate

In both flamelet equations, Eq. (3.30) and Eq. (3.31), a new parameter χ appears which is formally related to the gradient of the mixture fraction field

$$\chi = 2D \left(\frac{\partial Z}{\partial x_j} \right)^2. \quad (3.32)$$

This parameter is denoted as the instantaneous scalar dissipation rate. It acts as a diffusivity in mixture fraction space and has the dimensions of an inverse time-scale. Because it does not rely on other flow variables, the scalar dissipation rate is invariant in the inertial range and does not depend on the Reynolds number. That means that the diffusive transport is controlled by χ and depends on the mixture fraction gradients that are only influenced by the turbulent eddies but not by the reaction zone itself. The changes in the turbulent flow field are stretching or compressing the iso-lines of stoichiometric mixture, hence, increasing or decreasing the scalar dissipation rate.

If the scalar dissipation rate is increasing and exceeding a critical value χ_q , the diffusive transport in mixture fraction space is larger than the chemical source-terms and the flame extinguishes. On the other limit the scalar dissipation rate can become very small and in the limit $\chi \rightarrow 0$ because the mixture fraction field gradient's are zero in the limit $\nabla Z \rightarrow 0$. In this case the flamelet equations are describing an homogenous

reactor as shown in [32, 40]. For simple flame configurations, the scalar dissipation rate is derived from the analytical solution of the mixture fraction field. In a one-dimensional unsteady laminar mixing layer, the scalar dissipation rate is derived as

$$\chi(Z) = \frac{1}{t} 2Z^2 [\operatorname{erfc}^{-1}(2Z)] . \quad (3.33)$$

To eliminate the time-scale, the scalar dissipation rate is normalized on its conditional value χ_{st} at stoichiometric mixture Z_{st} :

$$\chi(Z) = \chi_{\text{st}} \frac{f(Z)}{f(Z_{\text{st}})}, f(Z) = 2Z^2 [\operatorname{erfc}^{-1}(2Z)] \quad (3.34)$$

3.3 Modeling of Turbulent Transport

3.3.1 Turbulent Transport of Reactive Scalars

The transport of a reactive scalar in a turbulent flow imposes difficulties because a closure between the velocity fluctuations and fluctuations of the reactive scalars $\overline{\rho u_i'' \psi_i''}$ has to be found. Usually the counter gradient assumption is applied. However, this assumption is not justified in the case of a reactive scalar. Any turbulent reactive scalar can be decomposed in a Favre average and a fluctuation value

$$\psi_i(\mathbf{x}, t) = \tilde{\psi}_i(\mathbf{x}, t) + \psi_i''(\mathbf{x}, t) . \quad (3.35)$$

With that definition, Eq. (2.31) is re-written, yielding a transport equation for the mean value of the reactive scalar

$$\bar{\rho} \frac{\partial \tilde{\psi}_i}{\partial t} + \bar{\rho} \tilde{u}_j \frac{\partial \tilde{\psi}_i}{\partial x_j} = \frac{\partial}{\partial x_j} \left(\overline{\rho D_i \frac{\partial \psi_i}{\partial x_j}} \right) - \frac{\partial}{\partial x_j} \left(\overline{\rho u_j'' \psi_i''} \right) + \bar{\rho} \tilde{\omega}_i \quad (3.36)$$

and its variance as

$$\begin{aligned} \bar{\rho} \frac{\partial \overline{\psi_i''^2}}{\partial t} + \bar{\rho} \tilde{u}_j \frac{\partial \overline{\psi_i''^2}}{\partial x_j} = & \underbrace{-\frac{\partial}{\partial x_j} \left(\overline{\rho \tilde{u}_j'' \psi_i''^2} \right)}_{\text{turbulent transport}} \\ & + \underbrace{2\bar{\rho} \left(-\overline{u_j'' \psi_i''} \right) \frac{\partial \tilde{\psi}_i}{\partial x_j}}_{\text{production}} - \underbrace{\bar{\rho} \tilde{\chi}_i}_{\text{dissipation}} + \underbrace{2\bar{\rho} \overline{\psi_i'' \omega_i''}}_{\text{chem. source term}} . \end{aligned} \quad (3.37)$$

The Favre-averaged scalar dissipation rate is similar defined as in Eq. (3.32).

$$\tilde{\psi}_i = 2D_i \left(\frac{\partial \widetilde{\psi_i''}}{\partial x_j} \right)^2 \quad (3.38)$$

The integral time-scale of the flow as given in Eq. (2.70) can also be derived from the Favre-averaged scalar dissipation rate $\tilde{\chi}_i$ and the fluctuations of the Favre-averaged scalar $\tilde{\psi}_i$:

$$\tau_i = \frac{\widetilde{\psi_i''^2}}{\tilde{\chi}_i} \quad (3.39)$$

Both time-scales are of the same order and the proportionality constant is denoted as c_χ :

$$\tau = c_\chi \tau_i \quad (3.40)$$

A value of $c_\chi = 2.0$ is applied usually. From Eq. (3.40), Eq. (3.39) and Eq. (2.70), an equation is found to model the scalar dissipation rate

$$\tilde{\chi}_i = c_\chi \frac{\tilde{\varepsilon}}{k} \widetilde{\psi_i''^2}. \quad (3.41)$$

3.3.2 Modeling of Non-Premixed Turbulent Combustion

3.3.2.1 Turbulent Mixture Fraction Field

Solving the species conservation equations Eq. (2.81) directly is not possible. Instead, a transport equation for the mixture fraction $Z(\mathbf{x}, t)$ is applied. Hence, the gradient assumption remains valid since it is a non-reactive scalar. The mixture fraction variable Z is decomposed into a Favre averaged mean value and its fluctuation

$$Z(\mathbf{x}, t) = \tilde{Z}(\mathbf{x}, t) + Z''(\mathbf{x}, t). \quad (3.42)$$

Introducing that decomposition into Eq. (3.21) yields a transport equation for the mean value and its variance:

$$\frac{\partial(\bar{\rho}\tilde{Z})}{\partial t} + \frac{\partial}{\partial x_j} (\bar{\rho}\tilde{u}_j\tilde{Z}) = -\frac{\partial}{\partial x_j} (\bar{\rho}\widetilde{u_j''Z''}) \quad (3.43)$$

$$\frac{\partial(\bar{\rho}\widetilde{Z''^2})}{\partial t} + \frac{\partial}{\partial x_j} (\bar{\rho}\tilde{u}_j\widetilde{Z''^2}) = -\frac{\partial}{\partial x_j} (\bar{\rho}\widetilde{u_j''Z''^2}) + 2(-\bar{\rho}\widetilde{u_j''Z''}) \left(\frac{\partial\tilde{Z}}{\partial x_j}\right)^2 - \bar{\rho}\tilde{\chi} \quad (3.44)$$

The gradient assumption is made for the unclosed correlations $(\bar{\rho}\widetilde{u_j''Z''})$ and $(\bar{\rho}\widetilde{u_j''Z''^2})$:

$$(\bar{\rho}\widetilde{u_j''Z''}) = -D_t \frac{\partial\tilde{Z}}{\partial x_j} \quad (3.45)$$

$$(\bar{\rho}\widetilde{u_j''Z''^2}) = -D_t \frac{\partial\widetilde{Z''^2}}{\partial x_j} \quad (3.46)$$

Closure of the correlations yields the conservation equation of the mean mixture fraction

$$\frac{\partial(\bar{\rho}\tilde{Z})}{\partial t} + \frac{\partial}{\partial x_j} (\bar{\rho}\tilde{u}_j\tilde{Z}) = \frac{\partial}{\partial x_j} \left(\frac{\mu_t}{\text{Sc}_{\tilde{Z}}} \frac{\partial\tilde{Z}}{\partial x_j} \right) \quad (3.47)$$

and its mean variance

$$\frac{\partial(\bar{\rho}\widetilde{Z''^2})}{\partial t} + \frac{\partial}{\partial x_j} (\bar{\rho}\tilde{u}_j\widetilde{Z''^2}) = \frac{\partial}{\partial x_j} \left(\frac{\mu_t}{\text{Sc}_{\widetilde{Z''^2}}} \frac{\partial\widetilde{Z''^2}}{\partial x_j} \right) + \frac{2\mu_t}{\text{Sc}_{\widetilde{Z''^2}}} \left(\frac{\partial\tilde{Z}}{\partial x_j}\right)^2 - \bar{\rho}\tilde{\chi}. \quad (3.48)$$

The turbulent diffusivity coefficient is expressed by the turbulent Schmidt numbers $\text{Sc}_{\tilde{Z}}$ and $\text{Sc}_{\widetilde{Z''^2}}$, equally 0.7, and the turbulent viscosity μ_t . The influence of molecular diffusivity is assumed to be small compared to the turbulent transport and therefore neglected here.

The mean scalar dissipation rate $\tilde{\chi}$ is defined similar to Eq. (3.41) as

$$\tilde{\chi} = c_\chi \frac{\tilde{\varepsilon}}{\bar{k}} \widetilde{Z''^2}. \quad (3.49)$$

The proportionality constant is proposed as 2.0 [91] which is also found in [37] for $\text{Da} \rightarrow 0$ but other authors suggested a value of 1.0 [94] or even higher values between 2.0 and 3.0 from results of DNS-simulations in [148] and [99]. Here, a constant value of $\tilde{\chi} = 2.0$ will be used.

3.3.2.2 PDF-Approach for Non-Premixed Turbulent Combustion

In the flamelet equations Eq. (3.30) and Eq. (3.31) the only dependent variables are the mixture fraction Z and the scalar dissipation rate $\chi(Z)$. However, in a turbulent

flows, their statistical distribution must be known if statistical moments are calculated. The probability distribution function (PDF) is the joint PDF in Z and χ , denoted as $P(Z, \chi; \mathbf{x}, t)$. Its Favre-average is given by

$$\tilde{P}(Z, \chi; \mathbf{x}, t) = \frac{\rho(\mathbf{x}, t)P(Z, \chi; \mathbf{x}, t)}{\bar{\rho}(\mathbf{x}, t)}. \quad (3.50)$$

The first moment Eq. (2.51) of the species mass fraction Y_i is given as

$$\tilde{Y}_i(\mathbf{x}, t) = \int_0^1 \int_0^\infty Y_i(Z, \chi) \tilde{P}(Z, \chi; \mathbf{x}, t) d\chi dZ. \quad (3.51)$$

The use of a joint PDF that depends on two variables is not very practical. The joint PDF is decomposed by applying Baye's theorem into a marginal PDF $\tilde{P}(Z; \mathbf{x}, t)$ and a conditional PDF $\tilde{P}(\chi|Z; \mathbf{x}, t)$:

$$\int_0^1 \int_0^\infty \tilde{P}(Z, \chi; \mathbf{x}, t) d\chi dZ = \int_0^1 \int_0^\infty \tilde{P}(Z; \mathbf{x}, t) \tilde{P}(\chi|Z; \mathbf{x}, t) d\chi dZ$$

Under the assumption of statistical independence of χ on Z , it follows that

$$\int_0^1 \int_0^\infty \tilde{P}(Z; \mathbf{x}, t) \tilde{P}(\chi|Z; \mathbf{x}, t) d\chi dZ = \int_0^1 \tilde{P}(Z; \mathbf{x}, t) dZ \cdot \int_0^\infty \tilde{P}(\chi; \mathbf{x}, t) d\chi. \quad (3.52)$$

By assuming that the PDF $\tilde{P}(\chi)$ is a Dirac delta function

$$\tilde{P}(\chi) = \delta(\chi - \tilde{\chi}), \quad (3.53)$$

the last term on the r.h.s of Eq. (3.52) reads as

$$\int_0^\infty \tilde{P}(\chi; \mathbf{x}, t) d\chi = \tilde{\chi}(\mathbf{x}, t). \quad (3.54)$$

The made assumption of statistical independence between χ on Z has been investigated theoretically in [19] but following the arguments in [130, 131], that assumption is only valid for high Reynolds number flows.

If Eq. (3.34) is combined with Eq. (3.49) a conditional value at stoichiometric mixture is obtained to determine $\tilde{\chi}$

$$\tilde{\chi} = \tilde{\chi}_{st} \int_0^1 \tilde{P}(Z; \mathbf{x}, t) \frac{f(Z)}{f(Z_{st})} dZ = c_\chi \frac{\tilde{\varepsilon}}{\tilde{k}} \widetilde{Z''^2}. \quad (3.55)$$

It follows that the conditional mean scalar dissipation rate $\tilde{\chi}_{st}$ is given as

$$\tilde{\chi}_{st} = \frac{c_{\chi} \tilde{\tilde{Z}}''^2}{\int_0^1 \tilde{P}(Z; \mathbf{x}, t) \frac{f(Z)}{f(Z_{st})} dZ} . \quad (3.56)$$

Alternatively, Pope [167] and Jones in [96] proposed a scalar transport equation for the mean scalar dissipation rate whereas [91] uses a transport equation for $\tilde{P}(Z; \mathbf{x}, t)$ where the conditional mean scalar dissipation rate appears in the diffusive operator. Another attempt to account for the conditional PDF $\tilde{P}(\chi|Z; \mathbf{x}, t)$ was proposed by Barths [11] in the Eulerian Particle Flamelet Model (EPFM). Imaginary marker particles are used to track domains that have a different evolution of the scalar dissipation rate and therefore represents different trajectories in a 3-dimensional manifold that is spanned by the mixture fraction, the scalar dissipation rate and the time as coordinates. However, this trajectory depends on the start-point as initial condition and the step-width that is pre-scribed by the turbulent flow as boundary conditions.

From Eq. (3.51), the first moment for the species mass fraction is obtained by

$$\tilde{Y}_i(\mathbf{x}, t) = \int_0^1 Y_i(Z, \tilde{\chi}) \tilde{P}(Z; \mathbf{x}, t) dZ . \quad (3.57)$$

Still the marginal PDF of Z , $\tilde{P}(Z; \mathbf{x}, t)$, needs to be determined. Here, $\tilde{P}(Z; \mathbf{x}, t)$ is taken as a presumed β -PDF as shown by Girimaji [64] and Liew[117]. The shape is defined by the cumulants $K_1 = \tilde{\tilde{Z}}$ and $K_2 = \tilde{\tilde{Z}}''^2$, as introduced in analogy for the PDF of \mathbf{u} in Eq. (2.56) and Eq. (2.57), respectively:

$$\tilde{P}(Z; \mathbf{x}, t) = Z^{\alpha-1} (1-Z)^{\beta-1} \frac{\Gamma(\gamma)}{\Gamma(\alpha)\Gamma(\beta)} \quad (3.58)$$

γ , α and β are related to $\tilde{\tilde{Z}}$ and $\tilde{\tilde{Z}}''^2$:

$$\gamma = \frac{\tilde{\tilde{Z}}(1-\tilde{\tilde{Z}})}{\tilde{\tilde{Z}}''^2} - 1, \alpha = \tilde{\tilde{Z}}\gamma, \beta = (1-\tilde{\tilde{Z}})\gamma \quad (3.59)$$

For small variances, the β -PDF becomes similar to a Gaussian distribution. However, the β -PDF is unable to describe mixture where only fuel or only oxidizer occurs. These singularities at $Z = 0$ or $Z = 1$, expressed as a Dirac delta function, can be included in a clipped Gaussian distribution as proposed by Effelsberg [46] based on the work of Lockwood [119]. For turbulent, gaseous jets, the β -PDF is a good assumption [97].

3.4 The RIF-Model

The separation between the turbulent integral time-scales and the time-scale of chemistry is a major benefit of the flamelet approach. The diffusive transport in the flamelet space is independent of the Reynolds-number and only controlled by the scalar dissipation rate. Furthermore, the one-dimensional nature of the thin reaction zone allows to use a detailed reaction mechanism. The complete flow domain is assigned by a single flamelet solution denoted as Representative Interactive Flamelet (RIF) - model. The coupling between the solution of the gas phase equations on behalf of the CFD code and the solution of the flamelet equations on behalf of the flamelet code is shown in Fig. 3.4. In order to solve the flamelet equations, the initial conditions and the

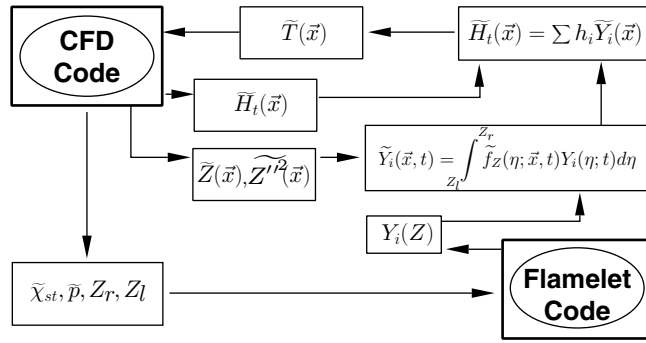


Figure 3.4: Interaction between CFD- and RIF-code

scalar dissipation rate are evaluated in the computational domain. An initial value of the pressure is obtained by volume-averaging

$$\hat{p} = \frac{\int_V \tilde{p} dV}{\int_V dV}. \quad (3.60)$$

The local conditional scalar dissipation rate in Eq. (3.56) is evaluated in every computational and averaged as shown in [162] to yield a representative value

$$\widehat{\chi}_{st} = \frac{\int_V \chi_{st}^{3/2} \bar{\rho} \tilde{P}(Z_{st}) dV'}{\int_V \chi_{st}^{1/2} \bar{\rho} \tilde{P}(Z_{st}) dV'}. \quad (3.61)$$

Both, the domain averaged pressure and conditional scalar dissipation rate are often denoted as "flamelet parameters". Mean species mass fractions can be computed if

the β -PDF is obtained from the solution of the turbulent mixture fraction field. The turbulent enthalpy and the enthalpy of the flamelet are used to compute the local mean temperature field $\tilde{T}(\mathbf{x}, t)$ iteratively from Eq. (2.17).

3.5 Chemical Reaction Mechanism

The one-dimensional flamelet equations allow to include a chemical source term based on a detailed reaction mechanism with finite-rate chemistry. Typical technical fuels as Diesel fuel consists of several hundreds and more different hydrocarbon species. The composition is varying and depending on the crude oil origin as well as on the refining process. Therefore, it is impossible to develop a chemical mechanism that represents the exact composition. In the framework of the IDEA-EFFECT program [36] a surrogate fuel of 70% n-decane and 30% α -methylnaphthalene, by liquid volume (denoted as IDEA-fuel), has been proposed as a model fuel for Diesel. Properties of IDEA-fuel are similar to that of Diesel. Engine experiments on a 1.9 l transparent Volkswagen DI engine have been conducted by Antoni [6] to compare Diesel with IDEA fuel. Pressure trace and emissions of IDEA fuel are in good agreement with the Diesel fuel. In [211], a comparison between IDEA-fuel, n-decane, n-heptane and Diesel with high amounts of EGR was investigated. Only IDEA-fuel shows the same ignition delay and heat release as Diesel fuel.

For the IDEA fuel, a detailed kinetic reaction mechanism has been compiled. The mechanism accounts for low- and high temperature auto-ignition, correct chemical heat release and formation of NO_x and soot precursors. The original n-decane part of the mechanism was taken from Pitsch[164]. The main reaction channels of the n-decane depletion are shown in Fig. 3.5. Two main reaction channel exist: one reaction channel is dominating at high temperatures that lead directly from n-decane to C_6 , C_5 and C_3 species, the other is the low temperature chain branching channel that depletes n-decane via the ketohydroperoxide ORO_2H or heptyl radical. Both reaction channels are competing and cause the negative temperature gradient of the ignition delay in Fig. 3.7.

The chemistry for $\text{C}_1 - \text{C}_2$ and O/H is mainly taken from data by Baulch [15]. Data for

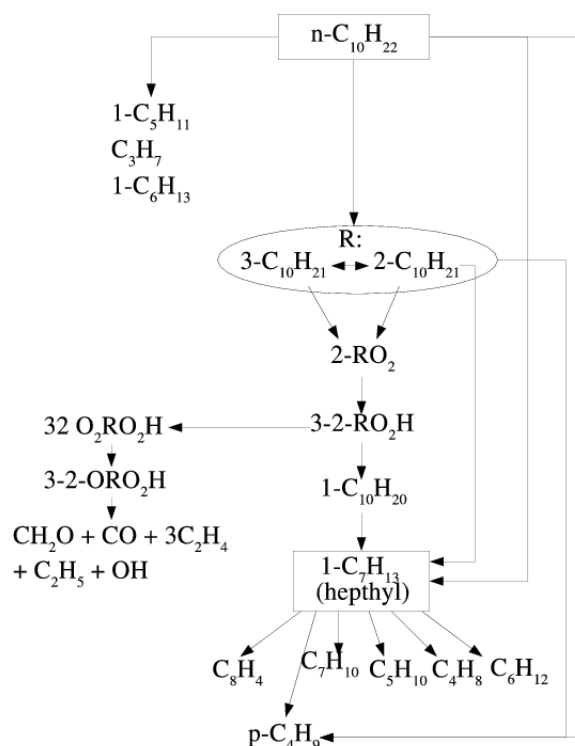


Figure 3.5: Fuel depletion of n-decane

low temperature chemistry is given in Benson [17] and Chevalier [30]. The NO_x sub-mechanism from Hewson [80] accounts for thermal, prompt, and nitrous oxide contributions to NO_x formation whereas NO_x reburn by hydrocarbon radicals and amines (NH_x) is included. The mechanism accounts for the chemistry of soot precursors up to benzene following Mauss [123] based on Frenklach et al. [56] and Miller et al. [134]. Soot particles are formed during the combustion process in fuel-rich regions by nucleation from polycyclic aromatic hydrocarbons (PAHs). C_2 and C_3 molecules form phenyl and benzene, the first cyclic molecule. Further reactions of acetylene are leading to higher cyclic compounds in a polymerization process. The mechanism includes the formation and growth up to four aromatic rings. The main reaction channels of the α -methylnaphthalene depletion are shown in Fig. 3.6. Here, different reaction channels are competing for oxidation of α -methylnaphthalene and reducing the numbers of aromatic rings. From phenyl and benzene C_6 , C_5 , C_4 and C_3 species are formed. On the other side, naphthyl is formed from benzene or by the depletion of

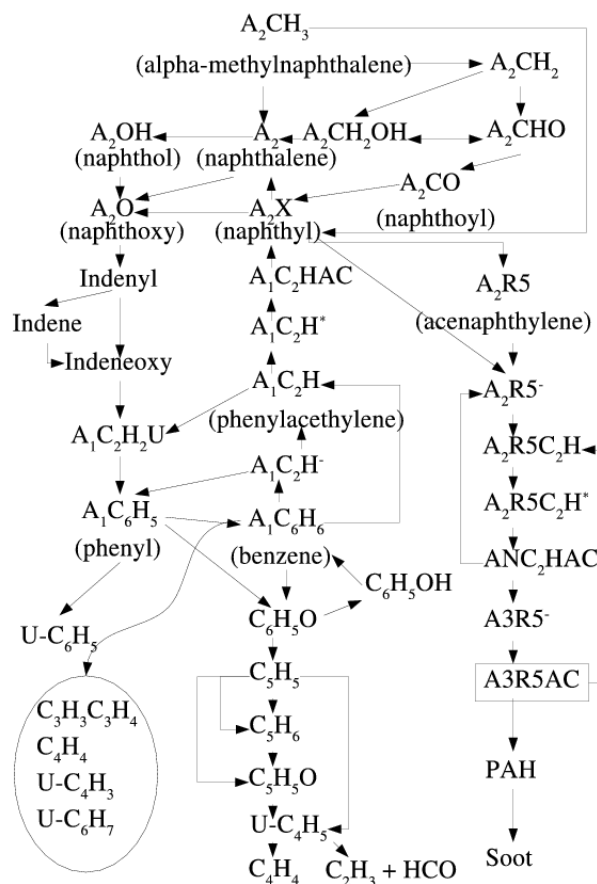


Figure 3.6: Fuel depletion of α -methylnaphthalene

α -methylnaphthalene by addition of carbon and hydrogen. Naphthyl is either oxidized to naphthoxy or form acenaphthylene from where ring growth lead to PAH in the gas phase.

3.5.1 Validation of Ignition Delay

Three different mechanisms are currently in use for the IDEA model fuel: nDaMV1, nDaMV3.1 and nDaMV3.5. nDaMV1 is a reduced mechanism, which comprises 118 chemical species and 506 elementary reactions. The included sub-mechanism of n-

decane has been reviewed in [18] and firstly applied to the Diesel engine simulation in [75, 12]. From that basis, the mechanism has been recompiled yielding version nDaMV3.1. It comprises 116 chemical species and 999 elementary reactions. Both mechanisms are tested in the engine simulation and in homogenous reactor calculations. It is found in section 6.3 that in the low temperature combustion regime neither nDaMV1 nor nDaMV3.1 is able to show a good ignition delay and a correct heat release.

Two reactions are identified to be very sensitive on the ignition delay:

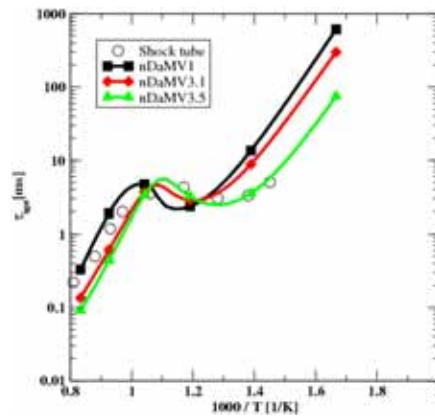


The Arrhenius parameters are modified and compiled in a new version, denoted as nDaMV3.5. The changes of the Arrhenius parameters for these reactions are summarized in Tab. 3.1. The mechanisms are compared with experimental data of ig-

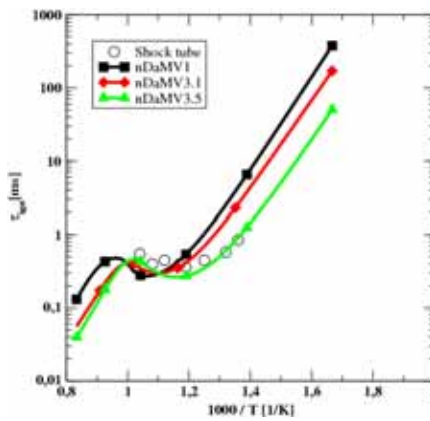
Reaction	Mechanism	A	n	E
	nDaMV3.1	2.048E13	0.0	24.9[14, 15]
r R140	nDaMV3.5	3.0E13	0.0	12.6
	nDaMV3.1	4.5E11	0.0	0.0 [140]
r R352	nDaMV3.5	2.5E11	0.0	0.0

Table 3.1: Arrhenius rate coefficients

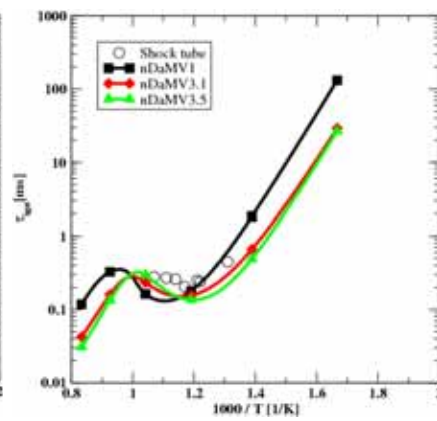
niton delay from shock-tube experiments [159] as shown in Fig. 3.7. Two different pressures of 13 and 50 bar, and two different equivalence ratios, $\phi = 1$ and 2, are investigated. Clearly to see is the negative temperature gradient between the low- and high-temperature reaction regime at $1000/T=1.1 \dots 1.3$ where the ignition delay increases with increasing temperature.



(a) $p=13\text{bar}$ and $\phi=1$



(b) $p=50\text{ bar}$ and $\phi=1$



(c) $p=50\text{ bar}$ and $\phi=2$

Figure 3.7: Ignition delay of IDEA fuel. Comparison of [159] with model fuel.

3.5.2 Pollutant Formation

The injection of Diesel into the combustion chambers generates a non-uniform fuel distribution. In fuel-rich regions, soot-particles are formed. Pollutants as unburnt hydrocarbons (HC) are resulting from a locally, incomplete combustion due to quenching at cold walls. Another major pollutant is NO_x that is formed in the reaction zone at high temperatures. The NO_x formation reactions are much slower than the time-scales of the flow field and are not relaxing to the equilibrium state. Therefore, NO_x reactions are frozen during the expansion stroke and cannot follow the change in temperature. The objective is to minimize both, NO_x and soot-emissions to meet the emission regulations. However, NO_x occurs at high temperatures where soot is burned. At low temperatures, NO_x -emissions are minimized but soot particles are not fully oxidized. This phenomena is denoted as soot- NO_x trade-off. In the ϕ -T space [2], soot and NO_x regions are indicated. Between both islands only a small band exists that potentially could be used to establish a combustion mode for a clean Diesel engine as seen in Fig. 3.8.

3.5.2.1 NO_x Formation

A sub-mechanism for NO_x -formation is included in the reaction mechanism for IDEA fuel that was compiled in [23, 80]. The included chemical reactions are shown in Fig. 3.9 [23]. NO_x is considered as the sum of NO_2 and NO . The reaction channels that lead to NO -formation are denoted as thermal- NO , prompt- NO , nitrous- NO whereas the oxidation channel is denoted as NO -reburn.

The most significant contribution to the formation of NO is the thermal- NO reaction channel. Oxidation of N_2 occurs at locally high temperatures greater than 1800 K [133] for which Zel'dovich [221] has proposed the following reactions:



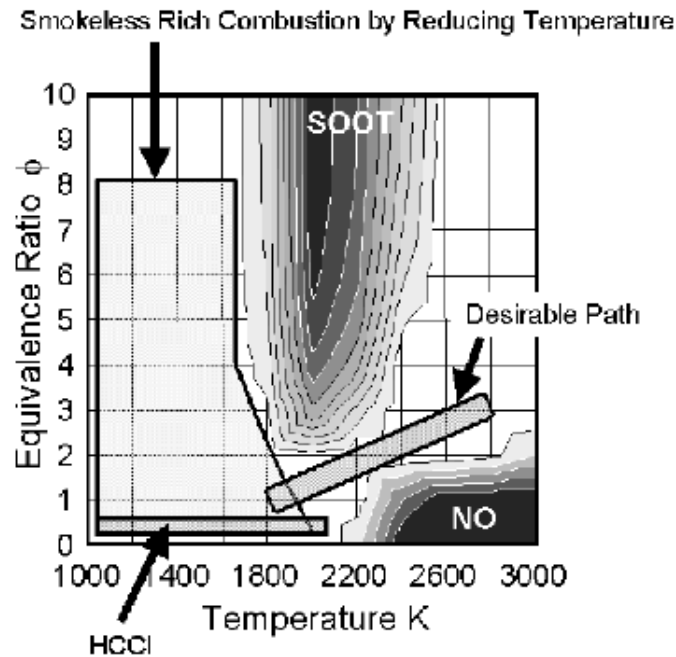


Figure 3.8: Combustion design in ϕ -T phase space with regions of soot, NO_x and the desirable path [2]

Both reactions are chain-branching, producing one NO molecule and either one atom N or O that is again oxidizing O_2 and N_2 , respectively. A third reaction was added by Lavoie [115] that establishes the extended Zel'dovich mechanism:



Since one oxygen atom is required in the initial step Eq. (R 3.5.3), NO can only be formed under locally stoichiometric or lean conditions. The Zel'dovich mechanism is the dominating path under Diesel engine conditions and its source terms are one magnitude larger than the other reaction channels, even under high rates of EGR [11]. Prompt-NO is a reaction path where the hydrocarbyl radical and N_2 forms HCN :



The reaction path given by [53] has a lower activation energy than Eq. (R 3.5.3). It is therefore less dependent on the temperature and faster at lower temperatures. Because of the fact that the hydrocarbyl radical is formed in fuel-rich conditions,

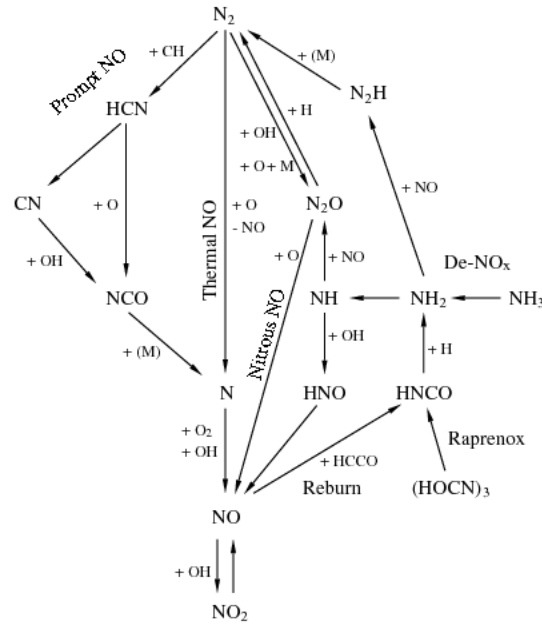


Figure 3.9: Reaction path analysis of NO_x formation [23]

occurring at $Z > Z_{st}$ in a diffusion flame, prompt-NO becomes more important under fuel-rich conditions than thermal-NO. From HCN, additional reactions by adding OH and O radicals follows to CN and NCO from where atomic nitrogen N is formed. By reactions Eq. (R 3.5.4) and Eq. (R 3.5.6), NO is formed again via the extended Zel'dovich mechanism.

Nitrous-NO is given by the oxidation via OH and O of nitrogene to form N₂O



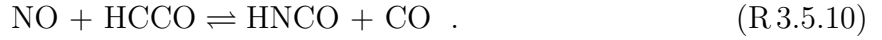
Under fuel-lean conditions, NO is formed by a further oxidation-step with O:



Eq. (R 3.5.8) is a trimolecular recombination reaction that is only important at high pressure conditions as it is in the case of a Diesel engine.

All three reaction channels, thermal-, prompt-, and nitrous-NO are forming NO. The

reburn-NO mechanism is initiated by the reaction



Further reactions via NH_2 and NH lead to N_2O and N_2H by consuming an additional NO molecule from where finally N_2 is formed.

The nitrooxide NO_2 is formed by oxidation of NO:



3.5.2.2 Soot-Model

Beside NO_x , particulate matter (PM) that consists mostly of soot has to be avoided during the combustion in a Diesel engine. Soot is an ensemble of particles of different size and numbers. These particles are formed from polycyclic aromatic hydrocarbons (PAH). By Van-der-Waals forces, PAHs are bounded and forming a spheriodical particle as sketched in Fig. 3.10. The smallest particles are of a weight of 2000 amu with a diameter of about 1.5 nm. These primary particles are formed in the nucleation process and are growing due to coagulation with other particles, condensation of carbon from the gaseous phase and by surface growth up to a size of 50 nm. The shape of the soot particles is changing from spherically particles to agglomerates. The soot growth and oxidation process depend on the local temperature, pressure and mixture conditions. In a non-premixed flame, soot is formed in fuel-rich regions. The temperature must be in a range between 1250 and 1800 K. The lower temperature limits the formation of soot precursors whereas soot particles are oxidized at higher temperatures. The soot volume fraction depends up to 10 bar quadratically on the pressure due to the effect of gas compression. At higher pressures, the soot volume fraction is a linear function of the pressure only [44, 199].

Oxidation occurs close to the iso-surface of stoichiometric mixture by OH- and O radicals. Local flame quenching at cold walls prevents the soot oxidation process and soot emissions are found in the exhaust gas of a Diesel engine.

The overall soot emissions are described by the number density N_{soot} , that is the total number of soot particles per unit volume, and the soot volume fraction

$$f_V = \frac{V_{\text{soot}}}{V} = \frac{\pi}{6} N_{\text{soot}} d^3 . \quad (3.62)$$

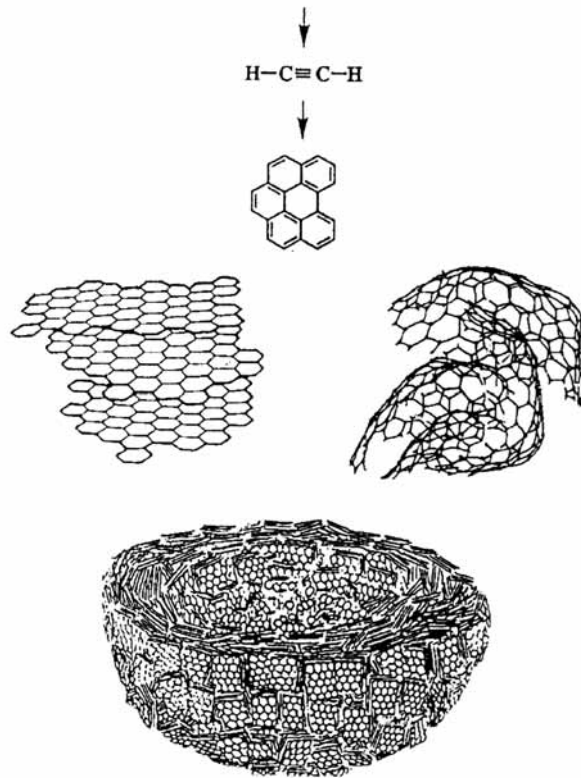


Figure 3.10: Formation of a spheroidal soot particle

Different approaches have been proposed to find an adequate model for the temporal evolution of the soot volume fraction and number density. Phenomenologically, the number density depends only on the nucleation, coagulation and oxidation process:

$$\frac{dN_{\text{soot}}}{dt} = \text{nucleation} - \text{coagulation} - \text{oxidation} \quad (3.63)$$

The soot volume fraction depends beside the nucleation, condensation and oxidation not on the coagulation but instead on the surface growth process:

$$\frac{df_v}{dt} = \text{nucleation} + \text{condensation} + \text{surface growth} - \text{oxidation} \quad (3.64)$$

Simple models only account for phenomenological effects. The widely used two-step model of Hiroyasu [83] express the temporal change of the soot volume fraction by a formation- and oxidation reaction of first order. Both are coupled to the fuel- and oxygen mass, respectively. The reaction rate constants have to be fitted to empirical

data. Patterson [150] extended the two-step model by the Nagle and Strickland-Constable oxidation model [139]. Further improvement was obtained by Fusco [62] who proposed an eight-step model by introducing two additional intermediate species. The additional reaction steps include already particle inception, particle coagulation, surface growth and surface oxidation and species formation from the fuel as well as oxidation of soot-particles.

A higher-level of modeling is achieved by a statistical approach that was proposed by Frenklach et al. [59, 60, 102] and Mauss [124, 125, 123]. The soot formation process is considered in three steps. First, the reaction mechanism includes paths that lead to the formation of the first aromatic molecules, phenyl and benzol, in the gas-phase. Second, reactions are included for the growth of PAHs up to four aromatic rings. Third, soot particles are formed by the nucleation process. Other processes as coagulation, surface growth and oxidation have to be included. The interaction between the different processes of the PAH and soot formation is depicted in Fig. 3.11.

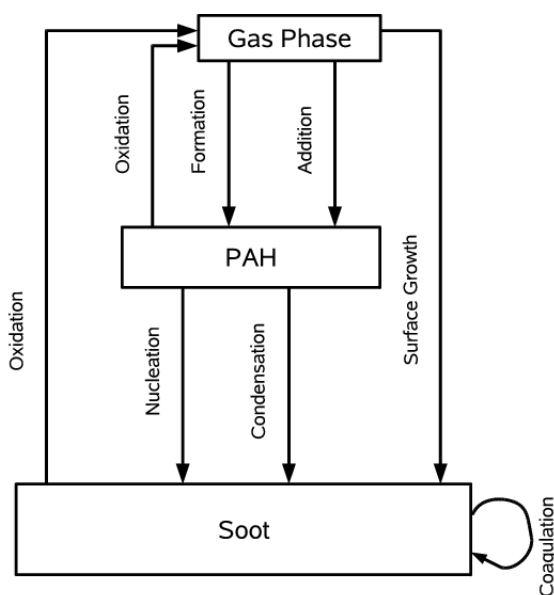


Figure 3.11: Modeled processes in the soot-model of Frenklach and Mauss

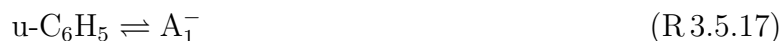
3.5.2.3 Formation of Benzene

The smallest PAH is a single aromatic ring, C_6H_6 , denoted as A_1 . Two reaction paths are indicated to form benzene (A_1) and its radical phenyl (A_1^-).

The first path describes the addition of ethylene to C_4 molecules [60, 213, 56, 59]:

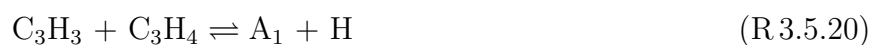


and

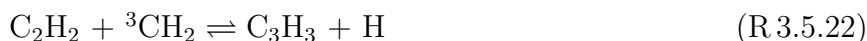


The radicals $u-C_4H_5$ and $u-C_4H_3$ are thermal unstable and dissociate above a temperature of 1500 K [134]. Their resonance stabilized isomers $i-C_4H_5$ and $i-C_4H_3$ occur in small concentrations but can not explain the measured benzene and phenyl concentrations in a flame [123].

The other reaction channel is the formation of benzene and phenyl from propargyl [196, 135]:



These reactions have a very high frequency factor of $1.2 \times 10^{12} \text{ cm}^3/\text{mol}\cdot\text{s}$ whereas for the reactions Eq. (R 3.5.14) and Eq. (R 3.5.17) $A = 2.8 \times 10^3 \text{ cm}^3/\text{mol}\cdot\text{s}$. The propargyl radical is formed by reactions between ethylene and singlet- or triplet-methylene:



Since the formation of the propargyl radical consumes ethylene these reactions are competing with Eq. (R 3.5.12) and Eq. (R 3.5.15). Oxidation of u-C₄H₅ and u-C₄H₃ lead to the formation of 2 formyl radicals:



Both are chain-branching reactions. The next step is the formation of CO by hydrogen-abstraction and further oxidation which is a strongly exothermic reaction. These reactions are promoted by propargyl and hence competing with the consumption in Eq. (R 3.5.21)-Eq. (R 3.5.22).

After that the first aromatic ring is initially formed, further growth of PAH has to be considered.

3.5.2.4 Growth of PAH

The main source of further growth of PAH is the hydrogen-abstraction and carbon-addition mechanism, so-called HACA [59]. First, one H-atom is abstracted and C₂H₂-molecule is added. Additional oxidation reactions with O₂ and OH are included. The HACA mechanism was firstly applied in [57] to the surface growth of PAHs and is schematically shown in Fig. 3.12. Every aromatic molecule A_n consisting of n cyclic rings requires 6 steps to achieve the next level A_{n+1} from where the next cycle may restart and yielding a polymerization process. Within the whole PAH distribution spatial structures are formed by coagulation processes. These can then be identified

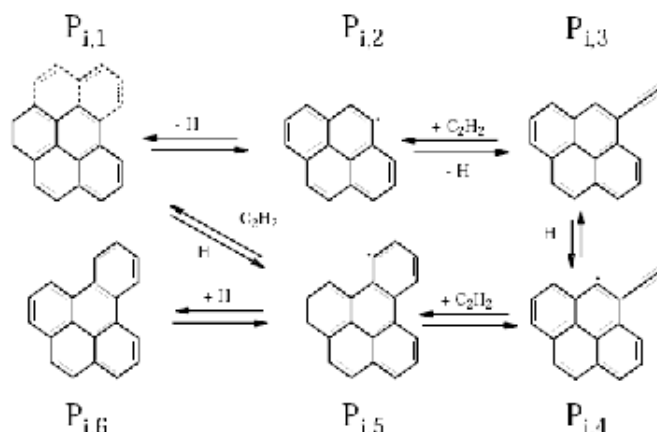


Figure 3.12: Surface growth by the HACA mechanism, taken from [123]

as initial soot particles and are excluded of the polymerization process. That step is denoted as nucleation or particle inception. Additionally PAHs are excluded by condensation on existing soot particles. Three models have been proposed in the literature to describe the polymerization process:

1. Frenklach [55] introduced the method of "linear lumping". The size of an aromatic ring A_n is characterized by its polymerization degree n . The complete ensemble of PAHs are described by a distribution function depending on the degree of polymerization. For this distribution function, statistical moments are used to summarise similar molecular structures. The HACA mechanism includes six different intermediate steps for the PAH growth. Thus, six additional moments are needed to describe every step of the polymerization process and six additional transport equations have to be solved to describe the complete process.
2. Instead of solving transport equations for all six moments, Mauss [123] introduced steady-state assumptions for the PAHs which is valid if the PAH consumption rate is much faster than the formation rate. That would lead to larger PAHs as it was found in experiments [191] which justifies the assumption of a fast polymerization process. From the steady-state assumption of PAH, a system of algebraic equations for the PAH-moments is obtained.

3. Another simplification was introduced by Yoshihara [219] for engine simulations and investigated by Pitsch [162] for flame calculations. Because PAH-consumption is limited by the particle inception, higher degrees of aromatics are neglected in comparison to aromatics on the first four degrees. From this assumption, the polymerization process is aborted after the formation of cyclopentapyrene A_4R_5 and particle formation is initiated. The present work follows this approach furthermore.

3.5.2.5 Soot Modeling

Soot formation is initiated by the nucleation reaction of cyclopentapyrene



By interaction between soot particles and PAH and by particle-particle interaction, the particles change in number and size. The distribution function of particles is discretized by introduction of a particle class of size j . The particle mass of the particle class j is given as

$$m_j = jm_2 . \quad (3.65)$$

The smallest unit m_2 is the mass of C_2 whereas the mass of hydrogen is neglected for simplicity. The number density of parcels of class j is obtained from

$$N_j = \rho \frac{Y_j}{W_j} . \quad (3.66)$$

The transport equation of the number density per unit volume of soot particles is derived in [126] and reads

$$\begin{aligned} \rho \frac{\partial N_j / \rho}{\partial t} + \rho u_i \frac{\partial N_j / \rho}{\partial x_i} &= \frac{\partial}{\partial x_i} \left(\rho D_{p,j} \frac{\partial N_j / \rho}{\partial x_i} \right) \\ &+ \frac{\partial}{\partial x_i} \left(0.55 \frac{1}{T} \frac{\partial T}{\partial x_i} N_j \right) + \dot{N}_j . \end{aligned} \quad (3.67)$$

The diffusion coefficient $D_{p,j}$ is derived [188] if particles are assumed to be small and to be in the free molecular regime where the Knudsen number $\text{Kn} \ll 1$

$$D_{p,j} = \frac{3}{2} \frac{1}{\rho} \sqrt{\frac{WkT}{2\pi}} \frac{1}{d_{p,j}^2} . \quad (3.68)$$

k is Boltzmann's constant and $d_{p,j}$ is the diameter of soot particles of class j

$$d_{p,j} = \sqrt[3]{\frac{6m_j}{\rho_s \pi}} = \sqrt[3]{\frac{6m_2}{\rho_s \pi}} \sqrt[3]{j}. \quad (3.69)$$

The diffusion coefficient is re-written as

$$D_{p,j} = j^{-\frac{2}{3}} D_{p,1}. \quad (3.70)$$

The second term on the r.h.s. of Eq. (3.67) accounts for the Sorret-effect which is usually neglected. The last term on the r.h.s., \dot{N}_j , contains the source terms from all processes that leads to the formation or consumption of soot particles of class j , which are particle nucleation, particle coagulation, condensation of PAH on soot particles, surface growth by molecules from the gas phase and particle oxidation:

$$\dot{N}_j = \dot{N}_j^{\text{nuc}} + \dot{N}_j^{\text{coag}} + \dot{N}_j^{\text{cond}} + \dot{N}_j^{\text{sg/ox}} \quad (3.71)$$

Two methods are proposed to solve this equation, either by sectional methods or by the method of moments.

Discrete sectional methods are used in [35, 212, 166] to solve Eq. (3.67) directly. Because up to 10^8 equations would have to be solved, a direct solution method is somehow prohibitive. A similar approach was followed in [7] to study the soot formation in pre-mixed acetylene flames. The particle growth is based on a polymerization process which degree of polymerization is interpreted as a discrete variable. Deuffhard et al. [42, 218] have applied a discrete h-p Galerkin method using orthogonal polynomials of type Tschebyscheff to reduce the numerical effort for the time integration of each level of polymerization [42, 218]. The approach was used in [207] to study the influence of a water-diesel emulsion on the evolution of the particle size distribution.

Sectional methods are of advantage to obtain detailed information of the number density of a specific soot particle class.

Frenklach introduced in [58] a statistical method where the particle size distribution is described by its statistical moments. The statistical moments are defined as

$$M_r = \sum_{i=1}^{\infty} i^r N_i. \quad (3.72)$$

From the method of moments, the particle size distribution function is derived but its shape must be pre-assumed. The method of moments is nevertheless quite useful

because the zeroth and first statistical moments represent the total number density and total number of C₂ units of the particle size distribution:

$$M_0 = \sum_{i=1}^{\infty} N_i = N_{\text{soot}} \quad (3.73)$$

$$M_1 = \sum_{i=1}^{\infty} iN_i = f_V \frac{\rho_s}{m_2} \quad (3.74)$$

where ρ_s is the density of soot equal to 1800 kg/m³. From Eq. (3.73) and Eq. (3.74), a particle mean diameter is derived

$$d_{\text{soot}} = \sqrt[3]{\frac{6}{\pi \rho_s} \frac{W_{\text{C}_2}}{N_A} \frac{M_1}{M_0}} \quad (3.75)$$

with the assumption of spherically soot particles. The molecular weight of C₂ is given as $W_{\text{C}_2} = 24$ kg/kmol. N_A is Avogardo's constant.

A transport equation for the r -th statistical moments is given as

$$\begin{aligned} \rho \frac{\partial M_r / \rho}{\partial t} + \rho u_i \frac{\partial M_r / \rho}{\partial x_i} &= \frac{\partial}{\partial x} \left(\rho D_{p,1} \frac{\partial M_{r-2/3} / \rho}{\partial x} \right) \\ &+ \frac{\partial}{\partial x} \left(0.55 \frac{1}{T} \frac{\partial T}{\partial x} M_r \right) + \dot{N}_j = 0 . \end{aligned} \quad (3.76)$$

Neglecting the Sorret-effect, transforming the equation into mixture fraction space and following the arguments for a thin reaction layer, a transport equation is obtained for the r -th soot moment

$$\rho \frac{\partial M_r / \rho}{\partial t} - \rho \frac{\chi}{2Le_{p,1}} \frac{\partial^2 M_r / \rho}{\partial Z^2} - \dot{M}_r = 0 . \quad (3.77)$$

$Le_{p,2}$ is the Lewis number of the smallest unit m_2 of a C₂ molecule. For simplicity,

$$Le_{p,2} \approx \frac{1}{2} Le_{p,A_1} \approx 1 , Le_{p,A_1} \approx 2.0 . \quad (3.78)$$

The source term \dot{M}_r includes in analogy to Eq. (3.71) PAH/particle-PAH interaction (nucleation and condensation), particle-particle interaction (coagulation), and particle-gas phase interaction (surface growth and oxidation)

$$\dot{M}_r = \dot{M}_{r,\text{nucl.}} + \dot{M}_{r,\text{cond.}} + \dot{M}_{r,\text{coag.}} + \dot{M}_{r,\text{surf.}} + \dot{M}_{r,\text{oxid.}} . \quad (3.79)$$

In order to close the system, the source terms must be expressed by M_0 and M_1 . The nucleation, coagulation and condensation process are described as a particle-particle interaction process which is expressed by the Smoluchowski equation for coagulation processes in the free-molecular regime [61]

$$\dot{N}_j = \underbrace{\frac{1}{2} \sum_{j=1}^{i-1} \beta_{j,i-j} N_j N_{i-j}}_{\text{formation}} - \underbrace{\sum_{j=1}^{\infty} \beta_{i,j} N_i N_j}_{\text{consumption}} . \quad (3.80)$$

The frequency factor $\beta_{i,j}$ depends on the particle size which is in the free-molecular regime given as

$$\beta_{i,j} = \varepsilon_{i,j} \sqrt{\frac{8\pi kT}{\mu_{i,j}}} (r_i + r_j)^2 . \quad (3.81)$$

$\mu_{i,j}$ denotes the reduced mass

$$\mu_{i,j} = \frac{m_i m_j}{m_i + m_j} \quad (3.82)$$

and $\varepsilon_{i,j}$ denotes an enhancement factor which depends on the particle size. It accounts for attractive or repulsive forces between the particles. A value of 2.2 was proposed from experimental data in [74] for the coagulation process due to the enhancement by Van-der-Waals forces. Expressing m_i and m_j by the smallest unit $m_i = i \cdot m_2$ and $m_j = j \cdot m_2$, the equation for the frequency factor is re-written

$$\beta_{i,j} = C \left(\frac{1}{i} + \frac{1}{j} \right)^{1/2} (i^{1/3} + j^{1/3})^2 . \quad (3.83)$$

The factor C is obtained as

$$C = 2.2 \left(\frac{8\pi R_m T}{W_{C_2}} \right)^{1/2} \left(\frac{3W_{C_2} \sqrt{N_A}}{4\pi \rho_s} \right)^{2/3} . \quad (3.84)$$

Further details on the derivation of the source terms is given in [123] and [162].

Surface growth and oxidation of soot particles follows the HACA-mechanism [60]. Mauss [123] added two reactions for the addition of acetylene and the closure of the aromatic ring, which is denoted as HACAR(ing)C(losure)-mechanism. That extension is build on the hypothesis that the ring-closure reaction is irreversible whereas the bonding of acetylene is reversible. At flame regions of high temperature, the bonding is broken and surface growth of soot particles is omitted. Surface growth is here the

addition of acetylene from the gas phase. This steps results in an active site. Acetylene addition and ring closure are competing with the oxidation of the active site and the higher polymerization level by oxygen and the OH radical. The details of the surface growth and the oxidation process formulation are shown by Mauss [123] and will not presented here.

4 Spray Modeling

In modern Diesel engines the mixture formation is accomplished by a direct injection of fuel into the combustion chamber that is filled by the hot, compressed charge of air. The injection pressure is typically in a range between 300 - 2000 bar to assist the atomization process. All processes that occur during the spray formation are presented in Fig. 4.1. Close to the nozzle exit, primary breakup occurs. Ligaments and initial

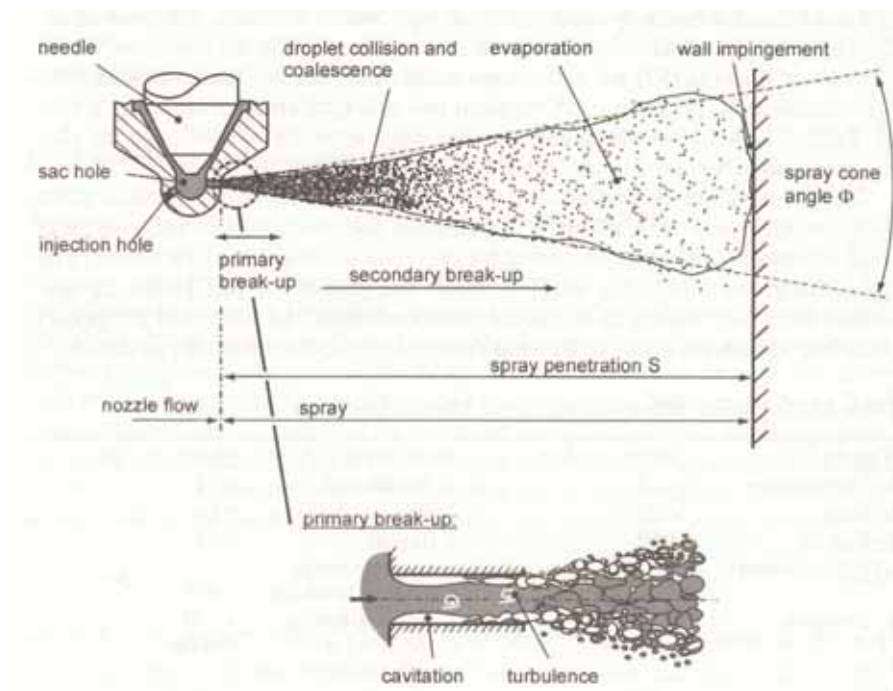


Figure 4.1: Formation of a Diesel Spray [16]

droplets are formed due to cavitation effects inside the nozzle and strong entrainment of the surrounded air. Downstream of the nozzle, droplets are subjected to secondary breakup, droplet-droplet interaction (collision and coalescence) and evaporation. At

the limit, the spray can impinge on the wall and forms a film. A reliable spray model has to accomplish all these phenomena but the main problem originates from the fact that the nozzle diameter is of $\mathcal{O}(100 - 200 \mu\text{m})$ whereas the dimensions of the flow domain is by factor of 1,000 larger. Thus, it is restrictive to solve the Navier-Stokes equation on the level of the liquid ligaments and droplets and on the level of the gas phase. Some effort has been achieved for this approach by either reducing the dimensions to obtain the one-dimensional, cross-section averaged transport equations [112, 205, 206] or by solving transport equations for the moments of the droplet distribution function [121][127]. A different approach is the widely used Discrete Droplet Model (DDM) that is applied in this work.

4.1 The Spray Equation

Down-stream of the nozzle's exit the spray is an ensemble of droplets with various size, location, velocity and temperature. The spray ensemble is quantified by its probability density function f which depends on the point in space \mathbf{x}_d , the velocity \mathbf{u}_d , the radius r_d , the temperature T_d and the droplet deformation y . Williams [215] proposed a transport equation for the droplet pdf, the so-called spray equation

$$\frac{\partial f}{\partial t} + \frac{\partial (f u_j)}{\partial x_j} + \frac{\partial (f \dot{u}_j)}{\partial u_j} + \frac{\partial (f r \dot{r}_d)}{\partial r_d} + \frac{\partial (f \dot{T}_d)}{\partial T_d} + \frac{\partial (f \dot{y})}{\partial y} + \frac{\partial (f \ddot{y})}{\partial \dot{y}} = \dot{f}_c + \dot{f}_b. \quad (4.1)$$

The terms on the r.h.s. \dot{f}_c and \dot{f}_b , account for droplet-droplet collision and droplet-breakup which must be modeled.

4.2 Discrete Droplet Model

It is numerically very difficult to integrate Eq. (4.1) directly because of the high-dimensionality of the droplet pdf. The discretization in 10 dimensions requires high memory consumption and large CPU-times. A different approach is the parcel-concept as proposed by Crowe [39]. Droplets of same properties are replaced by virtual

droplets, denoted as "parcels". In order to achieve a statistical convergency a sufficient number of parcels is used. Then, the ensemble of all parcels has the same distribution as the droplet pdf:

$$f(\mathbf{x}_d, \mathbf{u}_d, r_d, T_d, \dot{y}_d, \ddot{y}_d, t) = \sum_{k=1}^{N_P} N_{dk} \delta(\mathbf{x} - \mathbf{x}_k) \delta(\mathbf{u} - \mathbf{u}_k) \delta(r - r_k) \delta(T - T_k) \delta(\dot{y} - \dot{y}_k) \delta(\ddot{y} - \ddot{y}_k) \quad (4.2)$$

N_{dk} is the number of droplets that are assigned by the parcel k which is determined from the total injected mass by

$$\sum_{k=1}^{N_P} N_{dk} m_k = m_{\text{inj}}. \quad (4.3)$$

N_P is the total number of parcels that samples the distribution function. The spray equation is not directly solved but instead a Monte-Carlo simulation is applied on the level of the parcels [45]. The numerical effort is reduced if the phase space is discretized in a Lagrang'sche coordinate to decouple the treatment of the liquid spray from the solution procedure of the transport equations in the gaseous phase under the assumption of a small void fraction. Source terms between liquid and gaseous phase are exchanged.

4.2.1 Drag Force

Dispersed droplets in a flow are exposed to the drag force of the flow. The drag force is given in [13], yielding Newton's law for the state variable \dot{u}_j

$$\dot{u}_j = \frac{F_{\text{drag}}}{m_d} = \frac{3}{8} \frac{\rho_g}{\rho_l} \frac{1}{r_d} |\mathbf{u}_d - \mathbf{u}_g| (\mathbf{u}_d - \mathbf{u}_g) C_D + g_j + \frac{1}{\rho_l} \frac{\partial p}{\partial x_j}. \quad (4.4)$$

Acceleration by gravity forces, the Saffman lift force and the Magnus rotation force, are neglected. The last term on the r.h.s. of Eq. (4.4) is only significant in very dense spray and as well neglected [146]. The drag coefficient is proposed in [170]

$$C_D = \begin{cases} \frac{24}{\text{Re}_d} \left(1 + \frac{1}{6} \text{Re}_d^{2/3}\right) & \text{Re}_d \leq 1000 \\ 0.424 & \text{Re}_d > 1000 \end{cases} \quad (4.5)$$

and depends on the droplet Reynolds number

$$\text{Re}_d = \frac{d_d \rho_g |u_{\text{rel}}|}{\mu_g} \quad (4.6)$$

Corrections for the droplet evaporation and flow inside the droplet are not included. The time-integration of the presented equation Eq. (4.4) will yield a new update for the parcel velocity and location on every time-step.

4.2.2 Primary Atomization

Different mechanisms, as shown by Fig. 4.2, induce the primary breakup of the liquid fuel inside of the nozzle. Inside of the injector, the diesel fuel passes small pipes

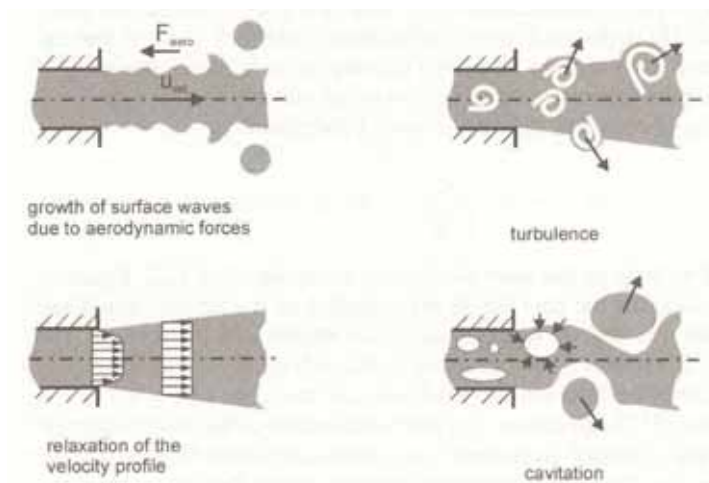


Figure 4.2: Primary breakup mechanisms from [16]

and valves. At the entrance of the nozzle's exit hole, it is redirected sharply and pressure losses occur. If the pressure inside the nozzle locally is lower than the vapor pressure, a vapor bubble is formed due to phase transition. This phenomena is denoted as cavitation. The small bubble reduces the cross-section, so that the exit velocity increases and mass flow is reduced. The increase in velocity also invokes an increase of velocity gradients and furthermore enhances turbulence production. If the bubble follows the flow further downstream into areas where the pressure re-increase, the

bubble will collapse and damages the material. Cavitation is characterized by the non-dimensional cavitation number

$$\text{KN}_{\text{crit}} = \frac{p_1 - p_2}{p_2 - p_{\text{vap}}} \approx \frac{p_1 - p_2}{p_2} . \quad (4.7)$$

p_1 is the nozzle's sac-hole pressure , p_2 denotes the pressure in the combustion chamber and p_{vap} is the vapor pressure which is much smaller than the sac-hole pressure and neglected therefore. Cavitation occurs at the limit for $\text{KN} \leq 5$ [22]. A reduction of cavitation effects is obtained by hydro-rounding of the nozzle hole inlet geometry and increasing the nozzle hole's conicity as it was experimentally observed in [187].

A physically well-based description of the entire cavitation process has not been developed yet. One attempt is the numerical simulations of the two-phase flow inside the nozzle and couple it with the Discrete Droplet Model as proposed in [122]. A more common approach is to neglect the primary breakup of the liquid. Instead a resulting droplet distribution of the primary atomization is assumed. In Fig. 4.3, different primary breakup regimes are identified. Whereas in Fig. 4.3 a), the spray

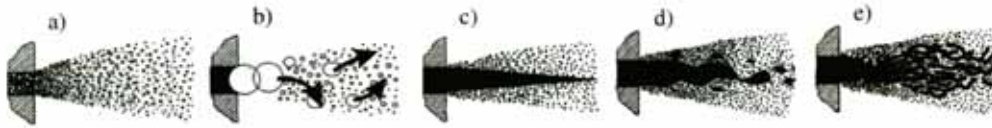


Figure 4.3: Primary breakup regimes according to [50]

is already completely atomized, Fig. 4.3 b) indicates that primary atomization and secondary droplet breakup occur close to the nozzle exit and are indistinguishable as postulated in [175]. In modern 3rd generation common rail diesel injection systems, fuel is injected at high pressures up to 2000 bar and breakup will presumably occur according to Fig. 4.3 a) and b). Based on that hypothesis, parcels are initialized with a radius equally to the hole size at the nozzle exit denoted as "blob"-method. Instead of choosing mono-disperse droplet size distribution commonly a χ^2 or Rosin-Rammler type size distribution is applied. Nevertheless, the Sauter mean radius of the distribution function is an input parameter that remains unknown. Other types of primary breakup in Fig. 4.3 c) - e) indicates a more or less stable, liquid core which may be realistic for non-cavitating nozzles.

4.2.3 Secondary Atomization

4.2.3.1 Droplet Breakup Regimes

The resulting liquid flow ligaments and droplets are due to the high injection pressure accelerated in the quiescent surrounding gas. The relative velocity between gas and liquid invokes instabilities which results in droplet breakup. The outcome of the droplet atomization depends on the balance between aerodynamical, surface, viscous and inertia forces and is expressed by the non-dimensional Weber number

$$\text{We} = \frac{\rho_g d_d u_{\text{rel}}^2}{\sigma_l}, \quad (4.8)$$

Ohnesorg-number

$$\text{Oh} = \frac{\mu_l}{\sqrt{\rho_l d_d \sigma_l}}, \quad (4.9)$$

and Reynolds-numbers that was already defined in Eq. (4.6). The Ohnesorg-number is related to Weber- and Reynolds-number

$$\text{Oh} = \frac{\sqrt{\text{We}}}{\text{Re}}. \quad (4.10)$$

Different droplet breakup regimes have been identified in the review of Pilch and Erdmann [161] shown in Fig. 4.4. The lower limit for the breakup is given as

$$\text{We}_{\text{crit}} = 12 (1 + 1.077 \text{Oh}_g^{1.6}) \quad (4.11)$$

For small Weber numbers $\text{We} < \text{We}_{\text{crit}}$, droplets are oscillating. If the excitation frequency is close to the eigenfrequency, smaller droplets are separated (vibrational breakup). For larger Weber numbers, the droplet forms a disk from where a bubble is formed without (bag breakup) or with a liquid column at the center (bag-and-stamen breakup). Finally the bubble breaks and forms small droplets. For even larger Weber numbers, small droplets are formed directly out of the drop surface by small-scale perturbations (sheet stripping and wave crest stripping) which can end in a catastrophic breakup.

The different droplet breakup regimes were experimentally investigated by Hsiang and Faeth [87] as shown in Fig. 4.5. The different breakup types depend on the balance

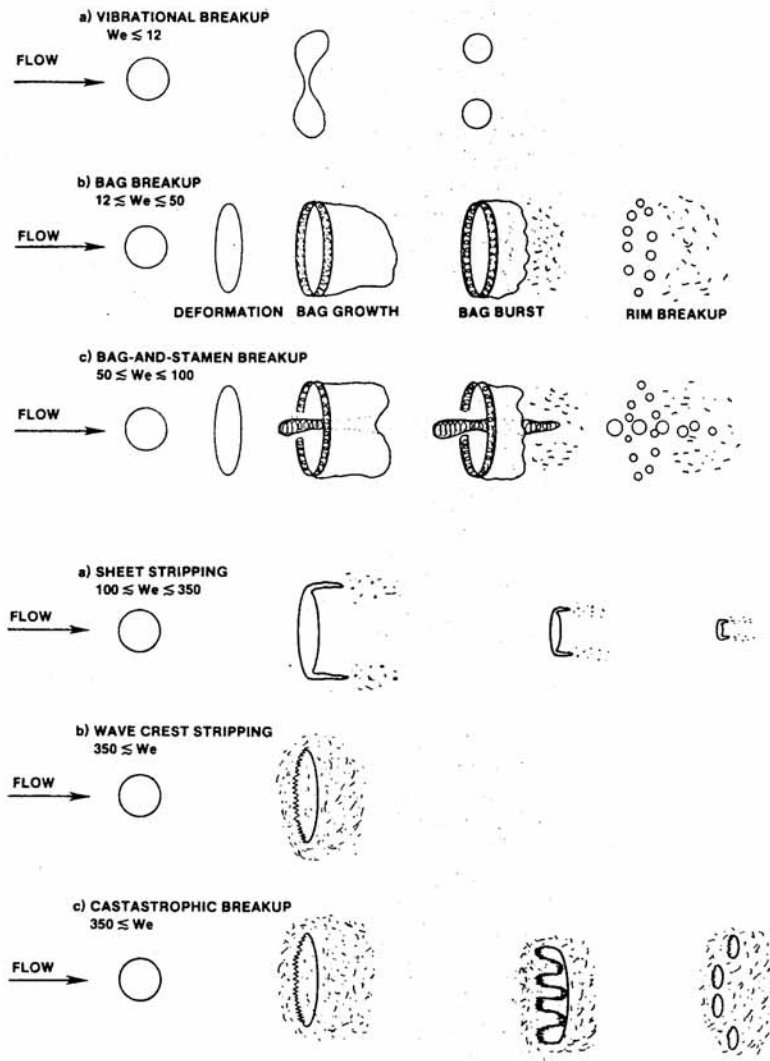


Figure 4.4: Secondary breakup types [161]

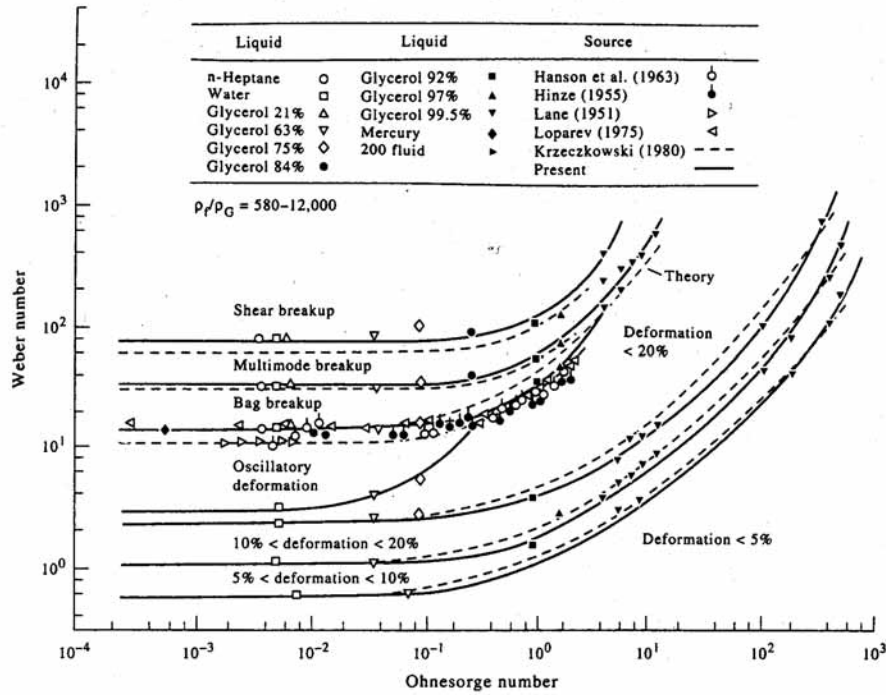


Figure 4.5: Secondary breakup regimes [87]

between viscous and surface forces. If viscous forces are small, the breakup regime only depends on the Weber number. Thus, at small Ohnesorg number $Oh < 0.1$, the influence of the viscous forces is neglectable. The critical Weber number is found to be

$$We_{crit} \approx 12 . \tag{4.12}$$

4.2.3.2 Modeling of Droplet Breakup

The modeling of droplet breakup in the high-dense diesel spray is mostly motivated by assuming that the intact droplet surface is a balance of viscous, surface and inertia forces. Small perturbations deteriorate the intact surface. Velocity gradients and density gradients between the droplet and the gas are considered to induce these small perturbations, leading to the so-called Kelvin-Helmholtz (KH) and Rayleigh-Taylor (RT) instabilities (Fig. 4.6). Both mechanisms are the basis for the breakup model that is used here. An alternative model was proposed by Taylor [200]. This

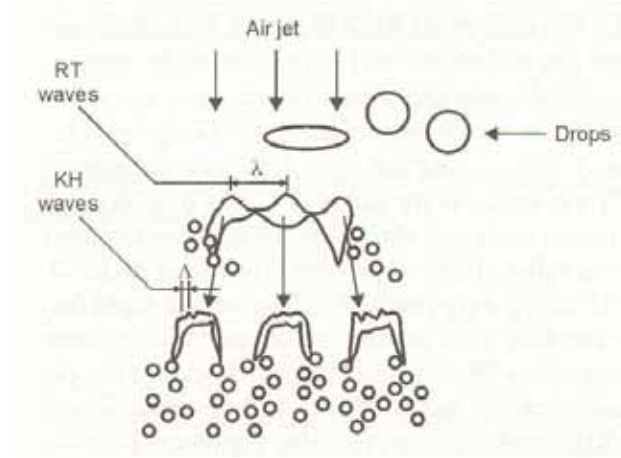


Figure 4.6: Kelvin-Helmholtz (KH) and Rayleigh-Taylor (RT) breakup mechanisms in a spray [16]

model consider the droplet in analogy to a spring-mass system. Later, O'Rourke et al. [147] introduced a damping term due to viscous forces. At high injection pressures, the TAB (Taylor Analogy Breakup)-model is underestimating the spray properties where the KH-RT breakup model is more suitable.

Kelvin-Helmholtz Breakup Model A stability analysis was carried out by Reitz and Bracco [174] assuming a fixed droplet surrounded by a gaseous flow. The resulting dispersion relation was fitted numerically [173]. For the fastest growing wave on the droplet's surface, the wavelength Λ

$$\frac{\Lambda}{r_0} = 9.02 \frac{(1 + 0.45\sqrt{Oh}) (1 + 0.4Ta^{0.7})}{(1 + 0.865We_g^{1.67})^{0.6}} \quad (4.13)$$

and the corresponding maximum growth rate Ω

$$\Omega \sqrt{\frac{\rho_l r_0^3}{\sigma_l}} = \frac{0.34 + 0.385We^{1.5}}{(1 + Oh)(1 + 1.4Ta^{0.6})} \quad (4.14)$$

are obtained. The Taylor-number Ta characterizes the ratio of viscous and surface forces and is expressed by the Ohnesorg and Weber-number

$$Ta = Oh\sqrt{We} = \frac{We}{Re} = \frac{\mu_l u_{rel}}{\sigma_l} . \quad (4.15)$$

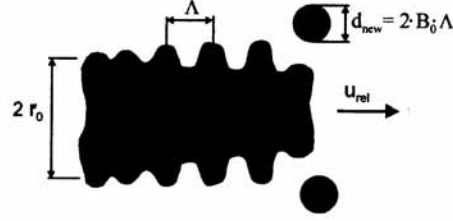


Figure 4.7: Growth of surface waves of Kelvin-Helmholtz type [16]

Small children droplets are separated from large parent droplets. The rate of change of radius of the parent drop r is described by the following rate equation [175]:

$$\frac{\partial r}{\partial t} = -\frac{r - r_c}{\tau_{\text{KH}}} \quad (4.16)$$

The breakup time τ_{KH} and the radius of a stable children drop r_c have to be modelled. The breakup time is proposed as

$$\tau_{\text{KH}} = 3.788 B_1 \frac{r_0}{\Omega \Lambda} . \quad (4.17)$$

B_1 is a constant that is varied and adjusted in a wide range between 1.73 and 60. The adjustment is required in order to account for upstream-events in the life-time history, e.g. cavitation, turbulence inside the injector and nozzle geometry [151].

From the stability analysis it is assumed that a newly formed stable children droplet has a radius proportional to the calculated wavelength Λ unless that the wavelength is large when compared to the droplet circumference as illustrated in Fig. 4.7:

$$r_c = \begin{cases} B_0 \Lambda, & B_0 \Lambda \leq r_0 \\ \min \left[\left(\frac{3}{2} \frac{r_0^2 \pi u_{\text{rel}}}{\Omega} \right)^{1/3}, \left(\frac{3}{4} r_0^2 \Lambda \right)^{1/3} \right], & B_0 \Lambda > r_0 \end{cases} \quad (4.18)$$

The model constant B_0 is set to 0.61.

Rayleigh-Taylor Breakup Model Surface waves of Rayleigh-Taylor type can also be identified by a wavelength Λ_{RT} and a growth rate Ω_{RT} derived by a stability analysis

$$\Lambda_{\text{RT}} = C_{\text{RT}} \frac{2\pi}{\sqrt{-\frac{a(\rho_l - \rho_g)}{3\sigma_l}}} . \quad (4.19)$$

$$\Omega_{\text{RT}} = \sqrt{\frac{2}{3\sqrt{3}\sigma_l} \frac{[-a(\rho_l - \rho_g)]^{3/2}}{\rho_l + \rho_g}} \quad (4.20)$$

C_{RT} is a constant equally 0.166 and a is the acceleration of the droplet in direction of travel. Two criteria decide if Rayleigh-Taylor instabilities induce the breakup of a parent drop. If the droplet radius is large enough

$$r > \frac{\Lambda_{\text{RT}}}{2} \quad (4.21)$$

and the time that the RT wave can growth is larger than the characteristic breakup time

$$\tau_{\text{RT}} = \frac{C_{\tau, \text{RT}}}{\Omega_{\text{RT}}} \quad (4.22)$$

the generated children droplets are of radius

$$r_c = \frac{\Lambda_{\text{RT}}}{2} . \quad (4.23)$$

KH- and RT-Breakup Model The use of both models invokes a competition. A criteria to switch between both breakup models is the liquid breakup length that is determined by a stability analysis [116]

$$L_b = Cd_0 \sqrt{\frac{\rho_l}{\rho_g}} . \quad (4.24)$$

The constant C is empirically determined from experiments. Close to the nozzle within the breakup length L_b , the KH-breakup model is applied to the droplet breakup. Beyond the breakup length L_b , only RT-breakup is used and remaining droplets are atomized in very small droplets. Fig. 4.8 shows the switching between both models.

4.2.4 Droplet-Droplet Interaction

In dense Diesel sprays, a very large number of droplet-droplet interaction (collision and coalescence) of approximately 10^8 $1/\text{cm}^3\text{s}$ occurs frequently [128]. The outcome of the collision event will significantly change the droplet velocity, size and number [63]. Thus modeling of droplet-droplet interaction is an important feature although it has proven difficult to model. Physical problems remain from the underlying mechanism

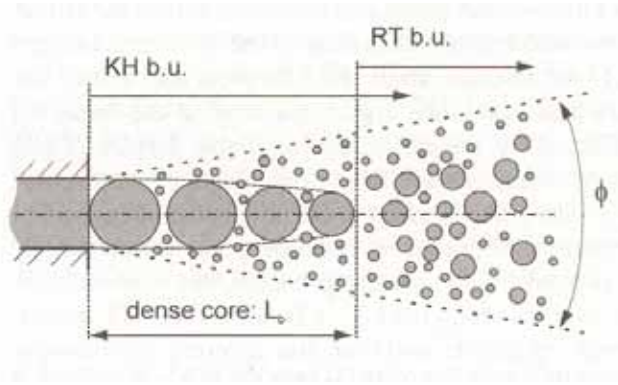


Figure 4.8: Liquid breakup length for transition from KH to RT breakup regime [16]

and from the outcome of the collision event while numerical problems influence the prediction of the collision incidence. The prediction of the collision rate is very grid sensitive due to inadequate numerical methods when the classical collision algorithm by O'Rourke [146] is applied [5, 141, 81]. One main disadvantage is that the classical approach only account for collision of a parcel pair located in the same cell. Thus the probability of the collision incidence relies on the mesh. An errors of the order of 100 % was reported in [186]. Particularly on cartesian meshes, the computed spray may turn into a "four-leafed clover" [185]. Beside the numerical issues, always a parcel pair is probed for interaction and $\frac{1}{2}N_P^2$ events must be evaluated. The immense computational effort and the numerical error are reduced by introducing a collision mesh [185]. A randomly subset of representative parcels is chosen as possible collision partners. That algorithm only includes the computation of $\mathcal{O}(N_P \log N_P)$ events.

4.2.4.1 Probability of Collision

The probability of a collision incidence is evaluated for all parcel-parcel pairs within a volume of a sphere V_s . The radius of that sphere is here an additional parameter that can be adjusted. The collision frequency for a parcel pair (i, j) is determined as

$$\nu_{ij} = \frac{\sigma_{ij} v_{ij}}{V_s} . \quad (4.25)$$

A larger collision sphere will include more collision events but decrease the collision frequency. The relative velocity between the parcel pair

$$v_{ij} = \sqrt{[u_j^2 + u_i^2 - 2u_j u_i \cos \phi]} \quad (4.26)$$

is obtained from the sketch in Fig. 4.9. The collision cross section σ_{ij} of two parcels

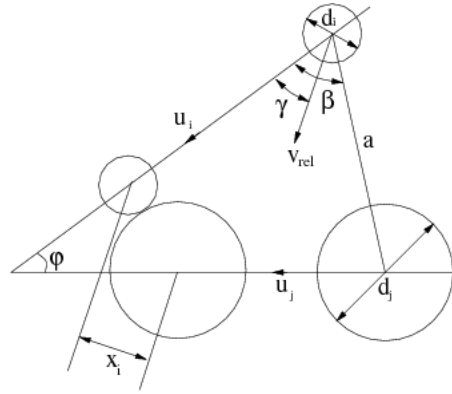


Figure 4.9: Schematic sketch of a colliding parcel pair

is defined as

$$\sigma_{ij} = \pi (r_i + r_j)^2 . \quad (4.27)$$

From the collision frequency, the collision probability

$$p_{ij} = \nu_{ij} \Delta t \quad (4.28)$$

is obtained. The mean expected number of collision events between the a parcel i and parcel j is given as

$$\bar{\mu} = N_j p_{ij} . \quad (4.29)$$

The number of collision events P_n is sampled randomly from a Poisson distribution

$$P_n = \frac{\bar{\mu}^n}{n!} \exp^{-\bar{\mu}} . \quad (4.30)$$

Once a parcel pair is considered for a collision incidence, the outcome has to be determined.

4.2.4.2 Outcome of Collision

Various types of the outcome of a collision incidence are possible and modeling is required. Based on the experimental observations of the binary collision of water droplets, Ashgriz and Poo [9] identified three different regimes as possible outcome: reflexive separation, coalescence and stretching separation. Although the study was only limited to water, a physically motivated criteria was derived to determine the collision outcome. Similar studies have been carried out for water and various hydrocarbon fuels by Jiang et al. [93] and also for water and tetradecane droplets by Qian et al. [171] at elevated pressure and different gas atmospheres. Additional regimes of bouncing and coalescence were identified as shown in Fig. 4.10 as a function of the impact parameter

$$B = \frac{x_i}{d_j + d_i} \quad (4.31)$$

and the Weber number. The different regimes are illustrated in Fig. 4.10. At very

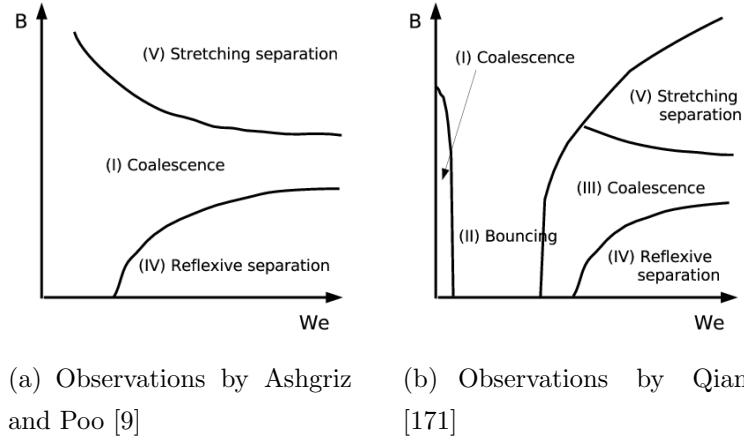


Figure 4.10: Different types of collision regimes

low Weber-numbers and elevated pressures, droplet bouncing was identified in [171] but is not considered here. A first model attempt was made in the work of Estrade [49] for ethanol fuel. In a review by Post et al. [168] that approach lacks of a required fit to experimental data and neglects the interaction of the droplets with the ambient gas. From the dimensional analysis, additionally dependence is given by the Reynolds

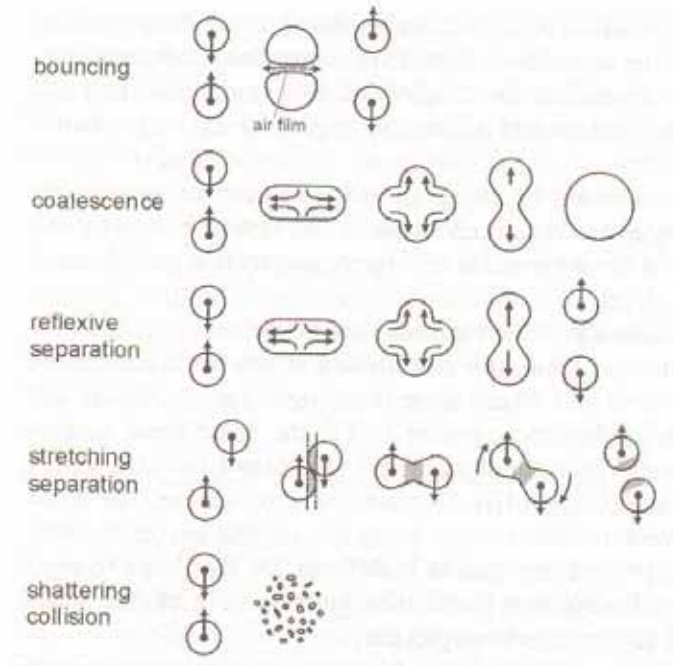


Figure 4.11: Collision modes [16]

number and the droplet diameter ratio

$$\Delta = \frac{d_j}{d_i}. \quad (4.32)$$

The impact parameter is at the limit 0 or 1, depending if head-on collision (center-center collision) or off-center collision occurs. The influence of Reynolds number was found to be weak [9]. Depending on the impact number, Weber number and diameter ratio, the observed outcome is analyzed and a modeling criteria has to be found.

Reflective Separation Collision At low impact numbers the head-on collision results in a disk-like or torus-like drop as seen from Fig. 4.12. The surface tension forces are leading to a contraction which is a reflective action of the pressure differences. For low Weber-numbers only an oscillating large droplet is resulting. Above a critical Weber-number the cylinder breaks into two drops. The number of droplets formed increase with the increase in Weber- number. For increasing impact number the surface reflex action becomes less and the total number of produced droplets is reduced. The limit

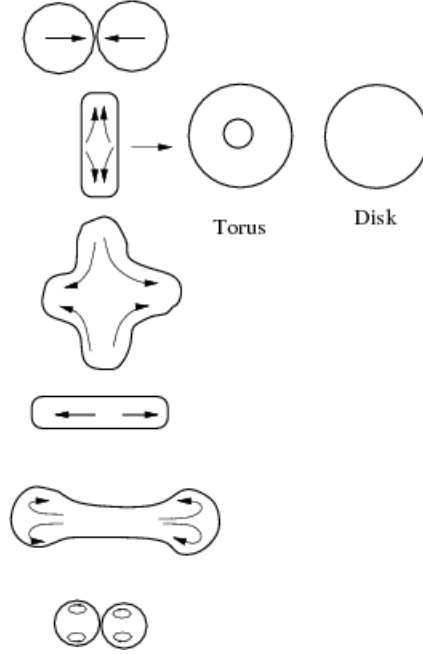


Figure 4.12: Reflexive action of droplet after collision incidence

between reflective separation and coalescence in Fig. 4.10 is determined by an analysis of the effective reflective kinetic energy

$$K_r = \sigma_{ij} \pi d_j^2 [(1 + \Delta^2) - (1 + \Delta^3)^{2/3} + \frac{\text{We}}{12\Delta(1 + \Delta^3)^2} (\Delta^6 \eta_1 + \eta_2)] \quad (4.33)$$

as postulated in [9]

$$K_r \geq \frac{3}{4} \sigma_{ij} \pi (d_j^3 + d_i^3)^{2/3} . \quad (4.34)$$

η_1 and η_2 are given as

$$\eta_1 = 2(1 - \xi)^2 (1 - \xi^2)^{1/2} - 1 \quad (4.35)$$

and

$$\eta_2 = 2(\Delta - \xi)^2 (\Delta^2 - \xi^2)^{1/2} - \Delta^3 \quad (4.36)$$

where ξ is defined as

$$\xi = \frac{1}{2} B(1 + \Delta) . \quad (4.37)$$

A model equation for the boundary between the reflective separation and coalescence regime is obtained by combining Eq. (4.33) and Eq. (4.34)

$$\frac{\text{We}}{\Delta(1 + \Delta^3)^2} (\Delta^6 \eta_1 + \eta_2) + 3[4(1 + \Delta^2) - 7(1 + \Delta^3)^{2/3}] = 0. \quad (4.38)$$

Coalescence Droplet coalescence is occurring on the onset of reflective separation for larger impact numbers or at small Weber-numbers. The modeling approach that is applied here is based on an energy balance approach by Brazier-Smith [26]. The coalescence efficiency is defined as

$$E_{\text{coal}} = \min \left[1.0, 2.4 \frac{f(\gamma)}{\text{We}} \right]. \quad (4.39)$$

The function $f(\gamma)$ is approximated by a polynomial fit

$$f(\gamma) = \gamma^3 - 2.4\gamma^2 + 2.7\gamma \quad (4.40)$$

where γ is a function of the droplet diameter ratio

$$\gamma = \frac{1}{\Delta}. \quad (4.41)$$

A critical off-set as coalescence criteria is obtained from the coalescence efficiency

$$b_{\text{cr}} = (r_j + r_i) \sqrt{E_{\text{coal}}}. \quad (4.42)$$

The impact parameter is not calculated directly but sampled randomly from a uniform distribution (yy) of the interval $[0; 1]$:

$$b = (r_j + r_i) \sqrt{(yy)} \quad (4.43)$$

The outcome of the collision incidence is coalescence if $b < b_{\text{crit}}$. The number of coalescence events n is determined by finding the random value (xx) for which

$$\sum_{k=0}^{n-1} p_k \leq xx < \sum_{k=0}^n p_k. \quad (4.44)$$

If $b \geq b_{\text{crit}}$, grazing collision occurs and only one collision is calculated for each droplet. The parcel's velocity is given as

$$u_j^{\text{new}} = \frac{u_j r_j^3 + u_i r_i^3 + r_i^3 (u_j - u_i) \frac{B - B_{\text{cr}}}{(r_j + r_i) - B_{\text{cr}}}}{r_j^3 - r_i^3}. \quad (4.45)$$

4.2.5 Droplet Evaporation

4.2.5.1 Evaporation Model

The hot charge in a Diesel engine requires that the spray model accounts for the phase transition between the liquid and the gas phase. Source terms have to be evaluated on the level of the parcels for the heat- and mass exchange between the liquid phase and coupled with the equations of the gas phase on the Eulerian mesh. From a balance around a single droplet the mass- and energy balance equations are derived. It is assumed that the heat conduction in the liquid droplet is infinitely fast (Infinite Conductivity Model, Uniform Temperature Model) so that the temperature of the droplet is assumed to be constant. Thus, heat and mass diffusion inside of the droplet are neglected.

The fuel mass balance at the droplet surface is given as:

$$\dot{m}_{F,s} = \dot{m}_s + j_{F,s} \quad (4.46)$$

Indici F, s denotes here the fuel on the droplet surface, \dot{m} and j denote the mass flow and the diffusive flux, respectively. Since solubility from gas phase species into the droplet is not considered the total exchanged mass flow is equal the fuel mass flow at the surface:

$$\dot{m} = \dot{m}_s \quad (4.47)$$

The diffusive mass-flux is expressed by Fick's law

$$j_i = -4\pi r^2 (\rho D_i) \frac{\partial Y_i}{\partial r} \quad (4.48)$$

where r denotes the radius of the droplet. Inserting Fick's law in Eq. (4.46) yields

$$\dot{m} = Y_{F,s} \dot{m} - (\rho D_i)_{\text{ref}} 4\pi r^2 \left. \frac{\partial Y_F}{\partial r} \right|_s . \quad (4.49)$$

Introducing the Spalding number

$$B = \frac{Y_{F,s} - Y_{F,\infty}}{1 - Y_{i,s}} \quad (4.50)$$

and Sherwood number

$$\text{Sh} = - \frac{2r}{Y_{F,s} - Y_{F,\infty}} \left. \frac{\partial Y_F}{\partial r} \right|_s \quad (4.51)$$

Eq. (4.49) is rewritten

$$\dot{m} = 2\pi r (\rho D_i)_{\text{ref}} \text{Sh} B . \quad (4.52)$$

Indici ∞ and ref are the state of the ambient conditions in the gas phase and reference conditions, respectively. The unknown Sherwood-number Sh is obtained by the integration of the mass balance equation in normal direction over the width of the boundary layer

$$\frac{\text{Sh}}{\text{Sh}_0} = \frac{\ln(1+B)}{B} . \quad (4.53)$$

Finally, Eq. (4.52) becomes

$$\dot{m} = 2\pi r (\rho D_i)_{\text{ref}} \text{Sh}_0 \ln(1+B) . \quad (4.54)$$

The energy balance around the droplet surface is given by

$$m_d c_p \frac{\partial T_d}{\partial t} - \frac{\partial m_d}{\partial t} \Delta H = 4\pi r \dot{Q} . \quad (4.55)$$

T_d, m_d, c_p and ΔH are the droplet temperature, droplet mass, heat capacity at constant pressure and latent heat of vaporization, respectively. \dot{Q} denotes the heat transfer from the ambient gas to the droplet surface

$$\dot{Q} = -4\pi r^2 \lambda \left. \frac{\partial T}{\partial r} \right|_s . \quad (4.56)$$

The heat gradient is expressed by the Nusselt-number

$$\text{Nu} = -\frac{2r}{T_s - T_\infty} \left. \frac{\partial T}{\partial r} \right|_s . \quad (4.57)$$

By this definition, the heat transfer from the gas phase to the liquid droplet is obtained as

$$\dot{Q} = \frac{\lambda_{\text{ref}} (T_\infty - T_d)}{2r} \text{Nu} . \quad (4.58)$$

From analogy of heat- and mass transfer, the Nusselt-number is given equally to Eq. (4.53) as

$$\frac{\text{Nu}}{\text{Nu}_0} = \frac{\ln(1+B)}{B} . \quad (4.59)$$

The Sherwood and Nusselt-number are calculated from the Reynolds, Schmidt and Prandtl-number [172]:

$$\text{Sh}_0 = 2 + 0.6 \cdot \text{Re}^{1/2} \text{Sc}^{1/3} \quad (4.60)$$

$$\text{Nu}_0 = 2 + 0.6 \cdot \text{Re}^{1/2} \text{Pr}^{1/3} \quad (4.61)$$

Schmidt and Prandtl-number in Eq. (4.60) and Eq. (4.61) are evaluated at a reference temperature determined by a 1/3 rule:

$$T_{\text{ref}} = T_s + \frac{1}{3} (T_\infty - T_s) \quad (4.62)$$

The viscosity and thermal heat conductivity of the gasphase is calculated by Sutherland's formula

$$\mu_{\text{ref}} = \frac{A_1 T_{\text{ref}}^{3/2}}{T_{\text{ref}} + A_2} \quad (4.63)$$

using constants $A_1 = 1.457 \cdot 10^{-6}$ and $A_2 = 110$ and

$$\lambda_{\text{ref}} = \frac{K_1 T_{\text{ref}}^{3/2}}{T_{\text{ref}} + K_2} \quad (4.64)$$

using constants $K_1 = 2.52 \cdot 10^{-3}$ and $K_2 = 200$.

The heat capacity at constant pressure $c_{p_{\text{ref}}}$ is determined by NASA-polynomina [68]. A mean density is calculated according to Han[73]:

$$\rho_{\text{ref}} = \left[\left(\frac{Y_{\text{ref}}}{\rho_{\text{vap}}} \right) + \left(\frac{1 - Y_{\text{ref}}}{\rho_\infty} \right) \right]^{-1} \quad (4.65)$$

The diffusivity is evaluated from the definition of the Lewis-number that is assumed to be equal to one.

Eq. (4.52) and Eq. (4.55) are coupled differential equations which are solved numerically. Both balance equations are combined together with Eq. (4.58) to obtain an equation for the droplet temperature T_d

$$\begin{aligned} \rho_d \frac{2}{3} r c_p \frac{\partial T_d}{\partial t} &= \lambda_{\text{ref}} (T_\infty - T_d) \text{Nu}_0 \frac{\ln(1+B)}{B} \\ &\quad - \Delta H (\rho D)_{\text{ref}} \text{Sh}_0 \ln(1+B) . \end{aligned} \quad (4.66)$$

The equation for the droplet temperature is implicitly discretized and solved by Newton's method numerically. After the droplet temperature is computed, Eq. (4.54) is used to obtain the droplet radius from an explicit discretization of

$$\frac{\partial r}{\partial t} = \frac{1}{2} \frac{(\rho D)_{\text{ref}} \text{Sh}_0 \ln(1+B)}{\rho_d r} . \quad (4.67)$$

4.2.5.2 Evaporation Time

The droplet's lifetime is a property of most interest. If the liquid density is assumed to be constant, Eq. (4.67) is integrated, yielding the well-known d^2 -law:

$$r^2 = R^2 - \frac{(\rho D)_{\text{ref}}}{\rho_d} \text{Sh}_0 \ln(1 + B) t \quad (4.68)$$

The integration is limited under the assumption of a constant Sherwood number ($\text{Sh}_0 = 2$) which holds for small Reynolds numbers to eliminate the dependence on the radius. The life-time of the droplet is obtained for $r = 0$ as

$$t_{\text{evap}} = \frac{R^2 \rho_d}{(\rho D)_{\text{ref}} \text{Sh}_0 \ln(1 + B)} \sim D^2. \quad (4.69)$$

The evaporation time of a droplet is proportional to the square of the initial diameter D . At larger Reynolds numbers $\text{Re} \gg 1$, the Sherwood number depends on the square root of the Reynolds number $\text{Sh} \sim \text{Re}^{1/2}$ and therefore the d^2 -law is modified as

$$t_{\text{evap}} \sim D^{3/2}. \quad (4.70)$$

Both laws are valid only if the wet-bulb temperature is quickly reached. The wet-bulb temperature is given in the limit from Eq. (4.66) as stationary solution ($\frac{\partial T_d}{\partial t} = 0$):

$$T_{\text{ad}} = T_{\infty} + \frac{\Delta H}{c_p} \text{BLe} \frac{\text{Sh}_0}{\text{Nu}_0} \quad (4.71)$$

The adiabatic droplet temperature can only be computed iteratively because fuel properties depend on the droplet temperature.

4.2.5.3 Influence of Temperature and Pressure on Evaporation

A single n-decane droplet of initial radius of $20 \mu\text{m}$ is exposed at different temperatures of 600 and 850 K and different pressures of 3, 15 and 50 bar to study the evaporation process by solving the equations Eq. (4.66) and Eq. (4.67) numerically. It is assumed that the initial droplet is injected into the surrounding quiescent gas with an initial velocity of 10 m/s . Momentum and mass exchange from the droplet on the surrounding

gas is neglected but the influence of drag-force is accounted for and will decelerate the droplet.

The temporal evolution of temperature and radius are presented in Fig. 4.13 and Fig. 4.14. The evaporation mostly depends on the ambient gas temperature. The increase in temperature from 600 to 850 K reduces the evaporation time by a factor of 2 for a pressure of 3 bar and by factor of 5 for 50 bar. The increase in pressure increases the droplet temperature because the mass transfer is reduced and less energy is disposed on the gas.

Regarding the evolution of droplet radius, the increase in pressure results in a shorter evaporation time at 850 K but at 600 K, the evaporation time is increasing. In the high pressure case at 850 K, a stationary wet-bulb temperature is not reached. The droplet is heated up to the critical temperature of $T_{\text{crit}} = 617.9$ K. At the critical point, the liquid phase cannot exist anymore and the droplet suddenly undergoes the phase transition to the gaseous state.

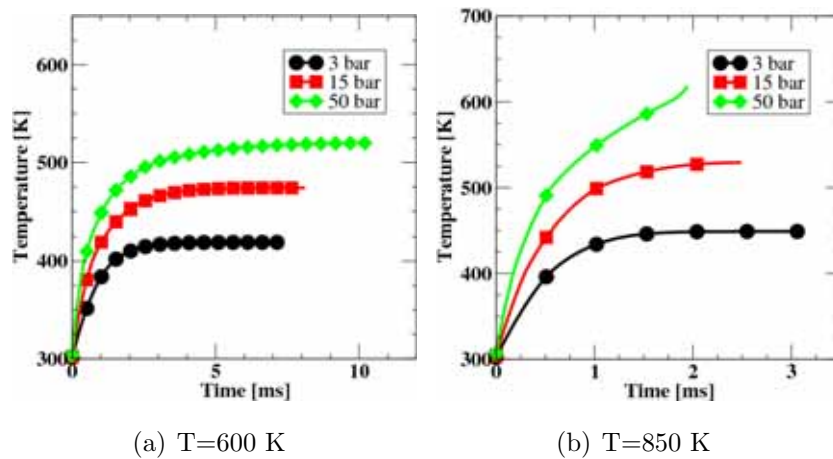


Figure 4.13: Influence of gas conditions on droplet temperature

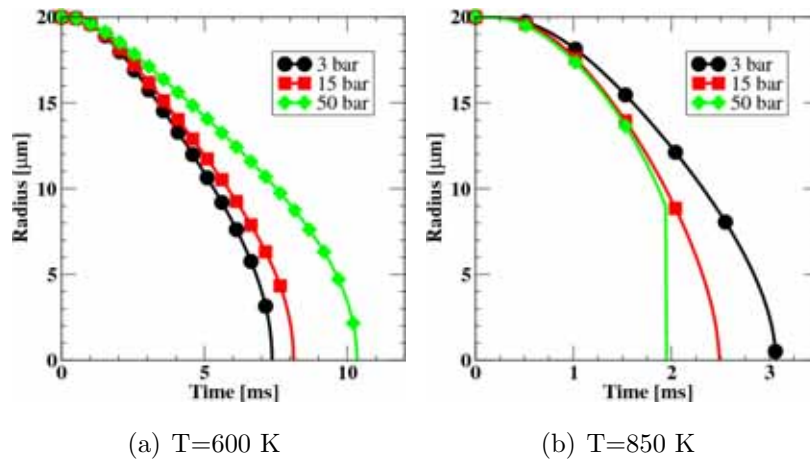


Figure 4.14: Influence of gas conditions on droplet radius

4.3 Turbulent Dispersion

Depending on the droplet size and the relevant Stokes number St Eq. (4.72)

$$St = \frac{\tau_a}{\tau_c} = \frac{\tau_a \mathbf{u}_p}{l_c} \begin{cases} St > 1 & : \text{dense spray} \\ St < 1 & : \text{dilute spray} \end{cases}, \quad (4.72)$$

the trajectories of the droplets as shown in Fig. 4.15 will depend on the interaction with the large eddies. This interaction between the turbulent flow of the gas phase

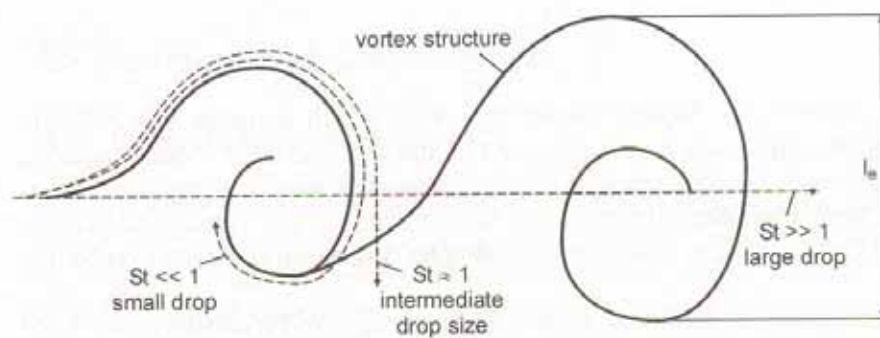


Figure 4.15: Drop trajectories in a turbulent flow [16]

and the liquid droplets is denoted as turbulent dispersion. Phenomenologically, the

turbulent dispersion increases the mixing of the droplets with the surrounding gas. The liquid droplets occupy a larger volume due to the stochastic velocity fluctuations so that the void fraction increases. On the side of the liquid phase, the injection, collision, coalescence and breakup of droplets will induce velocity fluctuations that interact with the fluctuations in the gas phase. Different domains of interaction are identified [48] as it is shown in Fig. 4.16. The parameter τ_p/τ_k is the ratio of the droplet response

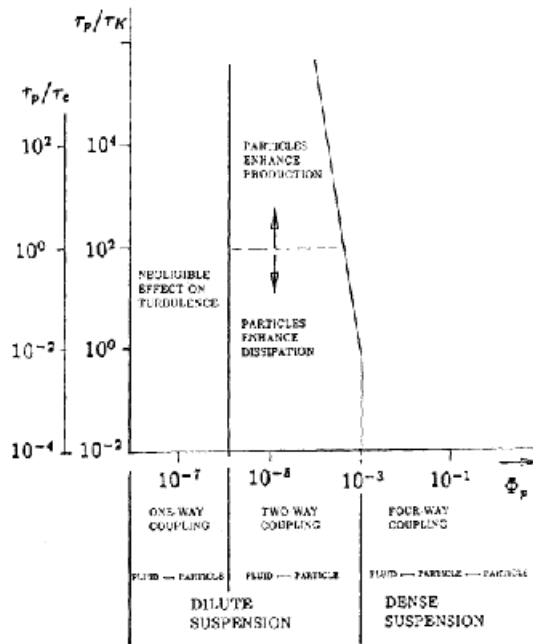


Figure 4.16: Flow regimes in turbulent sprays [48]

time to the Kolmogorov time scale, and Φ_P is the droplet volume fraction, equally to the void fraction Θ . If the void fraction is small, droplets are influenced only by the velocity fluctuations of the gas phase, denoted as "one-way coupling". In the next regime, denoted as "two-way coupling", velocity fluctuations of the droplets influence the gas phase vice versa. Depending on the response time, production or dissipation of turbulence is enhanced. Both regimes are considered as dilute suspensions. At larger void fractions above 10^{-3} the spray is considered as a dense suspension. Additionally to the two-way coupling, droplet collision has to be considered.

The probability distribution function of the droplet velocity fluctuations u'_p is reconstructed in [69] from the mean turbulent kinetic energy assuming a Gaussian distri-

bution function $G(u'_p)$

$$G(u'_p) = \frac{1}{\sqrt{2\pi}\sigma} \exp\left(-\frac{u_p'^2}{2\sigma^2}\right), \sigma = \sqrt{\frac{2}{3}k}. \quad (4.73)$$

u'_p is determined by sampling the Gauss distribution in a random walk.

5 Simulation of a Fuel Spray

5.1 Introduction

The non-premixed combustion in Diesel engines is controlled by the mixture formation which is dependent on the fuel injection system. The spray simulation is therefore a key-component that has to be mastered. Although the presented Discrete Droplet Model is a very popular approach, numerous problems exist. The modeling lacks of physical understanding that can be compensated by an adequate set of spray parameters and initial conditions of spray properties. However, high quality experimental spray data is mandatory. Such data is obtained by injection rate measurements and experiments carried out in a spray chamber at high-temperature, high-pressure conditions similar to the engine. Finding an optimal set of spray parameters is considered as an optimization problem. A Micro-Genetic Algorithm (μ GA) is suitable to address this problem and finds spray model parameters where the spray simulation agrees excellent with the experimental data.

5.2 Spray Data

5.2.1 Injection Rate Measurement Technique

On a Bosch type flow bench [24, 194] the injector nozzle is calibrated to establish on the one hand a correlation between injector energizing duration and injected fuel mass and on the other hand to determine the instantaneous rate of fuel injection. The injection rate technique operates on the principle of pressure wave propagation

through a liquid column. The injector discharges directly into a liquid filled tube of constant diameter and known length. The resulting pressure wave provides a signal that is representative to the instantaneous injection flow-rate. The injection delay (i.e. the time delay between start of energizing the injector and start of injection) and the injection duration is an additional result from the rate measurement.

5.2.2 Spray Chamber

A suitable test environment is required to investigate the process of fuel evaporation and mixture formation in dense atomized sprays. For this purpose, a spray chamber with a constant air flow is designed which serves as an environment for intermittent fuel injection. The design of the chamber enables three-sided optical access by quartz glass windows (116 mm length and 46 mm width), arranged in an angle of 90° to each other, for the use of optical measurement techniques as shown in Fig. 5.1. For purging the chamber, compressed air (up to 50 bar) passes through micro-filters and enters the heater. Here the air is heated to a temperature up to 800 K before entering the observation area of the chamber at a low velocity ($0.1\text{-}0.3\text{ m/s}$). On the chamber exit the hot pressurized air is cooled down in an external heat exchanger and throttled to ambient pressure.

5.2.3 Optical Measurement Techniques

5.2.3.1 Mie/Shadow Imaging Technique

A combined Mie/Shadow imaging technique is used for the simultaneous measurements of the spray penetration of the gaseous and liquid phase. Shadow images are the result of light removed from the optical path by two primary effects: a shadow effect and extinction. The shadow effect is caused by temperature and fuel concentration gradients (i.e. the derivative of the refraction index gradient) in the spray, while extinction is primarily the result of scattering from the liquid in the spray [142]. The Mie-scattering signal is collected at an angle of 90° to the illumination area and clearly

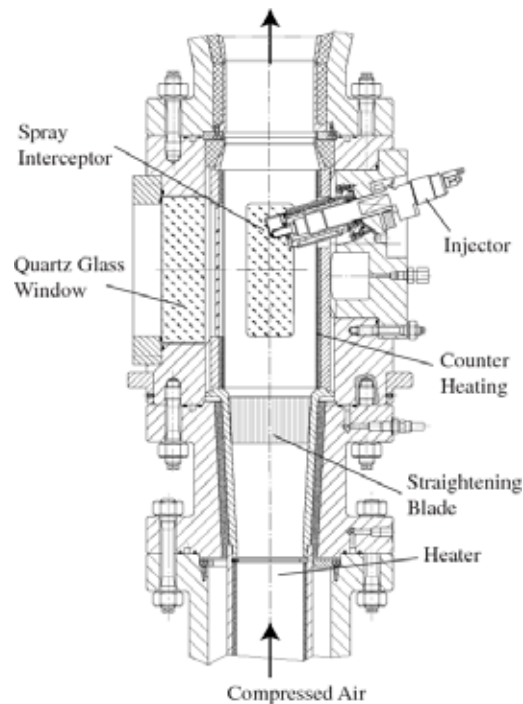


Figure 5.1: Design of spray chamber

indicates the liquid phase.

The optical set-up for the simultaneous Mie/Shadow imaging technique is shown in Fig. 5.2. A ruby laser (694 nm) and a spark flash lamp are applied as light source for the Mie images and for the shadow images, respectively. The Mie-scattering from the liquid phase and the shadow images are recorded with a CCD camera. The synchronization of the light sources, CCD cameras and fuel injection is controlled by the image acquisition system and a pulse delay generator. Both images are furthermore processed as shown in Fig. 5.3.

Since the gaseous vapor phase covers the liquid phase, only the gaseous penetration length is evaluated by the shadowgraph image. The shadow and Mie images are thresholded to pick out a binary image of the spray from the background. The spray tip penetration is calculated in two steps. First the whole spray area is determined by a spatial integration over all pixels which are marked as spray in the binary image. The tip penetration is defined as the distance between the nozzle tip and the location where the spatial integration reaches 99% of the prior calculated value. Additionally

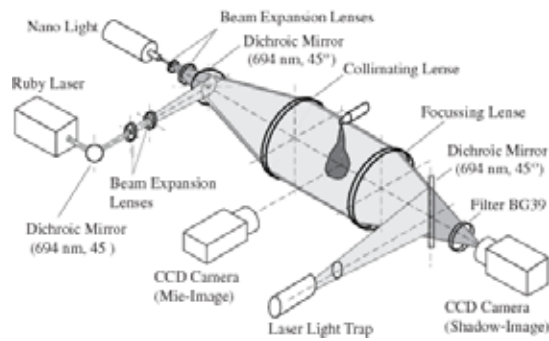


Figure 5.2: Setup of Mie-scattering and shadowgraph imaging

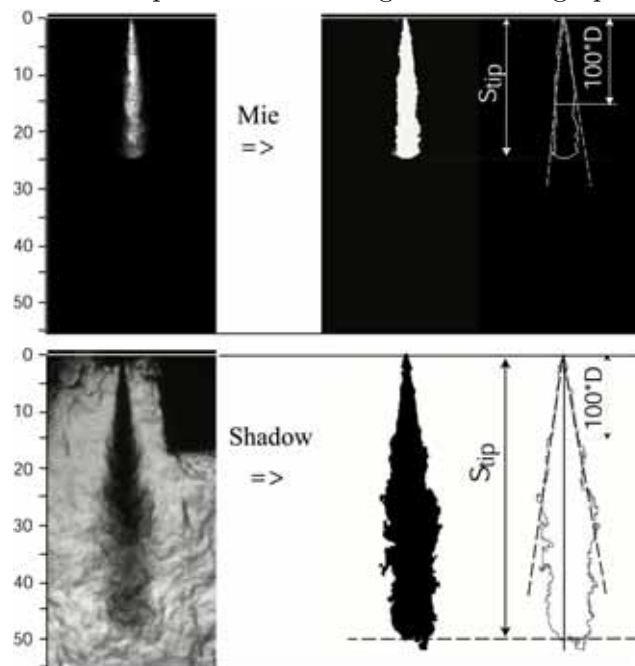


Figure 5.3: Processing of raw images from shadowgraph and Mie-scattering measurement techniques

the so called spray angle is defined as the angle between the tangents to the spray envelope. The spray angle is calculated at a position 100 times the nozzle diameter from the nozzle tip.

5.2.3.2 Raman Scattering Measurements

A non-intrusive measurement technique is based on spontaneous Raman scattering (RS) which allows to measure simultaneously quantitative and spatially resolved liquid and vapor concentrations in a dense, high-pressure spray if an alcohol is used as fuel. In general, the energy shift between the laser excitation and the Raman emissions depends on the excitation wavelength, the type of molecule and the temperature (the temperature dependence is negligible below 1000 K). The Raman scattering from N_2 -, OH - and CH stretching vibrations is used to measure spatially resolved vapor and liquid phase concentrations simultaneously. The discrimination between vapor and liquid phase is based on the observation that the hydrogen bonding in liquid alcohols results in a shift of the OH stretching vibration frequency to 2900-3700 cm^{-1} compared to the free vibration frequency of 3653 cm^{-1} for the gaseous alcohol. The hydrogen bonding generates a deformation of the electronic potential and therefore the OH liquid phase signal is strong spectral broadened and spectral shifted [129].

In Fig. 5.4 the experimental set-up for the 1D spontaneous Raman scattering technique is shown. The Raman scattering is induced by the unpolarized UV-laser light

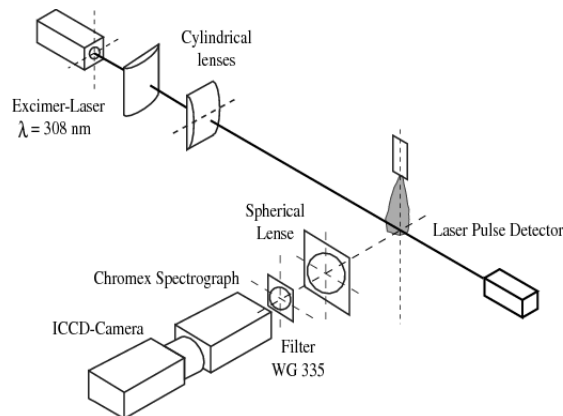


Figure 5.4: Setup of Raman spectroscopy

from a XeCl-excimer laser. The laser induced emissions are detected by an imaging spectrograph and an intensified CCD-camera. Even though the Raman signals are weak, it is possible to detect Raman and Mie-scattering signals with the same optical set-up by the chosen attenuation of the Mie-signal and the dynamic range of the

CCD-camera.

In Fig. 5.5 a recorded two dimensional spectrum and the extracted line spectrum on the spray axis of an ethanol spray at vaporizing conditions is shown. One axis of the

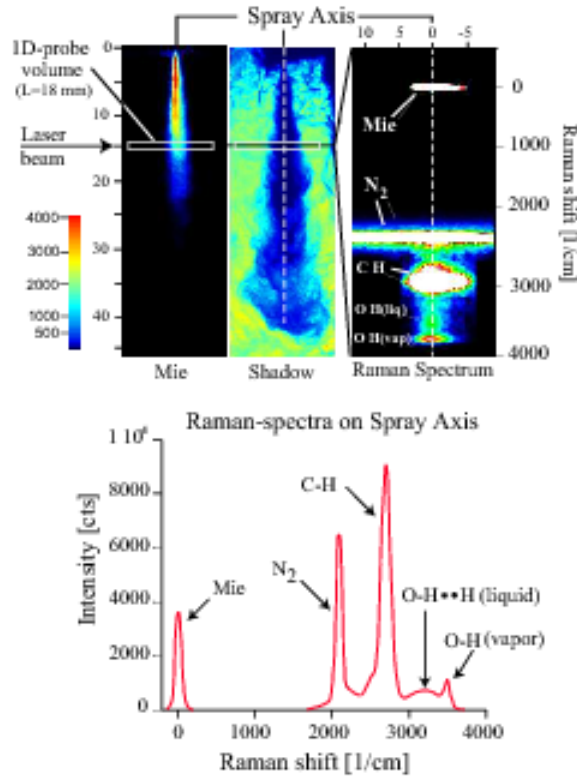


Figure 5.5: Raman spectrum of evaporating spray at $t=1.3$ ms aSOI, $T = 700$ K, $p = 44$ bar

image corresponds to the spatial extension of the 18 mm long probe volume and the second axis provides the spectral information. Since the measurements are performed at non-combusting conditions, the N_2 Raman signal is used as a marker for the determination of the fuel concentration. It is observed that the Raman signals of the CH and OH overlap. The extraction of the peak width and height for each Raman signal is implemented in the imaging analysis software by an computational algorithm.

From the Raman intensity ratio of fuel to nitrogen, the fuel mass fraction is derived for liquid and gaseous phase. Furthermore, the temperature in the gas phase is determined assuming the ideal gas law. From the spectral Raman peak position and magnitude, the temperature of the liquid phase is derived after calibration in a heated

optical cell filled with pure ethanol. Finally, an SMR distribution is obtained from the Raman/Mie signal ratio. A 2 component PDA system is used to calibrate the signal. Details of the combined Raman spectroscopy/Mie-scattering technique are presented in [210, 209].

5.2.3.3 Droplet Size and Velocity by PDA Measurements

The integral information gained by shadowgraph is supplemented by Phase-Doppler Anemometry (PDA) measurements. The PDA uses a laser as light source to create a small measurement volume. The PDA-system can determine the velocity and the diameter of single particles crossing the measurement volume by the light they scatter. For a detailed description of the technique see [3].

This technique has its difficulties when there is more than one particle in the measurement volume, therefore it cannot be applied to the dense part of a Diesel spray. Therefore, it is restricted to the area close to the stationary penetration length. A typical distance from the orifice to the measurement volume is 27.5 mm.

The setup at the pressurized chamber is shown in Fig. 5.6. In order to minimize the sensitivity to the temperature-depending refractive index of the fuel, the detector probes are positioned 65° off-axis. The size of the measurement volume has a diameter about $100\ \mu\text{m}$. At each radial position the data of 50,000 droplets or 500 injection events have been recorded.

5.3 Calibration of Spray Parameters

5.3.1 Spray Model Parameters

The sensitivity study in appendix B shows the influence of a variety of spray model parameters and physically based initial parameters. Some of these parameters are very sensitive with regard to spray penetration and evolution of SMR. Another constraint

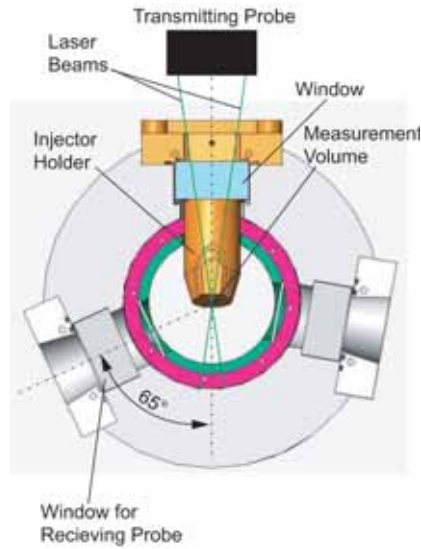


Figure 5.6: Experimental setup for PDA - top view [208]

is the demand for a low dimensionality of the parameter space to reduce the computational costs when the Genetic Algorithm is applied. Therefore, not all sensitive parameters will be included and the following parameters are finally chosen:

1. The initial droplet temperature "tpik" is the initial condition of Eq. (4.55).
2. The half-cone angle "cone" determines the elevation angle relative to the injection direction for initializing the parcel velocity, cf.[197].
3. The Sauter Mean Radius "SMR" determines the initial droplet distribution and thus the initial conditions used in Eq. (4.54).
4. Usually, the nozzle manufacturers only provide the geometrical nozzle diameter. However, no information on the discharge coefficient is given although it varies in a wide range. Siebers [189] investigated various nozzle types and found it in a range from 0.77 to 0.84. Geometrical factors such as hydro-grinding may improve the flow inside of the nozzle but factors that force cavitation will worsen it. An effective nozzle diameter " d_{eff} " and its area is introduced. It accounts

for the unknown discharge coefficient by which the parcels are initialized and controls the momentum of the injected fuel.

5. The scaling factor of the droplet breakup time due to Kelvin-Helmholtz instabilities "B₁" is between 45 and 60 in [197] but also set to 1.73 in [180].
6. The factor "C" scales the stable liquid cone length according to Levich's theory [116]. A value of 14.5 was found in [177].

Another aim of the sensitivity study is to find the limits and adequate resolution of the parameter space. A coarse parameter space has a fast convergence but the μ GA may not find the global optimum. On the other hand, a fine parameter space is desirable to find the global optimum more precisely but suffers of a low convergence rate. Thus, the limits of the parameter space and the resolution are individually defined.

5.3.2 Genetic Algorithm for Spray Calibration

Finding an adequate set of spray parameters where the simulation matches the data from spray chamber measurements is achieved by applying the Genetic Algorithm to the spray simulation. The optimization goal is expressed by the merit function. Every individual is addressed to this merit function, denoted as a fitness value. As a consequence, an independent spray simulation has to be carried out for every individual that represents a point of the parameter space. Since the evaluation of every individual would become very time consuming, the μ GA is preferred that chooses a small population size of 5 individuals. In the μ GA, the option of single-point crossover, mutation and elitism is retained. A convergence criteria is set by monitoring the merit function over a history of the last 30 generations.

5.3.3 Definition of a Merit Function

The comparison of penetration length of liquid and gaseous phase from the Mie-scattering and shadowgraph imaging with simulation results defines the merit function.

That criteria is expressed by

$$f_i = \frac{\int_{t_s}^{t_e} |x_{i,\text{exp}}(t) - x_{i,\text{sim}}(t)| dt}{\int_{t_s}^{t_e} x_{i,\text{exp}}(t) dt}, i = l, g. \quad (5.1)$$

where $x_{i,\text{exp}}$ and $x_{i,\text{sim}}$ are the penetration length from experiment and simulation results for indices $l = \text{liquid}$ and $g = \text{gaseous phase}$, respectively. t_s and t_e are start and end-time of the evaluated time-frame.

In the simulation, the penetration length itself is defined by the criteria

$$x_{i,\text{crit}} = x_{i,\text{min}} + c_i * (x_{i,\text{max}} - x_{i,\text{min}}), i = l, g \quad (5.2)$$

whereas $x_{i,\text{min}}$, $x_{i,\text{max}}$ and c_i is the minimum, maximum value and a penetration criteria. The criteria is chosen as 5 and 2% for gaseous and liquid phase, respectively.

Since the μGA cannot deal with a multi-objective optimization, the Euclidean norm Eq. (A.30) is chosen as penalty function. The inverse of the Euclidian norm is applied because the μGA is coded to find a maximum. Here, $r = 2$ denotes the number of partial objective functions for the liquid and gaseous phase. $\mathbf{x} = (x_1, x_2, \dots, x_k)^T$ is the point in parameter space and k denotes the number of parameters. For the present case, the merit function is simplified as

$$f(\mathbf{x}) = \frac{1}{\sqrt{\frac{f_l^2 + f_g^2}{2}}}. \quad (5.3)$$

5.4 Calibration of Fuel Sprays

5.4.1 Diesel Spray

Liquid Diesel fuel is injected inside of the spray chamber using a standard common-rail Diesel injector for detailed spray analysis. A shadowgraph imaging technique is applied to measure the spray penetration of liquid and gaseous phase of the spray as shown in Fig. 5.7. On the same spray, a Phase-Doppler Anemometry (PDA) measures droplet velocities and diameters in a small probe volume at 27.5 mm from the nozzle hole and at 4 radial positions, 0 to 3 mm, from the axis.



Figure 5.7: Single shadowgraph image [208]

5.4.1.1 Investigated Nozzles

Two different nozzles A and B are studied. All relevant nozzle data is summarized in Tab. 5.1. The KS factor of the nozzle geometry is the main, independent parameter

Nozzles A&B		
No. of holes		8
Hole diameter	A	131 μm
	B	130 μm
KS-factor	A	1.3
	B	3
Volumetric flow rate A&B		400 $\text{cm}^3/30\text{s}@100\text{ bar}$
Rail pressure		600, 900 and 1350 bar

Table 5.1: Nozzle parameters

which is varied. Additionally, three different rail pressures of 600, 909 and 1350 bar are studied for both nozzles. The ambient conditions in the pressurized chamber are similar to engine relevant conditions prior to the start of injection as given in Tab. 5.2. The hot conditions of the ambient gas promote the evaporation similar as

Temperature	800 K
Pressure	50 bar
Density	21.78 kg/m ³
Gas phase	Air
Fuel	Diesel

Table 5.2: Conditions in the spray chamber and injection parameters

for the conditions in an engine and is required to calibrate a Diesel spray. If cold spray chamber conditions are preferred, the droplet size and spray momentum distribution is the outcome of an equilibrium between droplet collision, coalescence and break-up, neglecting the mass transfer to the surrounding gas.

5.4.1.2 Diesel Spray Simulation

The spray chamber is represented by a cylinder with a length $L = 70$ mm and a diameter $D = 100$ mm. The z -axis is aligned with the injector axis. The injector position is located at the bottom of the cylinder close to the origin at $z = 0$ from where parcels are initialized and the spray formation starts. An O-type, block-structured mesh of 14,480 cells as shown in Fig. 5.8 is created for the geometry of this cylinder. The mesh is divided into two domains, meshed with a very high resolution on the inner part and surrounded by a coarse mesh on the outer part. At the interface between both blocks, treatment of "hanging nodes" is required by introducing a special boundary condition [76]. Therefore, the lower inner block has a resolution of 10x10x20 cells and 4x8x5 cells on the outer one with respect to radial, azimuthal and axial direction. Downstream at a height of 40 mm, the upper part is coarsened. Only 5x8x12 on the inner block and 4x8x12 cells on the outer block are used to limit the mesh size to 14,480 cells for sake of computational costs. A time-step size of 50 μ s is chosen and the end-time of the simulation is fixed to 1.5 ms according to the end-time of the experimental data. Input from injection rate measurements is used to initialize the parcel velocity.

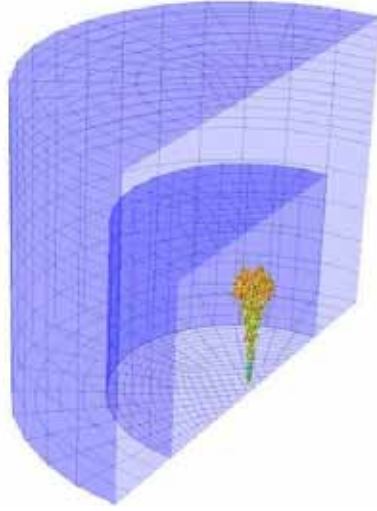


Figure 5.8: O-type, block structured mesh of a cylindrical geometry with 14,480 cells

5.4.1.3 Calibration of Spray Parameters

Applying the μ GA to two nozzles with a variation of the KS-factor and with a variation of rail pressures requires the individual spray parameter adjustment of six different cases. The six identified parameters with the used lower, upper range limit and binary resolutions are listed in Tab. 5.3. At the end of the optimization, the μ GA finds

x_i	Lower Limit	Upper Limit	Resolution
T_{fuel}	330 K	380 K	256 (8 bit)
Half-cone angle	5°	30°	32 (5 bit)
SMR	30 μm	100 μm	128 (7 bit)
d_{eff}	90 μm	135 μm	128 (7 bit)
B_1	5	100	64 (6 bit)
C	0	73	32 (5 bit)

Table 5.3: Limits and binary resolution of the parameter space

an optimum in parameter space as seen from from Fig. 5.10 and Fig. 5.13. All individuals are plotted by their partial objective functions f_l and f_g (Eq. (5.1)). The final optimum is located close to the origin. The overall merit function, Eq. (5.3), is

monotonously increasing over the iteration index j in Fig. 5.9 and in Fig. 5.12. The obtained achieved agreement of the penetration length between simulation and the experiment is excellent as the results in Fig. 5.11 for nozzle A and Fig. 5.14 for nozzle B illustrates. The overall merit function has in most cases a value larger than 20. However, the agreement for the liquid phase is inferior than for the gaseous phase. Since the gaseous phase is detected by an edge filter and not as for the liquid phase by a threshold value, the gas phase penetration is more reliable than the liquid phase penetration. Although the gas phase is in a good agreement for both nozzles, the penetration length of the liquid phase is much better resolved for nozzle A than for nozzle B as the scatter plots Fig. 5.10 and Fig. 5.13 illustrate.

The correct simulation of the gaseous phase is crucial with respect to the combustion modeling since it is on the level of the RANS equations whereas the simulation of the liquid phase is performed on the level of the parcels. It shows that the global momentum and mass exchange of the spray is correctly computed on a macroscopic level.

The set of spray parameters that are found are listed in Tab. 5.4 for all six cases. The

Nozzle	Rail pressure	T_{fuel}	Half-cone Angle	SMR	d_{eff}	C_d	B_1	C
Nozzle A	600 bar	368.8	9.8	31.1	101.3	0.6	5	37.7
	900 bar	332.2	5.8	91.2	117.3	0.8	87.9	16.5
	1350 bar	379.2	10.6	98.3	125.8	0.92	74.4	18.8
Nozzle B	600 bar	342.4	5.8	99.4	99.7	0.59	56.3	16.5
	900 bar	339.2	22.7	99.4	98.9	0.58	93.7	19.1
	1350 bar	336.9	16.3	96.1	126.1	0.94	68.3	16.4

Table 5.4: Spray model parameters of best point

effective nozzle diameter d_{eff} is expressed equally by a discharge coefficient C_d . By analyzing these values, no dependence neither on the rail pressure nor on the KS-factor can be identified which is requested for a predictive model. The main advantage is the use of an automatic algorithm. Once the μ GA has started, no further manual interaction and parameter adjustment is required. No human bias is involved except

for the definition of the parameter space and the definition of the merit function to find the best point.

5.4.1.4 Results from PDA-Measurements

The Phase-Doppler Anemometry (PDA) measurement enables to study details on a local scale and is a microscopic view inside of the spray. Applying the PDA to a Diesel spray is difficult since the spray is very dense close to the nozzle. Only limited areas are investigated that are close to the limit of the liquid phase. Four radial positions have been investigated at 0, 1, 2 and 3 mm off the spray axis at an axial position of 27.5 mm from the nozzle. The resulting data of the PDA measurements is the axial velocity of the liquid spray droplets in z-direction and the mean droplet diameter d_{10} . Both properties are compared with the simulation data. In the simulation, a torus of 2 mm height and 1 mm width is used as control volume where the axial droplet velocity and the mean droplet diameter are computed. This control volume is much larger than the volume of the PDA's probe volume and has the same length scale as the computational mesh. The approach to replace droplet by parcels follows that much less parcels than droplets are available. The number of used parcels and the resulting ensemble of parcels samples the droplet distribution on the entire computational domain but not on a local probe volume. A probe volume that had similar dimensions of the PDA's probe volume of $\mathcal{O}(100\mu m)$ would have required up to 1,000 times more parcels than currently used and would contradicted the discrete droplet model approach itself.

In order to compare PDA data with simulation data it is essential that the agreement of liquid spray penetration between simulation and experiment is excellent. This good agreement has been achieved only for nozzle A at a rail pressure of 600 bar. The axial droplet velocity and mean droplet diameter of experiment and simulation are compared in Fig. 5.15(a) - Fig. 5.15(d) and in Fig. 5.16(a) - Fig. 5.16(d), respectively.

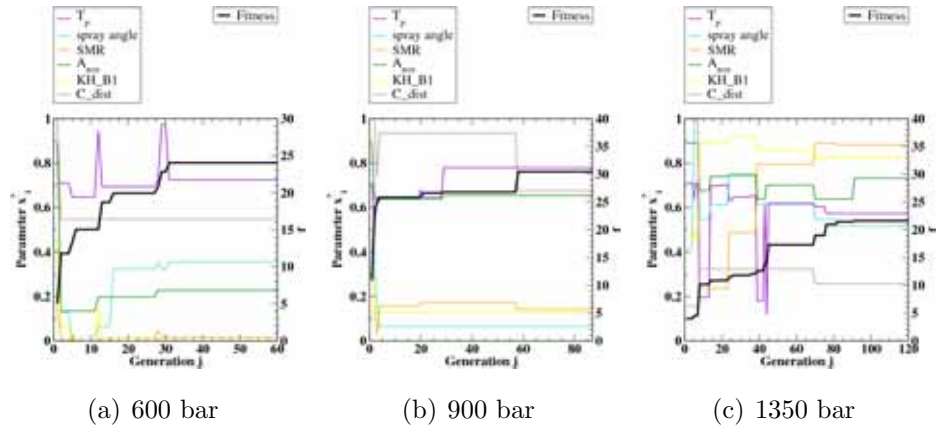


Figure 5.9: Spray parameters and merit function

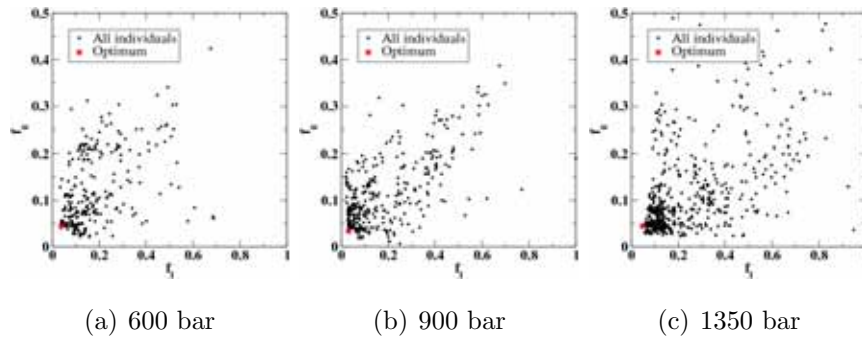


Figure 5.10: Merit functions of liquid and gaseous phase

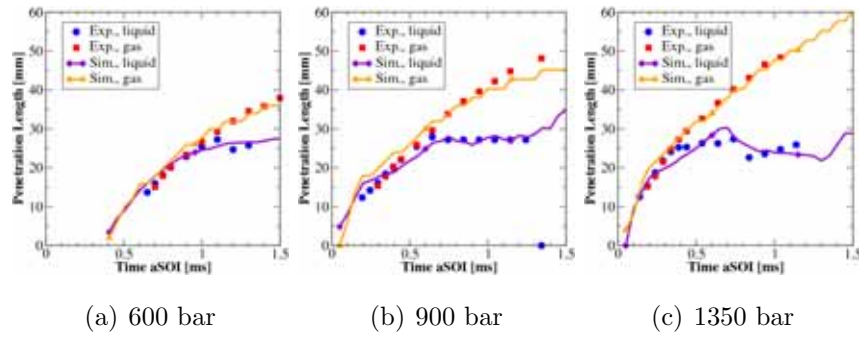


Figure 5.11: Spray penetration for nozzle A

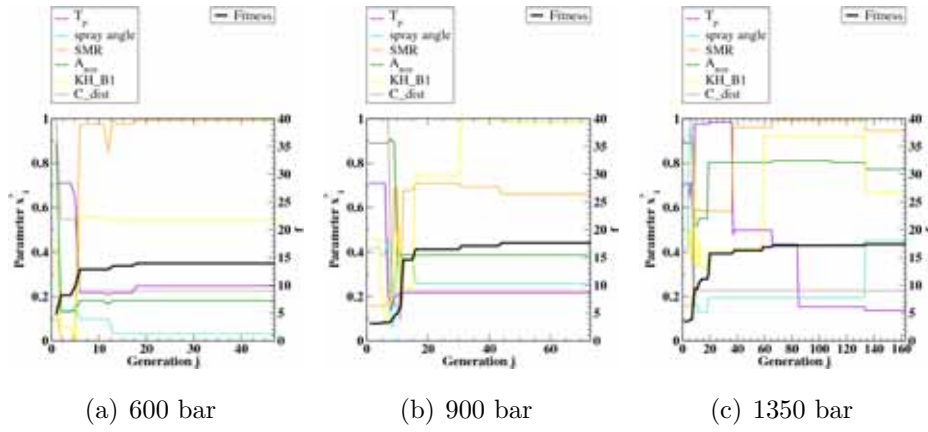


Figure 5.12: Spray parameters and merit function

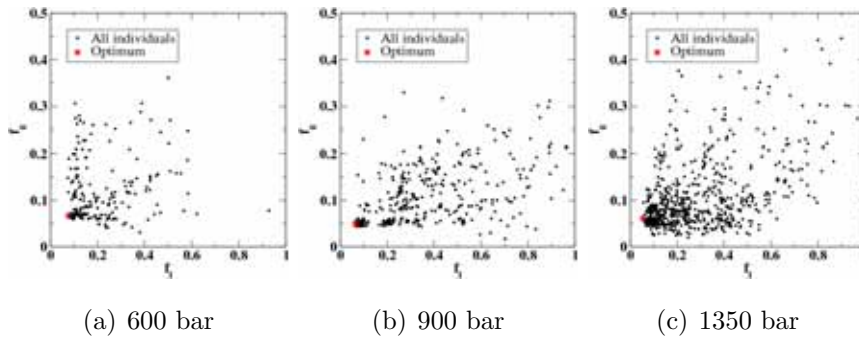


Figure 5.13: Merit functions of liquid and gaseous phase

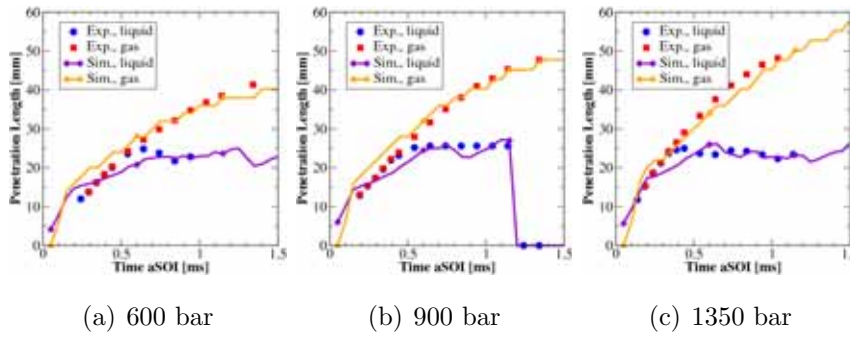
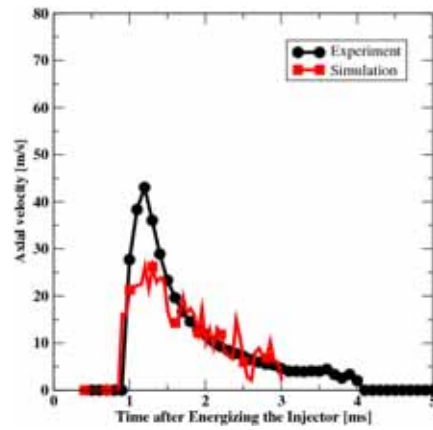
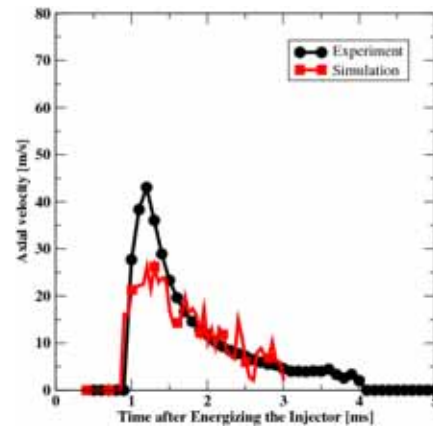


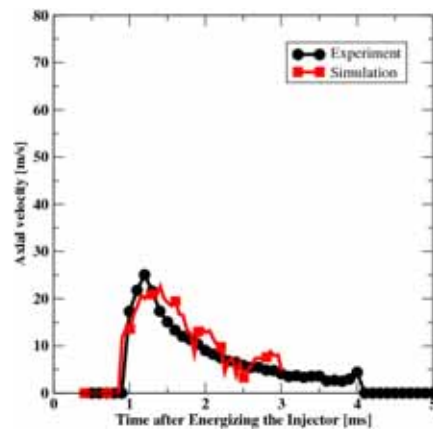
Figure 5.14: Spray penetration for nozzle B



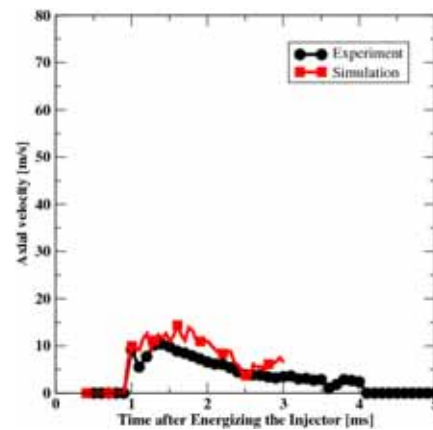
(a) Axial velocity at $r=0$ mm



(b) Axial velocity at $r=1$ mm

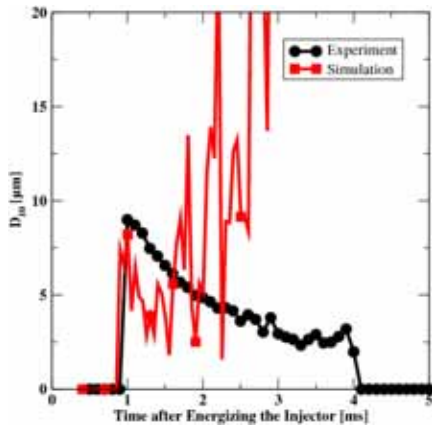


(c) Axial velocity at $r=2$ mm

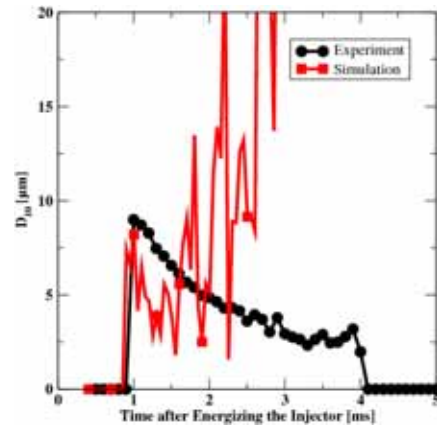


(d) Axial velocity at $r=3$ mm

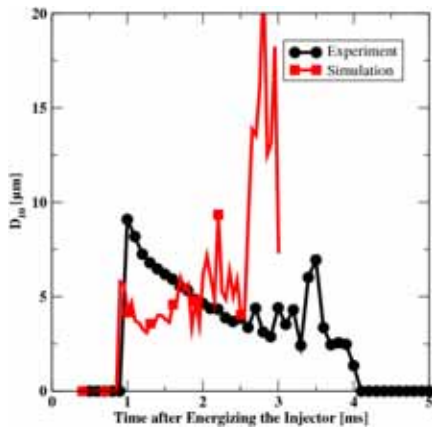
Figure 5.15: Axial velocity for nozzle A at 600 bar rail pressure



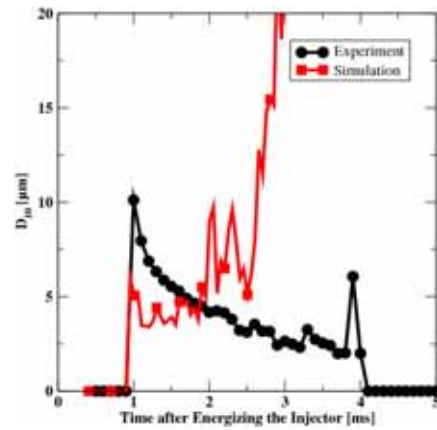
(a) Droplet diameter d_{10} at $r=0$ mm



(b) Droplet diameter d_{10} at $r=1$ mm



(c) Droplet diameter d_{10} at $r=2$ mm



(d) Droplet diameter d_{10} at $r=3$ mm

Figure 5.16: Droplet diameter d_{10} for nozzle A at 600 bar rail pressure

The evolution of the axial droplet velocity is in agreement for all radial positions. The maximum velocity is in an excellent agreement for a radial position of 2 mm and 3 mm. On the axis at 0 mm and 1 mm off-axis, the simulation underestimates the maximum velocity at 1.25 ms. Around times of 1 ms, the simulation underestimates the liquid penetration in Fig. 5.11(a) by a few millimeters which explains the discrepancy in the droplet velocity.

The other spray property determined by the PDA is the mean droplet diameter d_{10} . No good agreement between simulation and experiment is obtained for any radial position. Only the magnitude of droplet size at 1 ms is of the same order but the temporal evolution shows that quickly smaller droplets are formed due to the secondary breakup. These small droplets are evaporating faster than larger droplets and are already heated-up due to their long life-time. The mean droplet diameter is shifted to larger values after 1.5 ms in the simulation while the experiment shows that the droplet diameter decays monotonously. The secondary droplet model is not able to compute the correct temporal evolution. The breakup is controlled by the relative velocity between gaseous and liquid phase. Due to the injection process, the ambient gas is accelerated and therefore the relative velocity is decreased by time. Parcels that are injected at later times are more stable than earlier injected parcels.

Analysis of the number of droplets that the parcels are associated with is shown in Fig. 5.17. At times later than 2 ms, the comparison between simulation and experiment is not valid anymore. The number of droplets that are attached to the control volume of the simulation is decreasing within 0.5 ms from 1,000 to 40. These few parcels cannot accomplish for the statistics of the droplet distribution function.

5.4.1.5 Test Engine Case

The simulation of a test engine case uses the result from the spray parameter calibration. After the spray model is calibrated, the spray parameters in the engine simulation are not adjusted anymore. This test will show if the Diesel engine simulation can benefit from the spray calibration methodology. The engine simulation and the spray chamber simulation are quite different. In the spray calibration, a coarse mesh and a large time-step size are used. However, the computational mesh of the

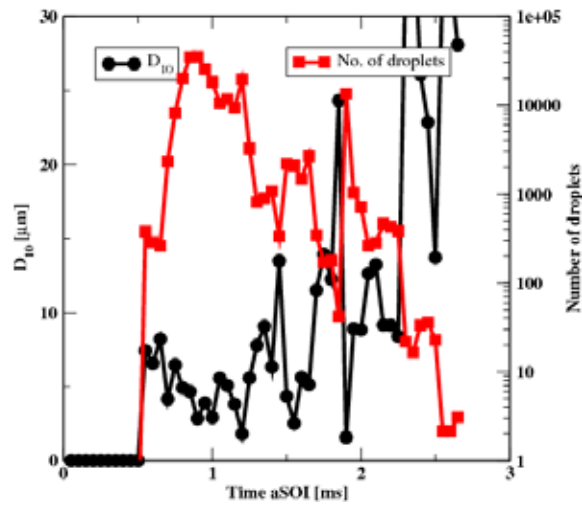


Figure 5.17: Evolution of droplet diameter and number of droplets

engine is much finer and includes a different topology as seen in Fig. 5.18. Due to

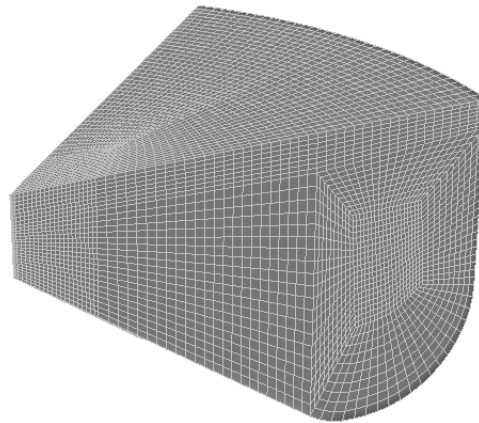


Figure 5.18: Geometry of the test engine case

symmetry of the 8 hole nozzle, a sector mesh of 45° and a quarter O-grid topology is created. The computational time-step is $1 \mu s$ and thus by a factor of 50 smaller than used during the spray calibration. The geometry of the engine has a bore of 120 mm and a bowl depth of 40 mm to exclude any spray-wall interaction for a fair comparison. For sake of simplicity, engine motion is not taken into account and a swirl flow motion is not considered. The thermal state conditions in the test engine and the spray calibration are defined equally.

In Fig. 5.19, the spray penetration in the test engine case is compared with the measurements and the result from the μ GA -optimization for nozzle A at a rail pressure of 600 bar. The result shows that the penetration length of the gaseous phase is similar.

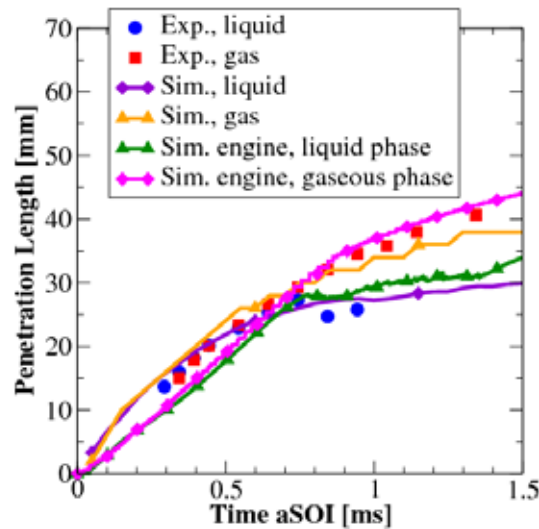


Figure 5.19: Spray penetration for nozzle A at 600 bar rail pressure: comparison of spray chamber, spray calibration and test engine case

During the start of injection, the penetration is less steep than in the spray calibration but matches better for times later than 1 ms. The liquid spray penetrates the engine bowl slightly deeper than in the spray calibration and the measured liquid spray penetration. In Fig. 5.20, the spray parcels and the mean mixture fraction \tilde{Z} are shown at $t=0.8$ ms. The shape of the spray is as to be expected and no deformation of the spray shape is detected in the images.

5.4.2 Ethanol Spray

5.4.2.1 Introduction

The mixture composition is one of the most important properties in fuel sprays and is difficult to measure because liquid and vapor fuel appear simultaneously. Information about the distribution of local fuel concentration, temperature and droplet size are properties that would be useful to validate the spray models. However, the Diesel

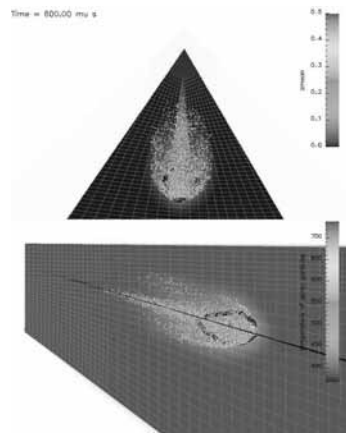


Figure 5.20: Mixture formation in the test engine case: cut-plane colored by mixture field, parcels colored by droplet temperature, iso-line represents stoichiometric mixture

sprays is too dense to study these properties. The high void fraction in dense areas forces multi-scattering of laser-light so that no reliable data can be accessed. Alternatively, alcohol fuels offer due to the molecular structure an option for quantitative Raman measurements. The phase-dependent spectral shift of the OH stretching vibration allows the Raman signal separation of liquid and vapor phase. The result provide simultaneous information on the propagation of liquid/vapor phase and quantification of the air/fuel ratio for comparison with the CFD spray simulation.

5.4.2.2 Injection System

A passenger car common rail injection system is equipped with a 5 hole valve covered orifice nozzle (VCO) with double needle guidance and mounted on a first generation Bosch common rail injector [84] with a maximum pressure capability of 1350 bar. The laboratory controller from Smart company allows variable settings of injector voltage and current and thus an independent control of injection timing and duration. In order to carry out 1D-Raman measurements, any impact from the fuel injection system on the purity of the fuel must be omitted to avoid broadband fluorescence. Therefore, a pneumatically driven high-pressure pump without lubrication in the hydraulic part of the pump and a custom made stainless steel rail is applied. Detailed information about

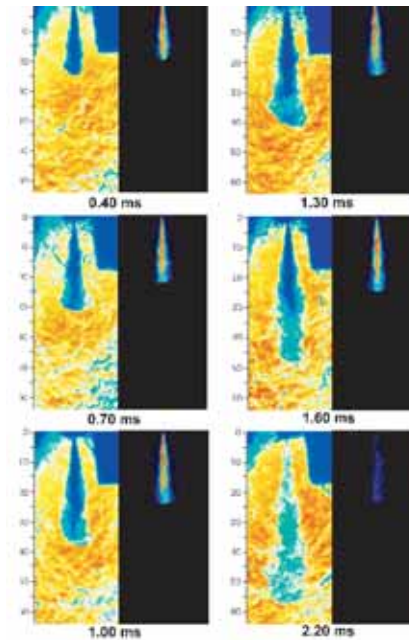


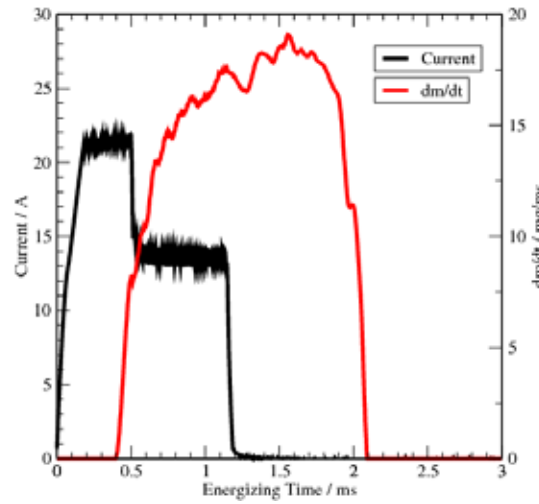
Figure 5.21: Single-shot shadowgraph image (left) and Mie-scattering (right) for different injection times aSOE

the injector nozzle is given in Tab. 5.5. The complete fuel system, including pump, rail, pipe-work and controller is calibrated on a flow bench as previously described in section 5.2.1. The resulting injection rate and the injector current are shown in Fig. 5.22. The ratio of the integral injection rate and the theoretical mass by Bernoulli's law results a discharge coefficient of $C_d = 0.7$.

5.4.2.3 Ethanol Spray Simulation

The simulation of the experimentally investigated ethanol spray in the chamber has the aim to resolve the local mixing of liquid and gaseous phase. In comparison to the spray penetration as studied in [100, 82, 51, 110], the benefit of the 1D-Raman measurement technique is to compare spatial resolved data of the experiment with simulation results. The input of the spray simulation are the chamber conditions as presented in Tab. 5.6. Under these conditions, auto-ignition will not occur because temperature is too low. A minimum ambient air temperature of about 900 K is required

Nozzle type	VCO
Number of nozzle holes	5
Hole diameter inlet (d_1)	138 μm
Hole diameter outlet (d_2)	137 μm
Orifice length to diameter	$l/d = 7.25$
Conicity	$K = \frac{d_1 - d_2}{10} = 0.1$
Rate of rounding	10.5 %
Volumetric flow rate	259 $\text{cm}^3/30 \text{ s}@100 \text{ bar}$
Injected fuel quantity	5 mg
Rail pressure	800 bar
Injection duration	1.695 ms
C_d	0.7

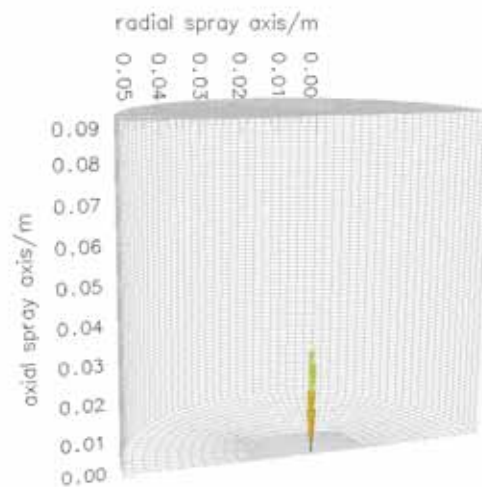
Table 5.5: Nozzle and injection parameters**Figure 5.22:** Measured injection rate by the flow bench

so that auto-ignition of ethanol occurs as reported by Siebers et al. [190]. Furthermore, investigations by Pitsch et al. [165] showed that auto-ignition for n-heptane occurs for a scalar dissipation rate of $\chi_{st} = 30 \text{ }^1/\text{s}$ in fuel-rich regions of $\phi = 2.5$. In this study, the presented experiments and simulations do not show any fuel-rich mixture parts due to the high volatility of ethanol.

Temperature	700 K
Pressure	44 bar
Rail pressure	800 bar
Density	21.4 kg/m^3
Gas phase	Air
Fuel	Ethanol

Table 5.6: Conditions in the spray chamber

The CFD simulation is carried out on a computational mesh that resolves the geometry of the spray chamber by a cylinder of length $L = 90 \text{ mm}$ and diameter $D = 100 \text{ mm}$ where the z -axis is aligned with the injector axis. The nozzle hole is located close to the origin at $z = 0$ at the bottom of the cylinder. The cylinder is meshed using an O-type, block-structured mesh as shown in Fig. 5.23. The resolution is $78 \times 12 \times 31$

**Figure 5.23:** O-type, block structured mesh of a cylindrical geometry

nodes in axial, radial and azimuthal direction, yielding a total mesh size of 170,940 hexahedronal cells. The resolution is much finer as used formerly in [209] because the original mesh using 14,480 cells did not resolve the width of the spray correctly.

5.4.2.4 Calibration of Spray Parameters

Similar to the calibration of spray parameters of a Diesel spray in section 5.4.1.3 the μ GA is applied to the spray simulation of the ethanol fuel spray. The limits of the parameter space is presented in Tab. 5.7 which is similar to Tab. 5.3. The influence of the breakup-length C is finer resolved within a smaller range whereas the fuel temperature has a lower resolution. After 188 generations, the μ GA has found an optimum

x_i	Lower Limit	Upper Limit	Resolution
T_{fuel}	330 K	380 K	32 (5 bit)
Half-cone angle	5°	30°	32 (5 bit)
SMR	30 μm	100 μm	128 (7 bit)
d_{eff}	90 μm	135 μm	128 (7 bit)
B_1	5	100	64 (6 bit)
C	0	22.8	64 (6 bit)

Table 5.7: Limits and resolution of the parameter space

representing 940 individual CFD simulations. The value of the merit function becomes $F(\mathbf{x}) = 27.95$ as shown in Fig. 5.24. The merit function is monotonously increasing until that a global optimum is found in the 159th generation. The global optimum is given by the point in Tab. 5.8 and compared with the measured experimental data.

A discharge coefficient of $C_{d,\text{sim}} = 0.62$ is derived from the effective nozzle diameter

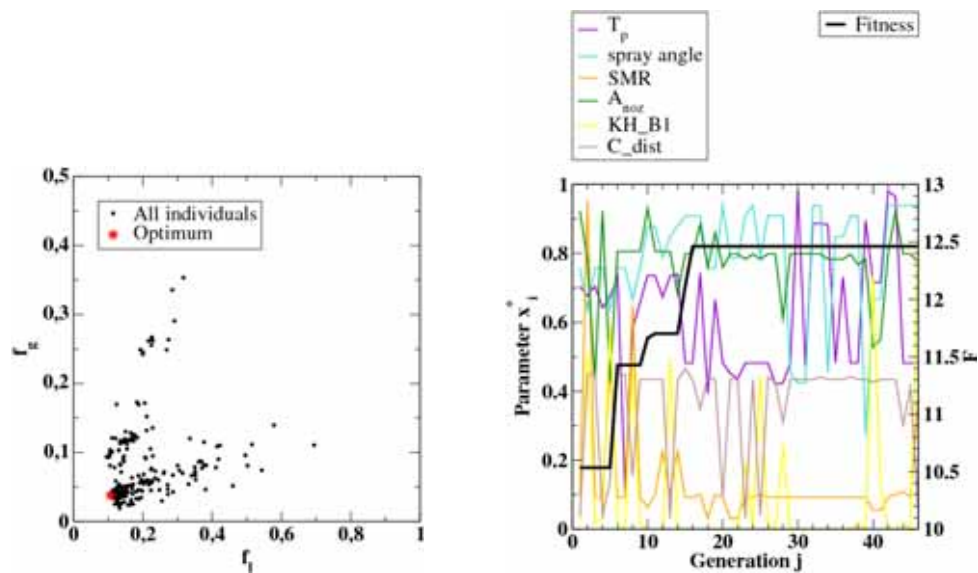
	T_{fuel}	Half-cone angle	SMR	d_{eff}	C_d	B_1	C
Simulation	345.3	12	54	124.9	0.82	23	2.19
Experiment	358	11.5	-	115.5	0.7	-	-

Table 5.8: Comparison of spray model parameters of best point with experimental data

which is a little smaller compared to the discharge coefficient that is yield by the injection rate measurement $C_{d,\text{exp}} = 0.7$.

Regarding the fuel temperature, the μ GA finds an optimum where the initial droplet temperature in the simulation is found to be 345.3 K. In order to measure the fuel temperature the same nozzle type with welded holes and equipped with a thermocouple is mounted on the injector. The fuel temperature is about 358 K while operating the chamber at the same conditions as the spray measurements. The measured temperature is an upper limit for the injected fuel temperature because the residence time is much longer than under injection conditions. Thus, the temperature found by the μ GA in the spray simulation is very close to this upper limit.

From the image processing of the shadowgraph imaging, the half spray-cone angle is derived and compared to the angle that is used to initialize the parcel velocities. The μ GA results in a point in parameter space where the half-cone angle of 10.6° is in a good agreement to the experimental half-cone angle of 11.5° .



(a) Individual merit functions with all individuals and found optimum

(b) Evolution of parameters and merit function

Figure 5.24: Final result of μ GA after 46 generations and 230 evaluated individuals

Spray Penetration The axial spray penetration from shadowgraph imaging and Mie-scattering is compared with the simulation results as shown in Fig. 5.25(a). Obviously,

a good agreement for the vapor phase is obtained for all times. Although the penetration of the liquid phase has a shift to later times, the slope and penetration length is still close to the experimental data. Additionally to the spray penetration, the width of the spray is derived from the Raman measurements as presented in Fig. 5.25(b). The agreement indicates a correctly computed shape of the spray. The same calibration of the ethanol spray was performed in [209] but using the coarse mesh as described in section 5.4.1.2 and shown in Fig. 5.8. The result from this study is again compared with the same experimental data, see Fig. 5.26(b). As already discussed in section B.1, the mesh sensitivity has an important influence on the spray simulation. The sensitivity anticipates a predictive spray modeling as required for a mixture-controlled combustion modeling. Although the spray calibration was successfully applied to both fuel simulations yielding a good agreement in the axial spray penetration in Fig. 5.25(a) and Fig. 5.26(a), the width of the spray as presented in Fig. 5.25(b) and Fig. 5.26(b) is computed only on the fine mesh correctly. Therefore, only results computed on the fine mesh are compared with the experimental data further on.

Fuel Concentration Fuel mass fractions from the 1D-Raman spectroscopy measurements for liquid and gaseous phase are compared at six times with the simulation data in Fig. 5.27 and Fig. 5.28. The shape of the fuel mass fractions in gas- and liquid phase is well matching the simulation. The area close to the nozzle is not visible due to the limiting view of the observation window. The penetration and the width is in agreement with the analysis of the previous section section 5.4.2.4. However, the simulation shows a much higher mass fraction close to the centerline for the gas phase in $t=0.4-1.6$ ms aSOI but the discrepancy decreases by time. At the latest time $t=2.2$ ms aSOI all liquid droplets are evaporated. The level of fuel mass fraction in the gas phase of the simulation has now the same order of magnitude as in the experiments. Turbulent mixing is dominating while mixture formation by evaporation has been completed.

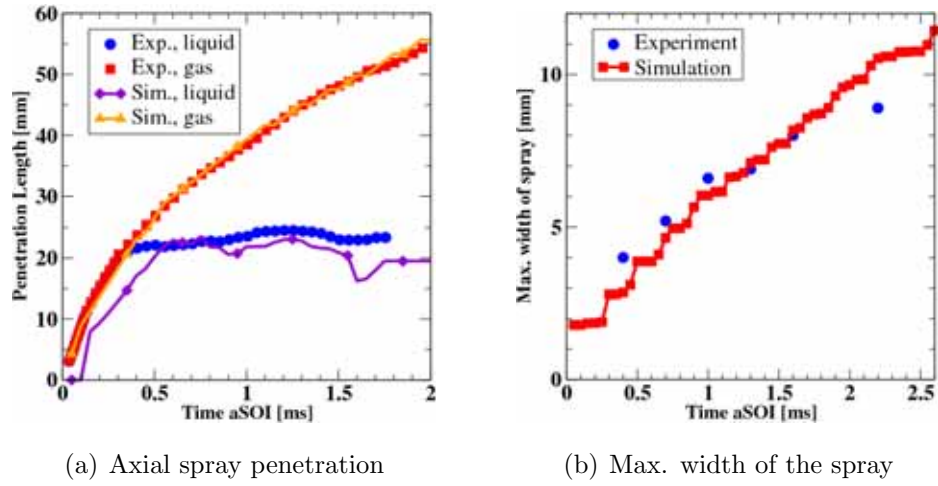


Figure 5.25: Spray penetration of ethanol on fine mesh (170,940 cells)

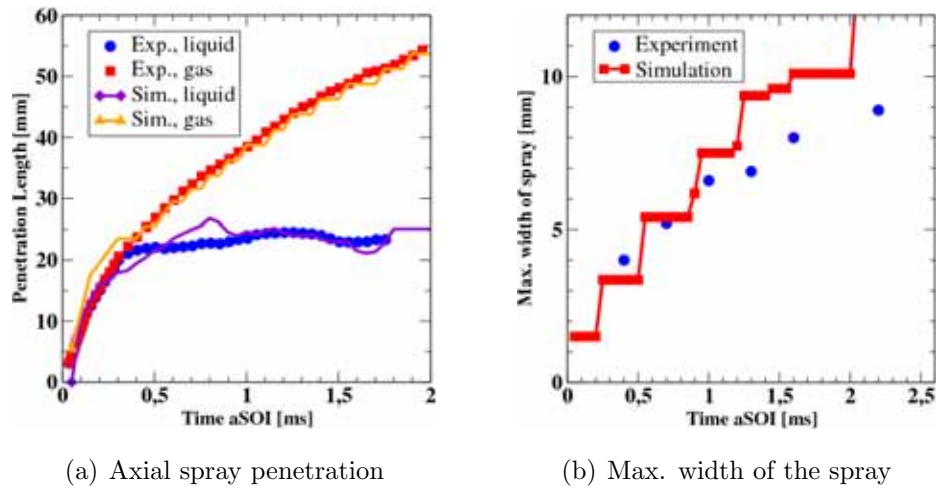


Figure 5.26: Spray penetration of ethanol on coarse mesh (14,470 cells)

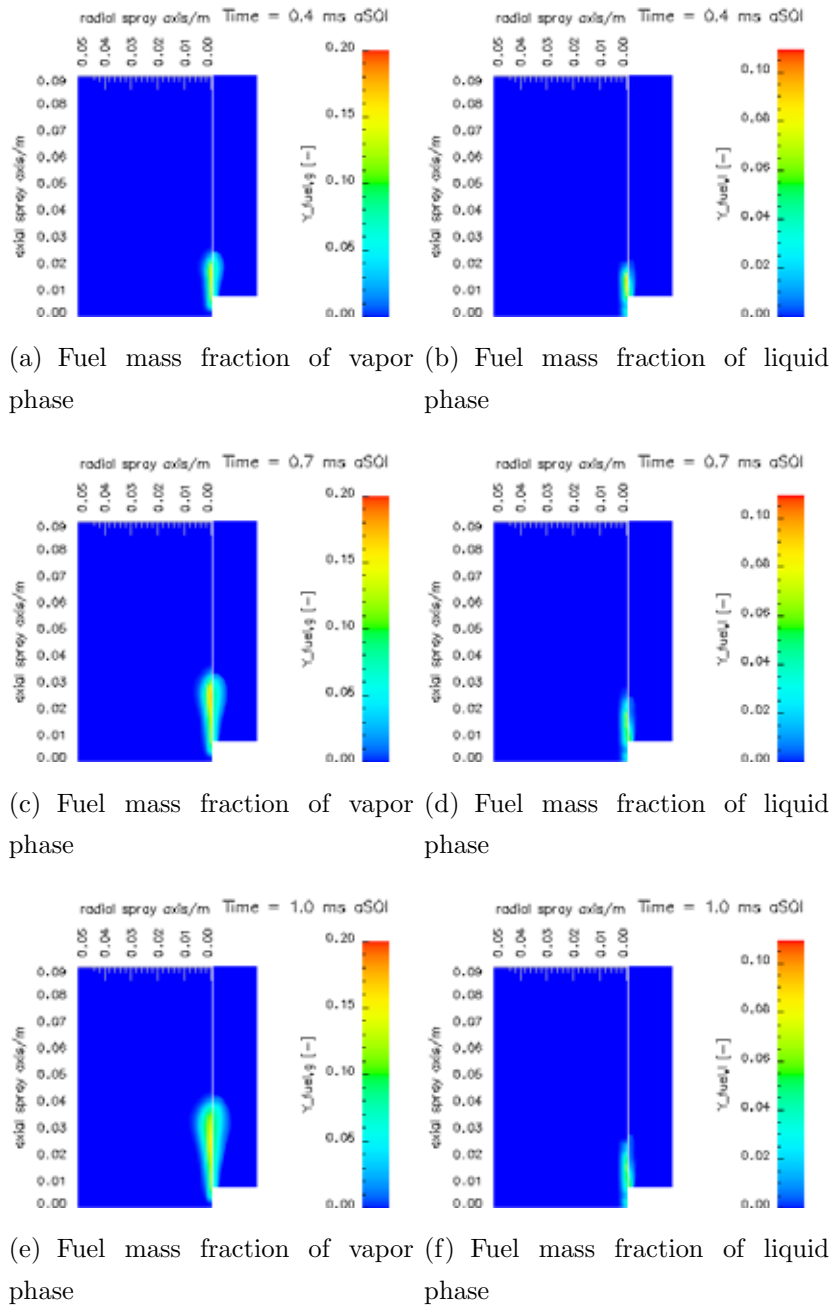


Figure 5.27: Comparison between simulation (left) and 1D Raman spectroscopy (right) for the fuel mass fraction distribution

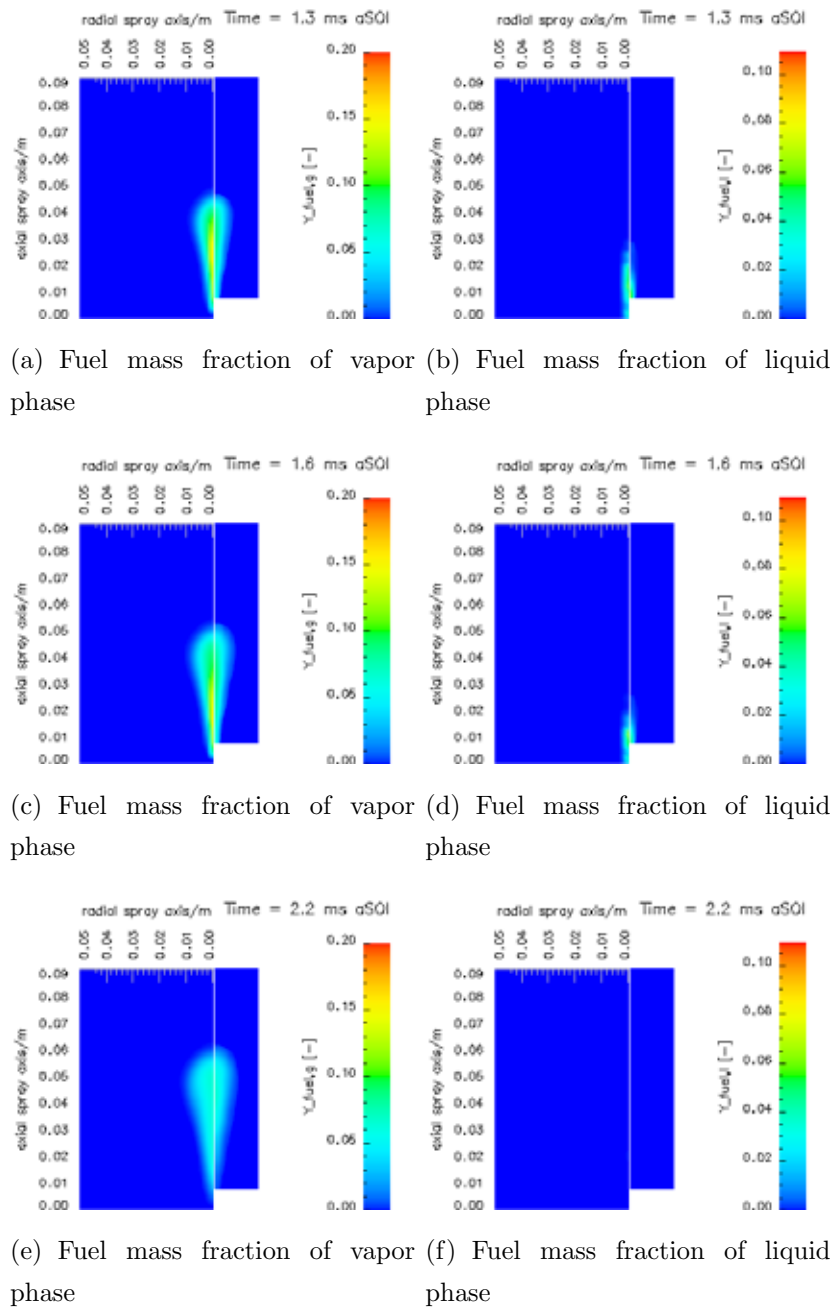


Figure 5.28: Comparison between simulation (left) and 1D Raman spectroscopy (right) for the fuel mass fraction distribution

Temperature Distribution The 1D-Raman spectroscopy allows to derive the time-resolved spatial temperature distribution in the gas and liquid phase of the spray. Although the order of magnitude agrees very well for all times, the spatial distribution of the temperature of the gas phase in Fig. 5.29 and Fig. 5.30 are not in agreement. However, the penetration with respect to the temperature is matched. For all times, the simulation shows a temperature distribution for the gaseous phase that is much higher close to the spray axis. For the liquid phase, the temperature in the simulation is much lower and uniform than the Raman data shows. Here, the droplet data has been interpolated from the parcels on the underlying mesh as illustrated in Fig. 5.31. Obviously to see is that the temperature of the liquid phase is attached very close to the parcels which are located in a narrow cone around the spray axis. The parcel temperature and the interpolated temperature of the liquid phase is nearly uniformly and cannot resolve the local gradients of the experimental data. The narrow spray cone angle and the resulting narrow spray shape explain the difference in the temperature of the gas phase. Mixing of enthalpy is not forced enough. The resulting temperature distribution of the gas phase encloses the liquid phase.

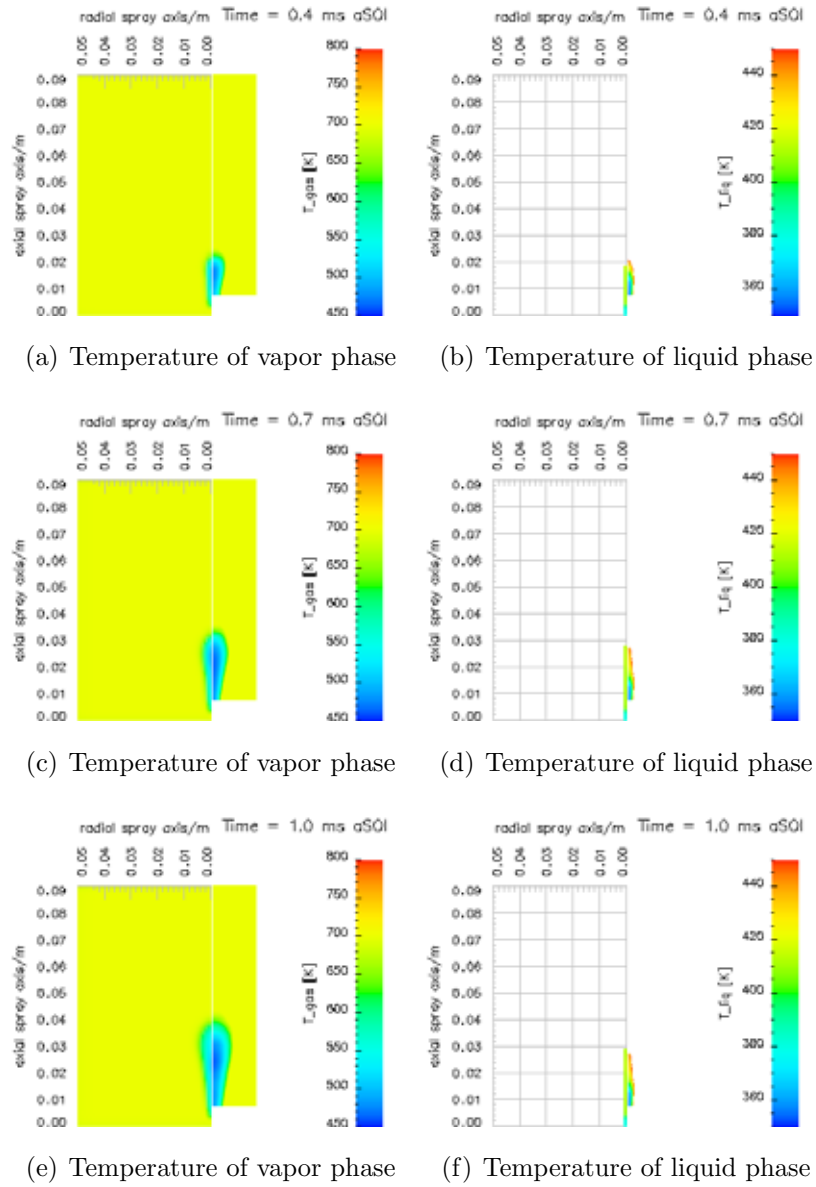


Figure 5.29: Comparison between simulation (left) and 1D Raman spectroscopy (right) for the temperature distribution

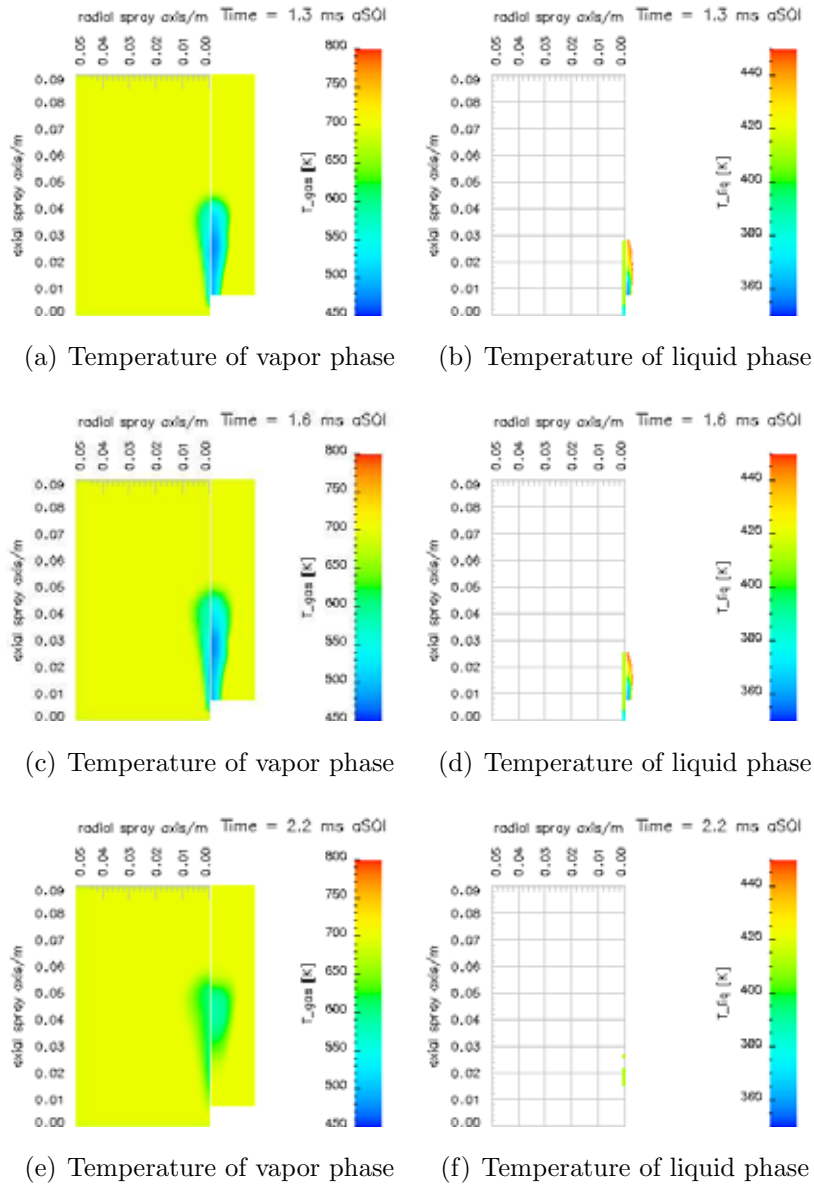


Figure 5.30: Comparison between simulation (left) and 1D Raman spectroscopy (right) for the temperature distribution

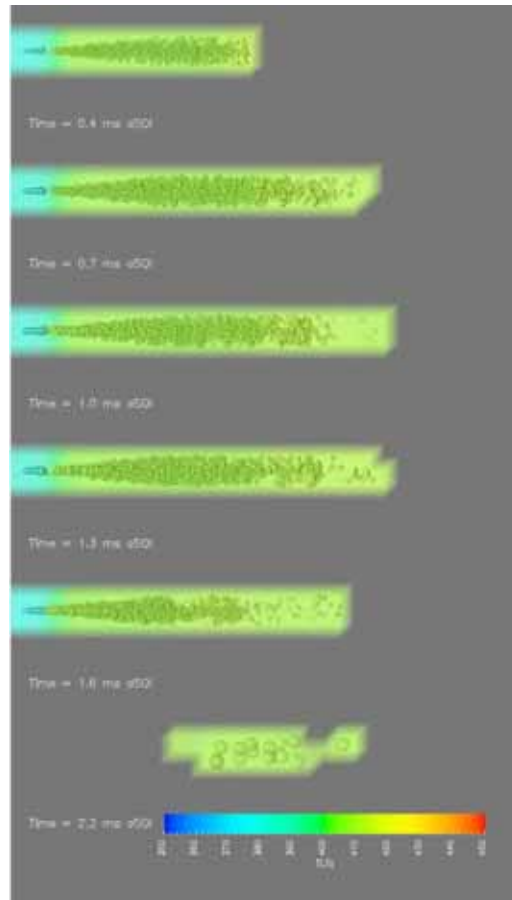


Figure 5.31: Temperature of parcels and liquid phase

Droplet Size Raman and Mie measurements are used to derive the SMR distribution in the spray. In the simulation, the SMR is interpolated from the parcel's position on the underlying cell for sake of comparison as shown in Fig. 5.32. Only close to the nozzle the SMR has an order of $\mathcal{O}(1 - 2\mu m)$. The small value of breakup-length $C = 2.19$ suppresses the droplet breakup by Kelvin-Helmholtz instabilities and forces the Rayleigh-Taylor breakup very close to the nozzle. Therefore, the resulting SMR distribution is located close to the nozzle whereas in the regime of Rayleigh-Taylor breakup, evaporation is overestimated.

5.5 Evaporation Controlled Mixing

The previous results have shown that the optimization can find an adequate set of spray parameters. In that optimum the macroscopic spray penetration between experiment and simulation agrees. Also locally, fuel concentrations and temperature are well matching. The droplet break-up forms very small droplet of size $\mathcal{O}(5 - 10\mu m)$ which evaporate much faster. Thus, the mass and momentum exchange at the spray tip is dominated by the evaporation process. That leads to the approach to omit the droplet's break-up and the droplet-droplet interaction process. The result of the break-up process is accounted by an smaller SMR as initial droplet diameter. By this approach, the number of spray parameters is reduced from 6 to 4.

The approach is evaluated for both, the diesel fuel spray of nozzle A at a rail pressure of 600 bar and the ethanol fuel.

5.5.1 Re-Definition of Parameter Space

The parameter space has been re-defined as presented in Tab. 5.9. The spatial resolution of temperature and half-cone angle has been increased and the upper limit of the breakup length is limited to 36.5 now. In Tab. 5.3, the effective nozzle diameter d_{eff} can exceed the geometrical one. Now, the diameter will be restricted to the geometrical one. In the case that droplets do not undergo breakup and collision, the limits

of the SMR are re-defined from $1 \mu m$ to $20 \mu m$. By this re-definition the droplets are initialized by a size distribution that would result from the droplet breakup process. Limits for the ethanol fuel spray are similar as for the Diesel fuel except for the upper

x_i	Lower Limit	Upper Limit	Resolution
T_{fuel}	330 K	380 K	64 (6 bit)
Half-cone angle	5°	30°	64 (6 bit)
SMR	$30 \mu m$	$100 \mu m$	128 (7 bit)
SMR	$1 \mu m$	$20 \mu m$	128 (7 bit)
d_{eff}	$90 \mu m$	$131 \mu m$	128 (7 bit)
With breakup: B ₁	5	100	64 (6 bit)
With breakup: C	0	36.5	64 (6 bit)

Table 5.9: Limits and binary resolution of the parameter space for Diesel spray calibration

limit of the effective nozzle diameter d_{eff} which is $135 \mu m$.

5.5.2 Comparison of Spray Penetration W/O Breakup and Collision Model

The comparison between both levels of modeling detail is presented for both, the diesel fuel spray of nozzle A at 600 bar rail pressure and for the ethanol fuel spray in Fig. 5.33. Without the breakup and collision model, the spray calibration of the Diesel spray results in a better agreement as the merit function shows in Fig. 5.33(b). In case of the ethanol fuel, the merit function decreases if the mixture formation is controlled by the evaporation only. The influence of model detail results in a difference in the spray penetration length. In case of the diesel fuel, the gas phase agrees much better without breakup and collision model although the liquid penetration shows the inverse trend. A similar trend has been observed for the ethanol fuel. The gas phase penetration is already in a good agreement if only the evaporation model is used but for the liquid phase, the agreement in spray penetration becomes worse.

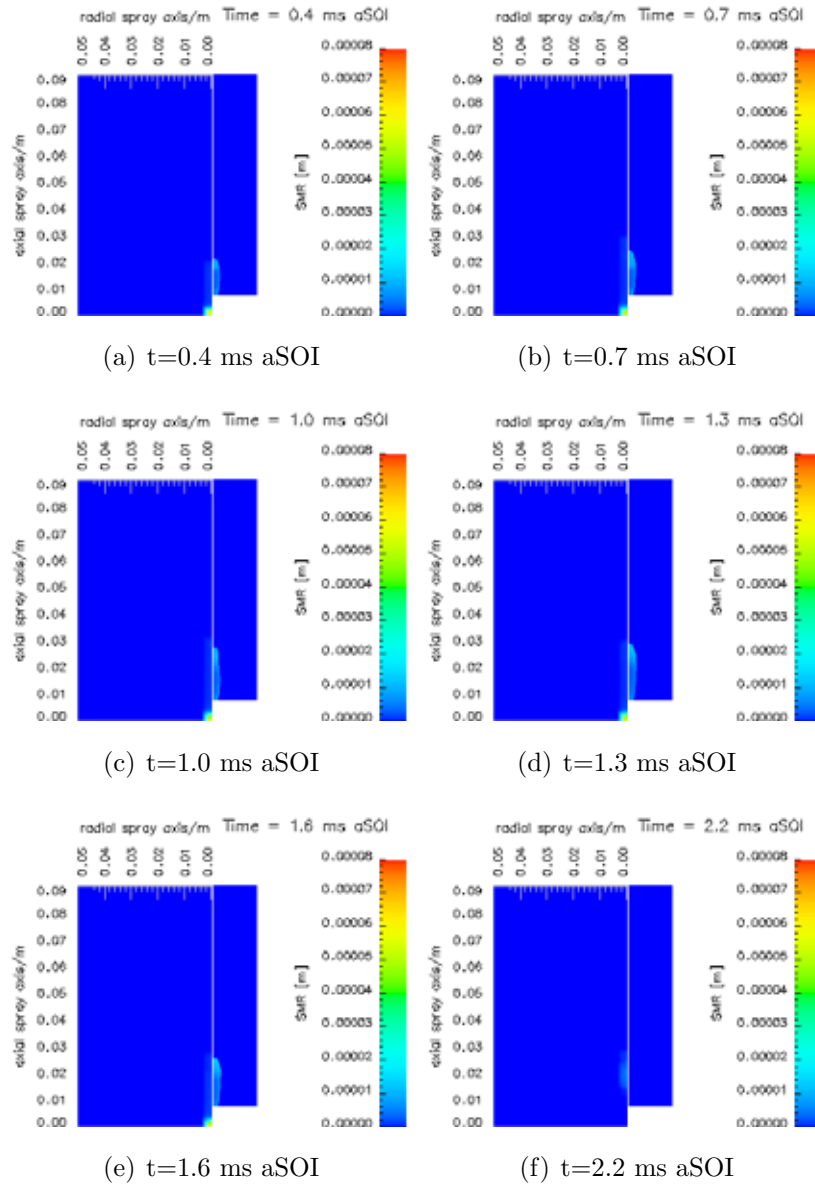


Figure 5.32: Comparison between simulation (left) and 1D Raman spectroscopy (right) for the SMR distribution of the liquid phase in the spray

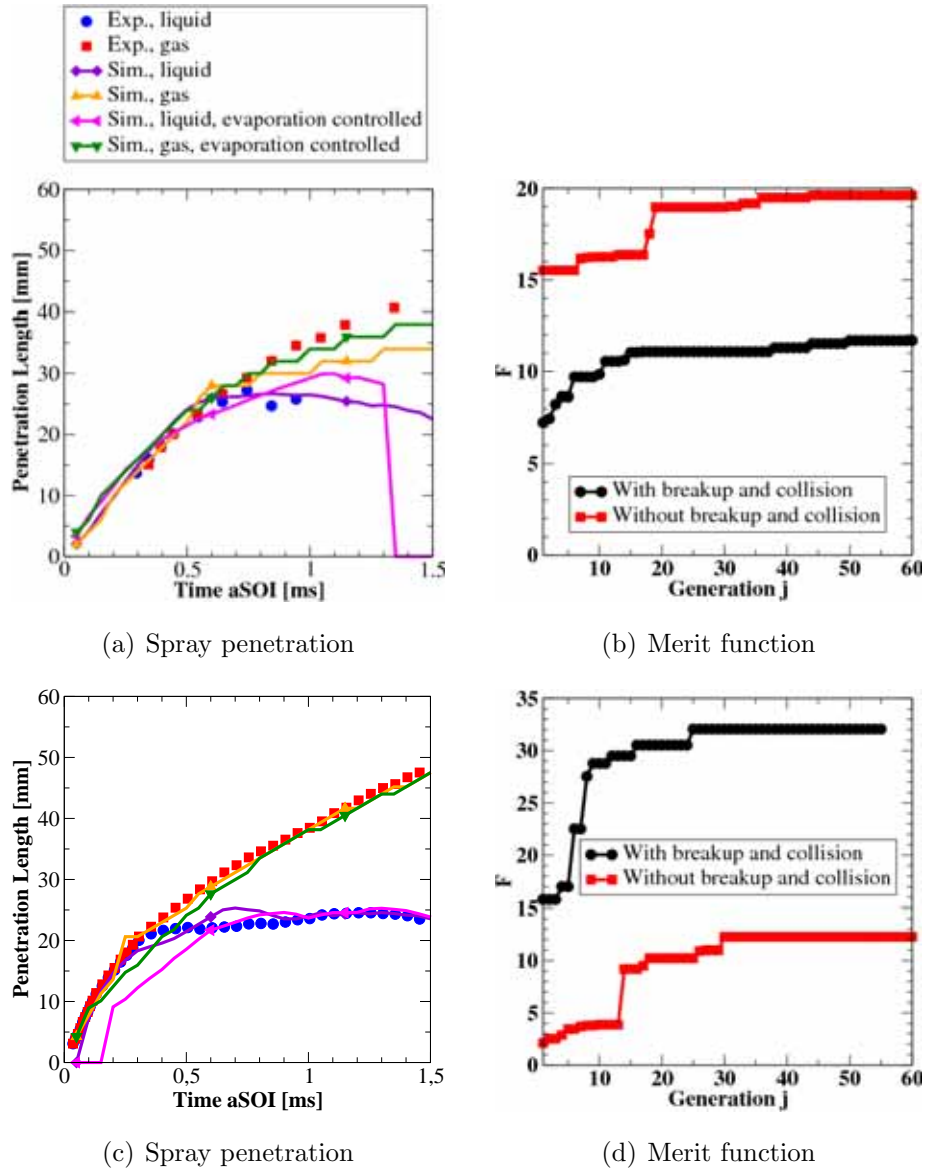


Figure 5.33: Comparison of Diesel (top) and ethanol (bottom) spray calibration w/ and w/o breakup and collision model

6 Diesel Engine Simulation

6.1 Optimization Methods for Diesel Engine Simulations

Three different engine types are investigated to demonstrate the beneficial use when the RIF-model is applied to different combustion modes and engine types.

Most problems in the Diesel engine simulation are due to uncertainties in the input data or an insufficient data-set. Especially for the mixture formation, spray data cannot always be provided. In that case, a spray calibration using the μ GA is not feasible and can thus not support the engine simulation. Nevertheless, pressure trace and heat release analysis are the major data set. In order to find a good agreement between simulation and experiment, model parameters are manually adjusted as illustrated by the flow-chart in Fig. 6.1. The work-flow of this optimization is split into three parts: compression, injection and expansion cycle as it will be outlined in the following.

6.1.1 Compression Cycle

The simulation of the Diesel engine starts with the compression cycle of the fresh charge. A correct choice of initial conditions and an accurate mesh that features all relevant details of the engine geometry is a prerequisite. Main input from the engine test are the thermodynamical state of the intake charge, cycle resolved data and the EGR rate. The thermodynamical state at intake valve closure (IVC) is characterized by the pressure, massflow-rate of air and volume.

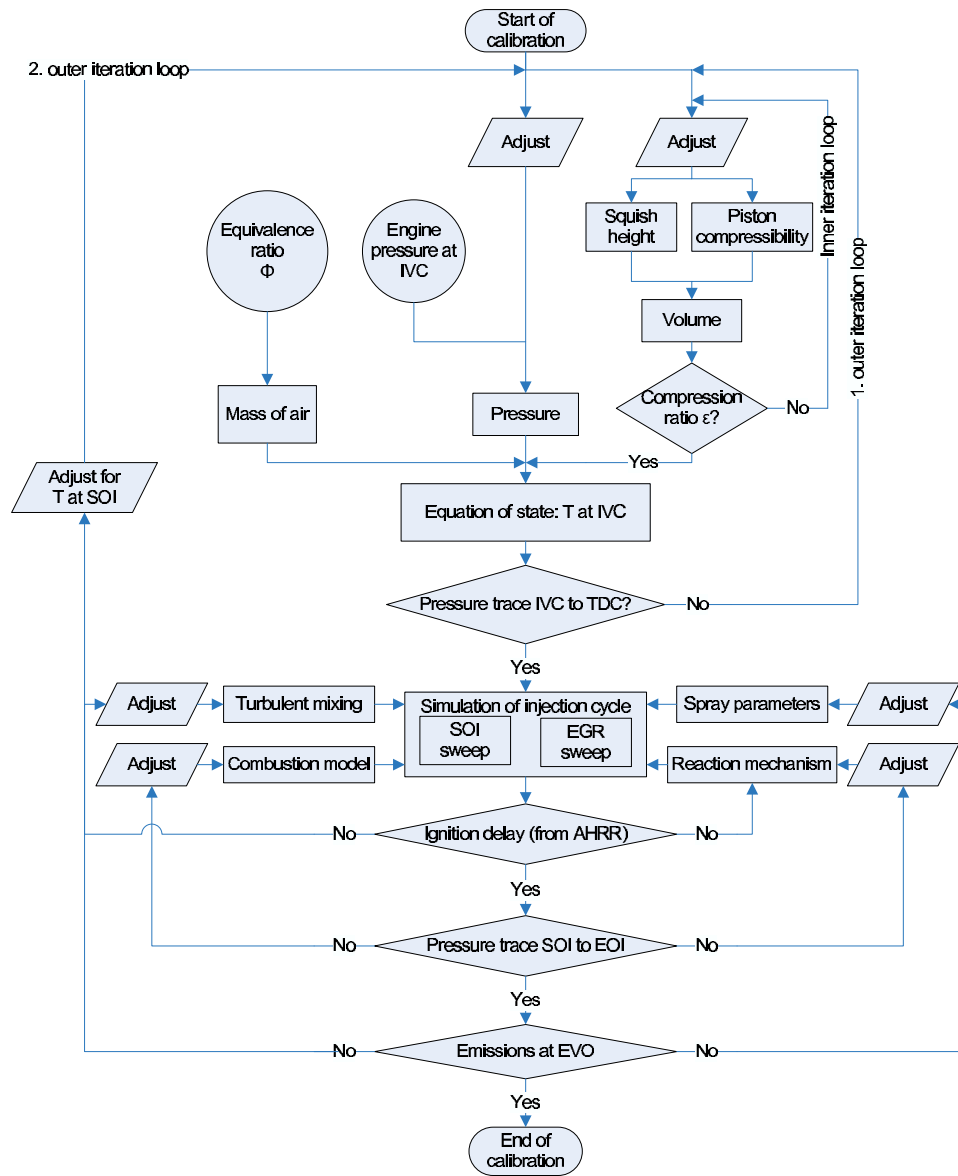


Figure 6.1: Work-flow for the Diesel engine simulation

6.1.1.1 Compression Ratio

The compression ratio is derived in the simulation directly from the analysis of the kinematics of piston motion. It is related to the ratio of displacement and dead volume and therefore depending on the squish height. Thus the squish height is a required input parameter from the engine data. Additionally, an effective Young's modulus is introduced to account for the elasticity of the piston, connecting rod and crankshaft. During the engine cycle, the pressure force acts on the piston surface and results in a normal stress and strain. This effective Young's modulus is similar to a dynamic squish height and denoted here as "piston compressibility". Both parameters can adjust the volume in order to achieve a correct compression ratio.

However, the resulting pressure trace has also to account for a correct compression ratio. The slope of the pressure is controlled by the squish height and therefore adjusted by comparison to motored engine data. If that data is not available, the pressure trace of the simulation is compared with experimental engine data until start of combustion occurs.

6.1.1.2 Intake Temperature

The intake temperature is not a variable parameter and defined by the equation of state of an ideal gas, the equivalence ratio, intake pressure and engine volume. The equivalence ratio and the resulting mass of air are quite well known. The intake pressure at IVC is not measured very accurately so that the initial condition of the pressure is adjusted. An increase of the intake pressure will increase the maximum pressure peak which is compensated by adjusting the squish height on an inner iteration loop. A change in squish height will as well change the volume and a new intake temperature is derived. Therefore, the adjustment of the squish height, intake pressure and compression ratio at a given massflow of air is on a first outer iteration loop. Overall agreement in the resulting pressure trace, equivalence ratio and squish height has to be insured.

6.1.2 Injection Cycle

After calibrating the compression cycle, the injection cycle is subject of optimization with regard to the pressure trace and ignition delay that is obtained from the apparent heat release rate (AHRR) analysis. According to chapter 5 most uncertainties occur from the spray model. The spray parameters are adjusted manually as it is done in section 6.2 and section 6.3.3 if sufficient experimental data is available. For a strategy that uses an early injection strategy at lower compression ratios as shown in section 6.3.4, the adjustment of spray parameters is not required because ignition occurs at later times when the injection has almost finished. The effect of turbulent mixing and the role of the scalar dissipation rate on the ignition event are also to be studied. Turbulent Schmidt and Prandtl numbers should be in the range between 0.5 and 0.9. Other model constants of the $\tilde{k}-\tilde{\epsilon}$ model may also be adjusted. The temperature at start of injection is a parameter that is usually fixed from the thermodynamical state at IVC. However, problems in ignition delay may require a higher intake temperature. Since the mass of air must remain constant, only the pressure, squish and piston compressibility may be re-adjusted in a second outer iteration loop unless an agreement is achieved.

6.1.3 Expansion Cycle

After the injection cycle, the simulation follows the expansion cycle until exhaust valve opening (EVO). Since the fuel injection has been finished during the expansion cycle spray parameters should not be adjusted anymore. At EVO, the simulation results for NO_x and soot emissions are compared with engine-out emissions. A sweep of SOI or EGR should be performed and the comparison should focus qualitatively the prediction of trends. A reliable model should predict at least this trend correctly otherwise another third outer iteration loop would be required. In this third outer loop, the temperature at IVC would be adjusted to control the temperature level.

Displacement volume	2.49 l/cyl.
Bore	137 mm
Stroke	169 mm
Connecting rod length	262 mm
Compression ratio	16.6
Clearance height	1.78 mm
Piston top land	0.1164 mm
No. of injection holes	6
Hole diameter	264 μ m
Swirl number	1
Intake valve closure (IVC)	-148° CA aTDC
Exhaust valve opening (EVO)	127° CA aTDC

Table 6.1: Data of the Cummins QSX engine

6.2 Cummins Engine

6.2.1 Engine Data

The QSX heavy duty engine from Cummins Inc. is a six cylinder in-line engine. Engine parameters are given in Tab. 6.1. Pressure, heat-release and engine-out emission data from a 75 % load operating point at a speed of 2100 rpm are available. The simulation is restricted for sake of simplicity and shorter simulation run-time to a closed cylinder mesh. The intake flow is approximated as a rotational flow of swirl number equal 1.0.

6.2.2 Computational Mesh

The computational mesh is generated using the commercial meshing tool ICEM-CFD. The mesh resolves the full 360° geometry of the engine at intake valve closure (IVC) as presented in Fig. 6.2. On the top face of the in-cylinder block, Fig. 6.3 shows that the

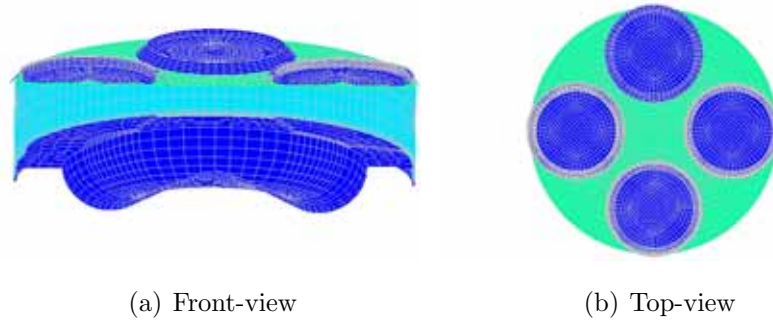


Figure 6.2: Meshed geometry of Cummins QSX engine

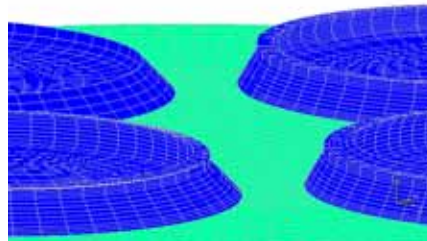


Figure 6.3: Detailed view of valve recess

valve recesses are meshed independently, separated from the in-cylinder block, using a special boundary type denoted as "shearing grid interface" [76]. This special boundary type enables the code to handle hanging nodes. Furthermore, block-independent mesh motion is available through this technique. The total mesh size is finally about 104,960 hexahedral cells at TDC and the mean cell size is about 2 mm.

6.2.3 Investigated Parameters

In this study a variation of start of injection (SOI) and spray angle is performed as listed in Tab. 6.2 in order to study the influence of start of injection (SOI) and spray angle independently for the same operating point. The injection duration was 35° CA.

Case no.	SOI / °aTDC	Spray Angle
Case 1	-6	126°
Case 2	-2	126°
Case 3	-6	120°
Case 4	-2	120°

Table 6.2: Investigated injection parameters

Parameter	Values	No. of points
$smr/\mu m$	(132, 200, 300, 400)	4
$B_1/-$	(5, 10, 15, 20, 40)	5
$C/-$	(18.24, 22.8, 27.36)	3
$d_{eff}/\mu m$	(144.8, 167.2, 187.0)	3

Table 6.3: Four dimensional parameter space

6.2.4 Optimization of Spray Parameters

First attempts of simulating the correct pressure traces and AHRRs did not succeed. The fuel spray did not penetrate far enough into the bowl of the combustion chamber and thus, mixing of fuel vapor with air was not well captured. A sensitivity study for initial spray conditions and spray model constant is performed similar as described in appendix B. In contrast to the six spray parameters found in section 5.3.1, only four parameters, namely the Sauter mean radius smr , the effective nozzle diameter d_{eff} , the model constants B_1 and C , are chosen for simplicity to reduce the numerical effort. These four parameters are listed in Tab. 6.3 and the design space has been explored by permutation. The permutation of these four parameters leads to 180 individual simulations. The objective is to find a good agreement between simulation and experimental pressure data. A merit function is used to evaluate each point in this four-dimensional parameter space

$$f = \int_{-6^\circ \text{aTDC}}^{40^\circ \text{aTDC}} \frac{|p_{\text{sim}}(CA) - p_{\text{exp}}(CA)|}{p_{\text{exp}}(CA)} dCA. \quad (6.1)$$

Case no.	SMR / μm	B_1	C	$d_{\text{eff}}/\mu\text{m}$	C_d	$f / \%$
Case 1	300	20	22.8	144.8	0.3	1.79
Case 2	400	20	27.4	167.2	0.4	1.82
Case 3	400	40	27.4	167.2	0.4	2.20
Case 4	400	40	27.4	167.2	0.4	2.36

Table 6.4: Optimal point in parameter space

The simulation time for evaluating the merit function is hence restricted from SOI to 40° aTDC. Only those five points which have the lowest merit function are considered as possible candidates to continue the simulation on the expansion cycle until EVO. The merit function itself is not a good criteria. Pressure data is only indirectly related to the spray model parameters. Spray data, e.g. the penetration length of liquid and gaseous phase, from an experimental spray characterization in a high-pressure, high-temperature chamber under diesel engine relevant conditions is a better criteria but seldomly provided by the nozzle supplier. If such data is available, spray model parameters could be calibrated as discussed in section 5.4 prior to the engine simulation. The final parameter sets are listed in Tab. 6.4. In all four cases, the effective nozzle diameter is found much smaller than the geometrical nozzle diameter of $264 \mu\text{m}$ yielding a discharge coefficient of 0.3 for case 1 and 0.4 for the other cases. Although these values seem to be too small in comparison to data from Siebers [189], the pressure trace and AHR is in a good agreement. By the artificial decrease of the nozzle hole area, parcels are initialized with a higher velocity and hence, the spray penetration and mixture formation is forced. These findings show that most difficulties in the engine simulation is contributed to the time-step and mesh dependence of the spray simulation. Adjustment of spray model parameters can compensate these dependencies. Therefore, a spray calibration is a proposed countermeasure but engine data is not sufficient.

6.2.5 Simulation Results

6.2.5.1 Pressure and Heat Release Data

Pressure traces and heat release rates from engine experiments are compared with the simulation results of the found optimum point. A good agreement is achieved for all four engine cases as shown in Fig. 6.4. The maximum pressure is well matched. Only for case 3 and 4 it is slightly over-predicted whereas the pressure traces for the compression and expansion cycle are in an excellent agreement again. Based on the pressure traces, the heat release rate is calculated. Engine and simulation data are presented in Fig. 6.5. After that auto-ignition has been occurred, no premixed peak

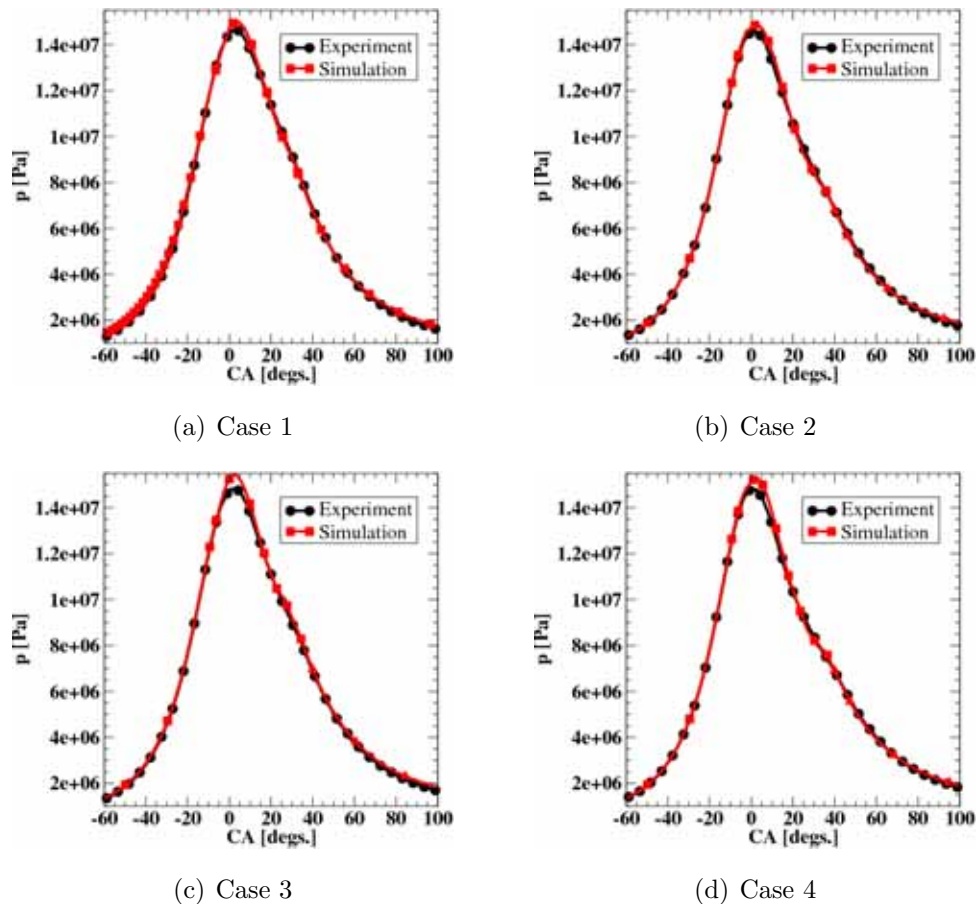


Figure 6.4: Comparison of measured and simulated pressure traces

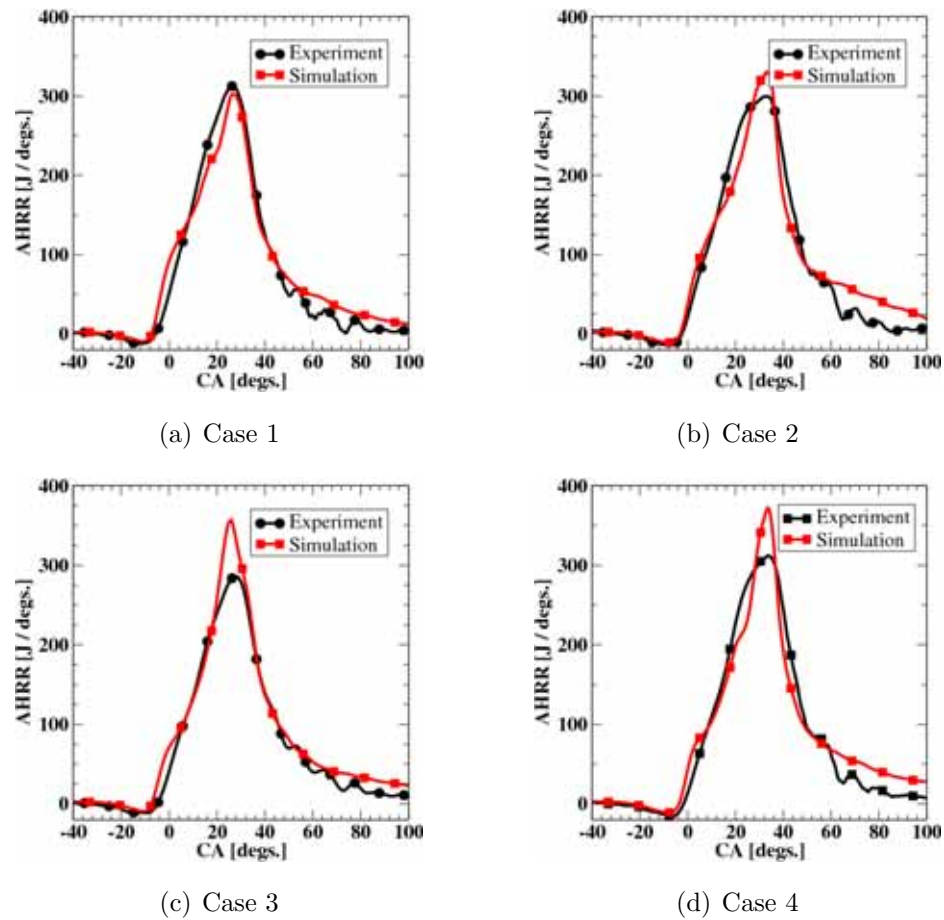


Figure 6.5: Comparison of measured and simulated heat release rate

is observed in all four examined cases. In general, the shape of the heat release rate is well matching and the ignition delay due to auto-ignition is well described by the chemical reaction mechanism. The maximum peak occurs at the right time but the magnitude is only in case 1 and 2 correct. In the case 3 and 4, the small difference of the pressure trace is magnified in the heat release rate. During, the expansion cycle, the experimental heat release rate reaches a smaller level and an offset of $20 \text{ J}/^\circ\text{CA}$ occurs in comparison to the heat release rate of the simulation.

6.2.5.2 Comparison of Emission Data

The comparison between computed and measured pollutant concentration at EVO in Tab. 6.5 shows an excellent agreement for NO_x emissions. Trends for the variation of spray angle and SOI are correctly calculated by the simulation. For SOI variation from -6 to -2° aTDC, less NO_x is formed for both spray angles. The variation of spray angle from 126° to 120° produces less NO_x for both injection timings.

The soot level at EVO is by a factor of 2.6 - 4 over-estimated. The current modeling of soot formation via the HACA (hydrogen-abstraction carbon-addition) mechanism can differ by a factor of 3 from experiments as found in [7]. More, the simulation of soot emissions is very sensitive to the mixing process with regard to the shape and location of the β -PDF and the overlapping area with the profile of the first soot moment in mixture fraction space. Thus the result of Eq. (3.30) is very sensitive to the profile of the β -PDF and therefore depending on the mixture formation which is controlled by the spray model. The calibration of the spray model with regard to pressure data involves uncertainties which may over-predict fuel-rich regions.

Regarding the trends of soot emissions, the variation in start of injection for case 1 and 2, and case 3 and 4 is not correctly calculated. Between case 1 and 2, the experiment shows the same amount of soot whereas the simulation indicates a small decrease of soot by 15%. For case 3 and 4, the trend is inverted and soot increases by 13% in the simulation whereas the experiment shows an decrease by 24%.

When the spray angle is decreased, the experiment shows an increase of soot by 97% and 49 % for both SOIs, -6 and -2° aTDC, respectively. The simulation has an increase of soot by 13% and 49 % for cases 1 and 3, and 2 and 4, respectively. Although absolute values are not matching, the simulation captures the trend of soot formation correctly.

6.2.5.3 Cycle Resolved Emission Data

In Fig. 6.6, the pollutants formation is shown as a function of crank angle. Until the end of injection (EOI), soot is formed in fuel-rich areas of the spray. After the injection has finished, soot is oxidized by OH and O radicals. As temperature decreases quickly,

Case	Soot / mg/m^3		NO_x / ppm	
	Experiment	Simulation	Experiment	Simulation
Case 1	7.3	33.6	662	660
Case 2	7.3	28.7	560	584
Case 3	14.4	37.9	579	565
Case 4	10.9	42.8	512	507

Table 6.5: Pollutant concentration in exhaust gas at EVO

the soot burn-out is retarded in the expansion cycle. For cases 2 and 4, the maximum soot level is about 50% and 29% higher than for the early injection times of cases 1 and 3. The variation of spray angle only indicates a small increase in the maximum soot level by 16 % for case 1 and 3 whereas for case 2 and 4, the soot level remains almost constant.

The NO_x emissions have its maximum after EOI at $50\text{-}55^\circ$ aTDC. For late injection timings, the maximum NO_x is 28% less than for case 1 and 2, and 23% for case 3 and 4, respectively. The variation in spray angle decreases the maximum NO_x by 20% for case 1 and 3, and 12% for case 2 and 4, respectively.

6.2.5.4 3D Temperature Field

A major benefit from the CFD simulation is the analysis of the data set on the computational mesh. In Fig. 6.7- Fig. 6.10, the temperature distribution on two different cut-planes from top- and diagonal views and the iso-surface of stoichiometric mixture, $Z_{\text{st}} = 0.065$, are colored by the temperature field at simulation times from -6 to 34° aTDC. The horizontal cut-plane in the top-view is 10 mm underneath the fire-deck. The spray parcels are colored by the parcel's temperature and equally sized.

Fig. 6.7 is at the beginning of the mixture formation when injection is starting. At -2° aTDC, auto-ignition has already been occurred but the temperature has not reached its maximum yet. The burning mixture penetrates the bowl and follows its shape until 26° aTDC in Fig. 6.9. The fuel-rich regions are already connected in Fig. 6.9

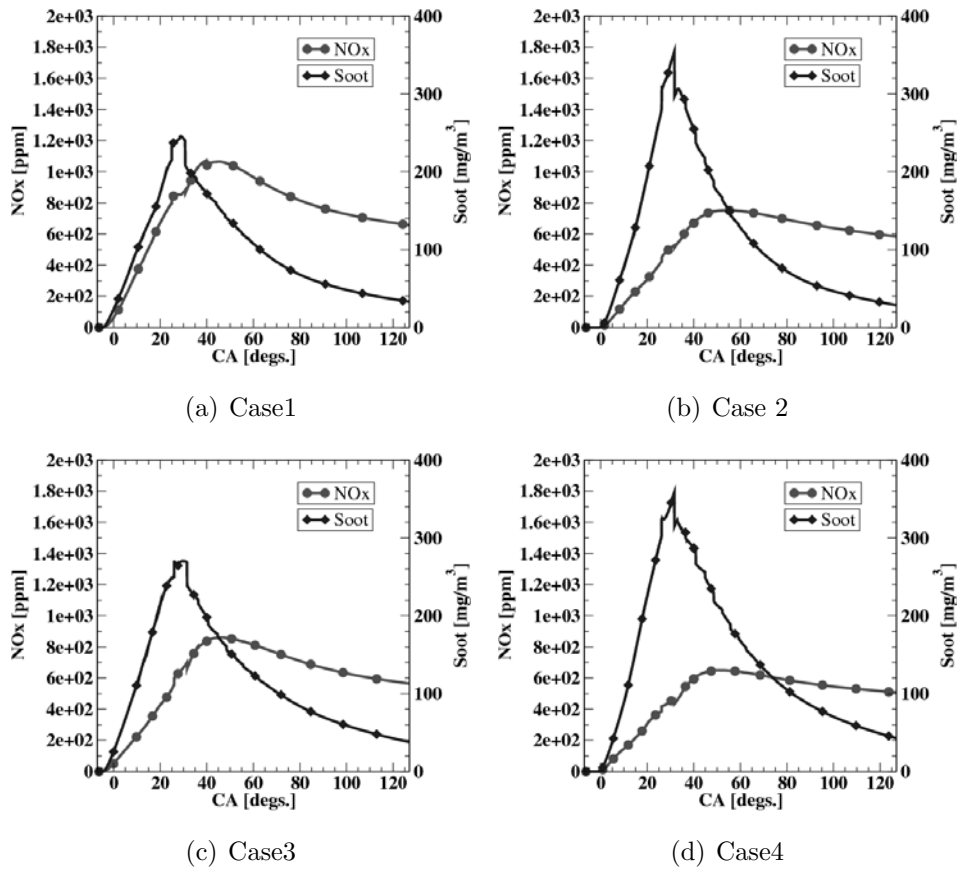
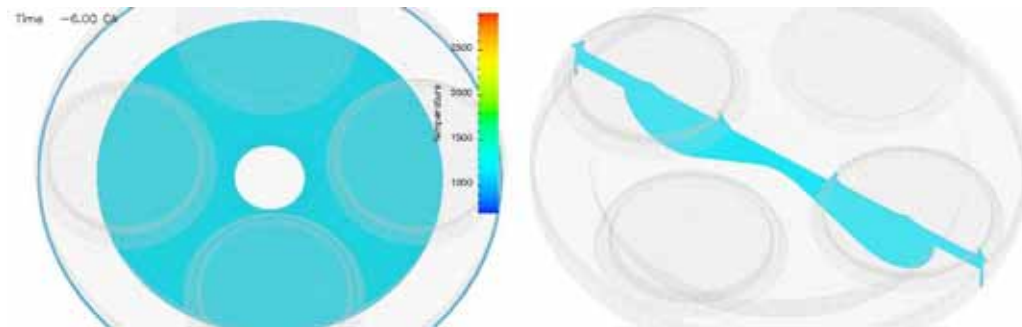
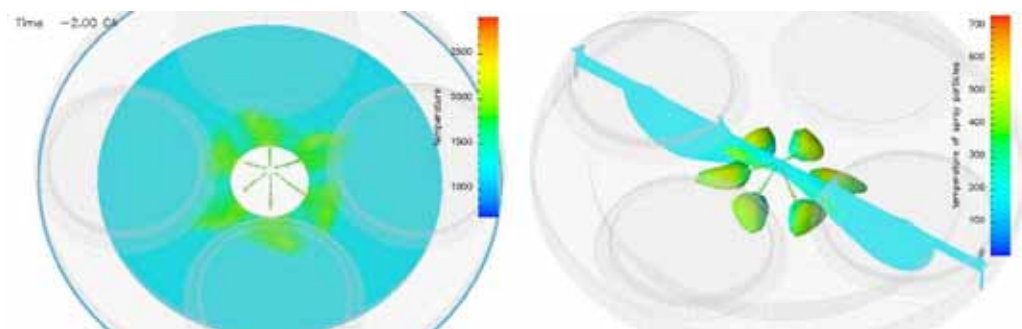


Figure 6.6: Cycle resolved emissions in simulation

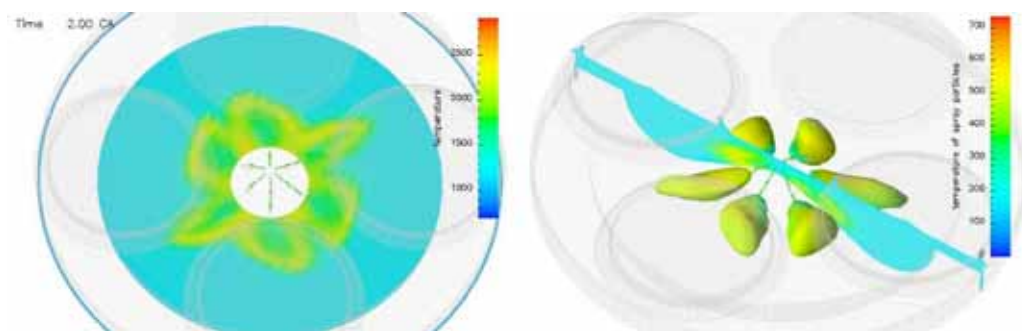
due to the swirl flow. High amounts of soot are produced in these fuel-rich areas. In Fig. 6.10, the fuel injection has ended but the temperature level is still high and fuel-rich regions exist but cannot burn-out completely.



(a) $t = -6^\circ$ aTDC



(b) $t = -2^\circ$ aTDC



(c) $t = 2^\circ$ aTDC

Figure 6.7: Analysis of 3D data set from simulation, temperature field and iso-surface of stoichiometric mixture

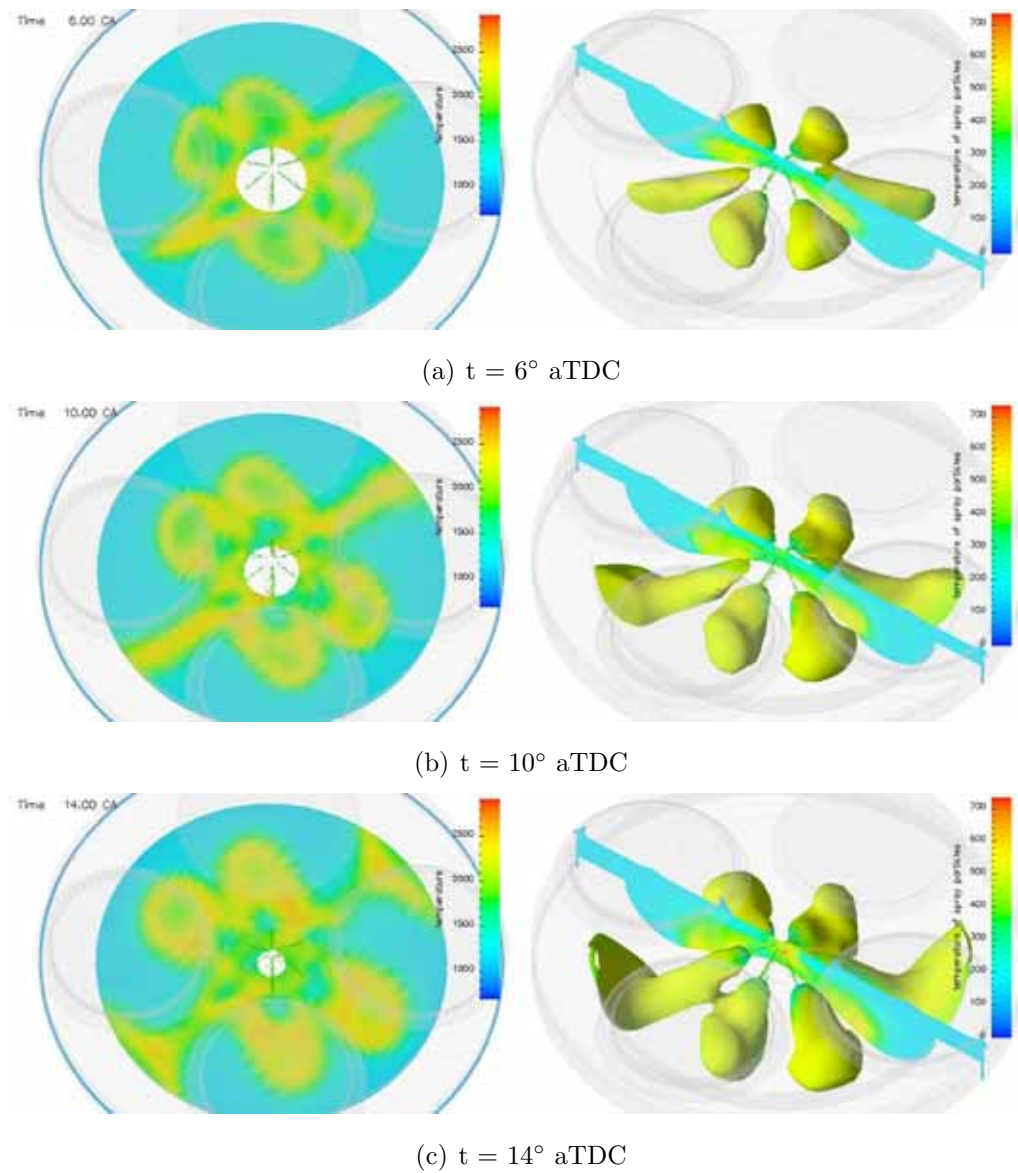
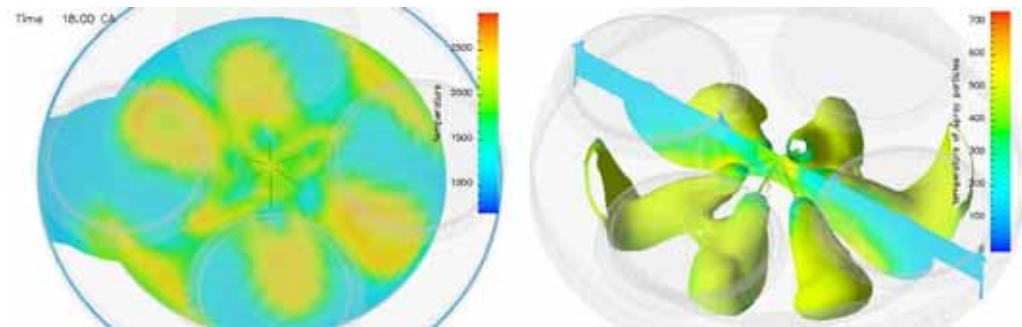
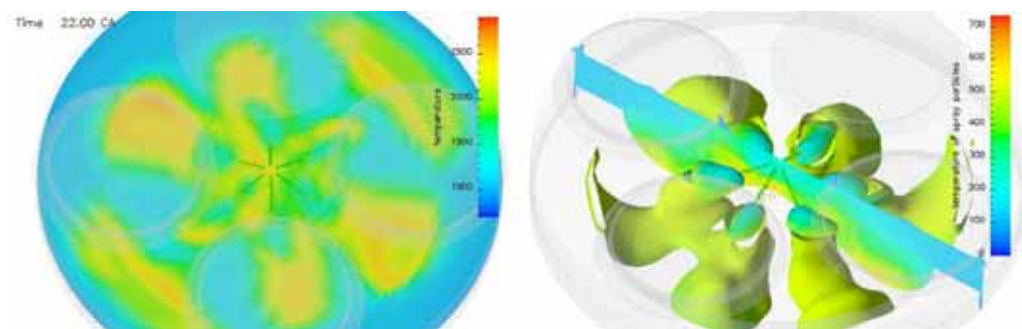


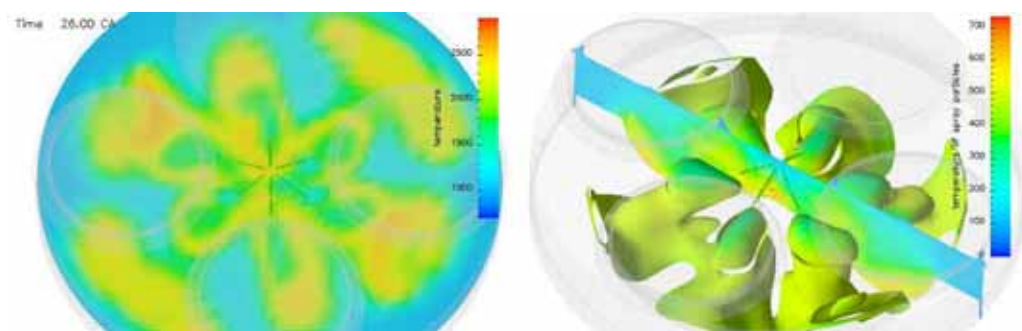
Figure 6.8: Analysis of 3D data set from simulation, temperature field and iso-surface of stoichiometric mixture



(a) $t = 18^\circ$ aTDC

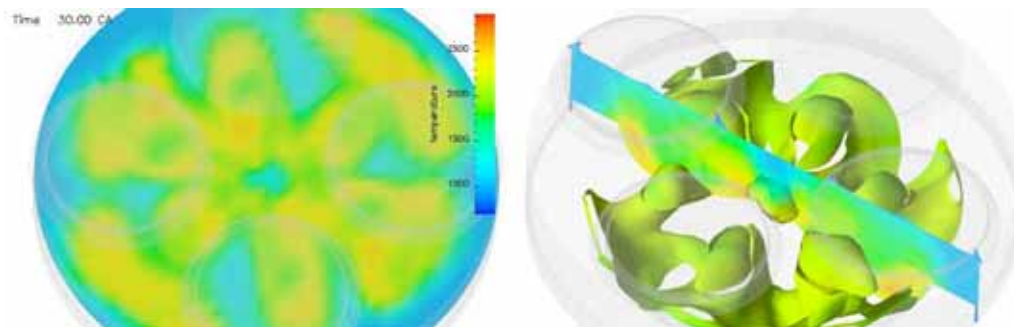


(b) $t = 22^\circ$ aTDC

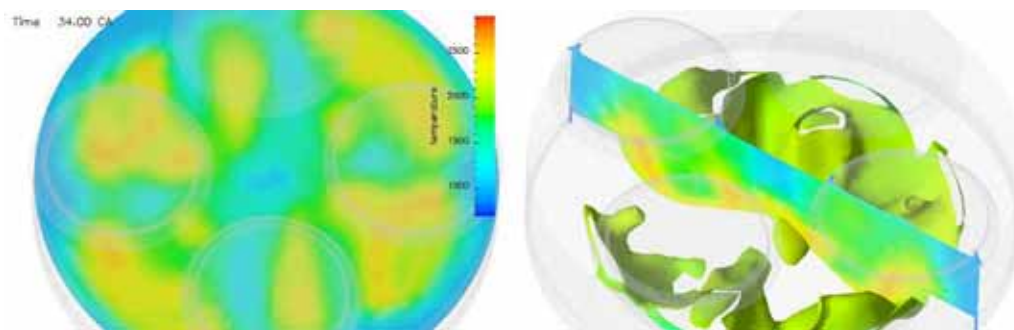


(c) $t = 26^\circ$ aTDC

Figure 6.9: Analysis of 3D data set from simulation, temperature field and iso-surface of stoichiometric mixture



(a) $t = 30^\circ$ aTDC



(b) $t = 34^\circ$ aTDC

Figure 6.10: Analysis of 3D data set from simulation, temperature field and iso-surface of stoichiometric mixture

6.3 Duramax Engine

6.3.1 Introduction

The Duramax 6600 V8 Diesel engine of GM in Fig. 6.11 is studied by the CFD simulation. The engine was re-built as a single-cylinder research engine. Two different combustion modes are investigated: a conventional combustion design with an sweep of start of injection and a premixed charge compression ignition (PCCI) combustion process using high rates of EGR. Similar to the previous engine case in section 6.2 spray parameters are again subject of adjustment for the conventional combustion mode because no spray data is available.



Figure 6.11: Duramax 6600 V8 Diesel engine of GM

6.3.2 Engine Set-Up

6.3.2.1 Specifications of the Duramax Engine

The specifications of the single-cylinder Duramax Diesel engine [192] are given in Tab. 6.6 while details of the multi-cylinder version of the engine and the common rail

fuel injection system are presented in [103, 144]. Particulate mass are calculated based

Displacement volume	0.825 l/cyl.
Bore	103 mm
Stroke	99 mm
Connecting rod length	188 mm
Offset	0.5 mm
Compression ratio	16:1
Squish height	0.7 mm
Swirl ratio	1.5
Injector tip	VCO
No. of tip holes	7
Hole diameter	144 μ m
Volumetric flow rate	490 cm ³ /30s@100 bar

Table 6.6: Specifications of Duramax engine

on the filter smoke number (FSN). The FSN numbers are readings from the AVL smoke meter "Model 415" and the emission index of dry soot in g/kg fuel is calculated in Eq. (6.2) for the "MIRA" correlation that was developed by a European research organization

$$\text{MIRA_Dry_Soot_Mass} = A \times \left[\frac{\text{AFR} + 1}{1000} \right]. \quad (6.2)$$

where AFR is the air-fuel ratio. A is a correlation factor that depends on the FSN number as

$$A = 0.0307 \times \text{FSN}^5 - 0.00669 \times \text{FSN}^4 - 0.702 \times \text{FSN}^3 + 14.621 \times \text{FSN}^2 + 7.363 \times \text{FSN}. \quad (6.3)$$

6.3.2.2 Mesh Generation for CFD-Simulation

The simulation of the engine is carried out on a sector mesh with a one quarter O-grid topology due to the symmetry of the injector located on the cylinder axis. For the

applied 7-hole nozzle, a sector angle of 51.4° is applied. Valve recess or piston cut-outs are not included. The created mesh is shown in Fig. 6.12. The mesh resolution is

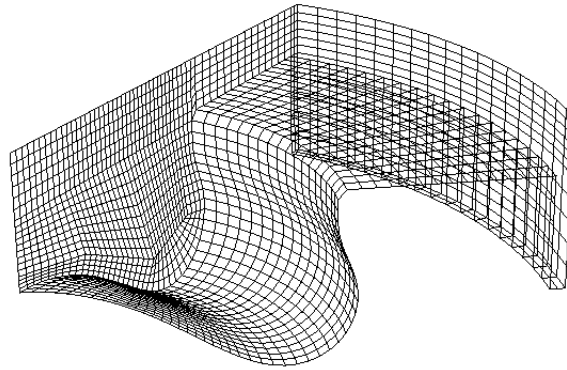


Figure 6.12: Sector mesh of the Duramax engine

about 0.9 mm in radial direction and 1.5 mm in azimuthal direction, respectively. For the bowl region, a cell height of 1.2 mm is achieved whereas for the in-cylinder region, a cell-layer removal algorithm similar to that of KIVA[4], denoted as "snapper" is applied in order to avoid a bad cell-aspect ratio during the mesh motion. The piston top land is resolved by a mean cell-height of 2.3 mm and width of 0.75 mm. The simulation starts at intake valve closure (IVC) where 45 cell-layers are used so that a cell-height of 2 mm is achieved in z-direction. A total number of 74,110 cells on the sector mesh are given at IVC. At TDC, a minimum number of 6 cell-layers is prescribed to resolve gradients in regions close to the cylinder head correctly.

6.3.3 Conventional Combustion Mode

A conventional combustion strategy is applied on the Duramax engine at a full load operating point and medium speed. The full load point requires a very fast injection of the fuel quantity which can be realized by a high rail pressure as seen from Tab. 6.7. The start of injection occurs close to TDC and is varied in a narrow range from -8 to

-5° CA aTDC with a conventional spray angle of 154°.

6.3.3.1 Operating Point

Speed	3100 1/min
IMEP _{dyno}	1632 kPa
MMEP _{multi}	437 kPa
BMEP _{multi}	1195 kPa
Manifold Pressure	244 kPa
Start of injection	-8, -7, -6.5, -6 and -5° CA aTDC
Injection duration	20.65 CA
Injection quantity	74.2 mg/cyl.
Included spray angle	154°
Rail pressure	1600 bar
Diesel Fuel cetane number	49.6
Intake valve closure (IVC)	-138° CA aTDC
Exhaust valve opening (EVO)	129° CA aTDC

Table 6.7: Operating conditions on the Duramax 6600 Diesel engine

6.3.3.2 Combustion Analysis

The comparison between the engine data and the simulation includes the analysis for pressure trace, apparent heat release rate (AHRR), accumulative heat release (AHR) and derived gas mean temperature. The engine pressure data shows some small oscillations which are amplified in the heat release rate analysis calculations since no filtering functions have been applied.

On the simulation, all three presented reaction mechanisms nDaMV1, nDaMV3.1 and nDaMV3.5 that have been presented in section 3.5.1 are used. The data is compared in Fig. 6.13 - Fig. 6.17 for every injection timing individually. The ignition delay from the AHRR in Fig. 6.13(c) - Fig. 6.17(c) is computed correctly and the maximum pressure

of the simulation is in agreement with the engine data in Fig. 6.13(a) - Fig. 6.17(a). In the expansion cycle, the pressure trace decreases by a shift of 3° CA earlier in the simulation than the measured data shows. That discrepancy in pressure trace results in a lower gas temperature (Fig. 6.13(b) - Fig. 6.17(b)) and a lowered accumulative heat release (Fig. 6.13(d) - Fig. 6.17(d)) and equivalent a shifted apparent heat release rate (Fig. 6.13(c) - Fig. 6.17(c)). It is not quite clear what causes this discrepancy in the expansion cycle. The spray parameters have been adjusted with respect to the maximum pressure peak and ignition delay. Spray parameters that showed a better agreement in the expansion cycle had a much higher peak pressure and were rejected.

6.3.3.3 Engine-Out Emissions

Engine emissions in the exhaust gas are compared with the results from the simulation at exhaust valve opening. In the simulation, the lower gas temperature of the simulation results in lower NO_x emissions as shown in Fig. 6.18(a) by a factor of 2.3 in comparison to the engine data. NO_x formation is mostly controlled by the temperature and originates from thermal NO_x . The three different reaction mechanisms show the same trend as observed for the engine data. With increasing SOI, NO_x emissions are decreasing. The initial version nDaMV1 has slightly higher NO_x emissions as the modified mechanisms nDaMV3.1 and nDaMV3.5.

The soot emissions are compared in Fig. 6.18(b). For all three mechanisms the same trend is observed. With increasing SOI the soot emissions in the engines are slightly increasing. The simulation confirms this trend. However the level of soot emissions of the simulation underestimates the engine data by 30%. The comparison of CO emissions in Fig. 6.19(a) and CO_2 emissions in Fig. 6.19(b) of simulation and engine data does not agree very well. On the engine side, the SOI variation does not show any effect on the emission index of CO and CO_2 because all fuel is injected close to TDC and completely converted. The conversion close to TDC is independent from the SOI and only phased in time. In the simulation, CO is slightly increasing whereas CO_2 is slightly decreasing with increasing SOI. From the low gas temperature and low heat release it may be concluded that the fuel is not completely converted. The analysis in

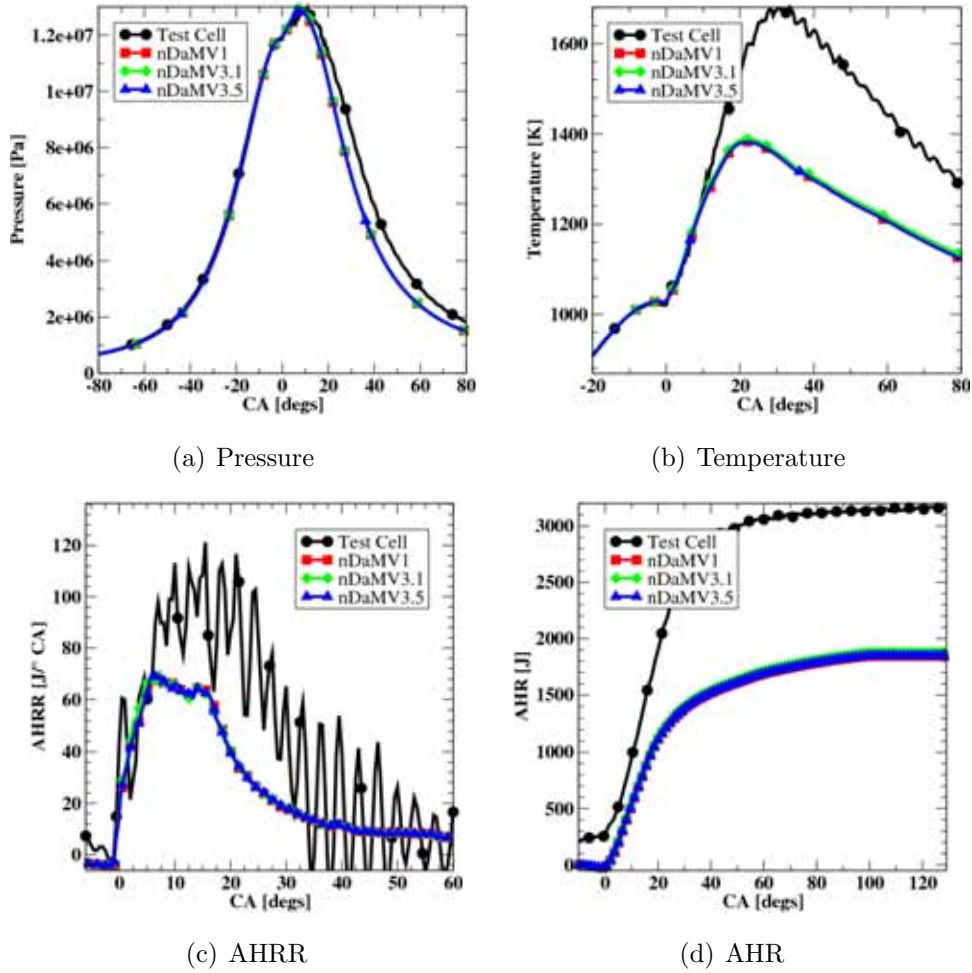


Figure 6.13: Comparison of simulation with engine data at SOI -8° CA aTDC

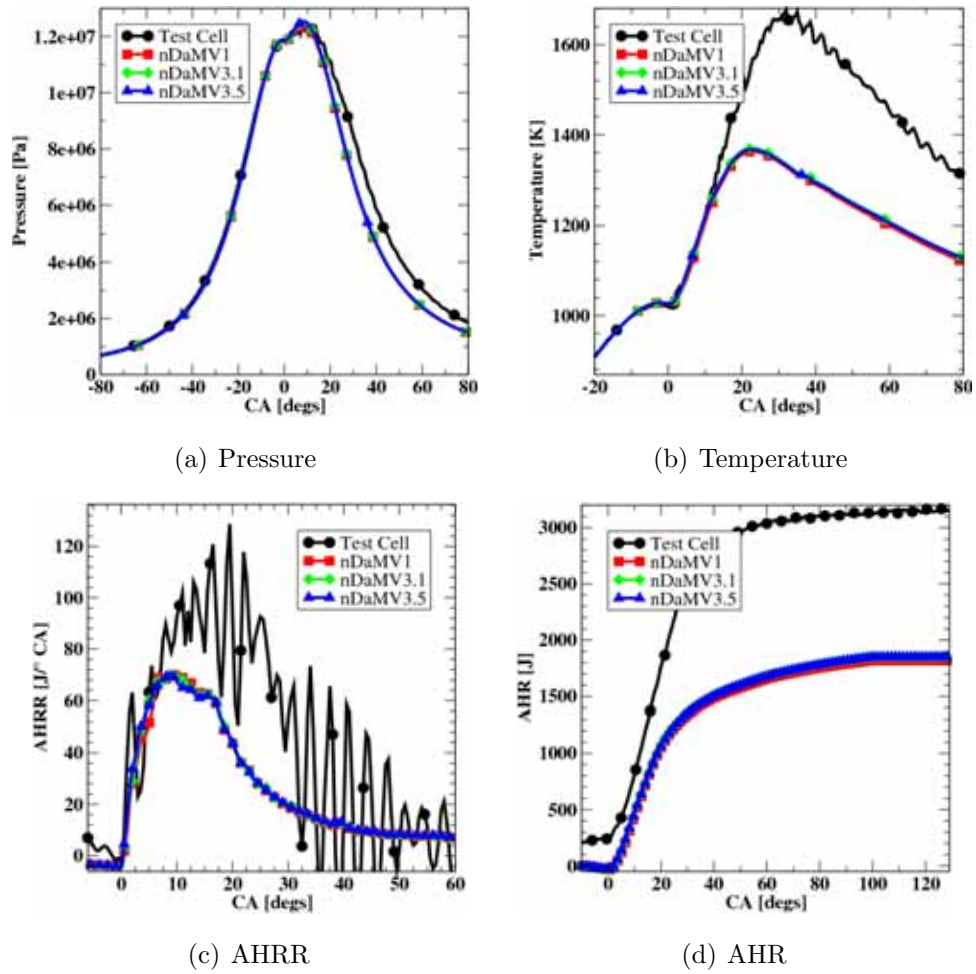


Figure 6.14: Comparison of simulation with engine data at SOI -7° CA aTDC

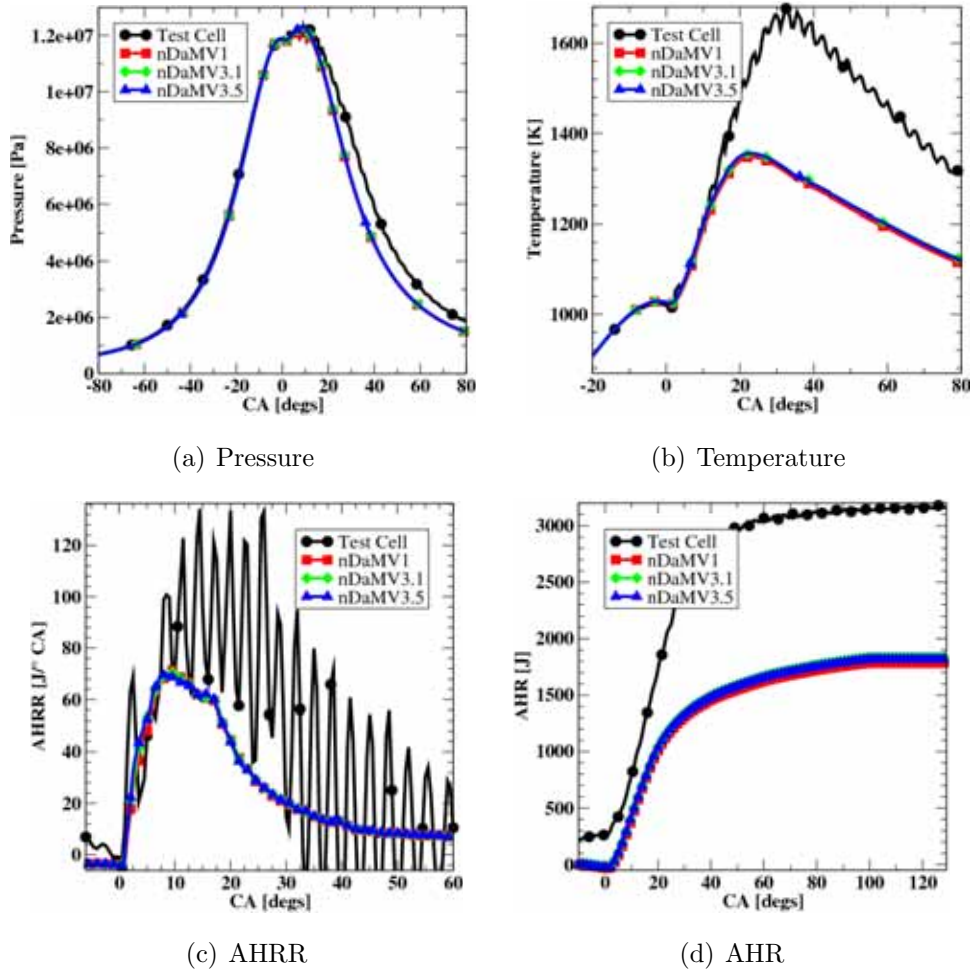


Figure 6.15: Comparison of simulation with engine data at SOI -6.5° CA aTDC

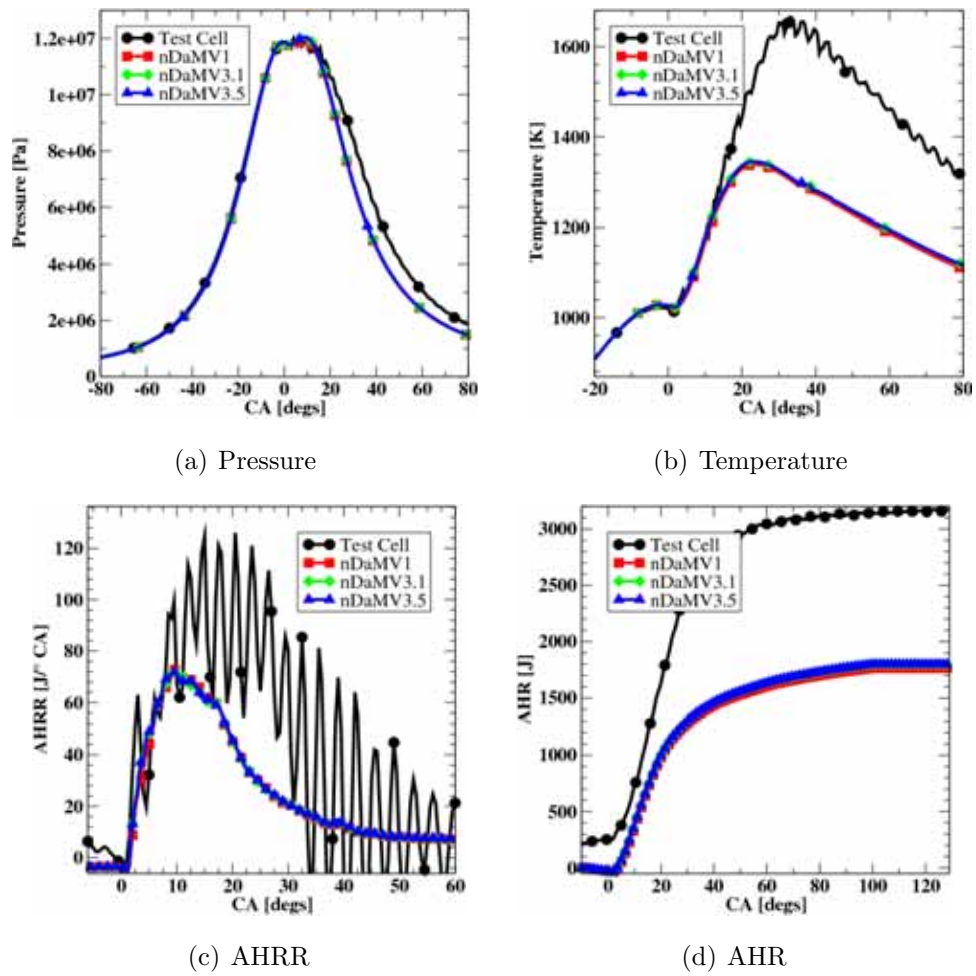


Figure 6.16: Comparison of simulation with engine data at SOI -6° CA aTDC

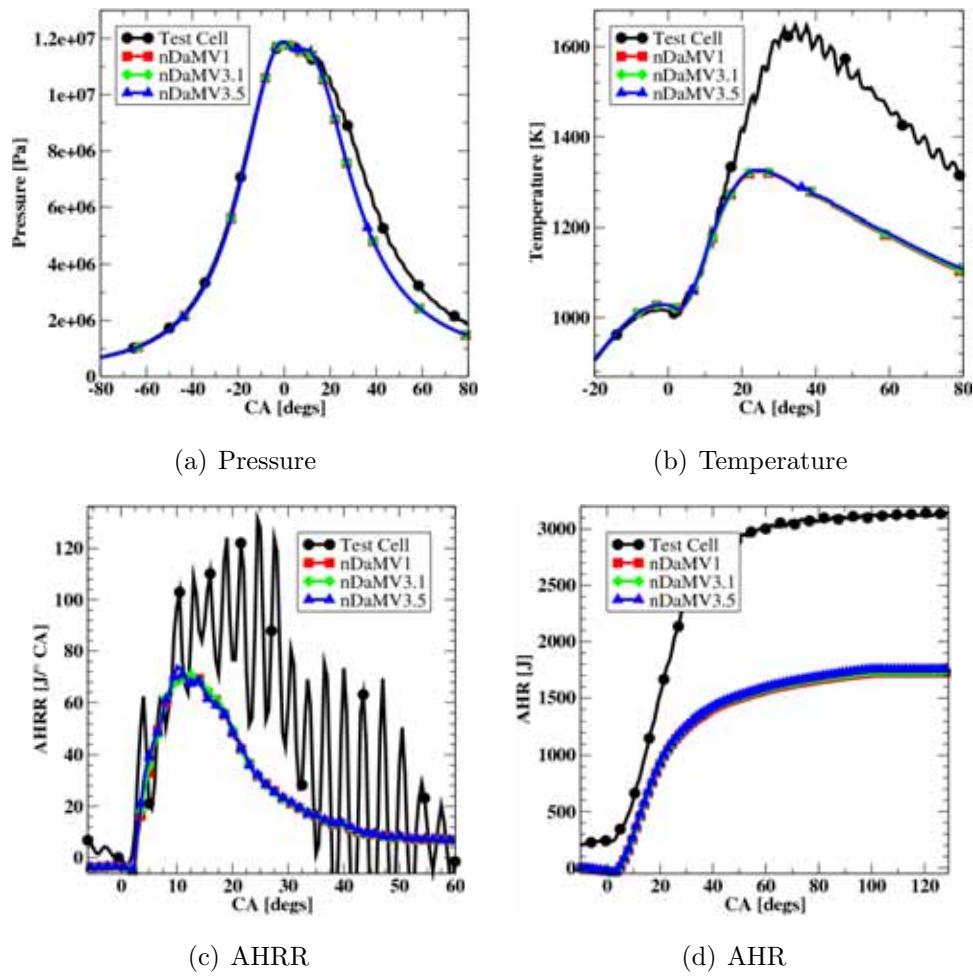


Figure 6.17: Comparison of simulation with engine data at SOI -5° CA aTDC

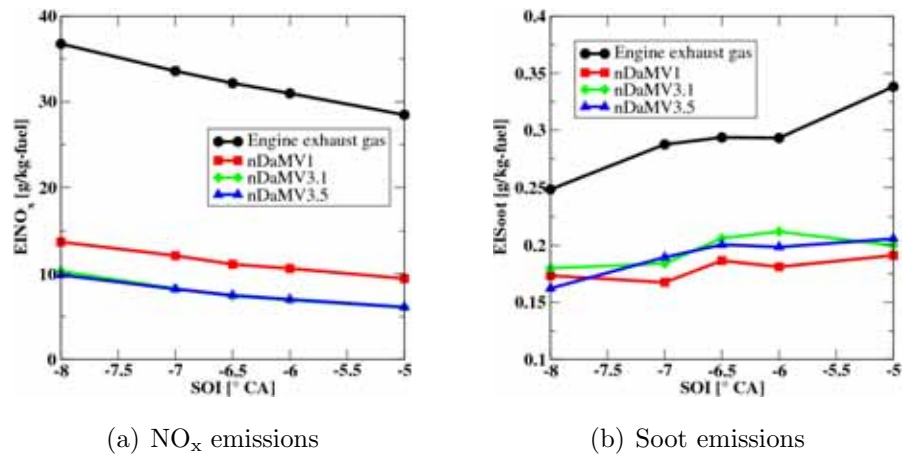


Figure 6.18: Comparison of soot and NO_x emissions from exhaust gas analysis and simulation at EVO

Fig. 6.20 indicates that fuel-wetting on walls occurs. The fuel that is assigned with the wall-film is not completely vaporized and converted. Thus, CO emissions are higher and CO₂ is lower in comparison to the engine data.

Emissions of UHC in Fig. 6.21 are by a factor of 4 for mechanisms nDaMV3.1 and

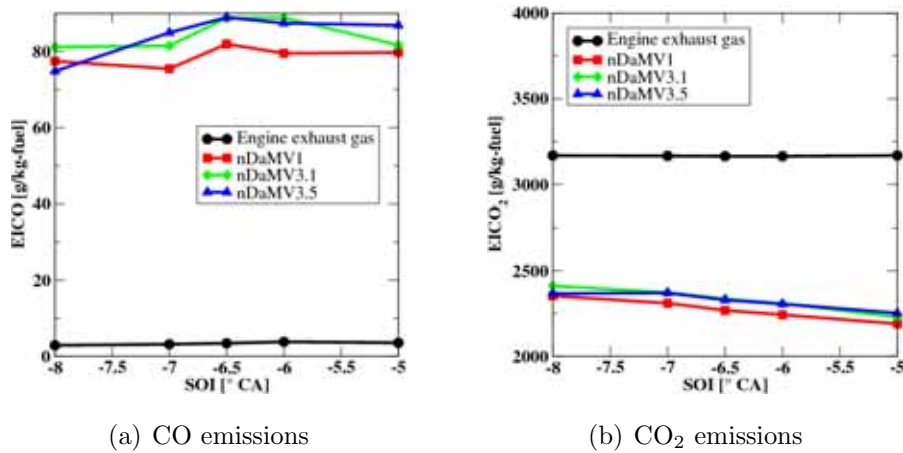


Figure 6.19: Comparison of CO and CO₂ emissions from exhaust gas analysis and simulation at EVO

nDaMV3.5 higher than for the engine data. The initial mechanism nDaMV1 has a better performance and only overestimates the engine data by a factor of 3. Similar as

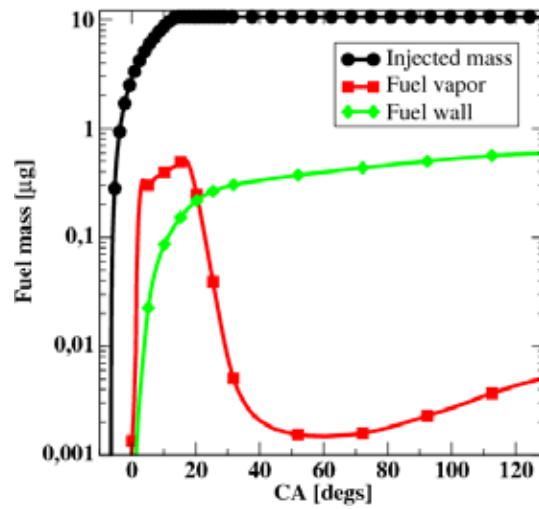


Figure 6.20: Spray analysis of fuel-wetting on walls

for CO and CO₂, high amounts of fuel-wetting are an explanation of this overestimation. Also, UHC emissions from engine data are nearly constant for the SOI variation whereas in the simulation, UHC increases slightly for later injection times.

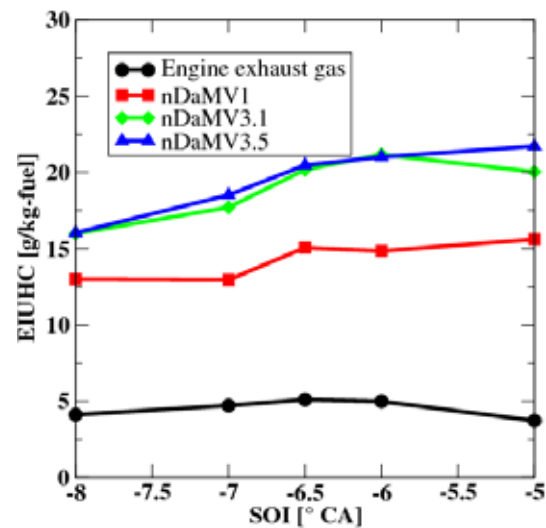


Figure 6.21: Comparison of UHC between simulation and exhaust gas analysis

6.3.4 Premixed Charge Compression Ignition Combustion Mode

One approach to reduce the emissions in a Diesel engine is the premixed charge compression ignition (PCCI) combustion mode which is studied in this section. PCCI has been studied over the past years by many researchers in engine experiments [193, 109, 145, 203, 90, 101, 136, 8, 43, 77] and simulation studies [178, 1, 105, 198]. The basic idea of PCCI is to enhance mixing and evaporation by an early fuel injection in the compression cycle before TDC. The injection system and the mixture formation are an effective mean to control the emissions because combustion is controlled by mixing as noted in [160, 158]. In the case of part-load conditions, early injection strategies are offering the possibility to enhance the mixing and evaporation process prior to the auto-ignition of Diesel fuel. Due to the early injection, ignition and evaporation are separated in time and space. As a result, less fuel-rich pockets are occurring from where soot is formed. The simultaneous reduction of NO_x can be achieved by the use of cooled EGR which dilutes the intake charge. The combustion is shifted to lower temperatures and less NO_x is formed. The conditions at start of injection (SOI) are very important for the ignition process. Above a rate of 50% EGR, the gas temperature is below 850 K as seen from Fig. 6.22. Mixing of the fresh air with EGR increases the heat capacity and density as shown in Fig. 6.23. Both effects are leading to a decrease in temperature. Therefore, ignition is retarded to later times and the evaporation time is enhanced. The concept of PCCI combustion is not applicable to all operating conditions. If higher amounts of fuel are injected, the start of injection has to be advanced to earlier times in order to separate the ignition and evaporation process but is limited by the nozzle design. Fuel-wetting on the liner due to spray-wall interactions has to be avoided by applying a narrow spray angle as proposed and studied in [204, 77, 106, 77]. The narrow spray angle limits the system only to early injection events and is not suitable to conventional combustion mode at high loads. The additional use of EGR is another mean to shorten the spray penetration, as observed in [106] and in [192] where moderately narrow spray angles are investigated, to prevent the fuel-wetting of the liner.

Another major benefit of EGR is to dilute the mixture by which soot and NO_x can be simultaneously reduced [202, 138]. Both, the reduction of soot and NO_x , is a goal that

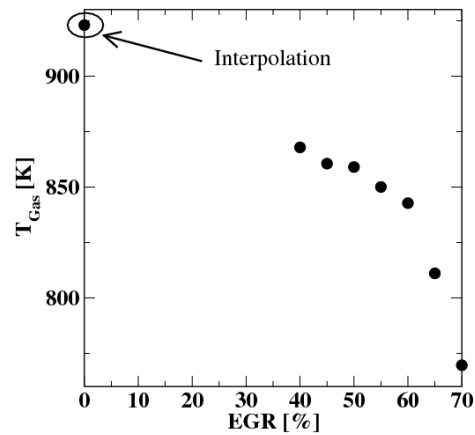
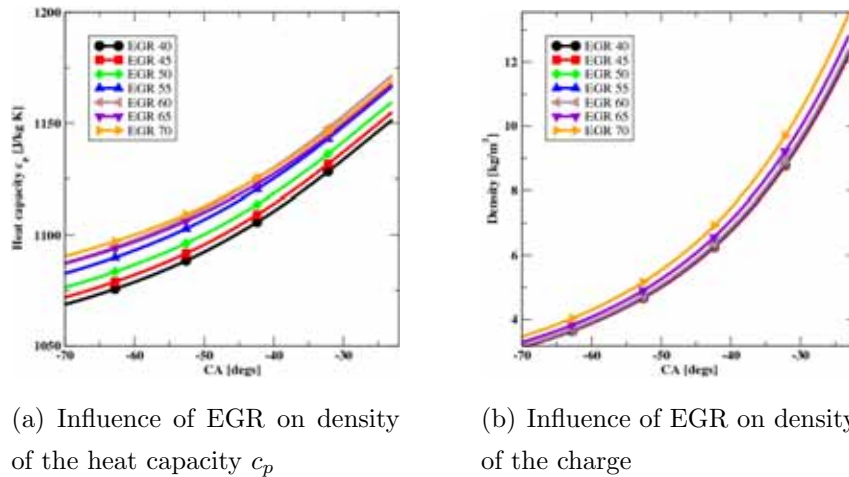


Figure 6.22: Influence of EGR on gas temperature at SOI



(a) Influence of EGR on density of the heat capacity c_p

(b) Influence of EGR on density of the charge

Figure 6.23: Influence of EGR on charge

has to be achieved and the PCCI combustion mode offers a solution. Limits of the PCCI combustion mode are given from the separation of evaporation and ignition and the amounts of EGR that can be applied. At high amounts of EGR, the combustion becomes unstable and miss-firing occurs due to a decrease of oxygen content [143]. For the present work, the combustion mode of PCCI is studied by the CFD simulation and compared to engine data from the Duramax 6600 Diesel engine. In the simulation, all three chemical reaction mechanisms nDaMV1, nDaMV3.1 and nDaMV3.5 are investigated in the low temperature combustion mode.

Although the flamelet approach has been applied successfully in the past to the conventional Diesel combustion, the effect of early mixing and homogenization is accounted by small values of the scalar dissipation rate so that it is as well applied to the PCCI combustion mode as demonstrated in [79, 88]. The effect of EGR on the combustion is accounted by adding carbondioxide and water as additional species on the initial flamelet solution as a boundary condition at $Z = 0$.

6.3.4.1 Operating Point

The part load operating conditions used in this study are given in Tab. 6.8. This particular load and speed would be heavily weighted for a 3,400 kg test weight vehicle on the US chassis-dynamometer FTP. The main parameter that is investigated is the variation of EGR from 40 to 70% in steps of 5%. In the simulation, EGR is assumed to comprise water and carbondioxide only. Other intermediate species cannot be considered since no analysis of the EGR composition is available.

6.3.4.2 Combustion Analysis

Influence of EGR on Pressure Trace Large amounts of EGR leads to a decrease in pressure peak at later times and a retarded pressure rise as it is shown in Fig. 6.31(a) for the engine and Fig. 6.31(b) for the simulation results with mechanism nDaMV3.5. The comparison of individual pressure traces between the engine data and the simulation is presented in Fig. 6.24 - Fig. 6.30 for all individually rates of EGR. At medium rates between 40 - 55 %, the pressure traces agree excellent. At higher EGR rates, the simulation has a smaller peak pressure than in the engine. The difference at EGR rates of 60% and 65% is small but the highest EGR rate of 70% shows a difference of about 20% for the new mechanism nDaMV3.5. nDaMV3.1 has a little smaller pressure peak and for nDaMV1 it seems that no combustion occurs. The disagreement at high EGR rates for nDaMV3.5 is not necessary unphysical as the comparison between Diesel and IDEA fuels shows in engine experiments in [211] but not as high as reported here.

Speed	1891 rpm
IMEP _{dyno}	464 kPa
MMEP _{multi}	140 kPa
BMEP _{multi}	324 kPa
Manifold pressure	150 kPa
Mixture temperature	120 °C
Start of injection	-22.3° CA aTDC
Injection duration	10° CA
Injection quantity	74.2 mg/cyl.
Included spray angle	105°
Variation of EGR	40 - 70 %
Rail pressure	1200 bar
Intake valve closure (IVC)	-138° CA aTDC
Exhaust valve opening (EVO)	129° CA aTDC

Table 6.8: Part load operating conditions in the Duramax 6600 Diesel engine for a PCCI combustion mode

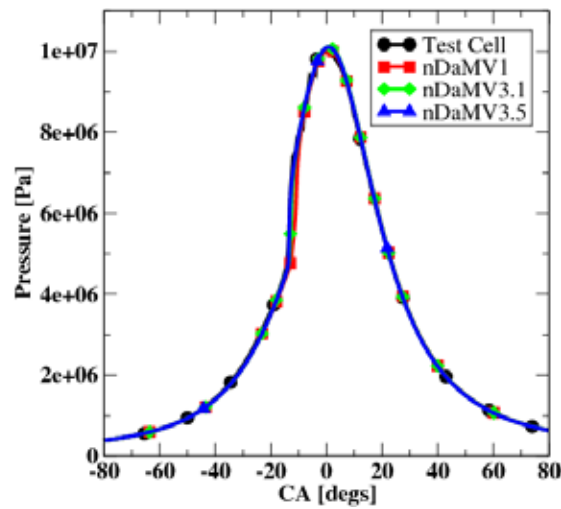


Figure 6.24: EGR 40% case, pressure trace for engine and simulation

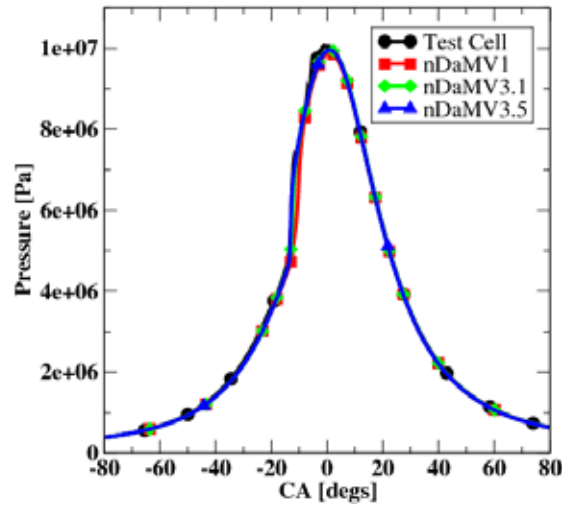


Figure 6.25: EGR 45 % case, pressure trace for engine and simulation

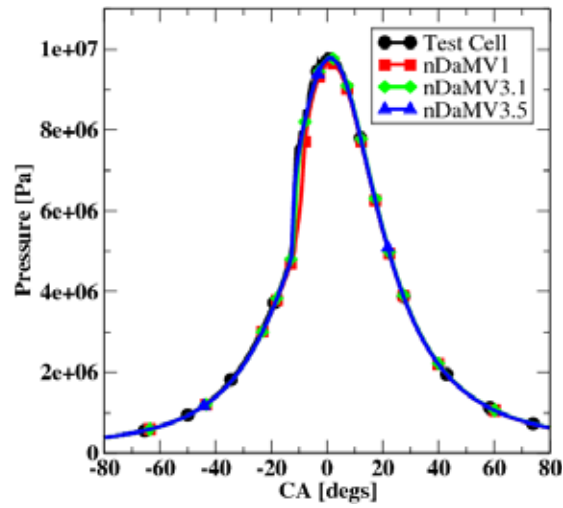


Figure 6.26: EGR 50% case, pressure trace for engine and simulation

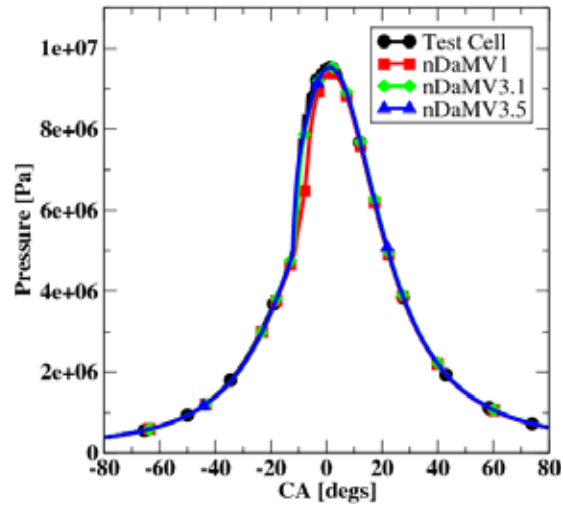


Figure 6.27: EGR 55 % case, pressure trace for engine and simulation

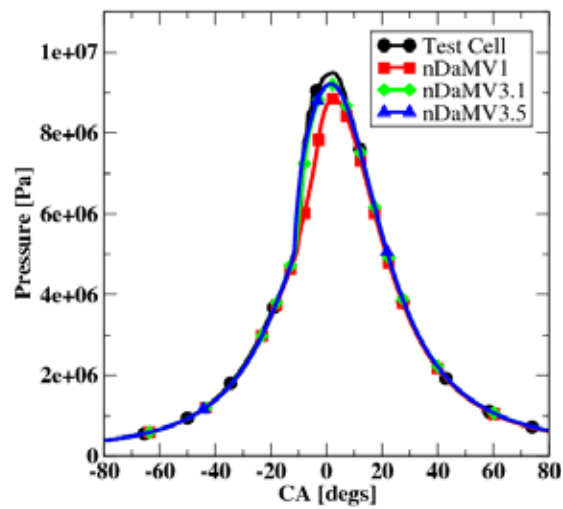


Figure 6.28: EGR 60% case, pressure trace for engine and simulation

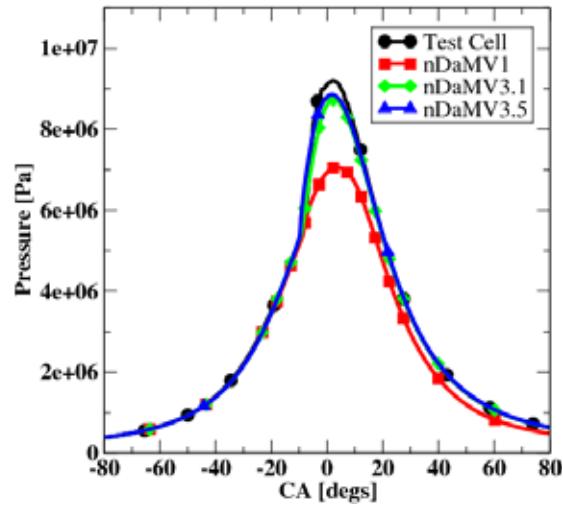


Figure 6.29: EGR 65 % case, pressure trace for engine and simulation

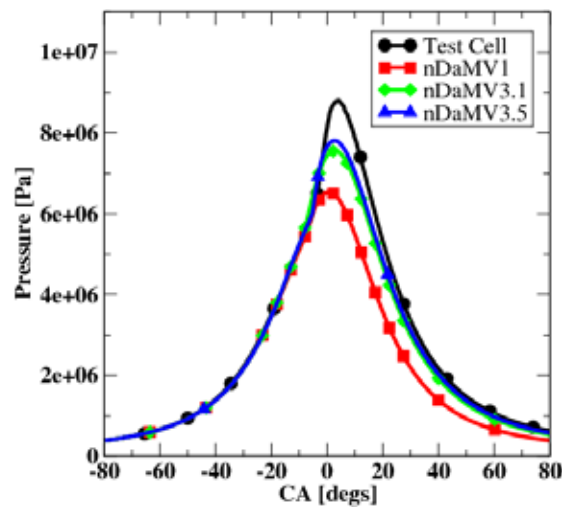


Figure 6.30: EGR 70% case, pressure trace for engine and simulation

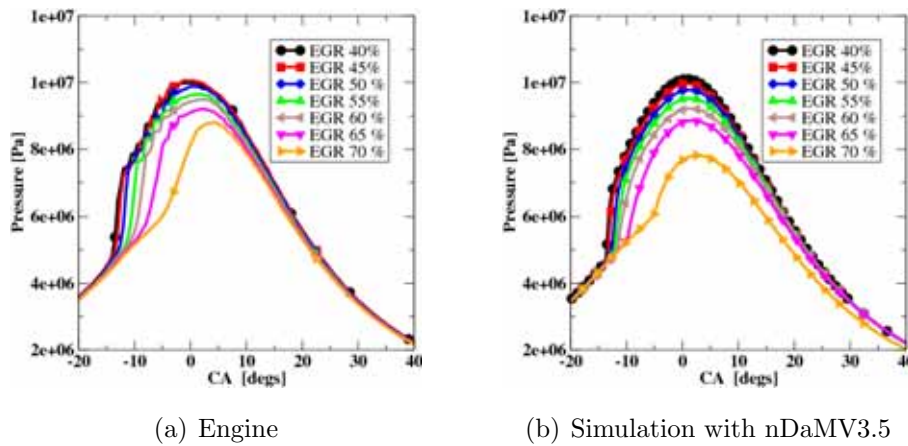


Figure 6.31: Influence of EGR on pressure

Influence of EGR on Heat Release Rate The influence of EGR on ignition delay is studied from the analysis of the apparent heat release rate (AHRR) as given in Fig. 6.32 - Fig. 6.38. The addition of EGR reduces the heat-release and retards ignition to later times as the comparison between experiment and simulation shows in Fig. 6.39(a) and Fig. 6.39(b). For EGR rates between 40 and 50%, only the new mechanisms nDaMV3.5 and nDaMV3.1 are in a reasonable agreement with the engine data. An unphysical behavior is observed for mechanism nDaMV1 which first shows a longer ignition-delay but suddenly the AHRR decreases and re-increases again. At higher EGR rates of 55 and 70%, ignition occurs in the engine at later times than in the simulation. nDaMV3.5 ignites much faster than nDaMV3.1 and nDaMV1 as previously seen in the homogeneous reactor calculations in Fig. 3.7.

Regarding the maximum peak level of AHRR, the simulation data with nDaMV3.1 and nDaMV1 do not agree with the engine data. Only nDaMV3.5 has a correct order of magnitude of AHRR at high EGR rates but is first over-estimating the AHRR of the engine at rates of 40 and 45% before under-estimating at a rate of 70%. Here, nDaMV1 and nDaMV3.1 do not ignite at all. Even at lower rates, these mechanisms show a poor heat release whereas nDaMV3.1 performs better than nDaMV1.

The first smooth increase of AHRR in the engine can be contributed to the premixed burning of the fuel-air mixture. However, that smooth increase is not captured by the simulation.

It should be noted that the engine and simulation heat release data is not calculated by the same tool. Thus, it cannot be answered if some of the discrepancies may also be addressed to the calculation method that has been applied.

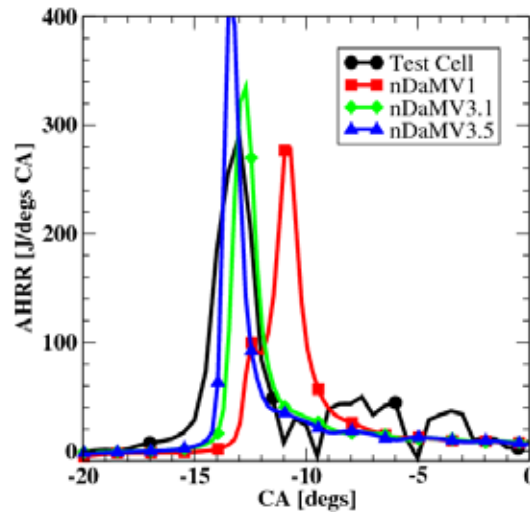


Figure 6.32: EGR 40% case, AHRR for engine and simulation

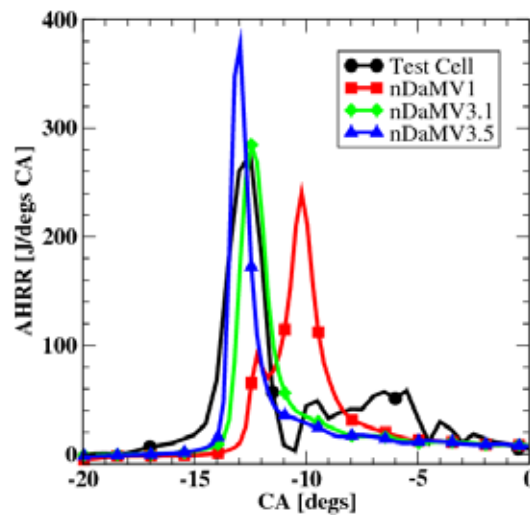


Figure 6.33: EGR 45 % case, AHRR for engine and simulation

Influence of EGR on Gas Temperature The thermodynamical analysis of the engine pressure data allows to derive a mean gas temperature which is compared in Fig. 6.40

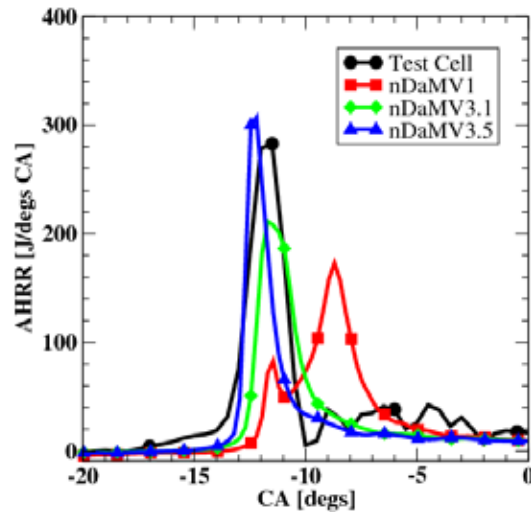


Figure 6.34: EGR 50% case, AHRR for engine and simulation

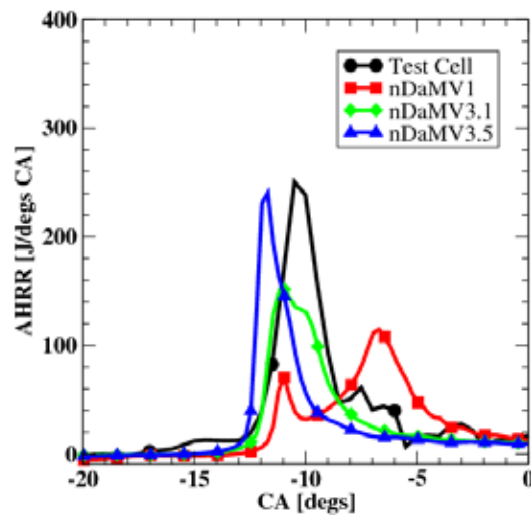


Figure 6.35: EGR 55 % case, AHRR for engine and simulation

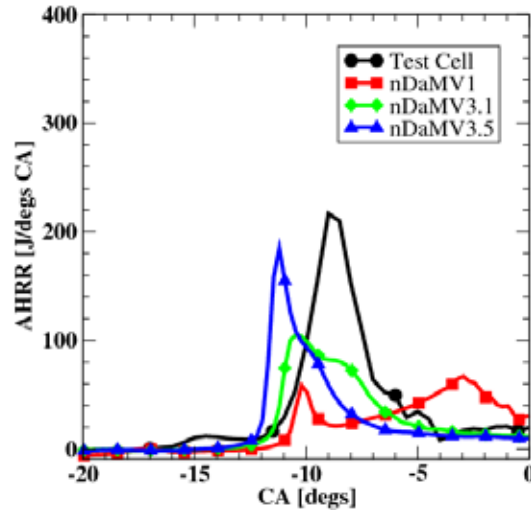


Figure 6.36: EGR 60% case, AHRR for engine and simulation

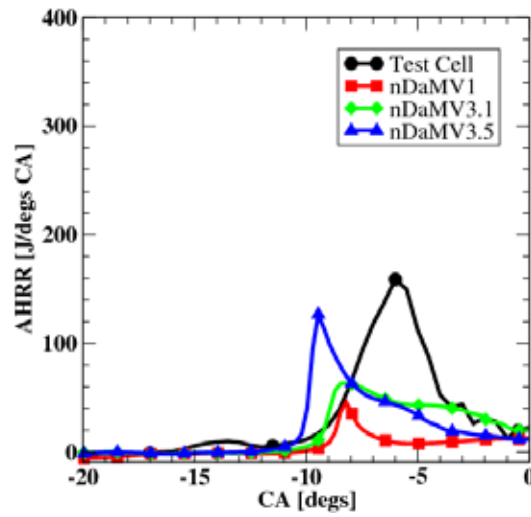


Figure 6.37: EGR 65 % case, AHRR for engine and simulation

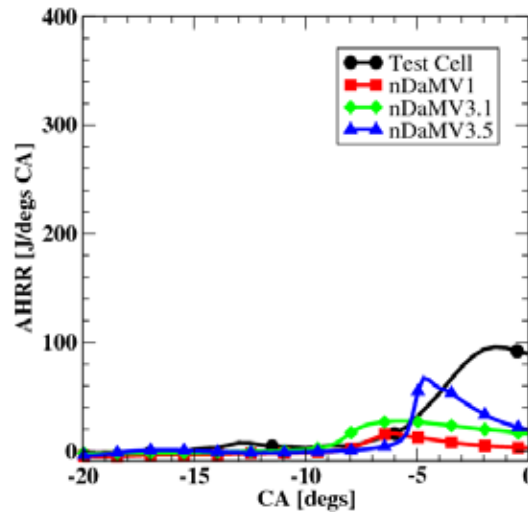
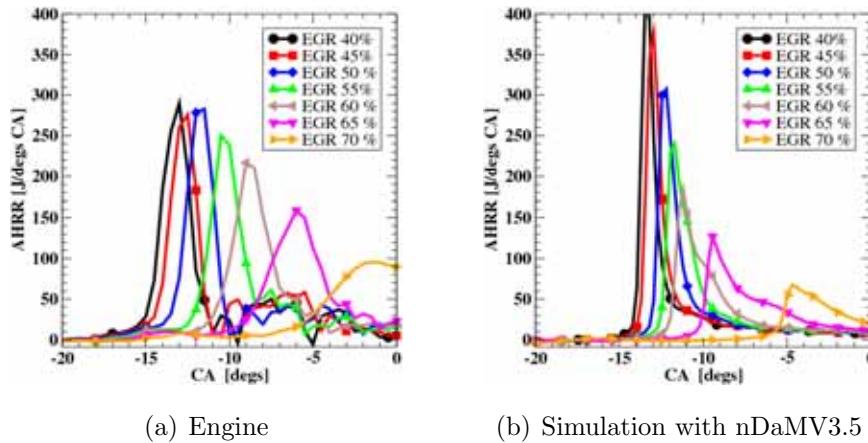


Figure 6.38: EGR 70% case, AHRR for engine and simulation



(a) Engine

(b) Simulation with nDaMV3.5

Figure 6.39: Influence of EGR on AHRR

- Fig. 6.46 with the temperature in the simulation for all three mechanisms. The simulation shows a good agreement for EGR rates between 40 and 60% for the new mechanisms nDaMV3.5 and nDaMV3.1. The original mechanism has a less steeper temperature gradient. At 60% EGR, the maximum temperature of nDaMV1 is already smaller than for nDaMV3.5 and nDaMV3.1. Similar to the pressure, that difference is not necessary an unphysical result. At high EGR rates of 65 and 70%, the simulation underpredicts the maximum temperature of the engine data. As for the pressure and AHRR traces, the new mechanism performs better than nDaMV3.1. The original

mechanism nDaMV1 differs significantly from the engine data and does not show any sufficient increase in the mean gas temperature.

The effect of EGR on the temperature is also seen in Fig. 6.39(a) and Fig. 6.39(b). Higher amounts of EGR reduce the maximum gas temperature and retard combustion to later times. Up to a rate of 65 % EGR, the trend of the simulation agrees very well with the engine data.

For all three mechanisms, a slightly higher temperature occurs in the compression and expansion cycle which may be addressed to unequalities of the initial conditions and geometry representation between simulation and engine.

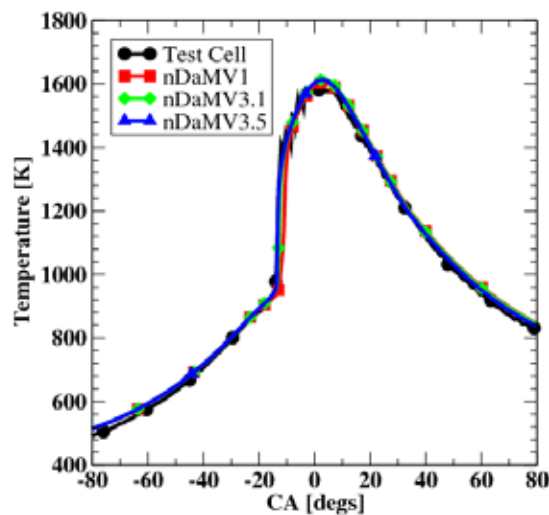


Figure 6.40: EGR 40% case, temperature trace for engine and simulation

6.3.4.3 Engine-Out Emissions

At exhaust valve opening (EVO), emissions from the simulation and from the exhaust gas analysis are compared. Although NO_x and soot are here of main interest, CO and UHC emissions are additionally studied.

In Fig. 6.48(a) NO_x emissions are presented as a function of EGR rate. The NO_x emissions are under-estimating the emissions of the engine slightly but the trend of the engine data is matched.

Regarding the soot emissions in Fig. 6.48(b), engine emissions are quite low due to the

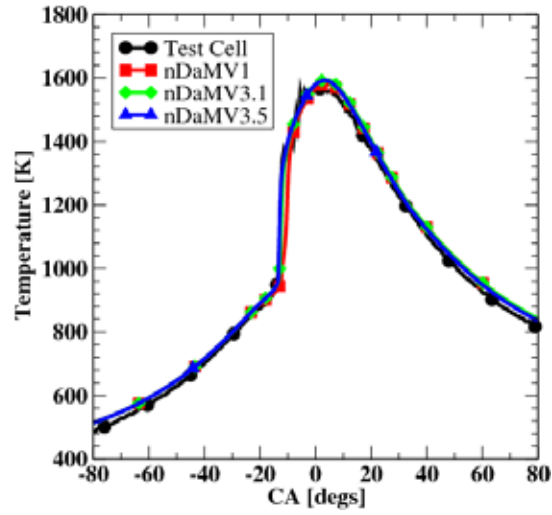


Figure 6.41: EGR 45 % case, temperature trace for engine and simulation

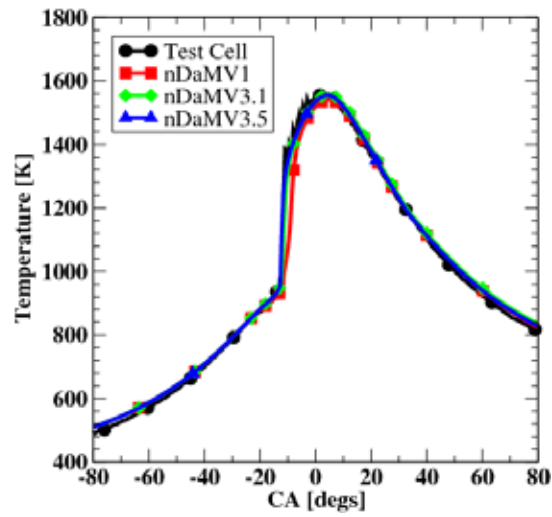


Figure 6.42: EGR 50% case, temperature trace for engine and simulation

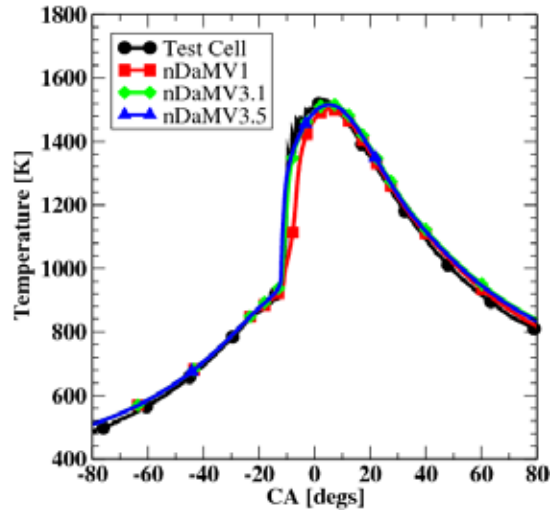


Figure 6.43: EGR 55 % case, temperature trace for engine and simulation

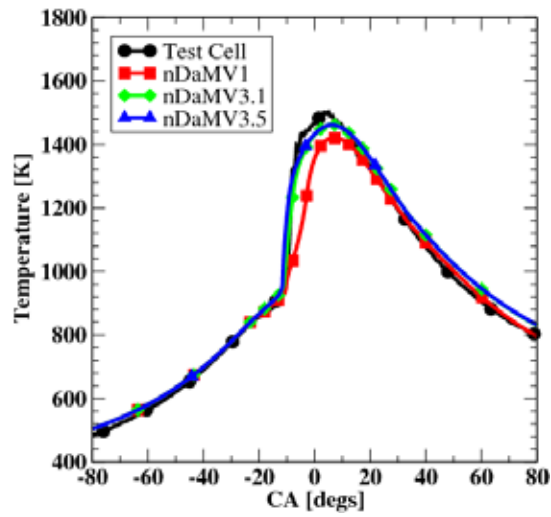


Figure 6.44: EGR 60% case, temperature trace for engine and simulation

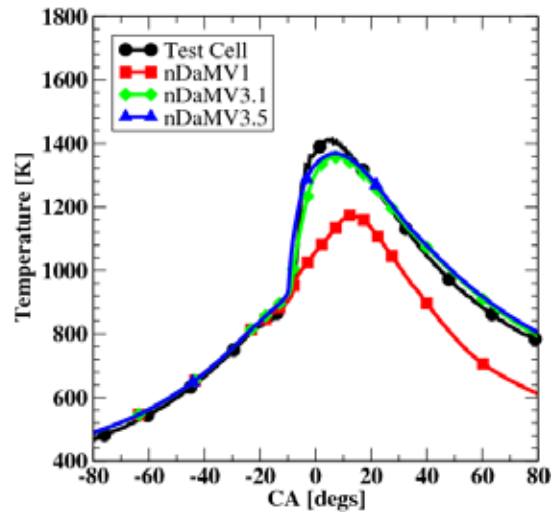


Figure 6.45: EGR 65 % case, temperature trace for engine and simulation

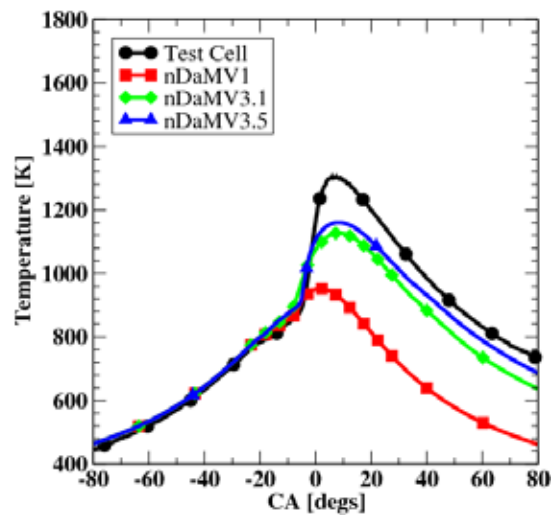


Figure 6.46: EGR 70% case, temperature trace for engine and simulation

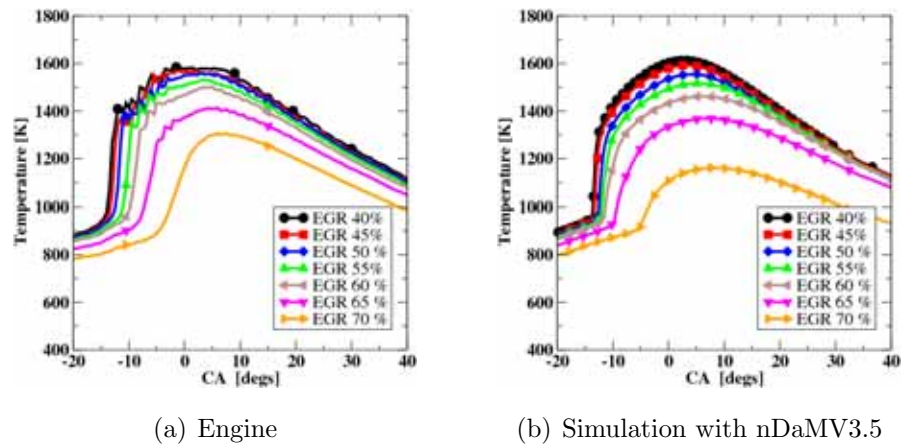


Figure 6.47: Influence of EGR on temperature

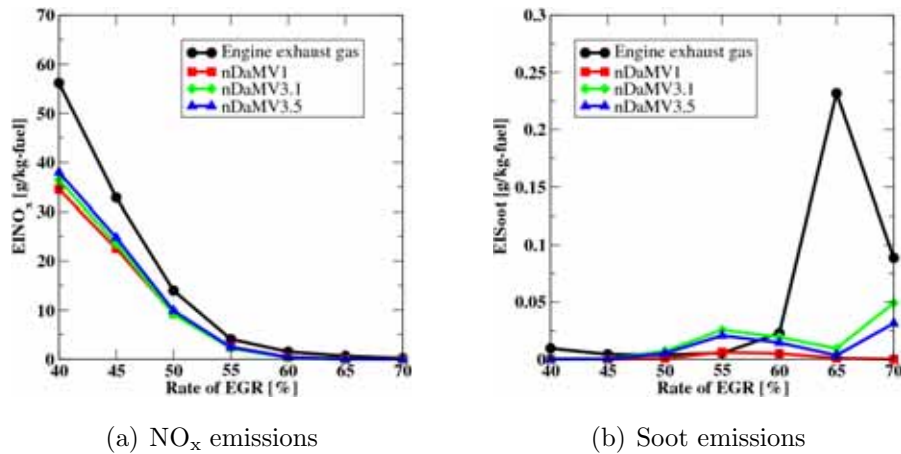


Figure 6.48: Comparison of emissions between simulation and exhaust gas analysis

early injection and homogenization of the fuel. The variation of EGR shows that soot emissions are first low but when EGR is increased up to 65 %, a peak in soot emissions occurs on the engine data. At a rate of 70% EGR soot emissions are decreasing again. The soot emission peak at 65 % EGR is not seen in the simulation data. nDaMV1 has nearly no soot emissions at very high EGR rates because combustion does not occur. nDaMV3.5 and nDaMV3.1 show low emissions but the soot emission peak is not predicted.

Since only CO₂ and H₂O are comprising EGR and added as additional species, it is an

open question if other intermediates are missing and need to be included. A detailed analysis of the EGR composition would be required. Other uncertainties remain from the behavior of the soot formation when high rates of EGR are in use. Already discussed in section 6.2.5.2, soot emissions are sensitive to the mixing process. The small overlapping area between β -PDF and first soot moment is illustrated in Fig. 6.49. A correct prediction of the turbulent mixture field and its β -PDF is required.

At low rates of EGR, CO emissions are low in the engine but increase with increas-

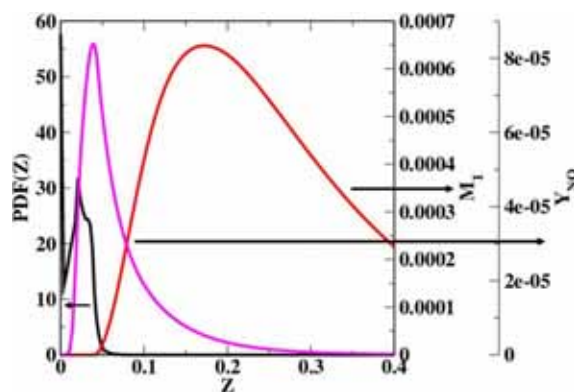


Figure 6.49: β -PDF, NO and first soot moment

in mixture fraction space

ing EGR rates as presented in Fig. 6.50(a). The engine and simulation data of CO emissions show the same trend. The agreement with the mechanism nDaMV3.5 and nDaMV3.1 is much better than for the original mechanism nDaMV1. Quantitatively, all three mechanisms over-estimate the engine emissions.

The analysis of unburnt hydrocarbons (UHC), shown in Fig. 6.51, indicates low emissions in the engine at nearly all rates of EGR. Only at the highest rate of 70%, small amounts of UHC exist. In the simulation, UHC is accounted by all species except fuel components, air, combustion products as CO_2 , H_2O and intermediate hydrogen compounds that do not comprise carbon. Since that approach is quite crude and unprecise, the simulation over-estimates the UHC emissions by a factor of 10-15 in comparison to the engine. Between an EGR rate of 40 and 60%, UHC emissions are relatively constant before increasing up to the highest EGR rate of 70%. The mechanism nDaMV3.5 and nDaMV3.1 produce lower UHC emissions at 65 and 70% EGR rates but cannot show here the engine trend. This increase in EGR indicates an

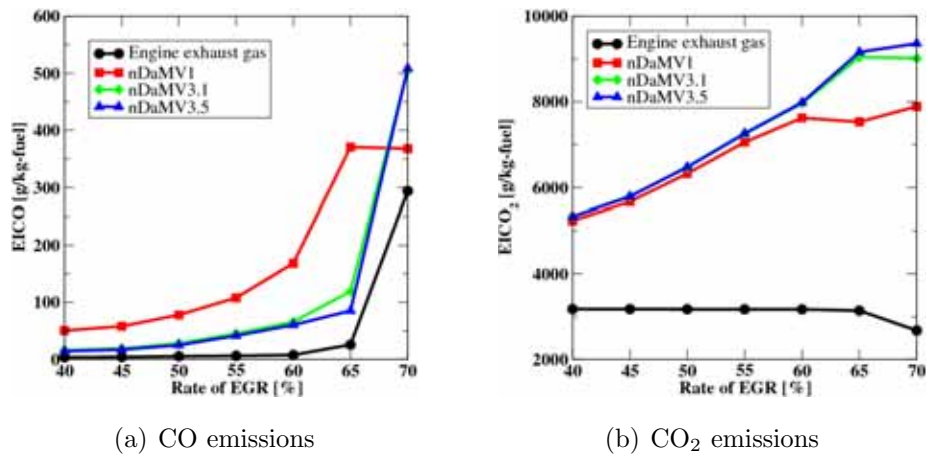


Figure 6.50: Comparison of emissions between simulation and exhaust gas analysis

incomplete fuel depletion without any significant heat-release. The modifications of the mechanism are made with regard to the sensitivity in ignition-delay and effect only the n-decane part of the mechanism but not the depletion of α -methyl-naphthalene.

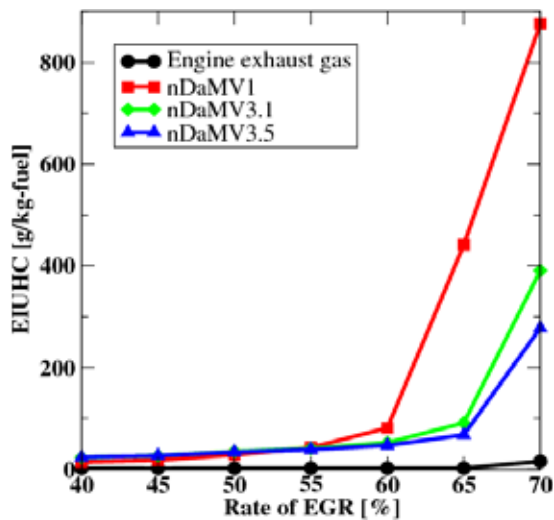


Figure 6.51: Comparison of UHC between simulation and exhaust gas analysis

6.3.4.4 Flow-Field Analysis

Better understanding of the combustion process is obtained from the visualization of the data set on the mesh. For 40, 55 and 70% EGR (from top to down), two different cut-planes, a vertical in the x-z plane at $y=0$ and a horizontal in spray-direction are chosen and colored by the scalar data as temperature, mean mixture fraction \tilde{Z} , species O_2, CO_2, CO, NO and soot concentration from first soot moment M_1 . Additionally, the velocity vector field and the black-colored iso-line of stoichiometric mixture are superposed.

Mixture Formation The mixing process is presented in Fig. 6.52. Additionally to the mean mixture fraction, spray parcels are colored by the droplet temperature and equally sized by the radius. During the initial needle opening phase, liquid fuel is penetrating the bowl. The evaporation starts and forms a fuel-rich mixture (Fig. 6.52(a)). At this time, the spray penetration of the liquid phase is already constant. Rayleigh-Taylor breakup is dominating and droplets are evaporating very fast at the spray tip. The fuel-rich gas phase of the spray continues to evaporate further down in the bowl. Since a narrow spray angle is applied here, the spray targets down to the bottom of the piston bowl. At the latest time of -10° CA aTDC, the injection process is finished. Due to the re-entrance bowl-shape, the momentum of the spray guides the mixture to move up to the cylinder top. The influence of EGR shows a shorter spray penetration in Fig. 6.52(a) and Fig. 6.52(b) when the EGR rate is increased.

Temperature Distribution The temperature distribution in Fig. 6.53 indicates a burning mixture already at -10° CA aTDC. Velocity vectors are superposed on the scalar temperature field. Due to the narrow spray angle, the spray induces a flow that is attached to the piston bowl. As already seen for the mean mixture fraction field, the burning gas occurs close to the bottom of the piston bowl. For later times, the strong momentum induces a large rotational flow by which the burning gas is lifted up to the cylinder head as seen from Fig. 6.53(c). In the vertical cut-plane, strong gradients still exists whereas in the horizontal cut-plane, the temperature field

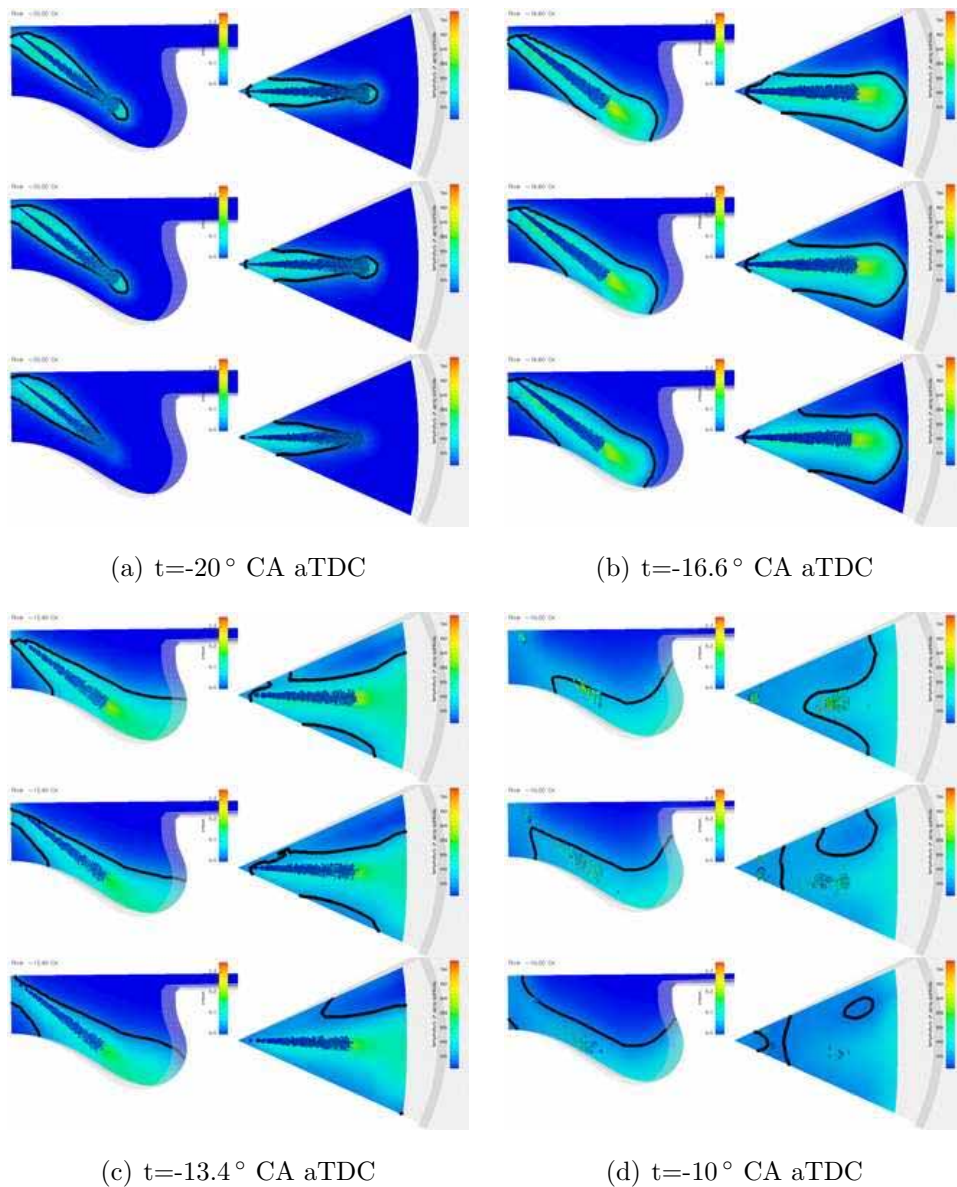


Figure 6.52: Mean mixture fraction \tilde{Z} for 40, 55 and 70% EGR

is almost homogeneous. With increasing EGR rate, the temperature of the burning gas is decreasing. At 70% EGR, no burning gas exist anymore. The local temperatures are around 1500 K and much less than 2600 K at 40% EGR. The fuel is not completely depleted because the oxygen content is reduced by these high amounts of EGR.

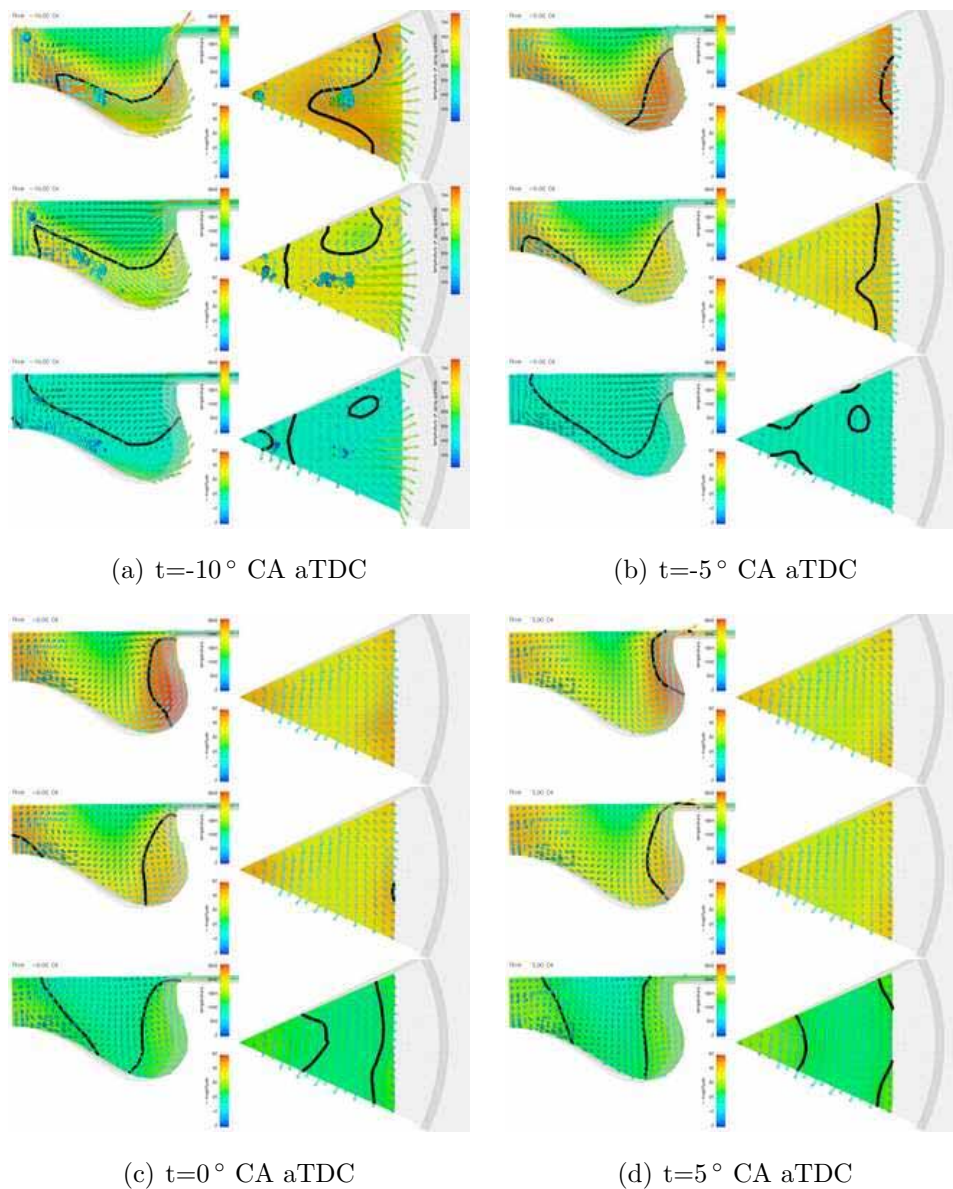


Figure 6.53: Temperature for 40, 55 and 70% EGR

O₂ Distribution The application of high EGR rates causes a dilution of the mixture. The resulting O₂ mole fraction distribution is decreasing with increasing EGR as seen from Fig. 6.54(a) when ignition starts. In Fig. 6.54(b), combustion occurs in both, 40 and 55 % EGR cases but not for the 70% case where only little O₂ is consumed. Only at very late times in Fig. 6.54(d), some fuel consumption occurs and reduces the O₂

concentration but without any recent heat release as the temperature distribution in Fig. 6.53(d) shows.

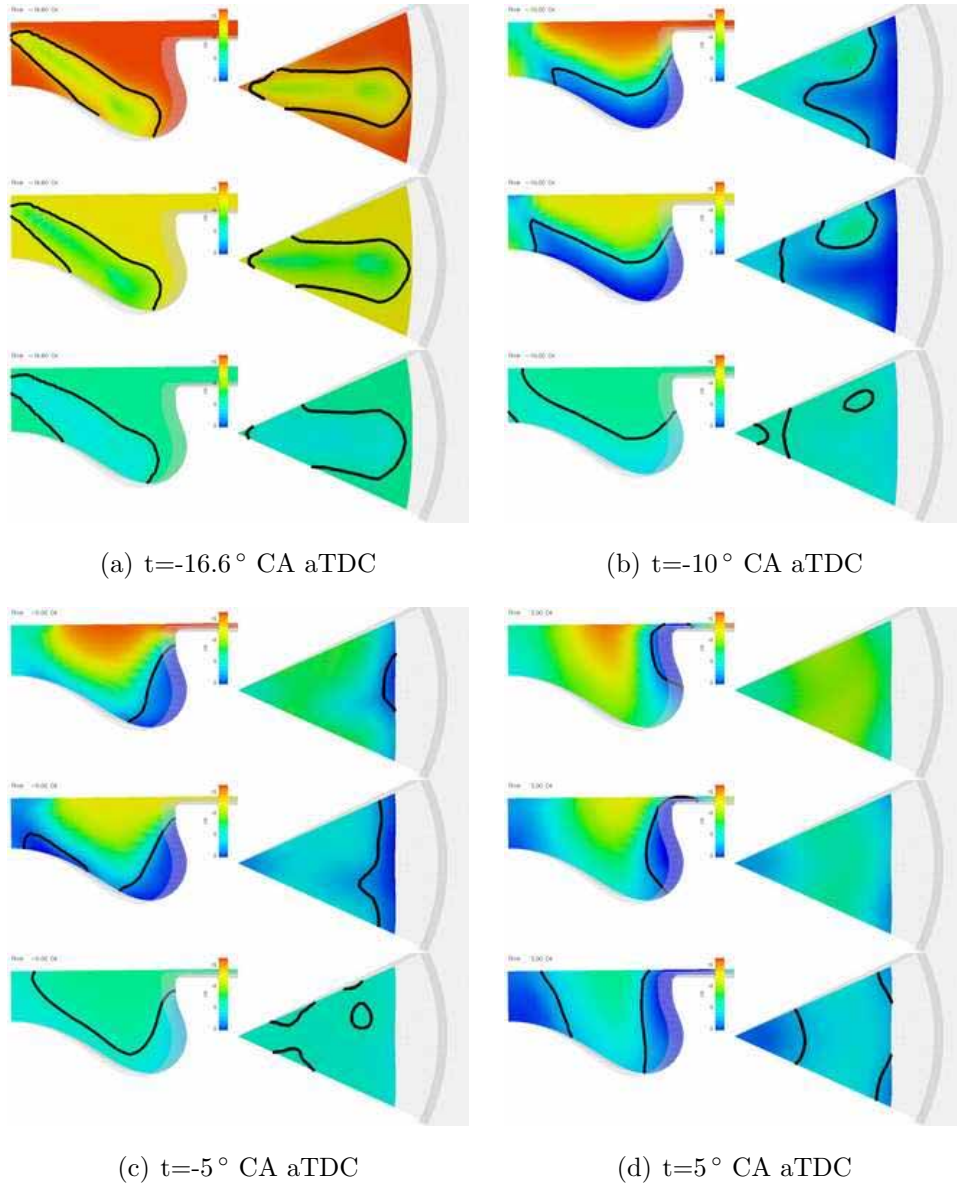


Figure 6.54: O_2 mole fraction for 40, 55 and 70% EGR

CO Distribution The main heat is released from the CO conversion to CO_2 so that it is a main target to reduce CO-emissions for sake of fuel efficiency. At early times, CO

is formed only at an EGR rate of 40% after the second stage of ignition (Fig. 6.55(a)). At higher rates of EGR, CO is not formed. For a rate of 55% EGR, recent levels of CO occur in Fig. 6.55(b) at -10° CA aTDC. Due to the narrow spray angle, fuel occurs close to the piston bowl. CO is attached to the wall on the rich side of the flame which may be explained by flame extinction at the wall. In the case of 70% EGR, no CO is available. Only at very late times, some CO is formed but only on a very low level (Fig. 6.55(d)). Due to the strong rotational flow motion, CO is further oxidized in the flame front and converted to CO_2 .

CO_2 Distribution Carbon-dioxide is mainly formed from CO. It is one of the stable combustion products and accumulated by time. Hence, it cannot be reduced anymore. The dilution of the mixture by EGR shifts the combustion to later times. Already at -10° CA aTDC, CO_2 occurs at EGR rates of 40 and 55% but no CO_2 is formed at a rate of 70% (Fig. 6.56(a)). At -5° CA aTDC, much more CO_2 is formed at rates of 40 and 55% than at 70% EGR (Fig. 6.56(b) and Fig. 6.56(c)). At a rate of 40% EGR, CO and CO_2 formation occurs earlier than for 55% EGR whereas at 70% EGR, CO_2 occurs at very late times in the expansion cycle only (Fig. 6.56(d)).

NO Distribution One of the major emissions is NO_x that mostly consists of thermal NO formed from the Zel'dovich mechanism. As already analyzed from Fig. 6.48, no NO_x is formed at higher EGR rates. In Fig. 6.57, NO emissions are only formed in the flame region at an EGR rate of 40%. For the EGR rates of 55 and 70%, no NO is formed for all times. Later in the expansion cycle, NO is reduced by the reburn-mechanism. NO that was located close to the wall of the piston re-entrance in Fig. 6.57(c) at 10° CA aTDC is partially reduced as seen in Fig. 6.57(d) at 20° CA aTDC.

Soot Concentration Distribution Beside NO_x , soot emissions are the second major engine-out emissions. Usually, soot is formed in fuel-rich areas. It occurs close to the wall as discussed in [41, 78, 71] because OH radicals are quenched and cannot promote the soot oxidation furthermore. Although soot oxidation close to the wall is omitted,

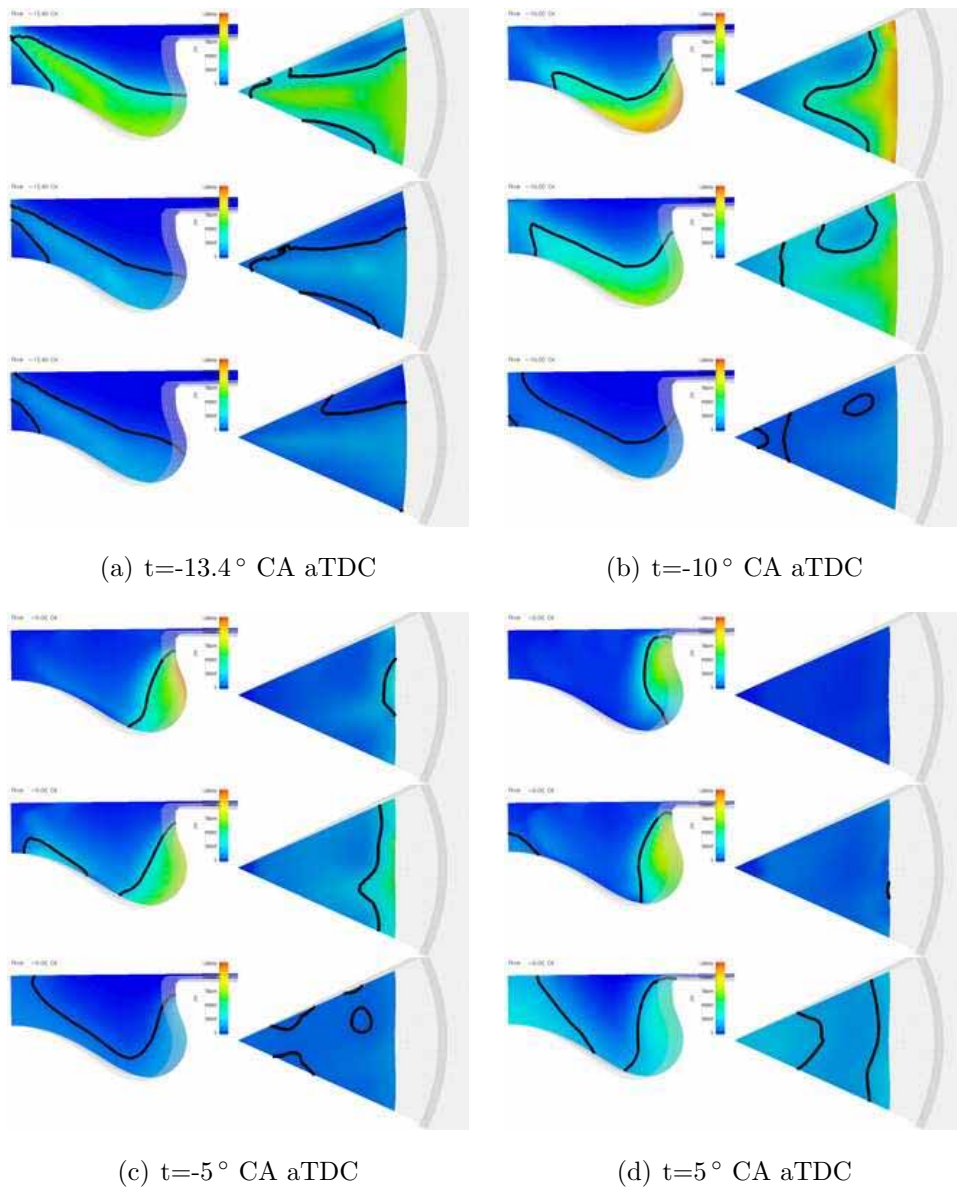


Figure 6.55: CO mole fraction for 40, 55 and 70% EGR

the strong rotation of the flow as presented in Fig. 6.53(c) and Fig. 6.53(d) transports the soot back from the wall into the hot flame where it is oxidized. In order to achieve that flow circulation, the bowl-shape and the injection parameters, namely spray-angle, nozzle tip protrusion and injection timing, have to be optimized.

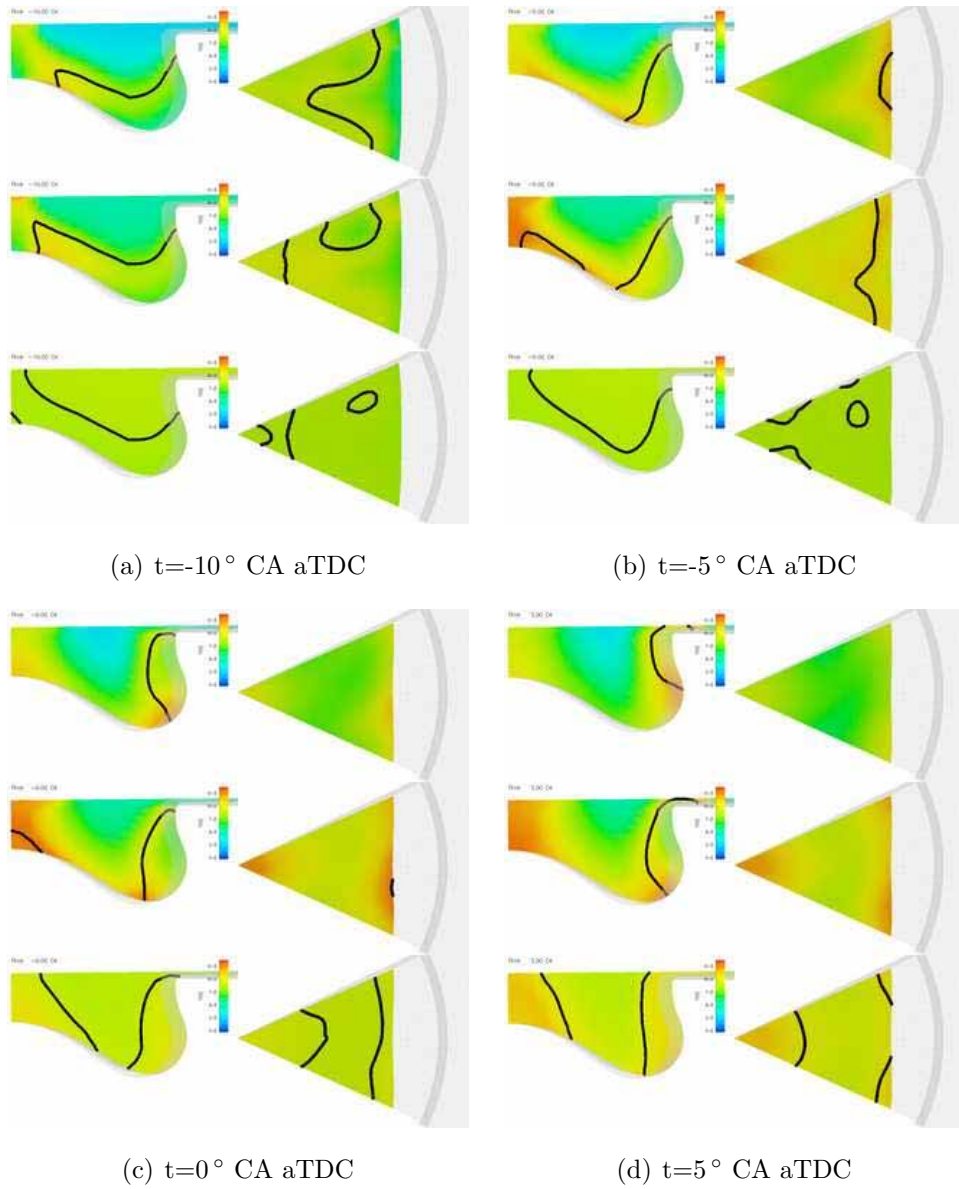


Figure 6.56: CO₂ mole fraction for 40, 55 and 70% EGR

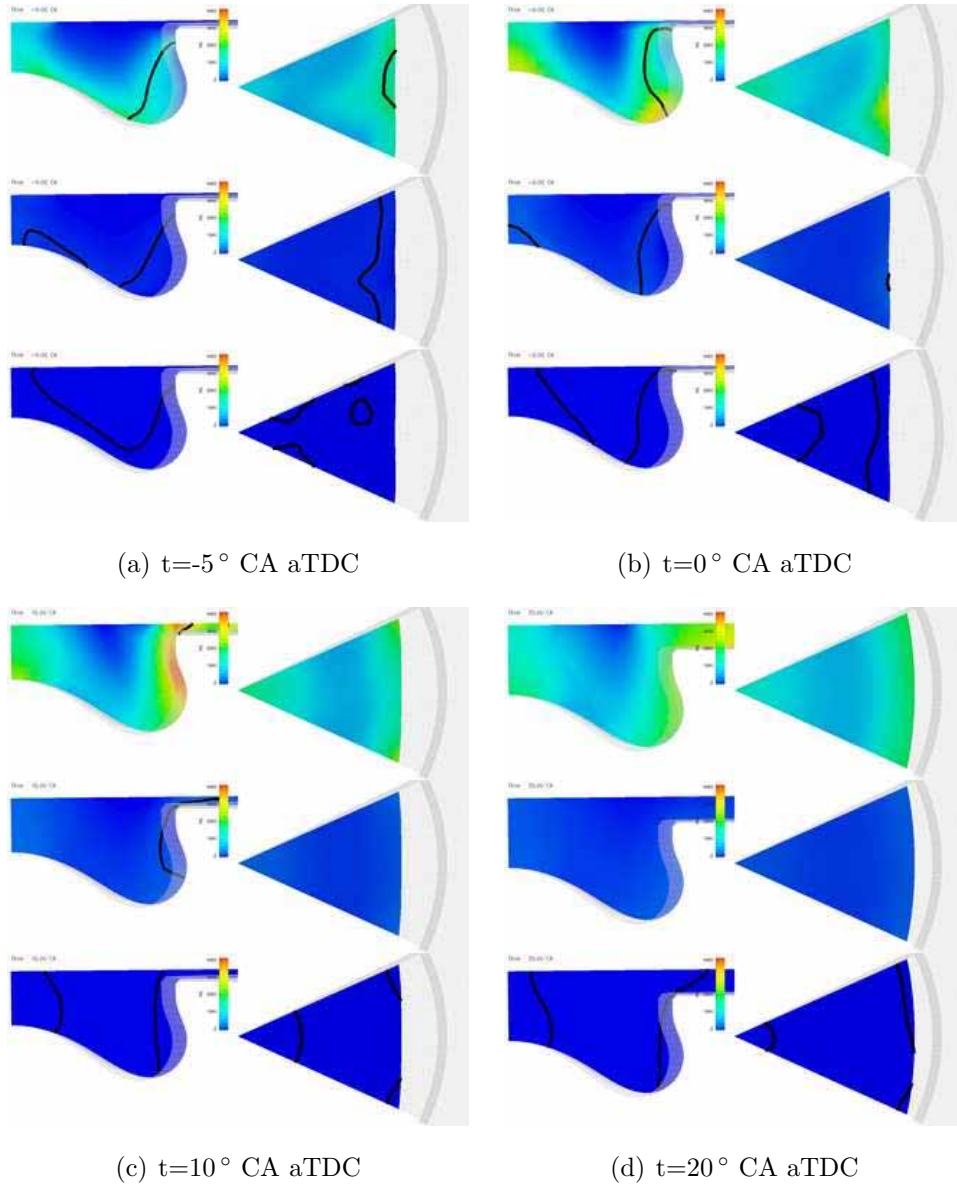


Figure 6.57: NO mole fraction for 40, 55 and 70% EGR

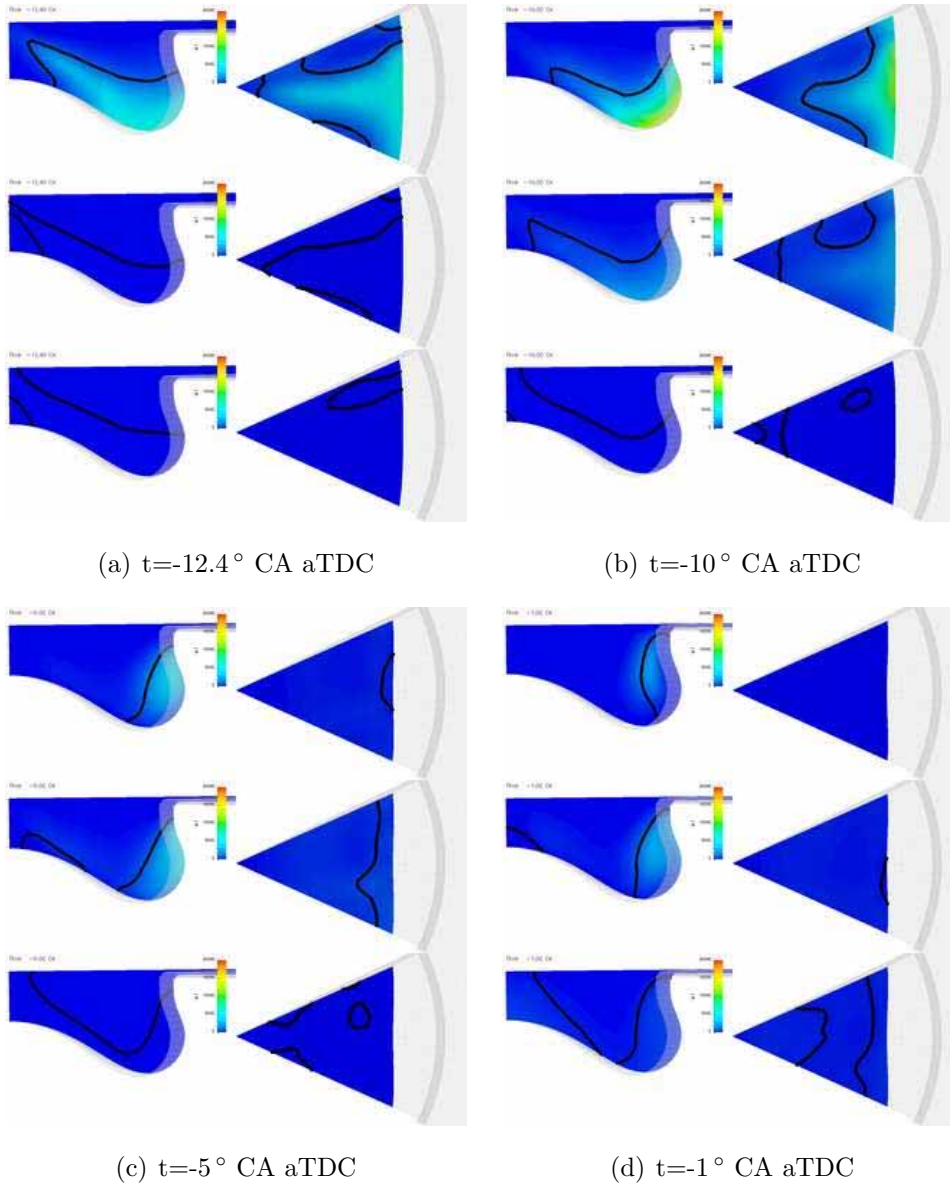


Figure 6.58: M_1 mass concentration for 40, 55 and 70% EGR

7 Summary

The optimization of the combustion and mixture formation process in Diesel engines by CFD simulations requires a reliable model approach as a pre-requisite in order to predict combustion and emissions. A general and commonly used model for the liquid spray is the discrete droplet model. Sub-models for droplet breakup, collision and coalescence, and evaporation are available in the CFD code. With regard to combustion, the flamelet model approach is interactively coupled with the CFD code, known as RIF model. It benefits from a one-dimensional description of the thin reaction zone in the flame. By this approach, a detailed reaction mechanism for the model fuel can be used. Sub-mechanisms for NO_x formation and a soot model are included. The reaction mechanism has been modified in this work to account for a correct ignition delay and heat-release at low-temperature conditions e.g. in the PCCI combustion. The modeling of the mixture formation in a spray contains uncertainties in the model constants and initial conditions. Spray data is required to calibrate the spray model. At least, the spray penetration has to be measured under engine like conditions as performed in a spray chamber. The spray penetration is interpreted as a criterion for the mass and momentum exchange between the spray and the surrounding gas on a macroscopic level. Finding a good agreement for the spray penetration between simulation and experiment defines an optimization problem. That agreement is expressed in an Euclidean norm as a merit function. The objective is to minimize this merit function. The search for an appropriate set of spray model parameters and initial conditions is denoted here as calibration of the spray model. Six parameters have been identified, spanning a six dimensional parameter space. A manual search is not feasible anymore but the implemented Genetic Algorithm is suitable to find a global optimum where a good agreement between measured and simulated spray penetration is obtained. If the same spray parameters are applied to a virtual engine

case, a similar good agreement is achieved although the mesh resolution is much finer and the mesh topology is different than for the spray chamber simulation. From this result, spray data for engine simulations should be provided and be used for sake of calibration before the engine simulation is conducted. Additionally data is obtained by PDA measurements at discrete points in the spray. That measurement technique is, however, limited to less dense areas. Nevertheless, it shows that also local data is in agreement with the simulation data. Agreement with spray penetration is thus a relatively good choice and accounts also for the physics on a local or microscopic level. That hypothesis is well supported by the data from the ethanol spray calibration. The excellent agreement with regard to the global spray penetration is reflected by the 2D comparison of liquid and vapor fuel concentrations and temperature, respectively. Furthermore, a similar good agreement in spray penetration is obtained if the breakup and collision model is not used. In that case, the spray penetration is only controlled by the evaporation process. The Genetic Algorithm finds a point in the parameter space with an initial SMR that is of the order of size of the outcome of the secondary droplet breakup.

However in engine simulations, spray data is not always available. In that case the spray parameters have to be adjusted. That adjustment is carried out following a methodology that is presented in this work. Mainly, SOI and EGR variations have to be used to calibrated the spray and combustion model. That approach has been investigated for three different engine data sets for conventional and PCCI combustion mode.

On the Cummins QSX engine, a conventional combustion has been studied. Spray parameters are subject of adjustment. On the Duramax 6600 Diesel engine, a conventional and PCCI combustion mode are investigated. For the PCCI combustion mode, the reaction mechanism is modified in order to account for a correct ignition delay in the low temperature combustion regime. The comparison between engine data and results from the simulation indicates a good agreement for the combustion and engine-out emissions. On the Duramax full load case, most uncertainties are addressed to the spray-wall interaction. Uncertainties from physical not well based models will always occur in the engine simulation. Therefore, calibration of these models is a mean to quantify its influence and minimize the discrepancies.

Bibliography

- [1] S. M. Aceves and D. L. Flowers. A Detailed Chemical Kinetic Analysis of Low-Temperature, Non-Sooting Diesel Combustion. *Paper No. SAE 2005-01-0923*, 2005.
- [2] K. Akihama, Y. Takatori, K. Inagaki, S. Sasaki, and A. Dean. Mechanism of the Smokeless Rich Diesel Combustion by Reducing Temperature. *Paper No. SAE 2001-01-0655*, 2001.
- [3] H.-E. Albrecht, M. Borys, N. Damaschke, and C. Tropea. *Laser Doppler and Phase Doppler Measurement Techniques*. Springer, Berlin, 2003.
- [4] A. A. Amsden, P. J. O'Rourke, and T. D. Butler. KIVA II: A Computer Program for Chemically Reactive Flows with Sprays. Technical Report LA-11560-MS, Los Alamos National Laboratories, 1989.
- [5] R. Aneja and J. Abraham. How Far Does the Liquid Penetrate in a Diesel Engine: Computed Results vs. Measurements ? *Combustion Science and Technology*, 138:233–255, 1998.
- [6] C. Antoni. *Untersuchung des Verbrennungsvorgangs im direkteinspritzenden Dieselmotor mit zyklusaufgelöster Emissionsspektroskopie*. PhD thesis, RWTH Aachen, 1998.
- [7] J. Appel, M. Frenklach, and H. Bockhorn. Kinetic Modelling of Soot Formation with Detailed Chemistry and Physics. Laminar Premixed Flames of C2 Hydrocarbons. *Combust. Flame*, 121,122, 2000.
- [8] M. Araki, T. Umino, T. Obokata, T. Ishima, S. Shiga, H. Nakamura, W.-Q. Long, and A. Murakami. Effects of Compression Ratio on Characteristics of

- PCCI Diesel Combustion with a Hollow Cone Spray. *Paper No. SAE 2005-01-2130*, 2005.
- [9] N. Ashgriz and J. Y. Poo. Coalescence and separation in binary collisions of liquid drops. *J. Fluid Mech.*, 221:183–204, 1990.
- [10] T. Bäck. Self-adaptation in genetic algorithms. In *Proc. of the 1st European Conf. on Artificial Life*, pages 263–271, 1992. citeseer.ist.psu.edu/14572.html.
- [11] H. Barths. *Simulation of Diesel Engine and Gas Turbine Combustion Using Multiple Flamelets with Detailed Chemistry*. PhD thesis, RWTH Aachen, 2001.
- [12] H. Barths, C. Hasse, G. Bikas, and N. Peters. Simulation of Combustion in DI Diesel Engines using an Eulerian Particle Flamelet Model. In *Proc. Combust. Inst.*, volume 28, pages 1161–1168. The Combustion Institute, Pittsburgh, 2000.
- [13] A. B. Basset. *A Treatise on Hydrodynamics*. Deighton Bell, 1888.
- [14] D. L. Baulch, C. J. Cobos, R. A. Cox, P. Frank, G. Hayman, Th. Just, J. A. Kerr, T. Murrells, M. J. Pilling, J. Troe, R. W. Walker, and J. Warnatz. Summary Table of Evaluated Kinetic Data for Combustion Modelling: Supplement 1. *Combust. Flame*, 98:59–79, 1994.
- [15] D. L. Baulch, C. J. Cobos, R. A. Cox, P. Frank, G. Hayman, Th. Just, J. A. Kerr, T. Murrells, M. J. Pilling, J. Troe, R. W. Walker, and J. Warnatz. Evaluated kinetic data for combustion modeling. *J. Phys. Chem. Ref. Data*, 21:411–429, 1992.
- [16] C. Baumgarten. *Mixture Formation in Internal Combustion Engines*. Springer-Verlag, 2005.
- [17] S. W. Benson. The Kinetics of Thermochemistry of Chemical Oxidation with Application to Combustion and Flames. *Prog. Energy Combust. Sci.*, 7:125–134, 1981.
- [18] G. Bikas and N. Peters. Kinetic Modelling of n-Decane Combustion and Autoignition. *Comb. Flame*, 126:1456–1475, 2001.

-
- [19] R. W. Bilger. Turbulent Flows with Nonpremixed Reactants. In P. A. Libby and F. A. Williams, editors, *Turbulent Reacting Flows*, pages 65–113. Springer-Verlag, Berlin, 1980.
- [20] R. W. Bilger. The Structure of Turbulent Nonpremixed Flames. *Proc. Combust. Inst.*, 22:475–488, 1988.
- [21] R.W. Bilger. Reaction Rates in Diffusion Flames. *Combust. Flame*, 30:227–284, 1977.
- [22] J. Bode. *Zum Kavitationseinfluß auf den Zerfall von Flüssigkeitsstrahlen*. PhD thesis, Max-Planck-Institut für Strömungsforschung, Göttingen, 1991.
- [23] M. Bollig. *Berechnung laminarer Kohlenwasserstoffflammen in Hinblick auf die Stickoxidbildung in Verbrennungsmotoren*. PhD thesis, RWTH Aachen, 1998.
- [24] W. Bosch. Der Einspritzgesetzindikator - ein neues Meßgerät zur direkten Bestimmung des Einspritzgesetzes von Einzeleinspritzungen. *MTZ Motortechnische Zeitschrift*, 25(7), 1964.
- [25] J. Boussinesq. Théorie de l'Écoulement Tourbillant. *Mem. présenté par divers Savants Acad. Sci. Inst. Fr.*, 23:46–50, 1877.
- [26] P. Brazier-Smith, S. Jennings, and J. Latham. The interaction of falling rain drops: coalescence. In *Proceedings of the Royal Society of London, Series A, Mathematical and Physical Sciences*, volume 326, pages 393–408, 1972.
- [27] S.P. Burke and T.E.W. Schumann. Diffusion Flames. In *Proc. Combust. Inst.*, volume 1, pages 2–11. The Combustion Institute, Pittsburgh, 1928.
- [28] D. L. Carroll. Chemical laser modeling with genetic algorithms. *AIAA Journal*, 34(2):338–346, February 1996.
- [29] R. A. Caruana and J. D. Schaffer. Representation and hidden bias: Gray versus binary coding for genetic algorithms. In *Proceedings of the Fifth International Conference on Machine Learning*, pages 153–162, 1988.

- [30] C. Chevalier, P. Louessard, U. C. Müller, and J. Warnatz. A Detailed Low-Temperature Reaction Mechanism of *n*-Heptane Auto-Ignition. In *Int. Symposium on Diagnostics and Modeling of Combustion in Internal Engines*, Kyoto, 1990. The Japan Society of Mechanical Engineers.
- [31] P. Y. Chou. On the Velocity Correlations and the Solutions of the Equations of Turbulent Fluctuations. *Quart. Appl. Math.*, 3:38, 1945.
- [32] P. J. Coelho and N. Peters. Numerical Simulation of a MILD Combustion Burner. *Combust. Flame*, 124:503–518, 2001.
- [33] C. Coello, A. Carlos, and G. Toscano Pulido. Multiobjective Optimization using a Micro-Genetic Algorithm. In Lee Spector, Erik D. Goodman, Annie Wu, W. B. Langdon, Hans-Michael Voigt, Mitsuo Gen, Sandip Sen, Marco Dorigo, Shahram Pezeshk, Max H. Garzon, and Edmund Burke, editors, *Proceedings of the Genetic and Evolutionary Computation Conference (GECCO 2001)*, pages 274–282, San Francisco, California, 2001. Morgan Kaufmann Publishers.
- [34] C. Coello, A. Carlos., D. A. Van Veldhuizen, and G. B. Lamont. *Evolutionary Algorithms for Solving Multi-Objective Problems*. Kluwer Academic/Plenum Publishers, 2002.
- [35] M. B. Colket and R. J. Hall. *Soot Formation in Combustion*, chapter Success and Uncertainties in Modeling Soot Formation in Laminar, Premixed Flames, pages 442–470. Springer Verlag, 1994.
- [36] European Community. Joule II: Final Report of the IDEA EFFECT Programe. Technical report, CEC, 1996.
- [37] S. Corrsin. The Reactant Concentration Spectrum in Turbulent Mixing with a First Order Reaction. *J. Fluid Mech.*, 11:487–416, 1961.
- [38] L. Crocco. Sulla trasmissione del calore da una lamina piana a un fluido sorrente ad alta velocita. *Aerotecnica*, 12:181–197, 1932. (translated as NACA TM 690).
- [39] C. T. Crowe, M. P. Sharma, and D. E. Stock. The Particle-Source-In Cell (PSI-Cell) Model for Gas-Droplet Flows. *J. of Fluids Engr.*, 99:325–332, 1977.

-
- [40] B. B. Dally, E. Riesmeier, and N. Peters. Effect of Fuel Mixture on MILD Combustion. *Combustion and Flame*, 137:418–431, 2004.
- [41] J. E. Dec. A Conceptual Model of Diesel Combustion Based on Laser-Sheet Imaging. *Paper No. SAE 970873*, 1997.
- [42] P. Deuffhard and M. Wulkow. Computational Treatment of Polyreaction Kinetics by Orthogonal Polynomials of a Discrete Variable. *Impact of Comp. Sci. Eng.*, 1, 1989.
- [43] N. Dronniou, M. Lejeune, I. Balloul, and P. Higelin. Combination of High EGR Rates and Multiple Injection Strategies to Reduce Pollutant Emissions. *Paper No. SAE 2005-01-3726*, 2005.
- [44] D. X. Du, H. Wang, and C. K. Law. Soot Formation in Counterflow Ethylene Diffusion Flames from 1 to 2.5 Atmospheres. *Combustion and Flame*, 113:264–270, 1998.
- [45] J. K. Dukowicz. A Particle-Fluid Numerical Model for Liquid Sprays. *J. Comput. Phys.*, 35:229–253, 1980.
- [46] E. Effelsberg and N. Peters. A Composite Model for the Conserved Scalar Pdf. *Combust. Flame*, 50:351–360, 1983.
- [47] A. E. Eiben, R. Hinterding, and Z. Michalewicz. Parameter Control in Evolutionary Algorithms. *IEEE Trans. on Evolutionary Computation*, 3(2):124–141, 1999.
- [48] S. Elghobashi. Particle-Laden Turbulent Flows: Direct Simulation and Closure Models. *Applied Scientific Research*, 48:301–314, 1991.
- [49] J. P. Estrade, H. Carentz, G. Lavergne, and Y. Biscos. Experimental investigation of dynamic binary collision of ethanol droplets - a model for droplet coalescence and bouncing. *Int. Journ. of Heat and Fluid Flow*, 20:486–491, 1999.
- [50] G. M. Faeth. Evaporation and Combustion of Sprays. *Prog. Energy Combust. Sci.*, 25(9):1–76, 1983.

- [51] P. V. Farrell, C. T. Chang, and T. F. Su. High Pressure Multiple Injection Spray Characteristics. *Paper No. SAE 960860*, 1996.
- [52] Charles L. Feffermann. Existence and Smoothness of the Navier-Stokes Equation. *Princeton University, Department of Mathematics*, 2000.
- [53] C. P. Fenimore. Studies of Fuel-Nitrogen in Rich Flame Gases. *Proc. Combust. Inst.*, 17:661–670, 1979.
- [54] J. H. Ferziger and M. Peric. *Computational Methods for Fluid Dynamics*. Springer, 2002.
- [55] M. Frenklach. Computer Modeling of Infinite Reaction Sequences: A Chemical Lumping. *Chemical Engineering Science*, 40(10):1843–1849, 1985.
- [56] M. Frenklach, D. W. Clary, T. Yuan, W. C. Gardiner, and S. E. Stein. Detailed Kinetic Modeling of Soot Formation in Shock-Tube Pyrolysis of Acetylene. In *Proc. Combust. Inst.*, volume 20, pages 887–901. The Combustion Institute, Pittsburgh, 1985.
- [57] M. Frenklach and W. C. Gardiner. Representation of Multistage Mechanisms in Detailed Computer Modeling of Polymerisation Kinetics. *J. Phys. Chem.*, 88:6263–6266, 1984.
- [58] M. Frenklach and S. J. Harris. Aerosol Dynamics Modeling Using the Method of Moments. *J. Coll. Interf. Sci.*, 118:252–261, 1987.
- [59] M. Frenklach and H. Wang. Detailed Modeling of Soot Particle Nucleation and Growth. In *Proc. Combust. Inst.*, volume 23, pages 1559–1566. The Combustion Institute, Pittsburgh, 1990.
- [60] M. Frenklach and H. Wang. *Soot Formation in Combustion*, chapter Detailed mechanism and modeling of soot particle formation, pages 165–190. Springer Verlag, Berlin - Heidelberg, 1994.
- [61] S. K. Friedlander. *Smoke, Dust and Haze*. Wiley and Sons, 1986.

-
- [62] A. Fusco, A. L. Knox-Kelecy, and D. E. Foster. Application of a Phenomenological Soot Model for Diesel Engine Combustion. In *COMODIA 94*, pages 571–576, 1994.
- [63] M. Gavaises, A. Theodorakakos, G. Bergeles, and G. Brenn. Evaluation of the Effect of Droplet Collision on Spray Mixing. *Proc. Inst. Mech, Engrs.*, 210:465–475, 1996.
- [64] S. S. Girimaji. Assumed β -PDF Model for Turbulent Mixing: Validation and Extension to Multiple Scalar Mixing. *Combust. Sci. and Tech.*, 18:177–196, 1991.
- [65] D. E. Goldberg. *Genetic Algorithms in Search, Optimization, and Machine Learning*. Addison-Wesley, first edition, 1989.
- [66] D. E. Goldberg. Real-coded Genetic Algorithms, Virtual Alphabets, and Blocking. *Complex Systems, Complex Systems Publications, Inc.*, 5:139–167, 1991.
- [67] D. E. Goldberg and K. Deb. A Comparative Analysis of Selection Schemes Used in Genetic Algorithms. In G. J. E. Rawlins, editor, *Foundations of Genetic Algorithms*, pages 69–93. Morgan Kaufmann Publishers, 1991.
- [68] S. Gordon and J. B. McBride. A Computer Program for Complex Chemical Equilibrium Compositions - Incident and Reflected Shocks and Chapman Jouguet Detonations. *NASA*, SP-273, 1971.
- [69] A. D. Gosman and E. Ioannides. Aspects of Computer Simulation of Liquid-Fuelled Combustors. In *19th Aerospace Science Meeting*, number 81-0323 in AIAA, 1981.
- [70] J. Grefenstette. Optimization of control parameters for genetic algorithms. *IEEE Transactions on Systems, Man and Cybernetics*, 16:122 – 128, January/February 1986. <http://portal.acm.org/citation.cfm?id=14123&dl=ACM&coll=portal>.
- [71] A. Greis. *Optische Untersuchungen des Verbrennungsprozesses in einem PKW-Dieselmotor mit Direkteinspritzung*. PhD thesis, RWTH Aachen, 2007.
- [72] K. Stephan H. D. Baehr. *Wärme- und Stoffübertragung*. Springer-Verlag, Berlin Heidelberg, 1994.

- [73] Z. Han, A. Aludogan, G. J. Hampson, and R. D. Reitz. Mechanism of soot and NO_x emission reduction using multiple-injections in a Diesel engine. *Paper No. SAE 960633*, 1996.
- [74] S. J. Harris and I. M. Kennedy. The coagulation of soot particles with van der waals forces. *Combustion Science Technology*, 59:443–454, 1988.
- [75] C. Hasse, G. Bikas, and N. Peters. Modeling DI-Diesel Combustion using the Eulerian Particle Flamelet Model (EPFM). *Paper No. SAE 2000-01-2934*, 2000.
- [76] D. C Haworth, M. S. Huebler, S. H. El Thary, and W. R. Matthes. Multidimensional Calculations for a Two-Stroke-Cycle Engine: a Detailed Scavenging Model Validation. *Paper No. SAE 932712*, 70, 1993.
- [77] N. A. Henein, A. Bhattacharyya, J. Schipper, A. Kastury, and W. Bryzik. Effect of Injection Pressure and Swirl Motion on Diesel Engine-Out Emissions in Conventional and Advanced Combustion Regimes. *Paper No. SAE 2006-01-0076*, 2006.
- [78] C. A. Hergart, H. Barths, and N. Peters. Modeling the Combustion in a Small-Bore Diesel Engine Using a Method Based on Representative Interactive Flamelets. *Paper No. SAE 1999-01-3550*, 1999.
- [79] C.-A. Hergart, H. Barths, and R. M. Siewert. Modeling Approaches for Premixed Charge Compression Ignition Combustion. *Paper No. SAE 2005-01-0218*, 2005.
- [80] H. C. Hewson and M. Bollig. Reduced Mechanisms for NO_x Emissions from Hydrocarbon Diffusion Flames. In *Proc. Combust. Inst.*, volume 26, pages 2171–2180. The Combustion Institute, Pittsburgh, 1996.
- [81] S. E. Hieber. An Investigation of the Mesh Dependence of the Stochastic Discrete Droplet Model Applied to Dense Liquid Sprays. Master’s thesis, Department of Mathematical Science, Michigan Technological University, 2001.
- [82] H. Hiroyasu and T. Kadota. Fuel Droplet Size Distribution in Diesel Combustion Chamber. *Paper No. SAE 740715*, 1974.

-
- [83] H. Hiroyasu, T. Kadota, and M. Arai. Development and Use of a Spray Combustion Modeling to PRedict Diesel Engine Efficiency and Pollutant Emissions (Part I: Combustion Modeling). *Bulletin of the HJSME*, 26:569–575, 1983.
- [84] K.H. Hoffmann, K. Hummel, T. Maderstein, and A. Peters. Das Common-Rail-Einspritzsystem - ein neues Kapitel der Dieseleinspritztechnik. *MTZ Motortechnische Zeitschrift*, 58(10), 1997.
- [85] J. H. Holland. *Adaption in natural and artificial systems*. MIT Press, 1975.
- [86] J. B. W. Howard. Invited Topical Review, Fullerenes Formation in Flames. *Proc. Combust. Inst.*, 24:933–946, 1992.
- [87] L. P. Hsiang and G. M. Faeth. Near-limit Drop Deformation and Secondary Breakup. *Int. J. Multiphase Flow*, 18(5):635–652, 1992.
- [88] T. Husberg, I. Denbratt, M. Ringvik, and J. Engström. Heavy-Duty Diesel Combustion with Ultra-Low NOx and Soot Emissions - A Comparison between Experimental Data and CFD Simulations. *Paper No. SAE 2005-01-0380*, 2005.
- [89] Clay Mathematics Institute. <http://www.claymath.org/millennium>.
- [90] T. J. Jacobs, S. V. Bohac, D. N. Assanis, and P. G. Szymkowicz. Lean and Rich Premixed Compression Ignited Combustion in a Light-Duty Diesel Engine. *Paper No. SAE 2005-01-0166*, 2005.
- [91] J. Janicka and N. Peters. Prediction of Turbulent Jet Diffusion Flame Lift-Off Using a Pdf Transport Equation. *Proc. Combust. Inst.*, 19:367–374, 1982.
- [92] H. Jasak. *Error analysis and estimation in the Finite Volume method with applications to fluid flows*. PhD thesis, Imperial College London, 1996.
- [93] Y. J. Jiang, U. Umemura, and C. K. Law. An experimental investigation on the collision behaviour of hydrocarbon droplets. *J. Fluid Mech*, 234:171–190, 1992.
- [94] W. P. Jones. Turbulence Modeling and Numerical Solution Methods for Variable Density and Combusting Flows. In P. A. Libby and F. A. Williams, editors, *Turbulent Reacting Flows*, pages 309–374. Academic Press, 1994.

- [95] W. P. Jones and B. E. Launder. The prediction of laminarization with a two-equation model of turbulence. *Int. J. Heat Mass Transfer*, pages 301–314, 1972.
- [96] W. P. Jones and P. Musonge. Closure of the Reynolds Stress and Scalar Flux Equations. *Phys. Fluid*, 31:3589–3604, 1988.
- [97] W. P. Jones and J. H. Whitelaw. Calculation Methods for Reacting Turbulent Flows: A Review. *Combustion and Flame*, 48:1–26, 1982.
- [98] K. A. De Jong and W. M. Spears. An analysis of the interacting roles of population size and crossover in genetic algorithms. In H. P. Schwefel and R. Männer, editors, *Parallel Problem Solving from Nature - Proceedings of 1st Workshop, PPSN 1*, volume 496, pages 38–47, Dortmund, Germany, 1-3 1991. Springer-Verlag, Berlin, Germany.
- [99] A. Juneja and S. B. Pope. A DNS Study of Turbulent Mixing of Two Passive Scalars. *Phys. Fluids*, 8:2177–2184, 1996.
- [100] T. Kamimoto, H. Yokota, and H. Kobayashi. Effect of High Pressure Injection on Soot Formation Processes in a Rapid Compression Machine to Simulate Diesel Flames. *Paper No. SAE 871610*, 1987.
- [101] T. Kanda, T. Hakozaiki, T. Uchimoto, J. Hatano, N. Kitayama, and H. Sono. PCCI Operation with Early Injection of Conventional Diesel Fuel. *Paper No. SAE 2005-01-0378*, 2005.
- [102] A. Kazakov, H. Wang, and M. Frenklach. Detailed Modeling of Soot Formation in Laminar Premixed Ethylene Flames at a Pressure of 10 bar. *Combustion and Flame*, 100:111–120, 1995.
- [103] J. Kerekes, S. Ohoka, and O. Horoda. The Design and Concept of the Duramax 6600 Diesel Engine. *Paper No. SAE 2001-01-2703*, 2001.
- [104] B. Khalighi, S. H. El Thary, D. C Haworth, and M. S. Huebler. Computation and Measurement of Flow and Combustion in a Four-Valve Engine with Intake Variations. *Paper No. SAE 950287*, 1995.

-
- [105] M. Kim, R. D. Reitz, and S.-C. Kong. Modeling Early Injection Processes in HSDI Diesel Engines. *Paper No. SAE 2006-01-0056*, 2006.
- [106] Y. Kim, H. Kim, K. kim, D. Lee, and K. Lee. A study on the characteristics of mixture formation and combustion in a PCCI engine using an early multiple injection strategy. In *Proceedings of the 10th International Conference on Liquid Atomization and Spray Systems (ICLASS-2006)*, 2006.
- [107] A. N. Kolmogorov. Local Structure of Turbulence in Incompressible Viscous Fluid for Very Large Reynolds Number. *Doklady AN. SSSR*, 30(1 and 2):299–303, 1941.
- [108] A. N. Kolmogorov. Equations of Turbulent Motion of an Incompressible Fluid. *Physics*, 6(1 and 2):56–58, 1942.
- [109] S. Kook and C. Bae. Combustion Control Using Two-Stage Diesel Fuel Injection in a Single Cylinder PCCI Engine. *Paper No. SAE 2004-01-0938*, 2004.
- [110] H. J. Koss. *Spektroskopische Untersuchungen zur Kraftstoffeinspritzung*. PhD thesis, RWTH Aachen, 1994.
- [111] K. Krishnakumar. Micro-Genetic Algorithms for stationary and non-stationary function optimization. In *SPIE*, number 1196-32, November 1989.
- [112] Christian Krüger. *Validierung eines 1D-Spraymodells zur Simulation der Gemischbildung in direkteinspritzenden Dieselmotoren*. PhD thesis, RWTH Aachen, 2001.
- [113] V. R. Kuznetsov. Effect of turbulence on the formation of large superequilibrium concentration of atoms and radicals in diffusion Flames. *Mehan. Zhidkosti Gasa*, 6:3–9, 1982.
- [114] B. E. Launder and B. I. Sharma. Application of the Energy Dissipation Model of Turbulence to the Calculation of Flow Near a Spinning Disc. *Letters in Heat and Mass Transfer*, 1(2):131–138, 1974.
- [115] G.A. Lavoie, J.B. Heywood, and J.C. Keck. *Combust. Sci. Technol.*, 1:313–326, 1970.

- [116] V. G. Levich. *Physicochemical Hydrodynamics*. Prentice Hall, 1962.
- [117] S. K. Liew, K. N. C. Bray, and J. B. Moss. A Stretched Laminar Flamelet Model of Turbulent Nonpremixed Combustion. *Combust. Flame*, 56:199–213, 1984.
- [118] A. Liñán. The asymptotic structure of counterflow diffusion flames for large activation energies. *Acta Astronautica*, 1:1007–1039, 1974.
- [119] F. C. Lockwood and A. S. Naguib. The prediction of the fluctuations in the properties of free, round-jet, turbulent, diffusion flames. *Combustion and Flame*, 24:109–124, 1975.
- [120] K. F. Man, K. S. Tang, and S. Kwong. *Genetic Algorithms*. Springer, first edition, 1999.
- [121] D. L. Marchisio and R. O. Fox. Solution of Population Balance Equation Using the Direct Quadrature Method of Moments. *Journal of Aerosol Science*, 36:43–73, Vol. 36, pp. 43-73, 2005.
- [122] R. Masuda, T. Fuyuto, M. Nagaoka, E. von Berg, and R. Tatschl. *Validation of Diesel Fuel Spray and Mixture Formation from Nozzle Internal Flow Calculation*. PhD thesis, SAE Paper No. 2005-01-2098, 2005.
- [123] F. Mauss. *Entwicklung eines kinetischen Modells der Rußbildung mit schneller Polymerisation*. PhD thesis, RWTH Aachen, 1997.
- [124] F. Mauss and H. Bockhorn. Soot Formation in Premixed Hydrocarbon Flames: Prediction of Temperature and Pressure Dependence. *Z. Phys. Chem.*, 188:45–60, 1995.
- [125] F. Mauss, T. Schäfer, and H. Bockhorn. Inception and Growth of Soot Particles in Dependence on the Surrounding Gas Phase. *Combustion and Flame*, 99:697–705, 1994.
- [126] F. Mauss, B. Trilken, B. Breitbach, and N. Peters. *Soot Formation in Combustion*, chapter Soot Formation in Partially Premixed Diffusion Flames. Springer Verlag, 1994.

-
- [127] R. McGraw. Description of aerosol dynamics by the quadrature method of moments. *Aerosol Sci. Tech.*, 27:255–265, 1997.
- [128] J. McInnes and F. V. Bracco. Comparisons of Deterministic and Stochastic Computations of Drop Collisions in Dense Sprays. In S. Orand and J. P. Boris, editors, *Numerical Approaches to Combustion Modeling*, volume 135 of *Progress in Astronautics and Aeronautics*, pages 615–642. 1991.
- [129] B. Mewes, G. Bauer, and D. Brüggemann. Fuel Vapor Measurements by Linear Raman Spectroscopy Using Spectral Discrimination from Droplet Interferences. *Applied Optics*, 38(6):1040–1045, February 1999.
- [130] R. R. Meyers and E. E. O’Brien. On The Joint PDF of a Scalar and Its Gradient. Informal Report BNL-28287, Brookhaven National Laboratory, 1980.
- [131] R. R. Meyers and E. E. O’Brien. The Joint PDF of a Scalar and Its Gradient at a Point in a Turbulent Fluid. *Combustion Science and Technology*, 26:123–134, 1981.
- [132] Z. Michalewicz. *Genetic Algorithms + Data Structures = Evolution Programs*. Springer, second edition, 1994.
- [133] J. A. Miller and C. T. Bowman. Mechanism of. Modeling of Nitrogen Chemistry in Combustion. *Prog. Energy Combust. Sci.*, 15:287–338, 1989.
- [134] J. A. Miller and C. F. Melius. Kinetic and Thermodynamic Issues in the Formation of Aromatic Compounds in Flames of Aliphatic Fuels. *Combustion and Flame*, 91:21–39, 1992.
- [135] J. A. Miller, J. V. Volponi, and J.-F. Pauwels. The Effect of Allene Addition on the Structure of a Rich $C_2H_2/O_2/Ar$ Flame. *Combustion and Flame*, 105:451–461, 1996.
- [136] A. Minato, T. Tanaka, and T. Nishimura. Investigation of Premixed Lean Diesel Combustion with Ultra High Pressure Injection. *Paper No. SAE 2005-01-0914*, 2005.

- [137] U. C. Müller. Der Einfluß von Strahlungsverlusten auf die thermische NO-bildung in laminaren CO-H₂-Diffusionsflammen. Master's thesis, RWTH Aachen, 1989.
- [138] M. P. B. Musculus. Multiple Simultaneous Optical Diagnostic Imaging of Early-Injection Low-Temperature Combustion in a Heavy-Duty Diesel Engine. *Paper No. SAE 2006-01-0079*, 2006.
- [139] J. Nagle and R. F. Strickland-Constable. Oxidation of Carbon between 1000-2000 °C. In *Proc. 5th Carbon Conference*, pages 265–325, 1962.
- [140] M. Nehse, J. Warnatz, and Ch. Chevalier. Kinetic Modelling of the Oxidation of Large Aliphatic Hydrocarbons. In *Twenty-Sixth Symposium (International) on Combustion*, pages 773–780, Pittsburgh, 1996. The Combustion Institute.
- [141] N. Nordin. *Complex Chemistry Modeling of Diesel Spray Combustion*. PhD thesis, Chalmers University of Technology, 2000.
- [142] H. Oertel. *Optische Strömungsmesstechnik*. G. Braun Verlag, 1989.
- [143] H. Ogawa, N. Miyamoto, H. Shimizu, and S. Kido. Characteristics of Diesel Combustion in Low Oxygen Mixtures with Ultra-High EGR. *Paper No. SAE 2006-01-1147*, 2006.
- [144] K. Ohishi and T. Maeda. The new common rail fuel system for the Duramax 6600 V8 Diesel engine. *Paper No. SAE 2001-01-2704*, 2001.
- [145] K. Okude, K. Mori, S. Shiino, and T. Moriya. Premixed Compression Ignition (PCI) Combustion for Simultaneous Reduction of NO_x and Soot in Diesel Engine. *Paper No. SAE 2004-01-1907*, 2004.
- [146] O'Rourke. *Collective Drop Effects on Vaporizing Liquid Sprays*. PhD thesis, Princeton, 1988.
- [147] P. J. O'Rourke and A. A. Amsden. The TAB Method for Numerical Calculation of Spray Droplet Breakup. *Paper No. SAE 872089*, 1987.

-
- [148] M. R. Overholt and S. B. Pope. Direct Numerical Simulation of a Passive Scalar with Imposed Mean Gradient in Isotropic Turbulence. *Phys. Fluids*, 8:3128–3148, 1996.
- [149] R. H. F. Pao. *Fluid Dynamics*. Charles E. Merrill books, Columbus, Ohio, 1967.
- [150] M. A. Patterson, S. C. Kong, G. Hampson, and R. D. Reitz. Modeling the Effects of Fuel Injection Characteristics on Diesel Engine Soot and NOx Emissions. *Paper No. SAE 940523*, 1994.
- [151] M. A. Patterson and R. D. Reitz. Modeling the Effects of Fuel Spray Characteristics on Diesel Engine Combustion and Emission. *Paper No. SAE 980131*, 1998.
- [152] N. Peters. Local Quenching of Diffusion Flamelets and Non-Premixed Turbulent Combustion. *Combust. Sci. and Technol.*, 30:1–17, 1983.
- [153] N. Peters. Laminar Diffusion Flamelet Models in Non-Premixed Turbulent Combustion. *Prog. Energy Combust. Sci.*, 10:319–339, 1984.
- [154] N. Peters. Numerical and Asymptotic Analysis of Systematically Reduced Reaction Schemes for Hydrocarbon Flames. In R. Glowinsky, B. Larrouturou, and R. Temum, editors, *Numerical Simulation of Combustion Phenomena, Lecture Notes in Physics*, pages 90–109. Springer-Verlag, Berlin, 1985.
- [155] N. Peters. Laminar Flamelet Concepts in Turbulent Combustion. *Proc. Combust. Inst.*, 21:1231–1250, 1986.
- [156] N. Peters. *Turbulent Combustion*. Cambridge University Press, 2000.
- [157] N. Peters and N. Rogg. Reduced Kinetic Mechanisms for Applications in Combustion Systems. In N. Peters and N. Rogg, editors, *Lecture Notes in Physics, M15*. Springer-Verlag, Heidelberg, 1993.
- [158] N. Peters and J. Weber. The effects of spray formation and evaporation on mixing, auto-ignition and combustion in Diesel engines. In *THIESEL 2006, Conference on Thermo- and Fluid Dynamic Processes in Diesel Engines*, 2006.

- [159] U. Pfahl, K. Fiewegger, and G. Adomeit. Shock Tube Investigation of Ignition Delay Times of Multicomponent Fuel/Air-Mixtures under Engine Relevant Conditions. Technical report, IDEA EFFECT, 1996.
- [160] L. M. Pickett and D. L. Siebers. Non-Sooting, Low Flame Temperature Mixing-Controlled DI Diesel Combustion. *Paper No. SAE 2004-01-1399*, 2004.
- [161] M. Pilch and C. A. Erdmann. Use of Breakup Time Data and Velocity History Data to predict the Maximum Size of stable Fragments for acceleration-induced Breakup of a Liquid drop. *Int. J. of Multiphase Flow*, 13(6):741–757, 1987.
- [162] H. Pitsch. *Modellierung der Zündung und Schadstoffbildung bei der dieselmotorischen Verbrennung mit Hilfe eines interaktiven Flamelet-Modells*. PhD thesis, RWTH Aachen, 1997.
- [163] H. Pitsch. Unsteady Flamelet Modeling of Differential Diffusion in Turbulent Jet Diffusion Flames. *Combust. Flame*, 123:358–374, 2000.
- [164] H. Pitsch and N. Peters. Reduced kinetics of multicomponent fuels to describe the auto-ignition, flame propagation and post flame oxidation of gasoline and Diesel fuels. Technical report, IDEA EFFECT, 1996.
- [165] H. Pitsch and N. Peters. Investigation of the Ignition Process of Sprays Under Diesel Engine Conditions Using Reduced n-Heptane Chemistry. *Paper No. SAE 982464*, 1998.
- [166] C. J. Pope and J. B. Howard. Simultaneous Particle and Molecule Modeling (SPAMM): An Approach for Combining Sectional Aerosol Equations and Elementary Gas-Phase Reactions. *Aerosol. Sci. Technol.*, 27:73–94, 1997.
- [167] S. B. Pope. Consistent Modeling of Scalars in Turbulent Flows. *Phys. Fluids*, 26:404–408, 1983.
- [168] S. L. Post and J. Abraham. Modeling the outcome of drop-drop collisions in Diesel sprays. *Int. Journ. of Mult. Flow*, 28:997–1019, 2002.
- [169] L. Prandtl. Über die ausgebildete Turbulenz. *ZAMM*, 5:136–139, 1925.

-
- [170] A. Putnam. Integratable form of the drop drag coefficient. *American Rocket Society Journal*, 31:1467–1468, 1961.
- [171] J. Qian and C. K. Law. Regimes of coalescence and separation in droplet collision. *J. Fluid Mech.*, 331:59–80, 1997.
- [172] W. E. Ranz and W. R. Marshall. Evaporation from Drops: Part I+II. *Chem. Eng. Prog.*, 48:141–146,173–180, 1952.
- [173] R. D. Reitz. Modeling Atomization Process in High-Pressure Vaporizing Sprays. *Atomization and Spray Technology*, 3:309–337, 1987.
- [174] R. D. Reitz and F. V. Bracco. Mechanisms of Breakup of Round Liquid Jets. In *Encyclopedia of Fluid Mechanics*. Gulf Publishing Company, Houston, 1986.
- [175] R. D. Reitz and R. Diwakar. Structure of High-Pressure Fuel Sprays. *Paper No. SAE 870598*, 1987.
- [176] L. M. Ricart, R. D. Reitz, and J. Deck. Comparisons of Diesel Spray Liquid Penetration and Vapor Fuel Distribution With In-Cylinder Optical Measurements. *Transactions of the ASME*, 122:588–595, 2000.
- [177] L. M. Ricart, J. Xin, G. R. Bower, and R. D. Reitz. In-Cylinder Measurement and Modeling of Liquid Fuel Spray Penetration in a Heavy- Duty Diesel Engine. *Paper No. SAE 971591*, 1997.
- [178] K. J. Richards, M. N. Subramaniam, R. D. Reitz, M.-C. Lai, N. A. Henein, and P. C. Miles. Modeling the Effects of EGR and Injection Pressure on Emissions in a High-Speed Direct-Injection Diesel Engine. *Paper No. SAE 2001-01-1004*, 2001.
- [179] J. C. Rotta. Statistische Theorie nichthomogener Turbulenz. *Zeitschrift für Physik*, 129:547–572, 1951.
- [180] C. J. Rutland, N. Ayoub, H. Han, G. Hampson, S.-C. Kong, D. Mather, M. Musculus, M. Patterson, L. Ricart, P. Stephenson, and R. D. Reitz. Progress towards Diesel Combustion Modeling. *Paper No. SAE 952429*, 1995.

- [181] B. Sareni and L. Krähenbühl. Fitness Sharing and Niching Methods Revisited. *IEEE Transaction on Evolutionary Computation*, 2(3):97–106, 1998.
- [182] A. Schack. Die Strahlung der Feuergase und ihre praktische Bedeutung. *Zeitung für Technischen Physik*, 5:267–278, 1924.
- [183] J. D. Schaffer, R. Caruana, L. Eshelman, and R. Das. A study of control parameters affecting online performance of genetic algorithms for function optimization. In J. D. Schaffer, editor, *Proceedings of the 3rd ICGA*, San Mateo CA, 1989. Morgan-Kaufmann Publishers.
- [184] K. Schmid. Vorlesung: Einführung in die Populationsgenetik -Genetischer Drift. Master's thesis, Friedrich-Schiller-Universität Jena, 2004.
- [185] D. P. Schmidt and C. J. Rutland. A New Droplet Collision Algorithm. *Journal of Computational Physics*, 164:62–68, 2000.
- [186] D. P. Schmidt and P. K. Senecal. Improving the Numerical Accuracy of Spray Simulations. *SAE Paper No. 2002-01-1113*, 2002.
- [187] C. Schugger and U. Renz. Einfluss der Düsengeometrie und der Druckrandbedingung auf den primären Strahlaufbruch bei der Diesel-Direkteinspritzung. In *Spray 2001*. TU Hamburg-Harburg, 2001.
- [188] J. H. Seinfeld. *Atmospheric Chemistry and Physics of Air Pollution*. New York, 1986.
- [189] D. L. Siebers. Liquid-Phase Fuel Penetration in Diesel Sprays. *Paper No. SAE 980809*, 1998.
- [190] D. L. Siebers and C. F. Edwards. Autoignition of Methanol and Ethanol Sprays under Diesel Engine Conditions. *Paper No. SAE 870588*, 1987.
- [191] K. Siegmann and K. Sattler. Formation mechanism for polycyclic aromatic hydrocarbons in methane flames. *Journal of Chemical Physics*, 112:698–709, 2000.
- [192] R. M. Siewert. Spray Angle and Rail Pressure Study for Low NOx Diesel Combustion. *Paper No. SAE 2007-01-0122*, 2007.

- [193] S. Simescu, T. W. Ryan III, G. D. Neely, A. C. Matheaus, and B. Surampudi. Partial Pre-Mixed Combustion with Cooled and Uncooled EGR in a Heavy-Duty Diesel Engine. *Paper No. SAE 2002-01-0963*, 2002.
- [194] W. J. Smith and D. J. Timoney. Fuel Injection Rate Analysis - A New Diagnostic Tool for Combustion Research. *Paper No. SAE 92224*, 1992.
- [195] C. G. Speziale, R. Abid, and E. C. Anderson. A Critical Evaluation of Two-Equation Models for Near Wall Turbulence. *AIAA Paper 90-1481*, 1990.
- [196] S. E. Stein, J. A. Walker, M. M. Suryan, and A. Fahr. A New Path to Benzene in Flames. In *Proc. Combust. Inst.*, volume 23, pages 85–91. The Combustion Institute, Pittsburgh, 1991.
- [197] T.F. Su, M. A. Patterson, R. D. Reitz, and P. V. Farrell. Experimental and Numerical Studies of High Pressure Multiple Injection Sprays. *Paper No. SAE 960861*, 1996.
- [198] Y. Sun and R. D. Reitz. Modeling Diesel Engine NO_x and Soot Reduction with Optimized Two-Stage Combustion. *Paper No. SAE 2006-01-0027*, 2006.
- [199] C. J. Sung, B. Li, H. Wang, and C. K. Law. Structure and Sooting Limits in Counterflow Methane/Air and Propane/Air Diffusion Flames from 1 to 5 Atmospheres. In *Proc. Combust. Inst.*, volume 27, pages 1523–1530. The Combustion Institute, Pittsburgh, 1998.
- [200] G. I. Taylor. The Shape and Acceleration of a Drop in a High Speed Air Stream. In *The Scientific Papers of G. I. Taylor*, volume 3, pages 457–464. Cambridge University Press, 1983.
- [201] A. S. Uyar, G. Eryigit S., and Sariel. An Adaptive Mutation Scheme in Genetic Algorithms for Fastening the Convergence to the Optimum. In *Proceedings of 3rd APIS: Asian Pacific International Symposium on Information Technologies*, 2004.

- [202] R. M. Wagner, J. b. Green, T. Q. Dam, K. D. Edwards, and J. M. E. Storey. Simultaneous Low Engine-Out NO_x and Particulate Matter with Highly Diluted Diesel Combustion. *Paper No. SAE 2003-01-0262*, 2003.
- [203] F. Wahlin, A. Cronhjort, U. Olofsson, and H.-E. Angström. Effect of Injection Pressure and Engine Speed on Air/Fuel Mixing and Emissions in a Pre-Mixed Compression Ignited (PCI) Engine Using Diesel Fuel. *Paper No. SAE 2004-01-2989*, 2004.
- [204] B. Walter and B. Gatellier. Development of the High Power NADITM Concept Using Dual Mode Diesel Combustion to Achieve Zero NO_x and Particulate Emissions. *Paper No. SAE 2002-01-1744*, 2002.
- [205] Y. Wan. *Numerical Study of Transient Fuel Sprays with Autoignition and Combustion under Diesel-Engine relevant Conditions*. PhD thesis, RWTH Aachen, 1997.
- [206] Y. Wan and N. Peters. Scaling of Spray Penetration with Evaporation. *Atom. Sprays*, 9:111–132, 1999.
- [207] J. Weber, N. Peters, H. Bockhorn, and R. Pittermann. Numerical Simulation of the Evolution of the Soot Particle Size Distribution in a DI Diesel Engine Using an Emulsified Fuel of Diesel-Water. *Paper No. SAE 2004-01-1840*, 2004.
- [208] J. Weber, N. Peters, A. Pawlowski, R. Kneer, C. A. Hergart, S. H. El Tahry, and A. Lippert. Diesel Spray Characterization Using a Micro-Genetic Algorithm and Optical Measurements. *SAE Paper No. 2006-01-1115*, 2006.
- [209] J. Weber, P. Spiekermann, and N. Peters. Model Calibration for Spray Penetration and Mixture Formation in a High Pressure Fuel Spray Using a Micro-Genetic Algorithm and Optical Data. *Paper No. SAE 2005-01-2099*, 2005.
- [210] J. Weber, P. Spiekermann, and N. Peters. Comparison of Experimental Investigation and Numerical Simulation of a High Pressure Fuel Spray. In *Proceedings of the 10th International Conference on Liquid Atomization and Spray Systems (ICLASS-2006)*, 2006.

-
- [211] J. Weber, H. W. Won, and N. Peters. Experimental Validation of a Surrogate Fuel for Diesel. *Paper No. JSAE 20077166*, 2007.
- [212] J. Z Wen, M. J. Thomson, S. H. Park, S. N. Rogak, and M. F. Lightstone. Study of soot growth in a plug flow reactor using a moving sectional model. *Proc. Comb. Inst.*, 30:1477–1484, 2004.
- [213] P. R. Westmoreland, A. M. Dean, J. B. Howard, and J. P. Longwell. Forming Benzene in Flames by Chemically Activated Isomerization. *J. Phys. Chem*, 93:8171, 1989.
- [214] D. C. Wilcox. *Turbulence Modeling for CFD*. DCW Industries, Inc., 1993.
- [215] F. A. Williams. Spray Combustion and Atomization. *Phys. Fluids*, 1958.
- [216] F. A. Williams. Recent Advances in Theoretical Descriptions of Turbulent Diffusion Flames. In S. N. B. Murthy, editor, *Turbulent Mixing in Nonreactive and Reactive Flows*, pages 189–208. Plenum Press, New York, 1975.
- [217] F. A. Williams. *Combustion Theory*. The Benjamin/Cummins Publishing Co., Menlo Park Ca., 1985.
- [218] M. Wulkow. Feature Article - The Simulation of Molecular Weight Distributions in Polyreaction Kinetics by Discrete Galerkin Methods. *Macromolecular Theory Simulation*, 5, 1996.
- [219] Y. Yoshihara, A. Kazakov, H. Wang, and M. Frenklach. Reduced Mechanism of Soot Formation - Application to Natural Gas-Fueled Diesel Combustion. In *Proc. Combust. Inst.*, volume 25, pages 941–948, 1994.
- [220] S. Zeiermann and M. Wolfshtein. Turbulent Time Scale for Turbulent-Flow Calculations. *AIAA Journal*, 24(10):1606–1620, 1986.
- [221] Y. B. Zel'dovich. The Oxidation of Nitrogen in Combustion and Explosions. *Acta Physiochim.*, 21, 1946.

A Genetic Algorithms

Many technical problems depend on a large number of variables where an analytical solution is not available due to missing informations or a high level of complexity. Finding the best solution is not always feasible in such circumstances and gives the key-motivation to use an optimization algorithm. Optimization is interpreted as a search strategy to find the best solution in a given parameter space. Different strategies are available depending on the the solution surface and the problem type. Among all various algorithms and strategies, Genetic Algorithms (GA) are a quite promising technique. .

A.1 Evolutionary Algorithms

A.1.1 Basic Evolutionary Operators

Genetic Algorithms belongs to the class of "Evolutionary Algorithms" (EA). Explorative and exploitative search methods are combined with probabilistic transition rules following Charles Darwin's principle "survival of the fittest" [85]. This principle is adopted from the observation that only those species who fit the most appropriate to their surrounding environment have the highest probability to conserve the population. Every possible solution of a problem is interpreted as an individual and evaluated by a fitness score. The parameters of each individual are interpreted as genes, forming a chromosome.

On the basis of the representation of a point in parameter space as an chromosome, several operators mimic the process of evolution. The flow-chart in Fig. A.1 illustrates the evolution process. First, the start generation is initialized randomly. At the begin-

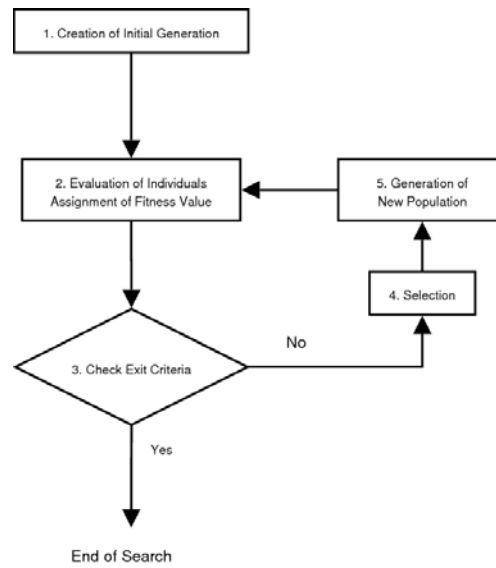


Figure A.1: Flow-Chart of Genetic Algorithm

ning of every iteration step, the individuals are evaluated by addressing a fitness value that is the response of the optimization problem. Next, the exit criteria is queried. If the exit criteria is false, the iteration continues. The selection operator determines the individuals in order to generate a new generation. Additionally, a mutation operator is included. The mutation operator prevents the Genetic Algorithm from finding a local optimum only. After the new generation is created, the iteration re-starts.

A.1.1.1 Encoding/Decoding

The point in parameter space that each individual represents has to be encoded in order to apply operators as selection, reproduction and mutation. Three different types of encoding are available: binary, gray and real encoding. Binary and gray coding [29] are a binary representation. Real coding [66, 120, 132] uses real values and has the advantage that the obtained optimum is independent of the discretization level of the parameter space. The Genetic Algorithm that is applied in this work uses a binary coding. The main advantage is the easy implementation of the various operators but every parameter has to be discretized.

Let the parameter space be defined by N parameters:

$$\mathbf{x} = (x_1, x_2, \dots, x_N)^T \in \mathbb{R}^N \quad (\text{A.1})$$

Every parameter x_i has a lower L_i and upper limit U_i which is discretized by N_i points. Assuming an equidistant distribution, the step-size I_i is given as

$$I_i = \frac{U_i - L_i}{N_i - 1} \quad (\text{A.2})$$

and every parameter x_i is written as

$$x_i = U_i + m_i I_i, m_i \in [0; N_i] \quad (\text{A.3})$$

The integer m_i is an integer and coded as a binary number, denoted as *gene*. The gene has the length l_i that is related to the number of discrete points N_i

$$N_i = 2^{l_i} \quad (\text{A.4})$$

as a power in 2. After encoding of every parameter, the binary representation of an individual is obtained if genes are aligned and forming the *chromosome* or *string*. Each bit of the binary string is denoted as *allele*. Summation over l_i yields the length L of the string

$$L = \sum_{i=1}^n l_i. \quad (\text{A.5})$$

After a new generation has been created, all new parameters are decoded into real parameters. The real parameter is obtained by converting the binary value of m_i into the integer value and computing the parameter x_i from Eq. (A.3).

A.1.1.2 Selection and Reproduction

After the evaluation, each individual are assigned to a fitness value and selected for the reproduction process in adoption of Darwin's principle. The selected individuals are inserted into the *mating pool*. The selection can be either "hard" or "smooth". In a "hard" selection, only strong individuals are chosen whereas in a "smooth" selection, weak individuals also obtain a chance to be considered for reproduction. Two methods are available for the selection process.

Roulette Wheel A very simple procedure is the roulette wheel which is a "smooth" selection process. Every individual is scored by a relative fitness

$$p_i = \frac{f_i}{\sum_{j=1}^N f_j} . \tag{A.6}$$

f_i is the fitness of a given individual i and N denotes the population size. As in a roulette, a disk is splitted into N segments. Every segment represents an individual and its area depends on the relative fitness p_i . Next, the roulette wheel starts turning. When the wheel stops, the individual where the ball rests is selected and joins the mating pool.

Tournament Selection As in a tournament, pairs of individuals are chosen randomly and their fitness values are compared. The individual with the higher fitness value wins and enters the mating pool. Tournament selection is a "hard" selection process.

A.1.1.3 Crossover

Crossover is an exploitative operator and promotes the local search. The mating pool is filled with individuals from which N pairs of parents are chosen randomly. The crossover operator merges the chromosomes from both parents to create a pair of children. Different versions of the crossover operator are possible: single-point, uniform and multi-point crossover. Other types e.g. "segmented crossover", "adaptive crossover" or "shuffle crossover" are discussed in [132].

Single-Point Crossover A random operator determines the position of the allele where the crossover takes place. The chromosomes are cut and swept, yielding the resulting offsprings. As an example, two parents with the following chromosomes of length $l = 6$

chromosome of 1st parent	1 1 0 0 0 1
chromosome of 2nd parent	0 0 1 1 0 0

are splitted at the second allele:

before		after
1 1 0 0 0 1	crossover operator	1 1 1 1 0 0
0 0 1 1 0 0		0 0 0 0 0 1

After merging the chromosomes, the children contains the information of both parents:

chromosome of 1st children	1 1 1 1 0 0
chromosome of 2nd children	0 0 0 0 0 1

Multi-Point Crossover In addition to the single-point crossover, the multi-point crossover operator defines the gene exchange by more than one allele position. Considering the previous single-point crossover, a two-point crossover at the 2nd and 5th allele reads as:

before		after
1 1 0 0 0	crossover operator	1 1 1 1 0
1		1
0 0 1 1 0		0 0 0 0 0
0		0

Uniform Crossover The uniform crossover is at the limit the capability to allow any allele to be exchanged. This type of crossover is controlled by the crossover probability p_c . Every possible combination of exchanging the alleles is therefore available.

Parent 1:	A ₁ B ₀ C ₁ D ₁ E ₀ F ₀ G ₁ H ₁ I ₀
Parent 2:	a ₁ b ₁ c ₁ d ₀ e ₀ f ₁ g ₁ h ₀ i ₁
possible child:	a ₁ B ₀ C ₁ D ₁ e ₀ F ₀ g ₁ h ₀ i ₁

A.1.1.4 Mutation

Single mutation in Genetic Algorithms introduces a random process promoting the exploration of the parameter space. It enhances the algorithm to a global search, forces

the evolution of the population in directions that cannot be detected by the exploitative crossover operator and avoid the concentration on a local optimum denoted as *genetic drift*. The operator switches a single allele with a given mutation probability p_m . Beside that basic mutation operator, other mutation operators have been proposed that work more efficiently.

Jump mutation denotes an operator where randomly one part of the chromosome string is replaced by that of another individual except the parent individuals.

Creep mutation increases or decreases the integer representation m_i of every parameter in Eq. (A.3) randomly, controlled by the creep mutation probability p_{cm} . In [28], the operator rates are chosen as

$$p_{cm} = \frac{L}{N} p_m \quad (\text{A.7})$$

and the rate of single mutation is determined from the population size N_p

$$p_m = \frac{1}{N_p} . \quad (\text{A.8})$$

The importance of mutation is lively and controversy discussed [65]. Mutation works as a "background" operator that is extremely helpful in the optimum search of multi-modal response surfaces. However, if the mutation probability p_m is too high, the explorative search is overweighted. The information of strong individuals is lost and the search performance is decreased.

A.1.2 Operational Rate Settings

The performance of a Genetic Algorithm depends mostly on a balance between exploration and exploitation that has to be adjusted according to the response surface. Unfortunately, the response surface is a priori unknown and must be estimated.

A.1.2.1 Population Size

One key parameter is the population size. A large population size forces the exploitation but for a time-consuming evaluation process, large population sizes are

prohibitive. In [67], the population size is determined from the length L of the chromosome and the arithmetic mean length of a gene \bar{l}_i :

$$N_p = \mathcal{O} \left(\frac{L}{\bar{l}_i} 2^{\bar{l}_i} \right) \quad (\text{A.9})$$

A different approach is obtained from a statistical analysis

$$N_p = \mathcal{O} \left(\left(1 + \frac{1}{B} \right) (L + 2) \right) . \quad (\text{A.10})$$

B is a statistical property that is set between 0.05...0.1.

A.1.2.2 Rate of Mutation

It is difficult to find a general value of the mutation probability p_m . Typically, values between 0.05...0.001 are given in the literature as shown in Tab. A.1. If the mutation

Author	De Jong [98]	Greffentette [70]	Carroll [28]
N_p	50	30	5
No. of generations	1000	n. a.	100
Type of crossover	2-point	2-point	uniform
Rate of crossover	0.6	0.9	0.5
Type of mutation	bit flip	bit flip	none
Rate of mutation	0.001	0.01	none

Table A.1: Reference rates for crossover and mutation

probability is larger than a value of 0.1, the optimization search becomes a random walk and the search performance decreases. However larger mutation rates prevent the genetic drift. A deterministic rule is presented in [184]

$$p_m \approx \frac{1}{N_p} . \quad (\text{A.11})$$

Alternatively, the following relation based on empirical data is proposed in [183]:

$$p_m \approx \frac{1.75}{N_p \sqrt{L}} \quad (\text{A.12})$$

A.1.2.3 Rate of Crossover

The rate of crossover is only applied in case of the uniform crossover operator. However when the population size is large, it can be useful to allow a crossover probability $p_c < 1$ even for the single- and multi-point crossover. Tab. A.1 gives an overview of values for p_c from the literature. At the limit, a child could become a copy of a parent and would be re-evaluated in the new generation. A similar technique is proposed by the elitism operator, section A.2.1.

A.1.2.4 Adaptive Methods

The problem to find appropriate values for the population size, rate of crossover and mutation can be omitted by the use a generation size that can grow or shrink depending on its evolution. That approach can only applied if the evaluation does not consume large calculation time. Independently of the population size, the mutation and crossover rate is adjusted according to the fitness history or its gradient. If the fitness does not change within a discrete time-window, the risk of sticking in a local optimum is omitted by increasing the mutation and crossover rate to find new points in the parameter space that yield a higher fitness value. Details on these methods are found in [70, 183, 10, 47, 120, 201].

A.1.3 Evaluation

All individuals are evaluated on every iteration step in order to assign each individual a fitness value. The Genetic Algorithm does not know anything about the optimization problem itself and treats it as a black-box with an interfaces for input and output. The input are the parameters of each individuals whereas the output or response is required to score every individual. Thus, the only bias is given by the choice of parameters and the discretization of the associated parameter space.

A.1.4 Building Block Hypothesis

Regarding the presented operators of crossover and mutation, it is not obviously that the Genetic Algorithm is able to find a global optimum [65]. An explanation is given by the introduction of the term *schemata* H , its defined length δ and order \mathcal{O} . $H_1 = 1**0**$ is an example where "*" marks those alleles that are not tested. All strings that have at the first and third allele a "1" and "0"-bit are fitting this schemata. The *defining length* $\delta(H_1) = 3$ is the number of alleles between the first and the last bit that defines the schemata. The number of defined bits of the schemata is the *order*, $\mathcal{O}(H_1) = 2$.

A chromosome of length L has 2^L different realizations and 3^L different schemata. A population of n individuals is characterized by the number of schemata that the individuals are differing. At a minimum 2^L and at a maximum $n \cdot 2^L$ schemata are possible. Schemata that have a short defining length are denoted as *building blocks*. They have a higher probability to survive in the next generation. The number of strings of a given population that match a schemata H at the generation t , $m = m(H, t)$ can be analyzed further on by this criteria.

Selection and Reproduction The probability that an individual is chosen for reproduction depends on the individual fitness as expressed in Eq. (A.6) in case of the *roulette wheel*. If the mating pool is filled by n individuals, the mean fitness of the mating pool is defined as

$$\bar{f} = \frac{1}{n} \sum_{i=1}^n f_i. \quad (\text{A.13})$$

Similar to an individual, each schemata H is scored by a fitness $f(H)$ which is the mean fitness of the strings to include the schemata H . The number of strings of schemata H that are filled in the mating pool is

$$m(H, t + 1) = m(H, t) n \frac{f(H)}{\sum_{i=1}^n f_i} = m(H, t) \frac{f(H)}{\bar{f}} \quad (\text{A.14})$$

The fitness of a schemata $f(H)$ is proportional to the mean fitness of the population by the proportionality constant c :

$$f(H) = c \cdot \bar{f} \quad (\text{A.15})$$

From the mating pool and the previous generation, the number of schemata that are obtained in the next generation is

$$m(H, t + 1) = m(H, t) \frac{\bar{f} + c\bar{f}}{\bar{f}} = m(H, t)(1 + c) . \quad (\text{A.16})$$

Assuming that the proportionality factor c is constant, the previous equation is related to the number of schemata at the start generation:

$$m(H, t) = m(H, 0)(1 + c)^t \quad (\text{A.17})$$

The selection mechanism yields an exponential increase in the number of schemata, depending on the average fitness and the fitness of a schemata.

Crossover The probability that a schemata overcomes the crossover operator is defined by

$$p_{sc} \geq 1 - p_c \frac{\delta(H)}{L - 1} \quad (\text{A.18})$$

and depends mostly on the defining length. Crossover is an operator that prevents the schemata transfer to the new generation. The smaller the crossover probability p_c and the smaller the relative defining length, the higher probability p_{sc} is obtained. Together with the selection and production operator, Eq. (A.14) is modified to account for the crossover effect to destroy a schemata:

$$m(H, t + 1) \geq m(H, t) \frac{f(H)}{\bar{f}} \left(1 - p_c \frac{\delta(H)}{L - 1} \right) \quad (\text{A.19})$$

Schemata with a large fitness and short definition length are represented by more and more strings during the iterative evolution process. That explains the exploitative character of the crossover operator. Local areas of large fitness values are exploited and only the random mutation operator enables to jump outside that region.

Mutation If a schemata has overcome the crossover, mutation is the last operator that may destroy a schemata. The probability that the schemata remains unchanged is expressed by

$$p_{sm} = (1 - p_m)^{\mathcal{O}(H)} . \quad (\text{A.20})$$

For small rates of mutation, the r.h.s. is approximated

$$p_{sm} = 1 - p_m \mathcal{O}(H) . \quad (\text{A.21})$$

The additional term yields the final expression for the number of strings of schema H which is transferred from the parent to the children generation

$$m(H, t + 1) \geq m(H, t) \frac{f(H)}{\bar{f}} \left(1 - p_c \frac{\delta(H)}{L - 1} - p_m \mathcal{O}(H) \right) . \quad (\text{A.22})$$

Since the mutation probability is small compared to the crossover probability, the *hypothesis of building blocks*[65] states that schemata which have a high fitness and small defined length and order are assigned to more and more strings in the evolution. Its number increases exponentially by time. The building block hypothesis gives an explanation for the efficiency of Genetic Algorithms.

A.2 GA-Specific Operators

A.2.1 Elitism

Elitism is an operator that re-uses the overall best individuals of the whole population. The schemata of the individual with the highest value is conserved, especially if its defining length or order is large.

A.2.2 Niching

Although exploration and exploitation are balancing and controlled by the operator's rates, the search for an optimum can end in a local optimum. *Niching* is an additional operator which accounts for a high diversity of the population. Sub-populations are created in order to search for multi-optima in parallel over a wider domain but that technique can only applied for a large population size. Among different niching methods, e.g. deterministic crowding [120], preselection and speciation [181], *fitness sharing* is a method to decrease the fitness value artificially if individuals are too self-similar.

The criteria that two individuals are too close to each other is determined by the *sharing function*:

$$\text{sh}(d_{ij}) = \begin{cases} 1 - (d_{ij}/\sigma_s)^\alpha, & \text{if } d_{ij} < \sigma_s \\ 0, & \text{if } d_{ij} \geq \sigma_s \end{cases} \quad (\text{A.23})$$

d_{ij} is a multi-dimensional distance between two individuals i and j which is derived from

$$d_{ij} = \frac{\sqrt{d_{ij}^*}}{n}, d_{ij}^* = \sum_{k=1}^n \left(\frac{x_{ki} - x_{kj}}{U_k - L_k} \right)^2 \quad (\text{A.24})$$

α is a triangular sharing function usually set equal 1.0. σ_s is a minimum self-similarity set equal 0.1. From the sharing function, a weight m_i is calculated for every individual which is the sum of the distance to all other individuals:

$$m_i = \sum_{j=1}^N \text{sh}(d_{ij}) \quad (\text{A.25})$$

The fitness function of every individual is scaled by that weight and an optional weight β that is equal 1.0

$$f'_i = \frac{f_i^\beta}{m_i}. \quad (\text{A.26})$$

A.2.3 μ GA

In many optimization problems the evaluation of every individual is very time consuming. Even though the evaluation is carried out in parallel, the number of available processors is a limiting factor if population sizes between 30 and 100 are used. A different method is followed in [111] by limiting the population size to five individuals. Therefore, this algorithm is denoted as micro (μ)-Genetic Algorithm (μ GA). At the end of the iteration, an additional operator performs a convergence test as shown in Fig. A.2. The test of nominal convergence compares the chromosome of every new individual with the best found individual.

$$D = \frac{\sum_{i=1}^N n_{\text{diff}}}{(N-1)L} \cdot 100\%, \quad (\text{A.27})$$

n_{diff} is the number of differing alleles. If the relative number of alleles differs by less than 5% the children generation is rejected and a new children generation is randomly

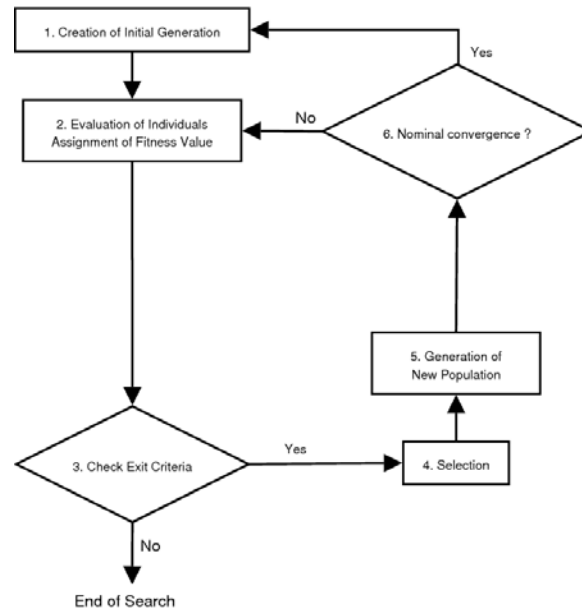


Figure A.2: Flow-Chart of μ GA

initialized. The restart from a random generation prevents the algorithm from the genetic drift. In the μ GA, mutation and niching operators are not useful and therefore are omitted.

A.3 Multi-Objective Optimization

In the simplest case, the fitness value is a single objective function. However, many optimization problems from real world applications are based on multiple objective problems. Genetic Algorithms are currently subject of research to face multi-objective optimization, e. g. Coello et al. [33] developed a Multi-Objective Genetic Algorithm (MOGA) [34]. Classical, single-objective optimization algorithms are nevertheless able to work if a global merit function F is constructed from the single objectives f_i as shown in Fig. A.3. These score the various objectives by the scaling function

$$\Psi_i : \text{objective}_i \longrightarrow f_i . \quad (\text{A.28})$$

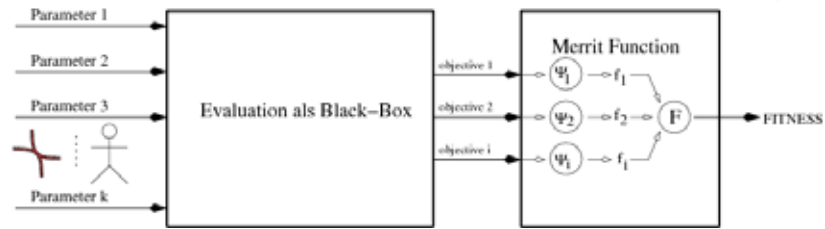


Figure A.3: Construction of merit function

The purpose of the scaling function is to obtain a fitness functions f_i that are all of the same order of magnitude. The final merit function F is computed either as a weighted sum

$$F(\mathbf{x}) = \sum_{i=1}^{N_{\text{obj}}} \omega_i f_i(\mathbf{x}) \quad (\text{A.29})$$

or by a penalty function [132]. Here, the Euclidean norm is applied

$$F(\mathbf{x}) = \left(\frac{1}{r} \sum_{i=1}^{N_{\text{obj}}} |f_i(\mathbf{x}) - y_i(\mathbf{x})|^r \right)^{1/r}. \quad (\text{A.30})$$

The idea of the penalty function is to reduce the distance to a given point $y_i(\mathbf{x})$ which can be viewed as a lower barrier.

B Spray Parameter Sensitivity Study

Most uncertainties in fuel spray simulations are addressed to the unknown initial conditions of spray properties and uncertainties in the underlying spray models. Since a sophisticated model for primary breakup is not existing, the initial conditions of spray model parameters have to address the influence of the nozzle-inflow on the primary breakup. The secondary droplet breakup due to the Kelvin-Helmholtz (KH) and Rayleigh-Taylor (RT) instabilities also requests to adjust model parameters e.g. as investigated in [176, 151, 177, 197]. The found model constants are shown in Tab. B.1. Since experimental data is missing to study the isolated physical processes, a validation

Model Constant	B_1 Eq. (4.17)	C_{RT} Eq. (4.19)	C Eq. (4.24)
Su et al. [197]	45-60	5.33	-
Ricart et al. [177]	-	-	14
Patterson et al. [151]	10	5.3	-
Ricart et al. [176]	60	0.1	14.5

Table B.1: Adjustment of model constants of droplet breakup

of these model parameters cannot be achieved. It is suggested to adjust these model constants with respect to experimental data from spray chamber experiments. For the spray calibration, the influence of spray parameters on the spray penetration has to be identified. Only parameters that show a high sensitivity are included in the parameter space. Independent variables as mesh size, time-step size and total number of parcels are studied as well.

The simulation is performed for engine-like conditions as discussed for the diesel fuel spray in section 5.4.1 but the cylindrical mesh has a diameter of 100 mm and a length

of 90 mm.

The sensitivity study starts from a base design given in Tab. B.2. Furthermore, the

Mesh size	21,000 cells
Time-step size	50 μ s
Number of parcels	50,000
Cone angle	20°
Nozzle discharge coefficient C_d	0.87
Fuel temperature	355 K
SMR of initial droplet distribution	65 μ m
Initial type of droplet distribution function	Mono-disperse
Droplet distribution function for droplet breakup	Rosin-Rammler
Droplet breakup model constant B_1	40
Liquid break-up length C_{dist}	2.5
Collision radius	8e-4

Table B.2: Base set of spray model parameters

influence of every single parameter on the spray penetration and additionally on the SMR of the droplet distribution is investigated.

B.1 Mesh Size

The dependency of the spray simulation on the mesh size can be addressed to the parcel approach itself. The spray distribution function cannot be solved directly but is sampled in Lagrangian coordinates instead. The exchange of properties would require to have a coincident conversion between the physical coordinates of the RANS approach and the Lagrangian coordinates. That request cannot be satisfied and would annihilate the benefit of the Lagrangian approach.

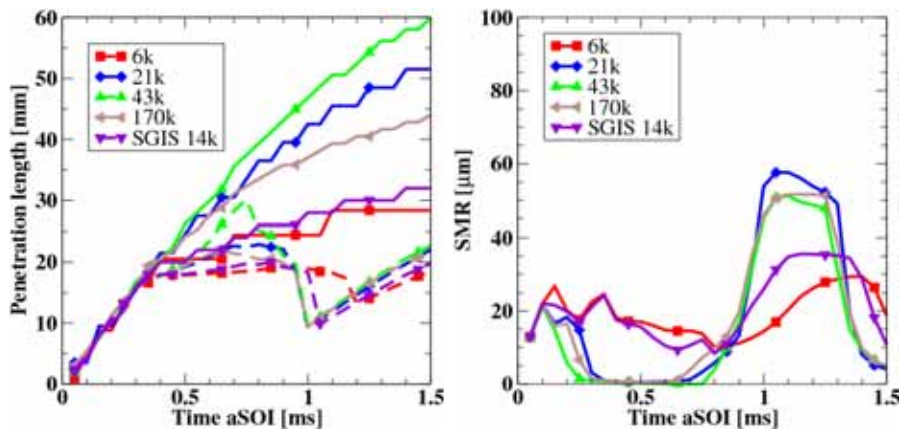
In order to determine the effect of mesh size on spray penetration and SMR, five different meshes of size 6,000, 21,000, 43,000, 170,000 and a non-uniform mesh of 14,480

(section 5.4.1.2) cells are compared. The resulting spray penetration is presented in Fig. B.1. The spray penetration of the gas phase in Fig. B.1(a) strongly depends on the mesh resolution. With increasing mesh size from 6,000 to 43,000 cells the gas phase penetrates faster while for the fine mesh of 171,000 cells the spray penetration is slower.

Concerning the penetration of the liquid phase, a convergent solution cannot be achieved. Similar as for the gas phase, the liquid penetrates deeper with increasing mesh size from 6,000 to 43,000 cells. At 0.7 ms, the liquid spray penetration differs 11 mm. For the fine mesh of 171,000 cells, the liquid spray penetration is similar as for the coarse, non-uniform mesh with 14,480 cells.

The evolution of SMR behaves differently for varying mesh size as seen in Fig. B.1(b). If the mesh size increases the temporal evolution of the SMR has a smaller minimum at 0.5 ms but a larger maximum at 1.2 ms. A convergent evolution is obtained for the mesh of 43,000 cells. A finer resolution does not show any significant changes.

Beside spray penetration, the shape of the spray is investigated and presented at



(a) Spray penetration for liquid and gas phase (b) SMR of droplet distribution

Figure B.1: Dependency of mesh size

two times of $t=500 \mu\text{s}$ and $t=700 \mu\text{s}$ in Fig. B.2. A clover-leaf structure cannot be observed. The width of the spray is a very little wider for the high mesh resolutions on the 43k and 170k mesh. These two meshes show a different axial spray shape than

the coarser meshes. At $t=700\ \mu\text{s}$ spray parcels still exist very far downstream above 22 mm. Spray parcels on the axis are remaining stable and do not break-up into small parcels. Therefore evaporation is less effective and parcels continue to penetrate. All other parameters are investigated for a mesh size of 21,000 cells from now on.

B.2 Time-Step Size

The time-step size is changed between 50, 25, 10, 1 and $0.5\ \mu\text{s}$. At smaller time-step sizes the spray penetrates slower as seen in Fig. B.3(a) for both, liquid and gas phase. At time-step sizes of 1 and $0.5\ \mu\text{s}$ the difference is small and the spray penetration does not change anymore.

The evolution of the SMR in Fig. B.3(b) indicates a similar convergent solution at small time-step sizes. The maximum peak at 1 ms occurs only at a large time-step size of 50 and $25\ \mu\text{s}$. Obviously the SMR is less sensitive to the time-step size than to the spray penetration.

B.3 Number of Parcels

The number of injected parcels is a parameter which has to be sufficiently large enough so that the parcel distribution function resolves the droplet distribution function correctly. Therefore, the number of parcels is varied from 5,000 to 100,000. Both, the spray penetration and the SMR in Fig. B.4 show that a minimum number of 10,000 parcels is mandatory to achieve an independent solution.

B.4 Cone-Angle

By the half-cone angle, the parcel velocity direction is initialized. From the shadow-graph imaging, the spray half-cone angle is determined and may serve as an input. However, the given value is not necessarily the spray angle that results from the spray

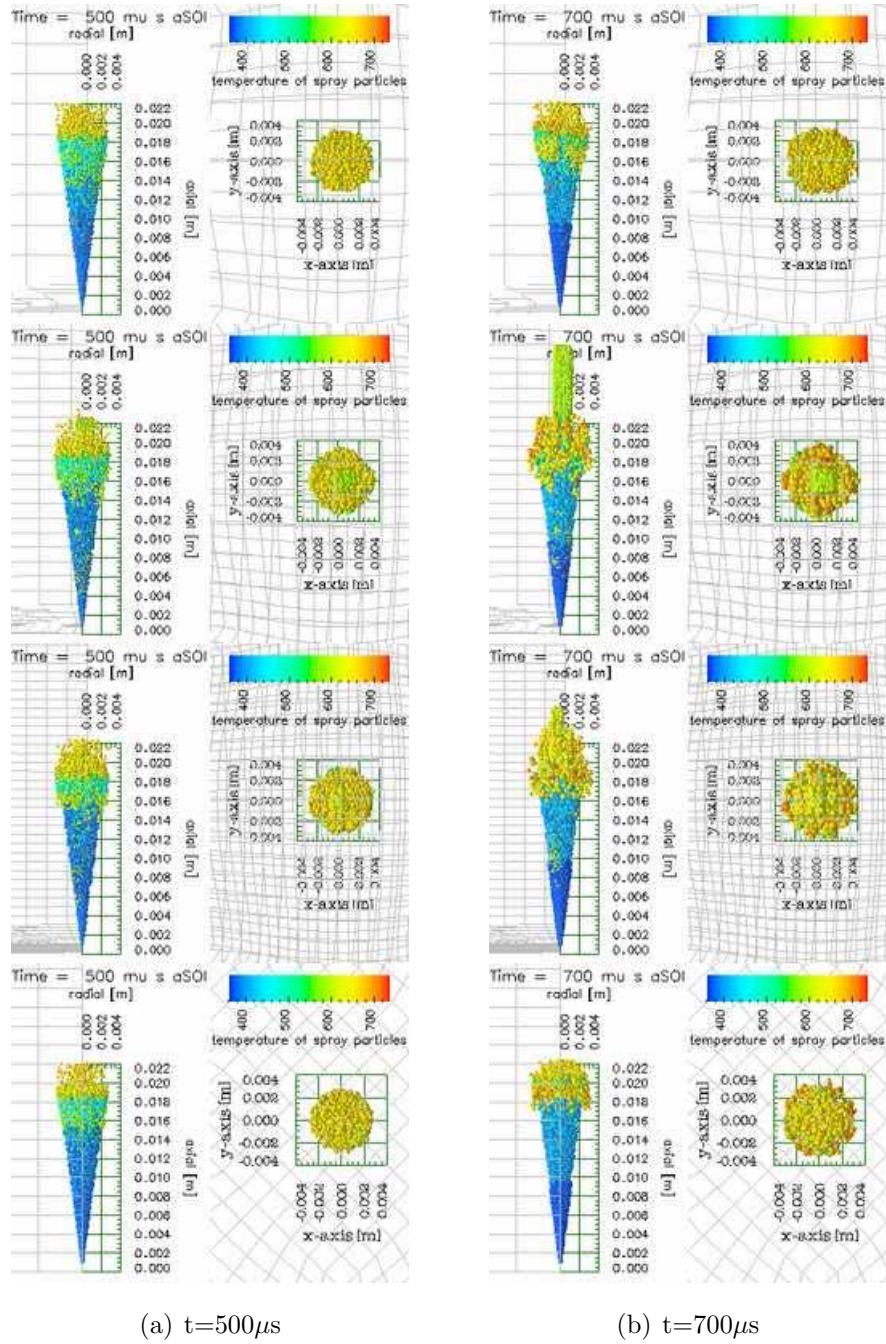
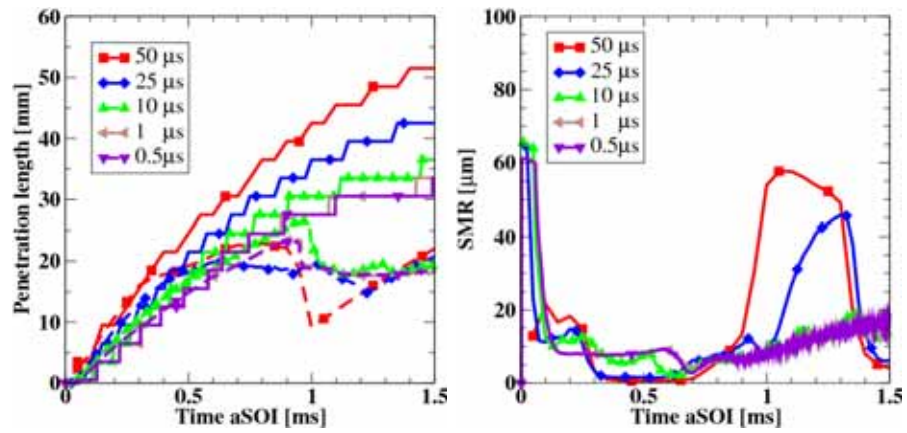
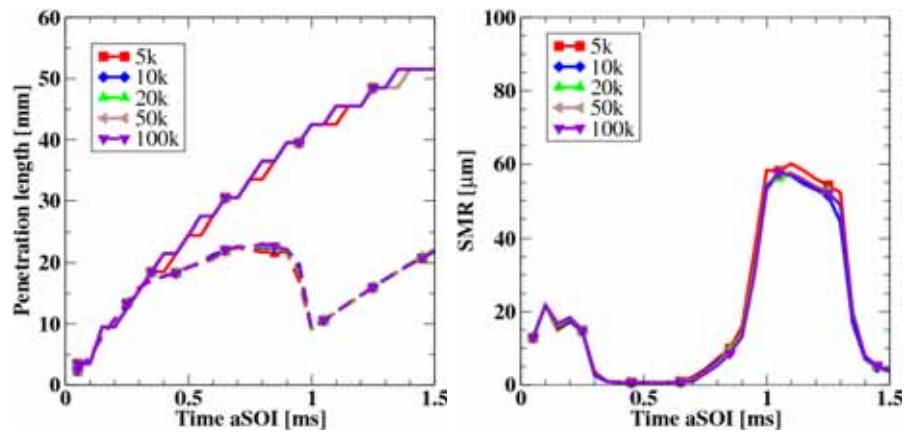


Figure B.2: Mesh analysis of spray shape: 6k, 43k, 170k and SGIS_14k from top to bottom



(a) Spray penetration for liquid and gas phase (b) SMR of droplet distribution

Figure B.3: Dependency of time-step size



(a) Spray penetration for liquid and gas phase (b) SMR of droplet distribution

Figure B.4: Dependency of number of parcels

experiment.

A parameter study from 5° to 20° is performed. The resulting spray penetration in Fig. B.5(a) is only decreasing for angles larger than 10° . A difference in the temporal evolution of the SMR in Fig. B.5(b) occurs only between 1 and $1.3 \mu s$. A half-cone angle larger than 10° results in a decrease of SMR.

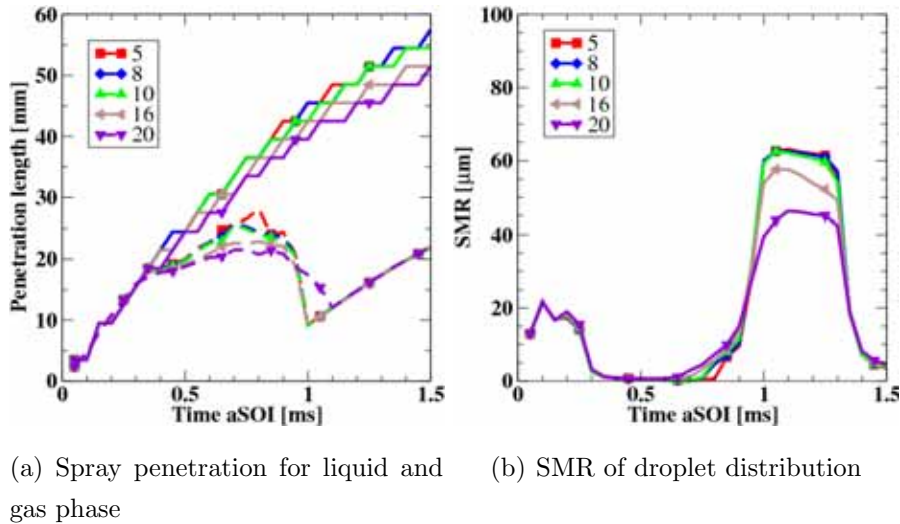
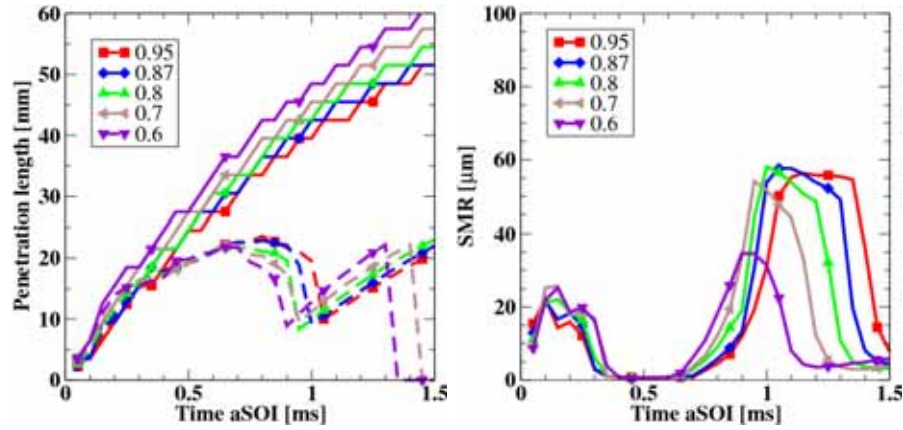


Figure B.5: Dependency of half-cone angle

B.5 Nozzle Discharge Coefficient C_d

The effective nozzle diameter and resulting discharge coefficient that accounts for the flow conditions inside the nozzle is prior to the simulation unknown and has to be estimated from similar nozzles or determined by injection rate and spray momentum measurements. This data is used to determine mass- and velocity independently. If only injection rate measurements are available, the computed velocity profile accounts for an effective nozzle area by introducing the discharge coefficient C_d . A smaller C_d will reduce the effective nozzle hole area and increase the velocity for sake of mass conservation. Therefore, the fuel vapor penetrates faster as presented in Fig. B.6(a) whereas the liquid droplets have a shorter penetration length. The breakup process

is enhanced due to the higher velocity. The breakup results in smaller parcels so that evaporation is forced. The influence on the SMR is seen at late times in Fig. B.6(b). At early times, no strong influence is observed.



(a) Spray penetration for liquid and gas phase (b) SMR of droplet distribution

Figure B.6: Dependency of nozzle discharge coefficient C_d

B.6 Fuel Temperature

The initial fuel temperature cannot be determined exactly. Only the temperature inside the rail is measured but not in the nozzle itself. The residence time is an important factor that influences the fuel temperature. The effect is studied by varying the temperature between 320, 340, 355 and 380 K. The fuel temperature is an initial value for the modeling of the droplet evaporation. If the fuel temperature is increased the evaporation is forced. Hence, the liquid penetration length is shortened and the SMR is increasing at later times. Small droplets are heating up and evaporating faster which is viewed in the penetration of the liquid phase in Fig. B.7(a) and from the SMR in Fig. B.7(b). However, the fuel temperature has no influence on the gaseous phase of the spray,

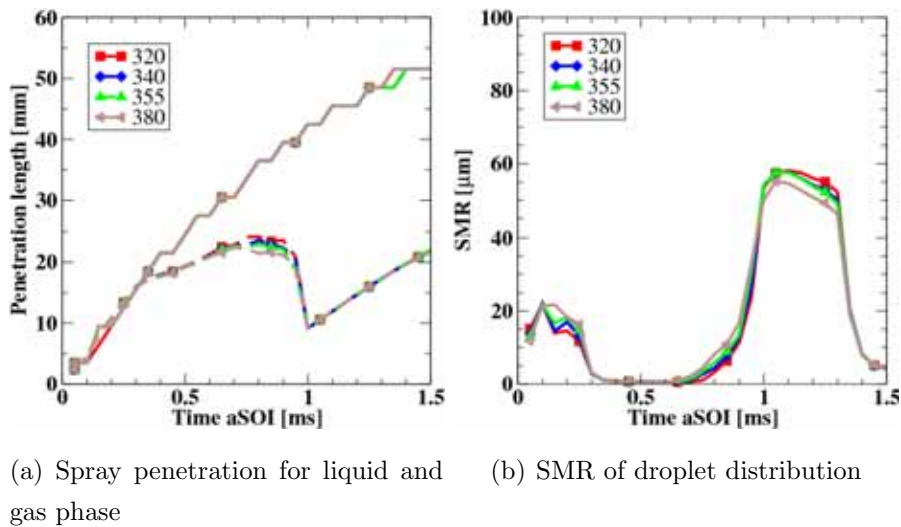


Figure B.7: Dependency of fuel temperature

B.7 Droplet Distribution Function

B.7.1 SMR of Droplet Distribution Function

The initial SMR must address the outcome of the primary breakup which cannot be modelled adequately. In Fig. B.8(a) the slope of the penetration is decreasing with a decreasing SMR from 90, 65, 50 to 10 μm . The initial SMR only has a little effect on the gas phase. For the liquid phase, the evolution of SMR depends strongly on its initial value as illustrated in Fig. B.8(b). A larger initial SMR yields a larger SMR in the early and late injection. At late times the momentum exchange with the entrainment reduces the relative velocity between liquid and gas phase.

B.7.2 Initial Droplet Distribution

The initial droplet distribution is either mono-disperse or according to a distribution function of Rosin-Rammler type. The type of distribution function does not have an influence on the penetration of the gas phase but on the liquid phase and the SMR at

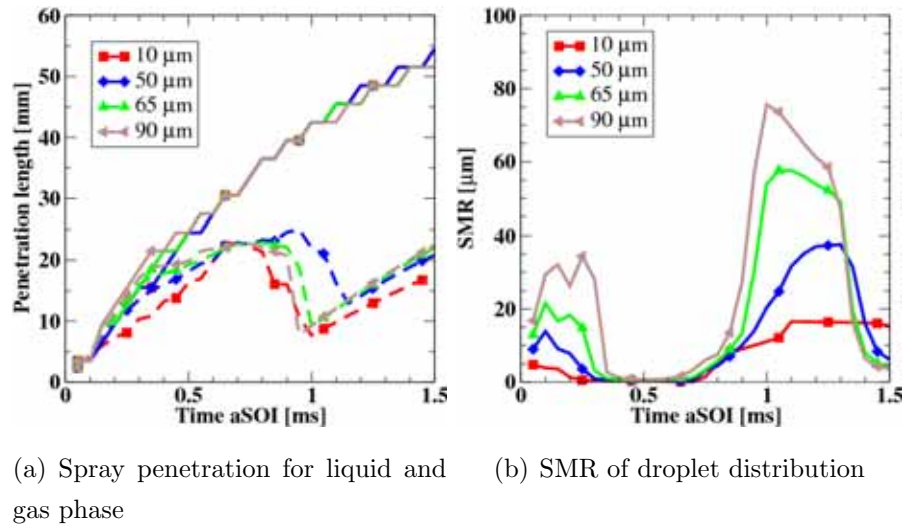
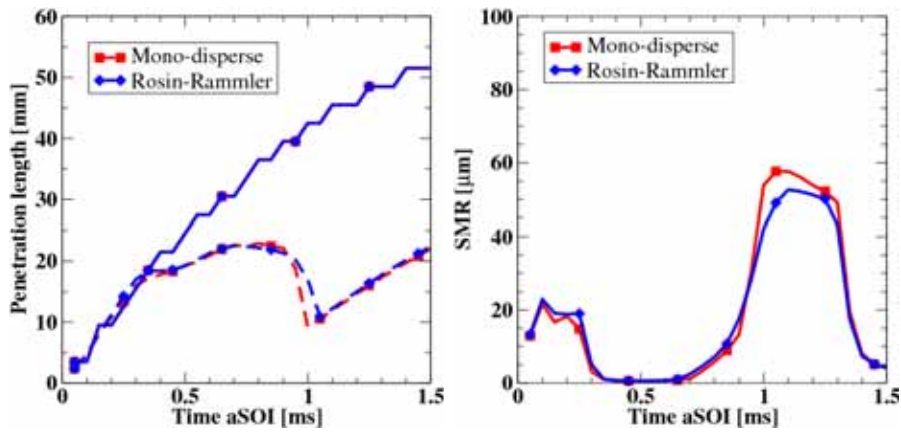


Figure B.8: Dependency of SMR of initial droplet distribution

late times as shown in Fig. B.9(a) and Fig. B.9(b).

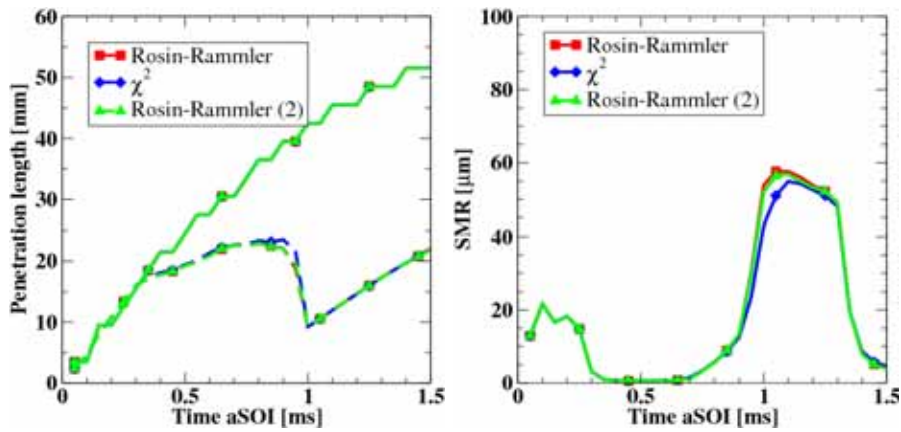
B.7.3 Distribution Function Type

The type of droplet distribution function is either of Rosin-Rammler type or of χ^2 -type. The Rosin-Rammler distribution offers more flexibility because the set of distribution parameter gives another degree of freedom (denoted as Rosin-Rammler type 2). All three distribution functions are compared with and without an initial mono-disperse droplet distribution in Fig. B.10 and Fig. B.11, respectively. The Rosin-Rammler distribution functions show a similar penetration for liquid and gas phase and a similar evolution of SMR. The χ^2 -type distribution function has a slightly larger penetration of the liquid phase but the SMR is a little bit smaller at late times. Without a mono-disperse function, the SMR is at early times a little bit larger. Generally, the mono-disperse function has a smaller SMR at early times and a larger one at late times.



(a) Spray penetration for liquid and gas phase (b) SMR of droplet distribution

Figure B.9: Dependency of type of initial droplet distribution



(a) Spray penetration for liquid and gas phase (b) SMR of droplet distribution

Figure B.10: Dependency of droplet distribution function w/ mono-disperse distribution for primary breakup

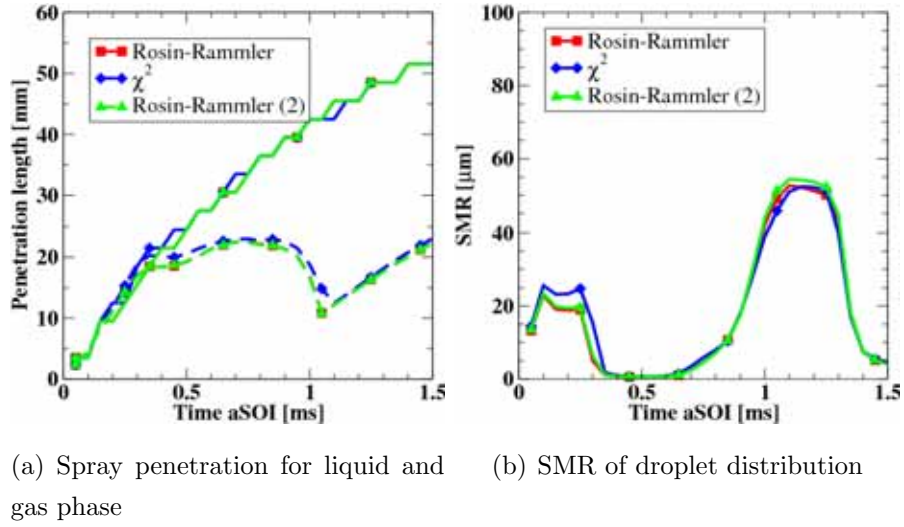


Figure B.11: Dependency of droplet distribution function w/o mono-disperse distribution for primary breakup

B.8 Droplet Breakup

B.8.1 Breakup Model Constant B_1

The breakup model constant B_1 in Eq. (4.17) has to be adjusted according to the experimental data. The main influence of B_1 is seen from Fig. B.12(a). Only the liquid phase of the spray depends on the breakup model constant whereas no influence is seen on the gaseous phase. B_1 is varying from 5 to 60. With increasing B_1 the breakup time τ_{KH} (Eq. (4.17)) is increasing and therefore, the rate of radius change from Eq. (4.16) will decrease. As a consequence, liquid droplets are more stable and less small droplets are formed. Then, evaporation is retarded and the liquid spray penetration increases. This effect is confirmed by the results of the spray penetration and the resulting SMR distribution in Fig. B.12(b).

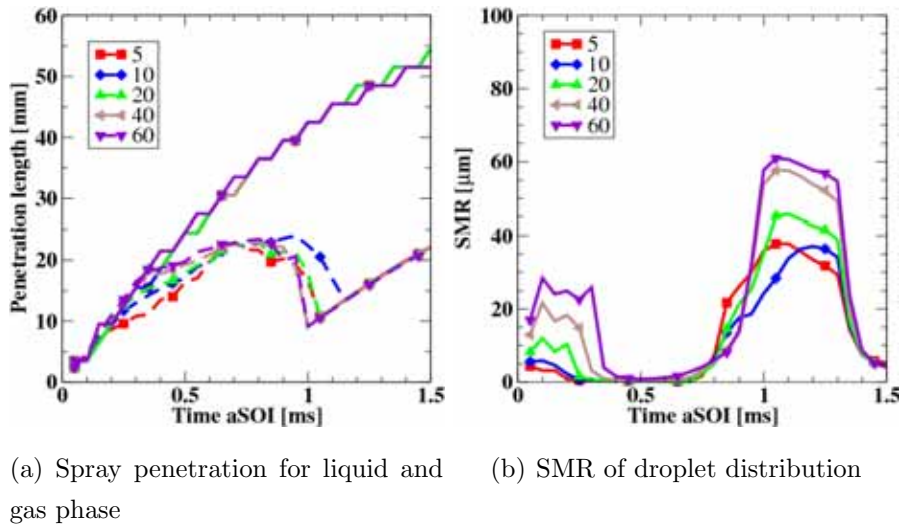


Figure B.12: Dependency of breakup model constant B_1

B.8.2 Liquid Breakup Length

The liquid breakup length from Eq. (4.24) is a criteria to switch from the Kelvin-Helmholtz to the Rayleigh-Taylor induced droplet breakup mode. Rayleigh-Taylor instabilities result in a very fast droplet breakup. The breakup length C , here divided by a conversion factor of 9.12, is varying from 1 to 5.5. As seen from Fig. B.13(a), the breakup length has an influence on the liquid gas phase only. With increasing breakup-length the liquid phase penetrates deeper. The SMR in Fig. B.13(a) becomes smaller with increasing breakup length. The Rayleigh-Taylor breakup does not only accelerate the breakup but more, very small droplets are generated so that evaporation is enhanced.

B.9 Droplet Collision Model

The sensitivity of the collision model is adjusted by the radius of the collision sphere. Only a parcel pair that is located within the same sphere volume and only if approaching each other is probed for an collision event. However since the collision frequency is

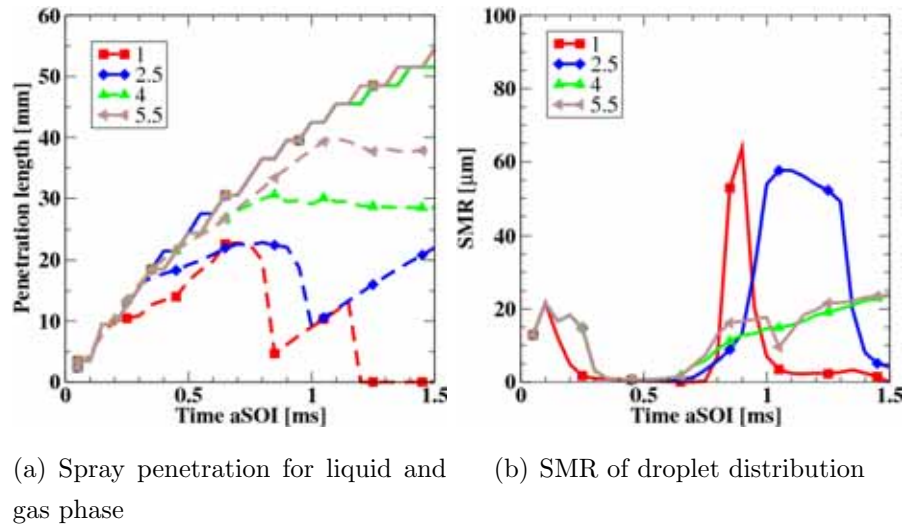
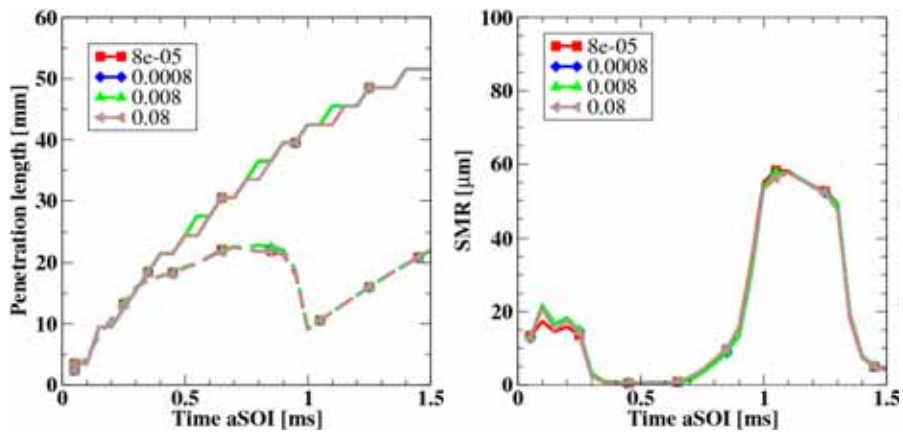


Figure B.13: Dependency of liquid breakup length C_{dist}

inversely proportional to the volume of the collision sphere, a larger or smaller probe-volume may increase or decrease the number of collision pairs but will not necessarily influence the outcome of the collision event itself as the temporal evolution of the spray penetration and SMR in Fig. B.14 indicates.



(a) Spray penetration for liquid and gas phase (b) SMR of droplet distribution

Figure B.14: Dependency of radius of collision sphere

Lebenslauf

Persönliche Daten

Name	Jost Weber
Geburtsdatum	24.04.1973
Geburtsort	Siegen
Familienstand	verheiratet
Nationalität	deutsch

Schulbildung

1979–1983	Grundschule "Am Giersberg" in Siegen
1983–1992	Gymnasium "Am Löhrtor" in Siegen Abschluss: Abitur

Studium

10/1993–10/1995	Grundstudium Maschinenbau an der Universität GH Siegen
10/1995–10/1999	Hauptstudium Maschinenbau an der RWTH Aachen Fachrichtung Wärmetechnik Abschluss: Diplom
9/1997–7/1998	Studium an der INSA de Lyon Fachrichtung Génie Energétique

Beruflicher Werdegang

1/2000 - 5/2000	Wissenschaftliche Hilfskraft am Institut für Technische Mechanik der RWTH Aachen
6/2000 - 1/2007	Wissenschaftlicher Mitarbeiter am Institut für Tech- nische Verbrennung der RWTH Aachen
Seit 2/2007	Mitarbeiter der Fa. DENSO Automotive Deutschland, Aachen Engineering Center, Wegberg

